CRANFIELD INSTITUTE OF TECHNOLOGY

School of Industrial Science

PhD Thesis

Academic Year 1983 - 85

HAMAYUN KABEER AHMED

REMOVAL OF INTERNAL POROSITY IN SUPRAL 150 BY HOT ISOSTATIC PRESSING

Supervisor : Roger Pearce
BA, BSc, FIM, C Eng.

To my Parents

ABSTRACT

In recent years, considerable concern has been shown about the effects SPF cavitation has on the mechanical properties of superplastic alloys. This investigation was undertaken to ascertain whether Hot Isostatic Pressure (HIP) eliminated this cavitation in Supral 150 and correspondingly brought about an improvement in the mechanical properties.

It was found that the density increased with various isothermal anneals; the activation energy for this process was close to that for grain boundary diffusion in aluminium (61.93 KJ mol^{-1}).

The rate of cavity sintering was seen experimentally to be enhanced by the application of pressures greater than 7 MPa, and had an activation energy of 62.42KJ mol^{-1}.

Complete cavity closure occurred when the external pressure was greater than the flow stress of the material at that temperature and strain-rate; the ratio of external pressure (P_e) to flow stress (σ_f) increased with falling HIP temperature. The activation energy at constant strain-rate ($Q_{\dot{\varepsilon}}$) associated with plastic flow under conditions of hole closure was found to be 53.54KJ mol^{-1}; giving a corresponding activation energy at constant stress (Q_σ), which is close to that for lattice diffusion in aluminium.

The alloy used contained a high level of hydrogen which caused blistering on heat treatment, and was also responsible for the reappearance of porosity in subsequently heat-treated material, previously returned to theoretical density; the extent of which was decreased by the use of higher temperatures and pressures or by vacuum degassing the material prior to HIP.

Post SPF room temperature ductility was enhanced by HIP. The scatter in the 0.2% PS and UTS values found in as-received SPF specimens was not altered by the use of low pressure HIP (up to 35 MPa), although higher pressures (100 MPa) did slightly enhance these values and drastically reduced the scatter.

Room temperature fracture of as-received Supral was by a 45^o ductile shear mechanism.

In the SPF cavitated material, the external characteristics of fracture had a more jagged appearance, as the cavitation alters the route of the propagating crack.

SPF material which has been HIPped to remove cavitation, fails in a manner similar to the as-received material.

ACKNOWLEDGEMENTS

I wish to acknowledge the help which I received from both academic and non-academic members in the School of Industrial Science.

In particular, my thanks to my Supervisor Roger Pearce, for his invaluable advice and assistance throughout this research. My thanks also to Freda Parsons and Nan in the Library for making life at Cranfield so much more cheerful.

I am also grateful to the MOD for providing financial assistance and in particular to Dr. D.S. McDarmaid and A. Shakesheff for their invaluable discussions. My thanks also to Superform Metals Ltd., for the supply of materials.

Finally, my thanks to Ann Hills for typing this thesis with patience, efficiency and accuracy.

CONTENTS

LIST OF FIGURES

1. INTRODUCTION

1.1 ALUMINIUM ALLOY DEVELOPMENT FOR AEROSPACE

Aluminium alloys have been developed for aircraft use over the last five decades, progressing from the Durals (Al - Cu - Mg alloys) used in the 1940's to the introduction in the 1950's of the higher strength Al - Zn - Mg - Cu alloys.

In the 1960's, development of supersonic flight raised the operating temperature of the aircraft skin to a level where it became necessary to develop new alloys and thus lead to the iron and nickel containing sheet version of the Al - Cu - Mg alloy known then as RR58 (designated 2618) which was capable of operating at temperatures up to 130°C.

By the late 1960's, aluminium alloy development was confined to improvements of existing conventional alloys (2024-T3, or 7075-T6) by means of microstructural control yielding a range of alloys (2048, 2124, 7050, 7475) which had improved toughness and stress corrosion resistance but little in the way of strength increases over their conventional alloy counterparts (1, 2, 3).

At this stage it would have been right to say that aluminium alloy development was well into the realms of diminishing returns for the effort expended. Yet, the ever present need to reduce weight in aircraft (not only because of the escalation of fuel costs in the early 1970's, but also because of the increasing load of avionics military aircraft now carry) led to a greater impetus for research into higher performance aluminium alloys (4, 5, 6).

1.2 SUPERPLASTIC ALUMINIUM ALLOYS

The phenomenon of superplasticity in metals was observed as early as the 1920's and publications on the subject appeared sporadically until the late 1960's, when interest from the aerospace industry led to research into superplastic aluminium alloys.

Figure 1 shows the number of published papers on superplastic aluminium alloys from 1966 to the present day (7). The publications in any particular year are split into three categories -

(a) Those papers concerned with superplastic aluminium alloy development

(b) Superplastic alloys which also have good room temperature mechanical properties

(c) Commercial alloys which have been thermomechanically treated to give a superplastic response.

The alloys in the first category were those which were developed to understand the phenomena of superplasticity. Initially, studies on the Al - 33% Cu eutectic were prevalent but more complex alloys (Al - Cu - Mg, Al - Zn - Mg, Al - Mg - Si) started to be investigated

as early as 1970, although work on eutectics such as Al - Cu, Al - Ca and Al - Si has continued. Other novel concepts were also studied such as the Al - Al_2O_3 Ga and Al - Ge alloys (7). As Figure 1 shows, research in this category peaked in the mid-1970's and at present further major developments are unlikely.

The second category includes development of superplastic aluminium alloys which exhibit good room temperature properties. Undoubtedly, the first alloy to be developed in this group was the medium strength Al - 6Cu - 0.5Zr (2004), known commercially as SUPRAL 100, which has been used in commercial production of engineering components for nearly 15 years at Superform Metals (8, 9), although none of these has been found useful for use in highly stressed situations.

The high strength version of the SUPRAL alloys (Supral 220) is currently undergoing mechanical and service property evaluation which may indicate its usefulness in highly stressed applications.

The third category consists of the work published in trying to develop superplasticity in materials already used in aircraft manufacture.

Basically, this approach utilises complex thermomechanical treatments (10, 11), which produce a fine grain structure in the sheet rendering it superplastic.

In the USA, the great bulk of research has tended towards this approach, resulting in the development of superplastic 7000 series alloys such as 7075 and 7475.

More recently, the development of Al - Li alloys (12, 13, 14, 15) and Al - SiC (7) composites, has led to reviewed effort in this area.

The interest in Al - Li alloys centres around the fact that Lithium can significantly increase the elastic modulus and decrease the density of the alloy.

In the past few years two international conferences have been held to discuss aluminium - lithium alloys (12, 13). The first conference in 1980 included papers on production, physical metallurgy, room temperature mechanical properties and corrosion behaviour of these alloys.

Much of the work now is on developing the various compositions and manufacturing techniques for achieving superplasticity in the Al - Li alloys. Typical compositions under investigation now include Al - Li - Zr, Al - Cu - Li - Zr and Al - Cu - Li - Mg - Zr. The as-received alloys are thermomechanically processed to create an ultra-fine grain size, so necessary for superplasticity.

A more detailed review of the Al - Li alloys is present in references 7, 12, 13 and 15.

In summary, Figure 1 shows how there has been an overall shift in interest in superplastic aluminium alloys, from being laboratory curiosities to materials which when superplastically formed, can be a viable manufacturing alternative to conventional forming techniques.

1.3 COMMERCIAL APPLICATION OF SP FORMING ALUMINIUM ALLOYS

Recent papers have shown SP aluminium alloy components will be used increasingly in the aerospace industry (16, 17, 18) giving rise to both cost and weight savings. In Britain, commercially formed Supral 100 components have been in use for many years (19), but so far parts made from this medium strength superplastic aluminium alloy have been restricted to non-stressed applications such as helicopter air intakes, ejector seat components, and box covers.

Work is now in progress to determine whether the higher strength aluminium alloys (SUPRAL 220, 7475), can be used superplastically to form components for use in highly stressed applications.

For the 7475 alloy, it has been recently shown (20), that superplastic forming of a helicopter skid shoe (Figure 2) made conventionally by welding eight parts made of steel, can be made superplastically using 7475 in two parts which again are assembled by welding, as long as the cavity content that develops in the sheet during forming is restricted by an imposed hydrostatic pressure. In this exercise, a mass reduction of 65% was envisaged, whilst keeping the same manufacturing cost as the conventional part.

Other studies in the USA on the viability of using SPF 7475 for applications in fighter aircraft show how the lower deck structure of an avionics compartment (Figure 3) can, when formed superplastically, give savings of up to 50% (21). In bomber aircraft (22), similar savings can be achieved using SPF aluminium parts to conventionally formed components as illustrated in Figure 4.

In Britain, an assessment of the potential SPF aluminium applications for future combat aircraft such as the Tornado, has revealed that replacement of conventionally formed parts by SPF structures (such as fins, fore planes and air intakes (Figure 5)), can produce up to 30% in cost savings (17). It is obvious from the literature that high strength SPF aluminium alloy components show great potential for use in highly stressed applications in the aerospace industry as long as the problem of cavitation, the level of which increases with increasing superplastic strain, is controlled.

1.4 CAVITATION IN SUPERPLASTIC ALUMINIUM ALLOYS

Most materials form internal voids when superplastically deformed (23). The occurrence of cavitation has been studied in a wide range of superplastic materials based on iron (24, 25), copper (26), zinc (27), titanium (28), aluminium (29) and other metals.

Cavitation in superplastic aluminium alloys has caused considerable concern to potential users of formed components. The reason for this reaction is that cavitation can lead to degradation of service

properties (30, 31, 32) such as tensile, creep, fatigue and stress-corrosion behaviour.

The causes and effects of cavity formation in superplastic alloys will be discussed fully later, but the heat-treatable, high strength superplastic alloys of interest (7475, Supral 220), belong to a group whose grain structure is stabilised by a dispersion of fine particles. It is these particles which are a main cause of cavity nucleation in the alloys as the extent of superplastic deformation is increased. For the 7475-T6 alloy sheet, at a strain-rate of forming of 4×10^{-4} sec^{-1} and the temperature of 521°C, negligible cavitation is produced in the component until a strain of 150%, after which cavitation increases rapidly with increasing strain and at 200% strain levels, cavitation levels of 12% are not uncommon (33). This cavitation decreases markedly the percentage elongation obtained in a room temperature tensile test for superplastic strains over 150% (33). The values of the tensile strengths are also seen to depreciate at strains above 180% (34). Cavity formation in Supral alloys behaves in a similar manner to 7475 and as Figure 6 shows (32) the void volume in both Supral 150 and Supral 220 rises very sharply after a true thickness strain of 0.7 (corresponding to a strain in the component of 100%), giving void volumes in the component greater than 8%. This is reflected in a reduction of the mechanical properties such as yield strength, elongation percent and fatigue strength (32).

It is obvious that reduction or elimination of cavitation in SPF components is necessary before they can be used for highly stressed applications. In principle, cavitation could be removed by sintering, but even if temperatures higher than those for forming are used, for instance when solution treating the alloy (as part of the heat-treatment), removal of only the smaller cavities occurs (19) and elimination of the larger voids would be a lengthy process. Cavitation, however, can be eliminated by the use of pressure, whether back pressure during forming (35, 36) or post-forming hot isostatic pressure (37, 38, 39).

1.5 HOT ISOSTATIC PRESSING (HIP)

It was Blaise Pascal (1623 - 62) who proposed a law to the effect that "pressure applied to a confined fluid at any point is transmitted undiminished through the fluid in all directions and acts upon every part of the confining vessel at right angles to its interior surfaces and equally upon equal areas".

It is the application of this law which explains densification of particulate matter contained in a flexible container when subjected to pressure acting through a suitable pressure transmitting medium. The pressure acts equally over the surface of the container which, being flexible, squeezes the powder uniformly to a compact whose external geometry is smaller, but of similar shape to the original container.

The terms 'isostatic pressing' and 'hydrostatic pressing' relate to the omnidirectional application of pressure inside a vessel, the

former term is generally used to include gases and liquids as the pressure transmitting medium whereas the latter applies only to liquid. The application of pressure at room temperature is referred to as Cold Isostatic Pressing (CIP) (40) and the simultaneous application of pressure and temperature is known as Hot Isostatic Pressing (HIP).

HIP development has gone from the laboratory to commercial usage in a relatively short span of time.

The first use of HIP was in the USA, as early as 1956, involving gas pressure bonding for cladding uranium dioxide fuel elements (41).

Much of the early work on consolidating powders by HIP was performed for the nuclear industry since many experimental fuel elements were derived from powder products. By the mid-1960's, HIP was being used for the consolidation of high quality pre-alloyed powders (produced by the gas atomisation process) for the production of high speed tool steels (40).

The healing of porosity and micro-defects (especially in castings) by HIP was first utilised in the mid 1970's (42, 43, 44, 133, 134) and as Table 1 shows there are many casting alloys currently processed by HIP (45). The improvement in the mechanical properties (strength, ductility, fatigue resistance) of these castings by HIP is well documented (45, 46, 47).

Currently HIP is used on a variety of engineering applications. For instance, in the consolidation of superalloy powders into near net shape turbine components of 100% theoretical density resulting in material of improved mechanical properties (48).

Metal-matrix composites and the bonding of corrosion-resistant sheets to gas turbine black airfoils are being developed with the use of HIP for gas pressure bonding (49). The application of gas pressure bonding can still be exploited, since the effects of pressure at elevated temperatures can be used to join dissimilar metals which cannot be constructed by conventional methods such as welding.

When interwoven carbon fibres are impregnated with a carbonaceous binder, such as pitch tar, and HIPped under suitable conditions, the resulting product known as Hot Isostatic Pressing Impregnation Carbon (HIPIC) (50) can be used in a cost effective manner to produce components (such as missile nose tips, nozzles and heat shields) where weight reductions are more paramount than performance.

By far the greatest use of HIP is the densification of components by the removal of flaws or voids contained within them, either because of the production process as in casting (45), ceramics (48) and carbides (53) or as a consequence of their service conditions, for instance, the creep cavitation present in gas turbine blades (51, 52).

Sintered carbide components are manufactured by taking the carbide powder, cold pressing, de-waxing and sintering. These are then

HIPped, which not only reduces the internal porosity and ensures a defect-free surface but also leads to the improvement of mechanical properties (53). Typical pressures employed for this HIP would be up to 100 MPa, with temperatures as high as 1500°C.

For the densification of ceramics, the pressures and temperatures used can be higher (up to 200 MPa and up to 2200°C), but the method employed is similar to that used for other materials. The part is enclosed in a glass container which is pre-heated until it becomes plastic; pressure and temperature are then employed simultaneously so that the material is sintered and HIPped in a single operation.

1.6 HIP OF CASTING DEFECTS

HIP is used frequently in removing casting defects, especially shrinkage porosity from precision-cast nickel and cobalt-based superalloy gas turbine components (45), rendering a product which not only has a more homogeneous microstructure but better creep and fatigue properties.

Titanium alloy castings produced predominantly from the Ti - 6Al - 4V alloy are used for many applications in the aerospace and marine environments because they offer good creep resistance, fatigue crack growth resistance, fracture toughness and tensile strength (54) and also because full densification of cast components can be brought about with the use of HIP, which not only closes the casting porosity, but because titanium alloys are able to dissolve their own oxides at high temperatures, sealing of pores through metal/metal diffusional processes is complete. The improved mechanical properties (after HIP), make it possible to employ titanium alloy castings in highly stressed, critical service applications. Typical examples are aerospace compressor impellors, compressor cases, inlet guide vanes, engine housings and helicopter rotor hubs (54).

The use of aluminium castings for aircraft structural components is restricted despite the low-cost manufacturing method. Casting alloys such as A357 (Al - 7Si - 0.6Mg) have mechanical properties below those of the wrought aluminium alloys, thus use of the former often entails a weight penalty. The other problem is that porosity and other casting defects lead to a scatter in the mechanical property data. Recent work has shown that HIPping cast A357 not only eliminates the casting defects, increases the values of proof stress, tensile strength and elongation, but also reduces the scatter in the mechanical property data (55).

A relatively new casting alloy, A201, which has better mechanical properties than the A357, is now being considered for use in structural applications. HIPping of this casting alloy (at 950°C 100 MPa, 3 hours) decreases the scatter and improves properties by healing the microshrinkage porosity giving property values approaching those of the wrought 7075 and 7050 alloys (56).

1.7 HIP OF SUPERPLASTIC ALLOYS

As discussed in Section 1.4, most fine particle stabilised

superplastic alloys cavitate during deformation. The amount of cavity formation being dependent on the extent of superplastic strain.

Superplastically formed cavities can be eliminated by pressure, whether applied during forming (35, 36), or post-forming hot isostatic pressure (37, 38, 39).

The use of back pressure to suppress cavity formation in the 7475 alloy system is now well documented (2, 34, 35) and generally a confining pressure of 4MPa is sufficient to reduce cavitation although this figure is dependent on the superplastic strain in the components, the rate of forming and hence the flow stress of the material (35).

Recent work on the Aluminium-Lithium alloys (17) has again shown that a back pressure of 3.5 MPa can eliminate cavitation in regions containing true strain levels greater than 1.2.

For the Supral 220 alloy, slightly higher back pressure is required (than for 7475 and Al - Li) for cavity suppression, this is believed to be a result of the higher flow stress of the material under the optimum forming conditions (17, 36). It is apparent that the range of back pressures used so far during forming limits cavity growth rather than inhibits cavity nucleation, the smaller voids being three or four orders of magnitude in number greater than the larger voids (36).

The application of confining pressures up to 5 MPa in a production environment would require investment in new forming equipment or adaptions of existing equipment for pressure use. Both these alternatives would lead to higher processing costs. Alternatively, the closing of cavities by a post-forming HIP does not compromise existing tools or forming presses but does require the development of cost effective HIPping processes (19).

Many of the commercial HIP units now available are capable of reaching temperatures of up to 2000°C and withstanding pressures greater than 200 MPa.

Preliminary work on the Supral 220 has shown that under a pressure of 100 MPa and a temperature of 350°C, cavitation in formed Supral 220 can be eliminated with the resultant improvements in tensile properties (19), although the cost of processing is high due to the higher pressure equipment used.

An alternative approach would be to ascertain whether lower pressures (up to 35 MPa) and temperatures (down to 350°C) would be effective in removing superplastically formed cavitation in aluminium alloys. So far very little work has been performed to quantify these parameters although recent work on the 7475 high strength aluminium alloy has shown that HIPping at 3 MPa and 516°C reduces the cavitation especially at lower superplastic strains (57), by increasing the rate of cavity sintering; however, they suggest that greater pressure is needed to eliminate cavitation completely.

The present investigation will determine the combinations of pressure, temperature and time required for cavity closure in the Supral 150 (clad 2004) alloy. In summary, Hot Isostatic Pressing can be used to prevent or eliminate internal porosity in a wide range of materials, whether caused by the manufacturing process (as in castings and SPF) or by the service conditions (creep cavitation in turbine blades). It is not clear if this process (either when applied as back-pressure during forming, or as a post-formed HIP) seals the porosity rather than just bringing the surfaces of the voids together. The extent of void sealing can be indicated by mechanical property data, although this property is also dependent on the condition of the material.

If dissolved gases are present in the material, then these may, under elevated temperature conditions, promote the re-opening of cavities closed during the HIPping operation.

1.8 INFLUENCE OF INTERNAL GASES

Industrial processes designed to yield metallic products are generally conducted in environments containing sources of gases which can be absorbed by the metal.

For many materials, retained hydrogen in the melt, even in trace quantities, can have a deleterious effect on the character and properties of the products.

In aluminium castings, although the solubility of hydrogen is low when compared to other metals, the ratio of solubility in the liquid to that in the solid at the freezing point is approximately twenty to one, resulting in the tendency for hydrogen to come out of solution causing porosity in the cast metal (58).

In ingots for wrought products, the presence of hydrogen gas in the voids inhibits healing, even under the extreme pressures and temperatures of hot working, and is responsible for such defects as bright flakes in forgings (58) and blisters on annealed or solution-treated materials (59). For aluminium alloys, hydrogen absorption can occur in the solid metal during manufacture, for instance during industrial annealing at 500°C of hot-rolled plates of pure aluminium (60).

Another source is water vapour in furnace atmospheres and work as early as the 1960's has shown that solid Al - Mg alloys readily absorb hydrogen from water vapour in the temperature range 400 - 500°C and the gas rapidly penetrates thin sections. This absorption is catalysed by sulphur which is often present in industrial furnace atmospheres (61, 62). Hydrogen therefore can exist in wrought products.

It follows that superplastic materials must also be susceptible to hydrogen absorption. Surface blisters and pores have been observed in the fine grained 7475 when subjected to elevated temperature exposure (above 500°C) for one hour, which are distinct from super-plastic cavitation. These are attributed to the outgassing of

hydrogen trapped in the alloy from earlier processing stages, principally the solidification process. It was also found that continued annealing at this temperature for longer periods of time eventually shrinks the internal pores, but only if hydrogen is able to escape from the sheet. Furthermore, if a high hydrogen content was present (at the elevated temperatures) at the surface of the material, this enhanced the growth of both internal pores and surface blisters (63). Apart from the work mentioned above, very little has been published on the effects of hydrogen gas on superplastic materials.

1.9 EFFECT OF HIP ON INTERNAL GASES

If, during HIP, the void contains gas,closure may be accompanied by : -

(a) Gas solution in the metal, if soluble

(b) If insoluble, reaction by the gas with the metal to form non-metallic inclusions,

(c) non-reaction with the metal, but merely compression.

For titanium alloys, porosity is not only closed but sealed by the HIP process, probably because perfect bonding of the void surfaces has occurred, as titanium dissolves its own oxide at elevated temperatures.

In aluminium alloys, porosity disappears with HIP but frequently reappears upon subsequent heat treatment. Recent work has shown that HIPping of the A356 (Al - 7.0 Si) casting alloys has successfully closed porosity. The hydrogen solubility is claimed to be directly related to the square root of the pressure and at 500°C hydrogen solubility in the alloy increases thirty two times at an external pressure of 100 MPa, thus during the higher pressures of HIP redistribution or repartition of hydrogen from the voids is assumed to occur, resulting in a state of closed porosity. Subsequent solution treatment of this casting alloy resulted in hydrogen diffusion to grain boundaries where porosity reappeared (47).

There is no published information as to whether heat-treatment subsequent to HIP causes the reappearance of porosity in superplastic materials, as most papers published on cavity closure just give details of the parameters used successfully to close cavities and the effect this has on the mechanical properties (34, 46, 37).

As mentioned earlier, work has shown that hydrogen out-gassing occurs in superplastic 7475 when annealed at 500°C (34). There is no reason to assume that the hydrogen present in this alloy will be removed by a HIP process (applied either during forming or after), especially when the surface of the material during HIP is experiencing a positive pressure. It is obvious that more attention needs to be paid to this problem.

CHAPTER 2 - SUPERPLASTICITY

2.1 INTRODUCTION

The phenomenon of superplasticity where specimens deformed in tension at low stresses exhibit essentially neck-free elongations of many hundreds of percent, was first reported by Jenkins (76) as early as 1928, and in 1934, it was Pearson (64) who pulled an extruded sample of the Bi - Sn eutectic alloy nearly 2000% at room temperature.

Interest in the field was revived following the work of Backofen et al (77) and since then a tremendous amount of research has been conducted in this and closely related fields with many excellent reviews by workers in the area on mechanical properties (65), metallographic and crystallographic texture changes (66, 67) and operative mechanisms (68), deformation mechanisms (67) and flow and fracture characteristics.

In the last decade, extensive work has been published on the development of superplastic materials for use in commercial applications, as discussed in Section 1.3.

General reviews on all aspects of superplasticity have also been published by Edington (68) and more recently by Padmanabahn and Davies (72). Major conferences on superplastic materials, held in 1982 (5) and in 1985 (6, 14), show how much of the interest in superplasticity has transferred from being a laboratory curiosity to a commercially viable forming process.

Superplastic materials can broadly be divided into two groups:-

(a) Environmentally superplastic materials

(b) Structurally superplasticity

For both groups, the applied stress for superplastic deformation is dependent on the strain rate, and can be characterised in terms of the strain-rate sensitivity index, m, as propounded by Backofen et al (77)

$$\sigma = K\dot{\varepsilon}^{m} \text{ and } m = \frac{\partial \log \sigma}{\partial \log \dot{\varepsilon}} \qquad (1)$$

where σ is the applied stress, $\dot{\varepsilon}$ is the strain-rate and K is a constant for a given set of testing conditions. Both K and m are dependent on testing parameters such as temperature and strain rate. This would suggest that for Newtonian-viscous solids ($m = 1$), elongation in tension should be uniform and without irregularities in the cross-section.

For superplastic materials, increased resistance to local necking and high elongations are observed for $m > 0.3$, although the elongation during superplastic flow is not neck-free, instead a

series of diffused necks develop leading to the large elongations (78).

2.2 *ENVIRONMENTALLY SUPERPLASTIC MATERIALS*

Edington (67) has compiled a list of environmentally superplastic alloys, and explains that the most common conditions under which this occurs are :-

(a) during temperature cycling through a phase change;

(b) during temperature cycling of a thermally anisotropic material;

(c) during neutron irradiation.

Superplastic behaviour is generally observed in these materials when a small stress is applied in conjunction with the above conditions.

As the main interest of this work lies in structurally superplastic materials, no further reference will be made to environmental superplasticity.

2.3 *STRUCTURAL SUPERPLASTICITY*

This type of superplasticity is associated with materials having a fine (< 10 μm), stable, equiaxed grain size at temperatures greater than 0.5 Tm, and posessing m-values greater than 0.3, at strain rates of between 10^{-2} to 10^{-4} sec^{-1}.

Most superplastic materials exhibit a sigmoidal logarithmic stress versus strain rate curve (Figure 7), which is conventionally divided into three regions. Superplasticity is observed in region II where the slope of the plot, (generated by step-strain rate technique), given by $m = (\ell n\ \sigma/\ell n\ \dot{\varepsilon})$ is at a maximum (Figure 7b).

Paton (80) has written an equation which fits the curves generated by the step strain-rate technique under conditions which do not favour work hardening of the material or when it is not subject to microstructural changes. This can be written as

$$\dot{\varepsilon} = K_1(\sigma - \sigma_o) + K_2\sigma^N \qquad (2)$$

where K_1, K_2 and N are constants and σ_o is the threshold stress.

If, as in some aluminium alloys, grain growth occurs, then the variation in the flow stress due to this and other variables has to be considered, suggesting an equation of the form (79) :-

$$\sigma = K\ \dot{\varepsilon}^m\ \varepsilon^n \qquad (3)$$

where n is the strain hardening exponent.

As mentioned earlier, a high strain-rate sensitivity (> 0.3) opposes the development of local necks and is therefore responsible for the large elongations observed, as shown by Woodford (104) Figure 8, where elongation to failure increases with rise in the m-value. Various methods of applied mechanics have been used to predict the elongations to fracture of materials that fail by necking (81, 82) and have been evaluated by Sherby et al (83).

Several factors can contribute to limited ductility in superplastic alloys :-

(a) The alloys cavitate during high temperature deformation, as will be discussed later in Chapter 4.

(b) Microstructural instability occurs due to loss of grain size control, which will also be discussed later.

2.4 *MICROSTRUCTURAL ASPECTS OF STRUCTURAL SUPERPLASTICITY*

The investigations on the microstructural aspects involve the role of grain shape and size, grain growth, grain rotation and grain rearrangement, dislocation activity and the distinction between phase boundaries and grain boundaries in the superplastic deformation process.

Despite the immense amount of work in obtaining structure-property correlations, several microstructural issues still remain unclarified, such as the role of grain growth, especially at low strain rates, the details of the process of accommodation at triple points due to grain boundary sliding (GBS) and migration, the role of dislocations in the deformation process and in the accommodation mechanisms.

Although attempts (68, 72, 78) have been made to resolve these issues, no major advances have been made in unravelling the sub-structural details of the mechanism and there is still a lack of satisfactory correlation between microstructure and mechanical properties.

This section will briefly review all the microstructural aspects of superplastic deformation.

2.4.1 *Initial Microstructures*

The ability to obtain fine grain sizes (< 10μm) in superplastic materials depends essentially on the alloy composition and/or on the thermomechanical treatment.

For two phase or multi-phase systems, such as the Al - 33% Cu eutectic, the diffusion path needed for grain growth is increased by the presence of the second phase, thus, the small grains produced by thermomechanical means in such alloys are relatively more stable; this stability is also enhanced by the greater difference between

the diffusivity of the two phases and by the presence of more boundaries between dissimilar phases.

Several superplastic alloys have been developed recently which use the presence of hard intermetallic compounds or precipitates to pin grain boundaries and inhibit grain growth. Unfortunately, such dispersions also influence the recrystallisation behaviour during hot working or static annealing and may produce microstructures which are not fully equiaxed (84). Instead, the grains are elongated in one or two directions as shown in Figure 9. Figure 9a, generally being due to extrusion or swaging and the Figure 9b from rolling. Characterisation of the elongated microstructure in superplastic alloys is by the grain aspect ratio (GAR), defined as the ratio of the longitudinal to the transverse dimensions of the grains. GAR values depend on alloy composition and the degree of working. Typical values range from 1.5 for a 60/40 brass (85), 4.67 for Ti - 6Al - 4V alloy (86) and from 1 - 7 for a Pb - Sn eutectic alloy depending on the thermomechanical treatment (84).

2.4.2 *Microstructural Instability*

Many publications show that microstructural instability occurs during superplastic deformation and this can be broadly divided into two categories :-

(a) Change of as-worked (also short-statically annealed) unstable microstructures

(b) Changes associated with the micromechanisms of deformation.

The presence of elongated grains results in initially higher values of the flow stress (85) and lower values of m (87), with the elongated structure gradually becoming equiaxed (85, 86), the GAR stabilising at ~ 1.2 during the early parts of deformation. The strain at which a stable, equiaxed structure is obtained is dependent on the alloy system, initial GAR, test temperature and strain rate.

The values for such strain level experimentally observed is listed in Table 2.

2.4.3 *Grain Growth*

Another microstructural feature now established is that grain growth takes place during superplastic deformation (84, 85, 86), resulting from either static annealing at elevated temperatures during deformation or strain enhanced growth due to the deformation.

For the Fe - 25.7Cr - 6.6Ni at 1000°C, the grain growth kinetics (88) are of the form :-

$$d \alpha t^{0.49} \simeq t_s^{0.19} \dot{\varepsilon}^{0.29} \simeq t_s^{0.19} \dot{\varepsilon}^{0.29} t_\varepsilon^{0.29} \qquad (4)$$

$$d \simeq \dot{\varepsilon}^{0.29} t^{0.48} \qquad (5)$$

where d is the grain size, t, t_s and t_ε are the time in minutes relating to combined, static and dynamic annealing and $\dot{\varepsilon}$ is the strain rate. Other workers (85) have concluded that post-deformation grain size is dependent on the time at temperature and not the strain.

In attempting to isolate the effect of strain-rate on grain growth, Clark and Alden (89) postulated the"growth enhancement parameter ($\Delta d/da$), where Δd is the difference between the grain size after deformation, d, and the grain size of a specimen statically annealed at the deformation temperature for an equal time, da.

Their results show that $\Delta d/da$ increases with strain, the rate of grain growth reaching a maximum at intermediate strain-rates, Figure 10. Wilkinson and Carceres (90) have analysed the data on several superplastic materials, Figure 11, which shows that the rate of grain growth at intermediate strain-rates seems linearly dependent on the strain rate, yet relatively insensitive at higher or lower values of strain-rate. It has been suggested that grain boundary mobility as a consequence of increasing vacancy concentration is responsible for grain growth during superplastic deformation, Figure 11a (90).

2.5 MICROSTRUCTURAL CHANGES ASSOCIATED WITH DEFORMATION MECHANISMS

Grain boundary sliding, diffusion and dislocation activity operate during the high temperature deformation of superplastic materials. Figure 12 illustrates the influence of these mechanisms in the different superplastic regimes for two alloys (84).

2.5.1 Grain Boundary Sliding

Extensive interface (either grain or phase boundary) sliding is commonly observed during superplastic flow, even in systems where diffusional creep is found to be the dominant mechanism (91). The contribution of grain boundary sliding, generally, is at a maximum in region II and decreases at higher (region III) and lower (region I) strain rates.

Grain boundary sliding is also dependent on the alloy composition and the conditions of deformation.

Chandra et al (92) measured grain and phase boundary sliding in α/β brass and found sliding occurred on α -β boundaries more rapidly than on α - α or β - β interfaces. Yet Vastava and Langdon (93) found sliding (in all three regions of the $\ell n\sigma$ vs $\ell n\dot{\varepsilon}$ curve) took place predominantly at the Sn - Sn boundaries in a Pb - Sn alloy and none occurred at the Pb - Pb interface; however, the extent of sliding between Pb - Sn boundaries was intermediate between the two. These observations have led to the suggestion (84) that maximum sliding occurs at interfaces with the highest values of δDg_b, where δ is boundary width and Dg_b is the grain boundary diffusion coefficient.

2.5.2 *Grain Boundary Migration*

The occurrence of grain boundary migration (GBM) during superplastic flow is well documented (94, 95). Lee (96) suggests that GBS is followed by GBM at triple points to minimise boundary energy, Figure 13, resulting in two adjacent grain boundaries having opposite curvatures, which explains the curved boundaries often observed after superplastic deformation. Yet this model cannot account for the bulbous aspect of the previously straight boundaries. A possible explanation (97) might be that further GBM is activated due to dislocation activity in the grain mantle.

The observation of denuded or precipitate-free zones near grain and interphase boundaries (95) can be attributed to strain-induced boundary migration which takes place in such a way that the boundary moves away from its centre of curvature (97), leaving an unusually curved shape, Figure 14. The moving boundary leaves behind a region which is cleaner, as migrating boundaries usually drag away impurity atoms.

2.5.3 *Grain Rearrangement*

This takes place during superplastic deformation and two grains which are neighbours may, after deformation, be many grain diameters apart. Grain rearrangement may be facilitated by grain rotation (98) and governed by GBS (99). In situ tensile straining experiments in a 1mV electron microscope by Naziri et al (100) of thin foil Zn - Al eutectoid alloy showed that extensive grain rearrangement takes place during straining.

Hazzledine and Newbury (101) suggested that during deformation voids open at interfaces and are filled by grains emerging from adjacent planes, Figure 15; they calculated that at a strain of 1.9, half of the grains in the plane section will be new grains from locations above and below it, leading again to extensive grain rearrangement.

2.5.4 *Dislocation Activity During Superplastic Deformation*

Much early electron microscopy work suggested that dislocation activity did not occur during superplastic deformation (95, 100). In situ straining experiments by Naziri et al (100) showed very little dislocation activity, yet it has been suggested that under the experimental conditions used an unusually high vacancy flux was created throughout the specimen, and this effect which facilitates dislocation climb may have masked or eliminated dislocation activity.

The lack of dislocations in transmission electron microscope examination of thin foils prepared from deformed specimens does not prove that dislocation mechanisms are inoperative during deformation, as they may either have been annihilated during unloading of the specimen at temperature, or lost during the preparation of the thin foils (84).

In recent years there is mounting evidence of dislocation

activity during superplastic deformation. These include direct observations in TEM studies (99, 102), where the tensile specimens were quenched under load, observations of slip lines on gauge surfaces (103) and the stabilisation and formation of new textures (104).

A more detailed discussion of this subject is presented in reference 84.

2.5.5 *Dynamic Recovery*

The fine substructure characteristic of recovered metals evolves during strain hardening where dislocations multiply and become entangled. This process occurs more readily in metals of high stacking fault energy (SFE) as the mechanisms involve climb, cross-slip and node unpinning.

Gardner and Grimes (152) indicate that increasing the magnesium content of an Al - Mg alloy reduces the stacking fault energy thus making dynamic recovery less probable.

2.5.6 *Dynamic Recrystallisation*

In dynamic recrystallisation, the migration of a high-angle grain boundary annihilates large numbers of dislocations producing a dislocation-free lattice. New grains continually replace the work hardened ones and maintain a fine equiaxed grain structure.

Aluminium alloys have a high stacking fault energy, making dynamic recovery more likely. Superplastic aluminium alloys (such as SUPRAL) rely on dynamic recrystallisation to achieve the fine grain size during deformation. It is necessary thus to retard dynamic recovery in these alloys and this is achieved by the addition of alloying elements.

The effect of solute additions is to retard dynamic recovery by causing more dissociation of the dislocation partials , making cross-slip more difficult. This increases the stored energy in the material, encouraging recrystallisation.

In the alloy of interest to this investigation, SUPRAL 150, the additions are present partially in solid solution and partially in the form of intermetallics.

The presence of copper in this alloy is thought to reduce the SFE and thereby encourage dynamic recrystallisation (121) during hot deformation, whereas the Zirconium, which exists as fine $ZrAl_3$ dispersion, is present to inhibit static recrystallisation after cold working and also to restrict grain growth by boundary pinning during hot deformation (121), thus allowing the superplastic mechanisms discussed to occur more rapidly.

Much work has been published on dynamic recovery and recrystallisation (152), further reference to these mechanisms will only be made in connection with the present investigation (Chapter 3).

In summary, the major microstructural characteristics of superplasticity are :

1. Elongated or non-equiaxed microstructure becomes uniform and equiaxed during the initial stages of deformation (up to 20% strain) and remains so even after thousands of percent strain.

2. Previously straight interfaces become curved, sometimes phase boundaries have a bulbous effect.

3. Strain-enhanced grain growth occurs with maximum sensitivity at intermediate strain rates.

4. Deformation zones are formed on boundaries approximately perpendicular to the tensile axis.

5. Extensive grain boundary sliding and migration as well as grain rotation takes place during deformation. Three dimensional grain rearrangement is also seen to take place.

6. Considerable dislocation activity occurs during superplastic flow, with dislocations generated at or near boundaries. Annihilation occurs in the grain boundaries.

2.6 MODELS FOR STRUCTURAL SUPERPLASTICITY

It is clear from Section 2.5 that GBS plays a major role in superplastic deformation. For this reason only models which are based on GBS are relevant, however, in order to maintain grain contact extensive material transport by grain boundary or bulk diffusion or by dislocation creep is necessary.

A complete review and discussion of the models of superplasticity are presented by Padmanabahn and Davies(72). The following section will review a few of the models which best fit the microstructural observations of superplastic deformation.

2.6.1 Grain Boundary Sliding, Dislocation Motion Accommodation Rate Controlling

Figures 16 a, b and c show schematically the model for superplastic flow in terms of GBS with rate-controlling accommodation at triple points by dislocation motion.

Ball and Hutchison (105) suggested groups of grains slide as a unit until obstructed by an unfavourable grain (Figures 16a). The resultant stress concentration being released by dislocation motion in the blocking grain. Dislocations pile up until the back stress stops the sliding process, and further sliding requires climb by the leading dislocations into and along the grain boundary, this further sliding being dependent on the rate at which dislocation climb occurs in grain boundaries towards annihilation sites.

Mukherjee (106) proposed a similar model except that grains slide individually whilst dislocations were produced by ledges and protrusions in the boundary (Figure 16b).

Gifkins (107) proposed accommodation of GBS required dislocation motion by their climb either in or near grain boundaries, the so-called mantle. No dislocations transversed the 'core' of the grain (Figure 16c).

Gittus (109) applied the core-mantle model to two phase eutectic/eutectoid superplastic materials and treated the sliding process by the motion of superdislocations in the interface.

2.6.2 *Grain Boundary Sliding, Diffusion Accommodated Flow Rate Controlling*

This theory developed by Ashby and Verrall (108) described the grain switching effect illustrated in Figure 17. GBS occurs with material transport by grain boundary and bulk diffusion to maintain grain continuity. Dislocation creep takes place but makes a smaller contribution as the strain rate is reduced, being insignificant at maximum strain-rate sensitivity, m.

None of the theories summarized here is entirely satisfactory and these and others have been discussed in detail elsewhere (72). Table 3 shows how the models discussed fit the microstructural observations during superplastic deformation.

2.7 *FAILURE IN SUPERPLASTIC MATERIALS*

If a cylindrical bar of a crystalline solid is pulled in tension (Figure 18), it may fail either by necking down until the cross-section, locally becomes zero. Alternatively, at high temperatures ($> 0.3\ T_m$), it may fail by various sorts of creep fracture, either transgranular or intergranular. At low temperature ($< 0.3\ T_m$), failure may occur by cleavage or brittle intergranular fracture; or it may fail in a ductile manner (110).

Failure of alloys under superplastic deformation conditions occurs either by intrinsic plastic failure (70) or by cavitation fracture (23). Practically, cavitation is present in all superplastic Aluminium failure processes, so that reductions in area at fracture are never 100%.

Failure in superplastic materials range from marked necking (with close to 100% reduction in area), to quasibrittle fracture with very little necking. Figure 19 illustrates the stress-strain curves for these types of alloys; a ductile PbCd alloy and a quasibrittle α/β brass (70).

2.7.1 *Intrinsic Failure*

This type of failure is determined only by the necking characteristics of the material which in turn are governed by the constitutive equations of flow. An incipient neck will not grow if the flow stress (σ_f) is less than the rate of hardening ($\partial\sigma_f/\partial\varepsilon$). The flow stress is a function of variables such as strain, strain-rate, temperature, surface energy and microstructural characteristics. A small increase in strain-rate sensitivity of the material does lead to marked retardation of necking.

Experimentally, Sagat and Taplin (111) took the non-cavitating Pb Cd eutectic and categorised its two stages of instability.

Instability I (slow neck growth) is reached early in the test with the formation and growth of several necks.

The second stage, which is the onset of intrinsic plastic failure, is strongly dependent on m and occurs when one of these necks becomes preferential and rapid.

Further discussion of this type of failure can be found in references 71 and 111.

2.7.2 *Cavitation Failure*

This process may lead to fracture with very little necking.

Cavitation in superplastic alloy systems is seen to increase at lower strain rates (112), be independent of strain-rate (113), or decrease with higher or lower strain-rates (29). The causes and effects of cavitation differ for each system, as will be discussed later in Chapter 4.

CHAPTER 3 - SUPERPLASTIC ALUMINIUM ALLOYS

3.1 INTRODUCTION

The development of superplastic aluminium alloys was discussed in Chapter 1. This section will concentrate on the various aspects of superplasticity in the class of alloys relevant to this work.

Several different approaches have been used to achieve a fine grain size in aluminium alloys and Lloyd and Moore (114) classify these into three types :

(1) Coarse particle stabilised alloys

(2) Dual phase alloys

(3) Fine particle stabilised alloys

It is not intended here to dwell on categories 1 and 2, other than to give an outline of the mechanics of their behaviour, as the type of material being investigated belongs to the third category.

3.2 COARSE PARTICLE STABILISED ALLOYS

In these alloys, particles of about 0.2 to 0.5 μm diameter are used to stabilise a fine grain structure. It was Zener (115) who showed the driving force for grain boundary migration, P, produces unpinning of grain boundaries when

$$P \geq \frac{3}{2}\frac{f\gamma}{r} \qquad (6)$$

and the critical radius R_1 of the grain when growth ceases may be described as :-

$$R = A.\frac{r}{f} \qquad (7)$$

where A is the proportionality constant, f is the volume fraction of particles of diameter r and γ is the boundary energy. This equation shows that fine particles can withstand higher driving pressures for the same volume fraction than coarser particles; thus a greater volume fraction of coarser particles is required to give an equivalent degree of stabilisation as obtained with fine dispersoids.

Aluminium has insufficient solute solubility to enable these large volume fractions to be produced by precipitation but may be obtained by binary and pseudo-binary eutectic alloys in which the intermetallic phase solidifies into a rod-like morphology. These rods are broken down by working to give particles in the size range required, with a very fine grain size after annealing.

Al-Ca and Al-Ca-Zn alloys (114) give good superplastic behaviour

for this type of material.

3.3 *DUAL PHASE ALLOYS*

Classical examples of these alloys are the Al - Cu eutectic and the Al - Zn eutectic or eutectoid alloys. The lamellar eutectic structure can be thermomechanically worked to give near equal volume fraction of the aluminium and the intermetallic phase, the latter stabilising the structure due to the low migration velocity of the aluminium intermetallic boundaries.

Although the Al - 33% Cu alloy can have very attractive superplastic properties (m = 0.7, elongations approaching 2000 %), it unfortunately has unattractive mechanical properties at room temperature.

3.4 *FINE PARTICLE STABILISED ALLOYS*

There are basically two approaches to grain refinement in superplastic aluminium alloys relevant to the aerospace industry; these are :

(a) The application of thermomechanical processing to suitable 'off the shelf' alloys (7075 and 7475) to render them superplastic.

The thermomechanical treatment involves solution-treating, overaging, rolling and recrystallisation.

(b) The addition of Zr (~ 0.3 to 0.5%) in a way which produces a fine dispersion of $ZrAl_3$ particles, which inhibits recrystallisation and restricts grain boundary migration (by boundary pinning) during superplastic forming at elevated temperatures.

Much work is published on alloys in the first category and examples can be found in references 10 and 11.

The second method is relevant as it is the production method used for the alloy under investigation : the Supral 150 (Al - 6Cu - 0.5Zr) and will be discussed in detail here.

3.5 *ALLOY DESIGN FOR FINE PARTICLE STABILISED MATERIALS*

A high driving force for recrystallisation, easy nucleation of recrystallised grains and grain boundary pinning are the necessary prerequisites needed to minimise the grain size in an alloy which recrystallises by a nucleation and growth process.

To maximise the stored energy produced during dynamic recovery, processes such as sub-grain formation need to be hindered, usually by the use of solute elements, (Mg, Cu), which interact with dislocations, reducing their mobility and hence their ability to rearrange themselves into low energy configurations. The development of a cellular substructure under different conditions is shown schematically in Figure 20.

Limited dynamic recovery is important in materials where the production of a fine grain size occurs by dynamic recrystallisation during the forming process. From the stored energy point of view it is preferable to have a high solute containing alloy.

Humphreys (116) shows that one way of achieving easy nucleation for recrystallisation is to have a high concentration of non-deforming particles, with diameters greater than 2 μm, in the matrix. Unfortunately, as yet the role of particles as recrystallisation nuclei is not understood, being influenced by many factors including particle shape and distribution.

It is also necessary to have some form of grain boundary pinning to restrict grain growth at the superplastic forming temperatures.

Equation 6 describes the driving pressure for grain boundary migration, P, which produces inpinning and shows that fine particles can stand higher driving pressures for the same volume fraction than coarser particles. It also shows that particle coarsening, which may occur at superplastic forming temperatures, results in a lower driving force for unpinning.

The above concepts have been used to develop superplastic alloys in the Al - Zn, Al - Mg, Al - Mg - Si (AA 6061), Al - Mg - Zn - Cu (AA 7075) and the Al - Cu systems.

Unfortunately, several factors may produce grain growth in superplastic alloys.

(a) Abnormal grain growth (secondary recrystallisation) can produce large grain sizes (118).

(b) Strain enhanced grain growth occurs during superplastic forming, which is dependent on the strain-rate (117).

(c) Inhomogeneous distribution of the alloying addition.

3.6 SUPERPLASTICITY IN Al - Cu - Zr ALLOYS

3.6.1 Introduction

It is evident from the previous section that to achieve superplasticity, an ultra-fine grained material which is not susceptible to grain coarsening under optimum superplastic deformation conditions has to exist.

There are several eutectic alloys (Al - Cu, Al - Mg, Pb - Sn) in which a fine stable grain size can be obtained by rapidly chilling from the melt and then warm-working the alloys to give a matrix in which grain growth is limited by a high volume of second phase particles (95).

Ahlborn et al (119) have shown that the Al - 5Cu recrystallises to a fine grain size, yet this structure is unstable at the superplastic temperatures of 400 - 550^{o}C, because a large proportion of the

Cu returns to solution and is not available in precipitate form for grain growth restriction. Therefore, a third component is required which not only will be retained in the form of second phase particles but also can be uniformly precipitated to inhibit grain coarsening via the 'Zener drag' mechanism (115).

Zirconium is a possible element which can be added to achieve this end. It can be precipitated in a suitable form (120), but as it has a low solubility in aluminium and because the binary Al - Zr system is a peritectic, it is necessary to chill the melt rapidly to achieve a high supersaturation of Zr.

Zirconium is also used as a grain refiner in aluminium castings and it can markedly inhibit recrystallisation (120).

3.6.2 Microstructural Aspects of Superplasticity in Al - 6Cu - 0.5Zr

This section will summarise the microstructural changes which occur during the production of this alloy, from casting, rolling and superplastically forming.

The alloy is prepared from super purity aluminium, high purity copper with the Zirconium being added in the form of a commercial purity Al - 6Zr master alloy (121). Recently, in-line hydrogen degassing procedures have also been adopted at the melting stage (19).

As an important feature for this alloy is to ensure an even distribution of zirconium, it is necessary to dissolve all the Zr in the melt and to retain it in solution until solidification of the alloy. Otherwise coarse particles of $ZrAl_3$ are produced which make no contribution to superplastic properties and reduce the amount of supersaturated Zr in the solid solution. The melt thus has to be held at temperatures above 800°C and D.C. cast so that a high proportion of the Zr is converted to a dispersion of fine $ZrAl_3$ precipitates. As the solution and precipitation behaviour of Zr is influenced by impurities, special care is taken to control the iron and silicon content of the alloy. In the as-cast state, the ternary alloy is characterised by dendritic branching near the edges, whereas closer to the central region of the cast block, the structure consists of aluminium cells of around 30 μm diameter, surrounded by a eutectic of $Al/CuAl_2$. In addition, some coarse tetragonal $ZrAl_3$ particles are observed (121).

The cast material is then given a preheat at 370°C and rolled from around 450°C (121, 122). Hot rolling of the material at ~ 360°C breaks the eutectic regions and at higher reductions a homogeneous distribution of Widmanstätten ($CuAl_2$) results.

On a sub-optical scale, the structure is characterised by the presence of small spherical particles of the metastable $ZrAl_3$ around 4.5nm in diameter which, as can be seen from equations 6 and 7, would be expected to be very effective pinners for grain boundaries even though the volume fraction of $ZrAl_3$ particles is low (153).

In summary, during rolling, the material develops a banded

structure such that fine Zr-rich regions occur at the central regions of cells, being characterised by a uniform distribution of dislocations, whereas, towards the cell or dendritic boundaries (regions of high Cu and low Zr), the alloy polygonises to give a fine sub-grain size.

On statically annealing this material at 460°C, the banded structure is still evident although in the peripheral regions of each cell (high Cu content) a fine grained recrystallised structure is produced, whereas the central regions (high Zr content) transformed from a dislocated state to polygonised cells (122).

It is evident from the extensive work performed on this alloy (66, 67, 114, 121, 122) that dependent on the fabrication route, the matrix can contain at least four distinct types of precipitates. These are :-

(1) Coarse ($\gtrsim$ 1 μm), θ particles ($CuAl_2$);

(2) Finer θ' ($CuAl_2$);

(3) Fine (between 4 - 10 nm) cubic $ZrAl_3$ precipitates

and (4) coarse tetragonal $ZrAl_3$.

Phases (2) and (3) are metastable, but cubic $ZrAl_3$ particularly, can remain unchanged to quite high temperatures.

It is obvious from equation 6 (Section 3.1), that cubic $ZrAl_3$ precipitates are 'fine' enough to be effective pinners for grain boundaries, even though their volume fraction is quite low in the alloy (< 0.005).

The presence of copper in the alloy seems to serve a variety of purposes :-

(1) In the melt, Cu leads to greater undercooling and thus restricts cell growth during solidification which renders more effective nuclei which is important in the production of a fine grained structure (123).

(2) It has also been claimed that $CuAl_2$ precipitates are responsible for both static and dynamic recrystallisation (122) and the role of copper in providing a more uniform distribution of Zr in castings, hence preventing grain growth.

(3) The role of copper in lowering the stacking fault energy sufficiently to inhibit recovery and encourage dynamic recrystallisation (114) during the early stages of the superplastic forming process is well documented. Generally, after the first 50% deformation a uniform equiaxed structure is evolved, and remains so, even after extensive deformation (122).

It is clear that the detailed processes occurring during re-

crystallisation are not completely understood, but the precipitation of intermetallics assists recrystallisation and the fine metastable $ZrAl_3$ provides a fine grain structure by grain boundary pinning.

The disadvantages of using Zr are the high casting temperature and the rapid solidification rates needed to retain it in solid solution. Coarse $ZrAl_3$ particles and θ $CuAl_2$ precipitates have been the cause of cavitation during superplastic forming and the next chapter will discuss this aspect more fully.

After superplastic forming, this age-hardening material is heat-treated to give it maximum strength.

Heat treatment involves :-

(1) Solution-treatment at a relatively high temperature (530°C, 1 hour for 2004) to dissolve the alloying elements (Cu), Figure 21).

(2) Quenching to room temperature to obtain a supersaturated solid solution (SSSS) of these elements in aluminium.

(3) Ageing (for example at 185°C, 5 hours for 2004) the material for a controlled decomposition of the SSSS to form a fine dispersion of precipitates. This is characterised by the formation of Guinier-Preston (GP) zones θ, θ' and θ'' which are ordered solute-rich clusters of atoms which may only be several atom planes in thickness.

These act as obstacles to dislocation motion providing the hardening mechanism for the alloy. This is discussed more fully by Polmear (153) in his book on Aluminium Alloys.

CHAPTER 4 - CAVITATION AND SUPERPLASTICITY

4.1 INTRODUCTION

Most known superplastic materials develop voids when deformed. This cavitation is viewed with trepidation by users of formed components as it can lead to degradation of service properties such as tensile, creep, fatigue and stress-corrosion cracking.

The occurrence of cavitation has been studied in a wide range of superplastic materials (23 - 29). Cavities are seen in eutectics, eutectoids, in solid-solution and in precipitate-containing alloys. In many cases, failure is dominated by the interlinkage of cavities and tensile test specimens show little necking and abrupt (quasi-brittle) fracture.

Most superplastics are multi-phase alloys and cavities are frequently located at inter-phase boundaries.

For example, in brasses, they occur preferentially at α/β boundaries and in stainless steel at α/γ interfaces (24).

As in conventional materials, inclusions are favourable sites for cavities, such as carbides and carbo-nitrides in steels (24) and primary intermetallics in Al - Zn - Mg - Zr alloys (124).

Livesey and Ridley (113) added elements to the PbSn eutectic to form hard phases (Cu_6Sn_5), and the material which shows little cavitation in the eutectic form showed extensive cavitation in the ternary alloy, the cavities being associated largely with the hard phases. An increase in the level of cavitation was seen with increasing volume fraction size and hardness of the intermetallic.

In dilute Al - Cu alloys (and the Al/Cu eutectic) voids form between α - Al and the θ phase during superplastic deformation as indicated by Sohal (125).

Although a finer grain size allows greater deformation by grain boundary sliding (GBS) and thus more potential for cavitation, the lower flow stress for a given strain rate tends to limit the extent of cavitation. Generally, decreasing the grain size reduces the level of cavitation (34).

The influence of strain-rate is less well defined. For instance, at a given strain, the cavity formation can increase (126), decrease (127) or go through a maximum (34) with change in strain-rate. It is apparent that the influence of strain-rate on cavitation is dependent on the material and the deformation conditions. Generally, the work published indicates that there are many factors which affect the level of cavitation in materials such as composition, deformation conditions and microstructure.

4.2 *MECHANISMS OF CAVITY FORMATION*

As the nature of cavitation in any system is unique, it is very difficult to form a complete theory which encompasses the behaviour of cavitating materials.

There are a wealth of publications (23 - 29, 34, 69, 73) on the mechanisms of cavity nucleation, growth and their role in failure. The following is a brief summary of the relevant points.

4.2.1 *Nucleation of Cavities*

The contribution of the deformation process in the development of cavitation is well established and generally, the number of cavities increases with imposed strain; however, the extent to which super-plastic deformation induces cavitation is less clear.

To nucleate a void under conditions where diffusion is rapid, it is necessary to accumulate sufficient vacancies to form a cluster of critical size. Raj and Ashby (74) applied classical nucleation theory to the formation of voids at hetrogeneities such as grain boundaries, triple points and particles located at grain boundaries.

For particles, two types of cavity were considered, as illustrated in Figure 22a the steady state nucleation rate, I, may be written as :-

$$I = \frac{4\pi\gamma}{\sigma_n \Omega} \frac{D_b \delta_b}{\Omega^{1/3}} \cdot N \exp\left(-\frac{4\gamma^3 F}{\sigma_n^2 KT}\right) \qquad (8)$$

where σ_n is the tensile stress normal to the interface on which the void is nucleating, N is the maximum density of nucleation sites and F is a geometric form factor.

N is related to the fraction of particles and F to the void dimensions, i.e. to its radius and volume which are extremely difficult to obtain accurately. This can lead to immense uncertainties in I the nucleation rate, as F exists in the most sensitive exponential part of the above equation.

Therefore, generally it is not feasible to evaluate nucleation rates in this manner.

An alternative approach, presented by Harris (75) is sometimes used. Grain-boundary sliding gives rise to stress-concentrations at particles intersected by grain boundaries, these can be relieved by grain boundary diffusion leading to conditions of no nucleation due to the relaxation of these stress concentrations. Following the work in this area of Harris (75) and Raj and Ashby (74), a lower bound strain-rate, ($\dot{\varepsilon}_c$) below which no nucleation occurs can be defined by :-

$$\dot{\varepsilon}_c = \frac{11.5\sigma\Omega}{\alpha d D^2} \quad \frac{D_b \delta_b}{kT} \tag{9}$$

where d is the grain diameter, D is particle diameter and α is fraction of total strain carried by grain-boundary sliding.

Using the approximate flow law (68) :

$$\sigma = K\dot{\varepsilon}^m / d^2 \tag{10}$$

Equation 9 can be rewritten as :-

$$\dot{\varepsilon}_c = \left(\frac{11.5K\Omega}{\alpha d^3 D^2} \quad \frac{D_b \delta_b}{kT}\right)^{1/(1-m)} \tag{11}$$

As can be seen, an increase in $\dot{\varepsilon}_c$ is predicted when T and m increase, or when α, grain size and particle size decrease.

It must be emphasized that lack of accommodation at grain boundaries and particles is responsible for nucleation, not growth of cavities. Once a void is greater than a supercritical size, it will grow.

Another problem is the detection of nucleating cavities during superplastic deformation, and to determine whether the cavities observed have grown from existing cavities or have been nucleated as a consequence of superplastic deformation. The diameter of a critical void nucleus is likely to lie in the range 0.12 - 1 μm (128) which cannot be detected by use of light microscopy. It is possible that cavities seen within the first stages of deformation may have grown from pre-existing voids, rather than being nucleated by the superplastic deformation process (23, 128). Further references to this subject can be obtained in an intensive review of the cavity nucleation models by Goods and Brown (73).

4.2.2 Cavity Growth Mechanisms

As Sohal (125) and others show, the analyses for cavity growth in superplastic materials are similar to those present for the high temperature growth of cavities residing on grain boundaries during creep cavitation. There are a host of publications on the mechanisms for growth in a variety of materials (29, 30, 39, 77, 125, 128), but basically, two different mechanisms of void growth are possible for a spherical cavity located on a grain boundary :-

(a) Stress-assisted vacancy diffusion - usually via grain boundaries or

(b) Plastic deformation of the matrix or by a combination of these processes.

The analysis of the first by Raj and Ashby (74) leads to the relationship :-

$$\frac{dr}{d\varepsilon} = \frac{\Omega D_B \delta}{2kT\dot{\varepsilon}r^2}\left(\sigma - \frac{2\gamma}{r}\right)\frac{1}{(\ell n\ \ell/r - 3/4)} \qquad (12)$$

where r is cavity radius, ε is the strain, $\dot{\varepsilon}$ the strain rate, Ω atomic volume, D_B grain boundary diffusion coefficient, δ is the grain boundary width, σ is the applied stress, γ is surface energy of the cavity, k is Boltzmann's constant, T is absolute temperature and ℓ is cavity spacing.

Another approach, which considers diffusion and deformation controlled void growth, has been put forward by Chen and Argon (131) who give an equation for the coupled volumetric growth rate of a void, represented in Figure 23, as :-

$$\frac{dv}{dt} = r^3\dot{\varepsilon}\ 2\pi\left(\frac{\Lambda}{r}\right)^3 \left|\ell n\left(\frac{r+\Lambda}{r}\right) - \frac{3}{4}\left(\frac{r}{r+\Lambda}\right)^2\left(1 - \frac{1}{4}\left(\frac{r}{r+\Lambda}\right)^2\right)\right|^{-1} \qquad (13)$$

where v is cavity volume, $\dot{\varepsilon}$ is the far field strain-rate and Λ is the diffusion distance parameter, given by :-

$$\Lambda = (D_B\delta_B\Omega\sigma/kT\dot{\varepsilon})^{1/3} \qquad (14)$$

In this analysis, matter transport close to the void (region I, Figure 23), is by grain boundary diffusion and the grains are separated by diffusing atoms, whereas in region II displacements normal to the boundary are accommodated by plastic deformation of the matrix.

When the normalised radius (a/Λ) is much less than unity, cavity growth is vacancy diffusion controlled and region I in Figure 23 extends to the outer radius, C.

When (a/Λ) is greater than unity, diffusive transport is slight and restricted to regions close to the void and grain plasticity controls void growth. In this case equation 13 predicts

$$\frac{dv}{dt} \simeq \frac{9}{8}v\dot{\varepsilon} \qquad (15)$$

This is very similar to the relationship for cavity growth by matrix deformation as suggested by Hancock (130):

$$\frac{dr}{d\varepsilon} = r - \frac{3\gamma}{\sigma} \qquad (16)$$

These analyses have ignored the effects of capillarity on inhibiting void growth. A cavity with a radius greater than $r^* = 2\gamma/\sigma$ will grow; if $r < r^*$ then capillarity drives the cavity to shrink.

Martinez and Nix (132) have modified the theory of Chen and Argon (131) to account for this effect.

Many publications (6, 31, 32, 34) have shown that the volume fraction of cavitation in superplastic alloys increases with strain.

Stowell (69) has developed a model which attempts to fit these observations. The model assumes

(i) All voids exist at zero strain, thus not allowing any contribution from nucleation events;

(ii) All voids are of the same initial size and non-interacting.

(iii) Void growth is plastically controlled and described by the equation :-

$$\frac{dv}{d\varepsilon} = \eta v \qquad (17)$$

The analysis suggests that the extent of cavitation (ϕ) has an exponential dependence on strain, given by :-

$$\phi = \phi_o \exp(\eta\varepsilon) \qquad (18)$$

where ϕ_o is the cavitation at zero strain.

Stowell (23) has listed the values of η and ϕ reported in the literature for different materials and concludes that it is dependent on the alloy, strain-rate, temperature and grain size.

From the literature, it is apparent that plastic deformation of the material surrounding a cavity contributes to, and dominates, its growth.

The effects of grain boundary sliding, diffusion and dislocation creep on the extent of cavitation in any system need to be evaluated further.

4.3 *CAVITATION IN THE SUPRAL ALLOY SERIES*

This section briefly describes the various parameters which can influence the cavitation in Supral alloys.

As in all fine-particle stabilised alloys such as Supral, the presence of hard intermetallic precipitates gives rise to cavitation (125).

During deformation, cavitation can be detected through densitometry or metallography at strains between 0.4 - 0.5 and increases linearly with strain (32).

The microstructural features considered to have influence on cavitation in Supral are grain size, grain size distribution, grain shape, particle size and distribution.

Cavity nucleation occurs at (θ) $CuAl_2$ particles as a result of decohesion from the Al matrix. As at the superplastic deformation temperature, the θ particles are much harder than the Al - matrix (125).

The cavities are found to be intergranular, non-uniform in size and distribution (32). Similar effects have been observed in the 7000 series alloys and have been attributed to, amongst other factors, high intermetallic contents and hydrogen outgassing (34).

There is little published work on the effects that parameters such as grain size, precipitate distributions ($ZrAl_3$ and $CuAl_2$) and hydrogen have on cavitation in the Supral alloys. These will be discussed later.

4.3.1 Effects of Cavitation on Mechanical Properties

The effects of superplastic strain and hence cavitation on the 0.2% proof stress (PS) and tensile strength (TS) of the Supral alloys in the as-formed condition is given in Figure 24 (32). These are seen to decrease with increase in strain above 0.7, when the void volume is also seen to increase rapidly with strain. These findings are in agreement with those observed in other aluminium alloys (30, 31, 34).

Heat treatment of the Supral alloys (the conditions of which are different for each and will be discussed later), reduces the level of cavitation, due probably to the sintering-up of the smaller cavities.

Figure 25 illustrates the influence that deformation and heat-treatment has on the micro-cavitation volume fraction (19). Recent work (32) has shown that the fatigue strength decreases with increased strain (above 100%) and fatigue crack growth rates are adversely affected by strain for the Supral series of alloys.

It is apparent that the cavitation present at strain levels greater than 100% (0.7 true strain) lead to a reduction in mechanical properties.

The average strain in most superplastically formed components is low relative to the elongation to failure, and thus cavitation damage is also low. However, certain parts of the components can undergo much higher strains and, as a consequence, cavitation damage can be severe.

Cavitation can either be supressed by the use of back-pressure during superplastic forming (35, 36), or eliminated by a post-forming Hot Isostatic Pressure (37, 38, 39) process.

Work on 7475 (35) and Supral 220 (36) has shown that the superimposition of confining pressures of approximately half the flow stress reduces both the volume fraction and size of the voids in the material, although there is no indication that the nucleation of the voids is inhibited by the HIP process. One problem of using this approach is the commercial cost of replacing or adapting existing superplastic forming equipment so it can be used at pressure; this may be difficult as most presses were not designed with the use of pressure in mind.

Alternatively, post-forming Hot Isostatic Pressure can be used to reduce cavitation. There are commercial sub-contractors who will HIP materials, yet the pressures used can be as high as 200 MPa and it would be expensive to utilise this route for superplastically formed components.

CHAPTER 5 - HOT ISOSTATIC PRESSING

5.1 INTRODUCTION

Generally, when compressive stresses are applied during fabrication of materials (by forging, rolling, extrusion), their soundness and mechanical properties are improved. However, these processes tend to apply compressive stresses in one or two dimensions, allowing material movement in the third.

Compaction using closed dies may produce equal magnitudes of stress in all directions but a major drawback is the severe restriction on component shape.

Frictional forces can also be a problem and can prevent equality of the overall stress distribution. Sticking and removal problems can also arise with dies which generally tend to wear and reduce tolerances.

In contrast, Hot Isostatic Pressing (HIP) can be applied to components of any shape. There is no tool or die wear and because the pressure is transmitted through a fluid medium, the stresses are uniform with the same pressure on all surfaces.

For compression at relatively low temperature (up to 350°C), the pressurising medium can be liquid although its use is limited to relatively low melting point materials. For wider applications, higher temperatures are necessary and for this the use of an inert gas for pressurisation is essential.

Modern equipment can reach temperatures up to 2000°C with operating pressures up to 200 MPa.

HIP can improve properties of materials (such as strength, toughness, fatigue resistance etc.) as discussed in Chapter 1.

5.2 PRINCIPLES OF HOT ISOSTATIC PRESSING

Commercial HIP equipment relies on argon gas as the pressurising medium as it is inert, and does not combine or react with other materials because of its inability to form significant chemical bonds.

The solubility of gases such as nitrogen, oxygen and hydrogen varies with the square root of the pressure. These gases dissolve in solids as atoms but exist in gaseous form as diatomic molecules. With argon there is a linear relationship between pressure and solubility, the molecules are single atoms and its solubility at even the highest attainable pressure is difficult to detect, as argon atoms do not enter the solid.

This lack of reactivity is not reflected in the impurities that are present in the argon gas. It is estimated that under pressures of up to 200 MPa, even 0.067% of oxygen can give an oxidation rate equivalent to that of heating the material in one atmosphere of

oxygen. This illustrates the extreme care needed in gas purification and handling, as well as in gas recovery because argon is too invaluable to use in just one pressure cycle.

At the higher pressures (~ 150 MPa), the density of the gas can vary with temperature, so that at 1400°C, the gas density near the vessel walls can be up to three times that in the hot zone (134). This implies the existence of massive driving forces for convection, the effects of which can be minimised by careful design of internal heaters, convection barriers, radiation shields and insultating inserts.

5.3 *DEVELOPMENT OF PRESSURE SINTERING THEORY*

The first atempt at a real theory was by Murray et al (141), who adopted a phenomenological approach, assuming materials to behave as either a linear viscous or a Bingham solid.

In more recent years, the phenomenological theories have fallen from favour, to be replaced by physical theories based on micromechanisms of deformation; diffusion in particular. These theories bring pressure sintering into the framework of solid state physics and the theory of deformation by the movement of point defects (vacancies and interstitial atoms) and line defects (dislocations).

There have been many appraisals of the mechanisms of densification (38, 39, 42, 44, 52, 133, 134, 135, 136, 137) and the following sections will give a brief review of these.

5.3.1 *Pressure Sintering Diagrams*

The most recent appraisals have led to the construction of diagrams (136, 137) for the pressure sintering of powders, showing the regions in which each densifying mechanism may in turn predominate for a range of values of density and pressure, P_H or temperature, T, where the latter parameters are made dimensionless by plotting ratios of (P_H/σ_y) and (T/T_m) respectively, where σ_y is the instantaneous flow stress and T_m the absolute melting temperature.

Such a diagram is depicted in Figure 26, which shows that porosity closure for less dense material under a high pressure occurs by yielding of the material, which is believed to involve dislocation glide, as will be discussed later.

The material then enters the region where hole closure relies on the process of power-law creep, where the flow rate is dependent on some exponent of the applied pressure, which is variable and dependent on the material and on the conditions.

Finally, as higher densities are approached, atom movement to fill in the holes may take place simply by atomic diffusion which interchanges the places between atoms and vacancies. This mechanism also occurs in pressureless sintering where its rate is dependent on 2(s/r), (where r is the pore radius and s the surface energy), yet with HIP, the much accelerated rate is given by :

$$2(s/r) + P_H \qquad (19)$$

in which P_H is a strongly dependent term.

The mechanism of pore closure by atomic diffusion has several striking features. One concerns the role of grain boundaries which absorb vacancies and conduct them to free surfaces. Thus holes situated on grain boundaries would be expected to shrink more rapidly than those within the grains (138), as in Figure 27.

Holes also have been seen to provide a pinning effect on boundaries as when some holes are eliminated the grain boundary is able to move, although if it sweeps too rapidly it may leave holes within the larger grains (139).

The second important feature of pore closure by atomic diffusion is that this mechanism of atom transport does not carry with it any particles; the diffusing atoms move around them and fill in the porosity with the matrix material as shown in Figure 28 (140). The following sections will review the mechanisms involved in pressureless and pressure sintering.

5.3.2 *Mechanisms for Pressure Sintering*

Table 4 shows the mechanisms which contribute to the sintering of a powder compact.

If an external pressure is applied, new mechanisms appear whilst some existing ones are enhanced.

For powder compacts, the pressure may cause particle fragmentation and rearrangement, it may induce plasticity (including plastic creep) in the particles and may also augment the effects of surface energy as a driving force for diffusion. Some mechanisms transport matter from within the particles to the porosity, whilst others merely transport from one part of the surface to another.

Ashby et al (135, 136, 137) predict the total sintering rate for a compact and the dominant mechanism during the process by formulating a set of neck growth and densification rate equations which give, as a function of known variables and physical constants, the contribution of each mechanism to total sintering.

The models developed here are restricted to powder compacts of pure, single-component materials, and do not take account of effects that occur in multi-component systems. For instance, different species diffuse at different rates and second phase particles can affect dislocation motion and lower grain boundary efficiency to act as sources and sinks for vacancies (137).

5.3.3 *Models for Pressure Sintering*

The existing models for pressure sintering take into considera-

tion plastic yielding, viscous flow, power law creep and diffusional processes (136, 137).

Ashby et al (135, 137) and Swinkels et al (136) distinguish two stages, according to the geometry of the pores.

During the initial stage, the compact is idealised as an aggregate of individual particles with small, sharply curved contacts between them. In the final stage, the pores are idealised as an array of isolated spherical holes.

Some authors (137) introduce a further intermediate stage, idealising the pores as a connected network of cylindrical holes, but this approach is seldom used. Figures 29 and 30 show the mechanisms which contribute during the various stages of densification. A more complete discussion of these mechanisms is given in references 135, 137 and 142. The models described below refer to these stages.

5.3.4 *Plastic Yielding*

If an external applied pressure P_e is large enough, the flow strength of the material is exceeded locally where the particles touch (136, 142). For the initial stage (relative density $\rho/\rho_o < 0.9$), the models are based on the slip-line field solution for a flat punch indenting an infinite plastic half space. The neck grows until the local indentation pressure P_1 is

$$P_1 \simeq 3\,\sigma_y \qquad (20)$$

where σ_y is the flow stress of the material. The relative density (ρ/ρ_o) of the compact can be related to the relative initial density (ρ_i/ρ_o) and the neck radius x by (136) :-

$$\left(\frac{\rho}{\rho_o}\right) = \left(\frac{\rho_i}{\rho_o}\right)\left|1 + \frac{3}{2}\left(\frac{x}{a}\right)^2\right| \qquad (21)$$

where a is the particle radius.

The density as a function of external pressure P_e is given by (136) :-

$$\left(\frac{\rho}{\rho_o}\right) = \left(\frac{\rho_i}{\rho_o}\right)\left|1 + \frac{P_e A_f}{2\pi n_f \sigma_y a^2}\right| \qquad (22)$$

where A_f is the surface area of a cell containing one particle ($\sim 4\pi a^2$) and n_f is the number of contacts (co-ordination number) of a particle. Final stage densification is modelled as the plastic collapse of a thick spherical shell with the pore at its centre as shown in Figure 31.

Yielding is said to occur if

$$P_3 > -\frac{2}{3}\sigma_y \ell n(1 - \frac{\rho}{\rho_o}) \qquad (23)$$

Here P_3 is the driving pressure for densification during this stage, given by :-

$$P_3 = P_e - P_i + 2\gamma_s/z \qquad (24)$$

where P_i is the internal gas pressure in the pore, z is the pore radius and γ_s is the surface energy.

The intermediate stage is modelled by replacing the spherical shell by a cylindrical one, constrained by the compact along the axis of the porosity (137). Yielding then occurs until

$$P_2 > -\frac{\sigma_y}{\sqrt{3}} \ell n\ (1 - \frac{\rho}{\rho_o}) \qquad (25)$$

where $P_2 = P_e + \gamma_s/z$.

As porosity is open during this stage $P_i = 0$.

In addition to these equations, certain empirical relationships have been proposed. Heckel (143) likens compaction to a first order chemical reaction.

$$\frac{d(\rho/\rho_o)}{d(P_e/\sigma_y)} = K(1 - \rho\frac{\rho}{o}) \qquad (26)$$

which on integration, gives

$$\ell n(\frac{1}{1 - (\rho/\rho_o)}) = K_1 \frac{P_e}{\sigma_y} + K_2 \qquad (27)$$

where K_1 and K_2 are dimensionless constants. Note that if K_1 is set to 3/2 equations 27 and 24 are almost identical. Moreover, at low ρ/ρ_o, it reduces to an equation similar to equation 21. Thus it approximates both the initial and final stage models. It has been found to fit the compaction data of iron, copper, nickel and tungsten powder well over a wide range of pressures and densities.

5.3.5 *Viscous Flow*

The earliest theories of pressure sintering were based on Newtonian-viscous flow, as in a liquid. The model works well for materials such as Silica but not for metals or ceramics.

The relationship between the viscosity, η, the applied pressure P_e and time t with density is given by

$$\ell n \frac{(1 - (\rho/\rho_o))}{(1 - (\rho_i/\rho_o))} = - \frac{3P_e}{4\eta} t \qquad (28)$$

5.3.6 *Power-Law Creep*

Earlier work on hot-pressing of metal powders found a power law relationship between densification rate and applied pressure P_e of the form :

$$\frac{\dot{\rho}}{\rho} \alpha P_e^n \qquad (29)$$

with n > 1.

The most complete treatment is that of Wilkinson (137) who developed models for each stage of pressure sintering using a constitutive law for power-law creep of the form :-

$$\dot{\varepsilon} = A\sigma^n \qquad (30)$$

where $\dot{\varepsilon}$ is the radial strain rate and A is a temperature dependent constant. Final stage densification is modelled by using the creep of a thick walled spherical shell centred on a pore (Figure 31).

The outer radius of the shell, b, is defined, such that matter is conserved :

$$\frac{\rho}{\rho} = 1 - \left(\frac{z}{b}\right)^3 \qquad (31)$$

The densification rate is given by (136)

$$\frac{\dot{\rho}}{\rho_o} = \frac{A\left(\frac{\rho}{\rho_o}\right)\left(1 - \frac{\rho}{\rho_o}\right)}{2\left|1 - \left(1 - \frac{\rho}{\rho_o}\right)^{1/n}\right|^n} \left(\frac{3}{2n} P_3\right)^n \qquad (32)$$

Densification during the intermediate stage is achieved by replacing the spherical shell by a cylindrical one (137) giving

$$\left(\frac{\dot{\rho}}{\rho_o}\right) = \frac{\sqrt{3}\, A \frac{\rho}{\rho_o}\left(1 - \frac{\rho}{\rho_o}\right)}{\left|1 - \left(1 - \frac{\rho}{\rho_o}\right)^{1/n}\right|^n} \cdot \left(\frac{\sqrt{3}}{n} P_2\right)^n \qquad (33)$$

For the initial stage, Wilkinson (137) developed a model by drawing on theories for hot hardness tests leading to :-

$$\left(\frac{\dot{\rho}}{\rho_o}\right) = \frac{3}{4\pi}\left(\frac{\rho}{\rho_o}\right)^2 \frac{n_f A_f x}{a^3} A \left(\frac{3}{2n} \frac{A_f}{\pi x^2} P_e\right)^n \qquad (34)$$

where n_f if the coordination number of the particle and A_f is the surface area of a 'cell' containing one particle (137). A fuller account of all these models can be found in references 135, 136, 137, 142.

5.3.7 *Diffusion Mechanisms*

Matter may be transported from the contact zones to the surface of a sintering neck by both grain boundary and lattice diffusion.

During the initial stage, the volume of the material deposited on the surface of the sintering necks of one particle per second by boundary diffusion is given by (137) :

$$\dot{V} = 4\pi \frac{(\delta D_b + a D_v)}{kT} \Omega\, n_f P_1 \qquad (35)$$

where D_b is the boundary diffusion coefficient times its thickness, D_v is the lattice diffusion coefficient, Ω is the volume of the diffusing atom, k is Boltzmann's constant.

The densification rate for this mechanism during the initial stage is given by (137)

$$\left(\frac{\dot{\rho}}{\rho_o}\right) = \frac{12\rho^2}{\rho_o a^3 g(D)} \cdot \frac{(\delta D_b + r D_v)}{kT} \Omega\, n_f\, P_1 \qquad (36)$$

where g(D) is a purely geometric term. During the final stage, matter is transported along the grain boundaries onto the surfaces of spherical grain-boundary voids. The solution for this case is (137)

$$\left(\frac{\dot{\rho}}{\rho_o}\right) = \frac{54\Omega\delta D_b}{kTa^3} \frac{\left|I - (I - \rho)^{2/3}\right| P_3}{3(1-\rho)^{2/3} - \left|1+(1-\rho)^{2/3}\right| \ell n(1-\rho)^{-3}} \qquad (37)$$

All the mechanisms described above represent the current understanding for densification during hot isostatic pressing of powders. But, the rates can be influenced by factors which have been ignored in deriving the rate equations. The most important being grain growth, especially in view of the long cycle times which exist during HIP.

Grain growth may remove grain boundaries (which act as sources and sinks for vacancies) from the necks between powder particles. This would have no effect on plasticity or power-low creep, but would suppress diffusional densification (142). As yet, an adequate model to account for this phenomena is not available.

5.4 *EFFECT OF HIP ON CREEP CAVITATION*

Apart from the theories concerning the compaction of powders during HIP, several workers (6, 38, 39, 52) have investigated the effect of hydrostatic pressure on the sintering behaviour of casting porosity and creep cavitation and discussed it in terms of vacancy diffusion in the stress fields of the hydrostatic pressure and pore surface tension.

The sintering of enclosed cavities has been studied by Brett and Seigle (140), who noted that cavities resulting from dezincification in brass closed during annealing only if on or near grain boundaries. However, intragranular cavities in aluminium, introduced by quenching, have been seen to anneal out at a rate consistent with volume diffusion (144).

Beere and Greenwood (39) examined the contribution of hydrostatic pressure (up to 30 MPa) to sintering of creep cavities in magnesium and copper. They found the decrease in sintering rate with time and the increase in rate with higher pressures were consistent with a model of cavity closure by grain boundary self diffusion.

Similar results were reported by Stevens and Flewitt (38) on the sintering of creep cavities in a Ni - 2% Cr alloy.

5.4.1 *Theories of Sintering of Grain Boundary Cavities*

The cavitation in a polycrystalline material subject to creep deformation consists of discrete voids having a range of sizes distributed along the grain boundaries.

The diffusional growth of such cavities under the action of an external force has been described by Hull and Rimmer (129). Various workers have used this to examine the reverse effect. Greenwood (145) has discussed the validity of this relationship when applied to cavity shrinkage.

Ashby (135) has applied this model to the sintering of a spherical cavity of radius r sited on a grain boundary.

Each cavity is surrounded by a concentric sink situated midway between cavities to which vacancies diffuse. The rate at which such a cavity sinters is given by :

$$\frac{dr}{dt} = \frac{D_b \delta \gamma \Omega}{2r^3 kT} \quad \frac{1}{\ell n(\frac{x}{r}) - \frac{3}{4}} \tag{38}$$

where D_b is the grain boundary diffusion coefficient, δ is grain boundary width and x is the intercavity spacing.

If the cavity contains gas at a pressure P_I and is subject to an external hydrostatic pressure P_e, then following Hull and Rimmer (129), the difference in the vacancy concentration between the cavity C_c and the grain boundary sink C_b is :-

$$C_c - C_b = C_e \exp \left| \frac{2\gamma}{r} - P_I + P_e \right| \frac{\Omega}{kT} \tag{39}$$

where C_e is the equilibrium vacancy concentration. Thus equation 38 becomes :-

$$\frac{dr}{dt} = \frac{D_b \delta \Omega}{4r^2 kT} \left| \frac{2\gamma}{r} - P_I + P_e \right| \left| \frac{1}{\ell n(\frac{x}{r}) - \frac{3}{4}} \right| \tag{40}$$

Beere and Greenwood (39) suggest creep cavities in copper contain gas pressures up to 10 MPa. The gas pressure develops during creep by diffusion of external gas along grain boundaries and bulk diffusion of interstitial gas atoms. The problem of analysing the contribution of the gas within a pore is complicated. Essentially, it reduces to the need to consider gas diffusion throughout the sintering process which is regulated by the diffusion of vacancies along the grain boundary. The gas may not also necessarily behave as 'ideal' when the cavity becomes smaller.

For the present, the extreme case of continuously increasing internal pressure, as the cavity shrinks, is taken to account for the behaviour of gas in a pore under isostatic pressure (38).

If the initial cavity radius is r_i, and the initial pressure P_i, then

$$P_I = P_i (\frac{r_i}{r})^3 \tag{41}$$

Thus equation 40 becomes :-

$$\frac{dr}{dt} = \frac{A}{r^2} \left| \frac{2\gamma}{r} - P_i (\frac{r_i}{r})^3 + P_e \right| \left| \frac{1}{\ell n(\frac{x}{r}) - \frac{3}{4}} \right| \tag{42}$$

where $A = \frac{D_b \delta\Omega}{2kT}$

To evaluate the change of cavity size with sintering time, integration of equation 42 gives :-

$$\int_0^t dt = \int_{r_i}^{r} \frac{r^2}{A} \times \left|\frac{2\gamma}{r} - P_i\left(\frac{r_i}{r}\right)^3 + P_e\right|^{-1} \left|\ln\left(\frac{x}{r}\right) - \frac{3}{4}\right| dr \qquad (43)$$

Equation 43 can be evaluated numerically by using Simpsons Rule.

Plots using this analysis have been produced by Stevens and Flewitt (38) for Nickel-Chromium alloys (Figures 32 and 32a). These clearly show that increasing the hydrostatic pressure (with no gas present in the pores) results in a significant decrease in time for cavity closure (Figure 32).

If the initial cavity contains an internal pressure of P_I = 0.1 MPa, then Figure 32a shows the variation of r with time for the range of pressures used in Figure 32. Comparing the two shows the variation of r is of the same form except a critical size is reached where the internal gas pressure balances the hydrostatic pressure and the gas pressure as defined by equation 39. The analysis also shown that increasing the external pressure ensures greater removal of gas filled cavities.

Finally, they suggest that extensively cavitated material requires significantly longer time for recovery than material containing a few small widely spaced cavities.

It seems clear from the literature that no one unique mechanism is operating during HIP and that no single formula can cover all the stages.

CHAPTER 6 - HYDROGEN IN ALUMINIUM

The failure of metal parts because of an associated excess of contained hydrogen is usually associated with catastrophic failure. Whilst this may be true for structural steel failures arising from hydrogen embrittlement, in aluminium alloys excess hydrogen shows itself, for example, in the form of casting porosity or as surface blistering in fabricated parts (58, 59). The subject of hydrogen in metals is vast, thus much of this chapter will be concerned with the behaviour of hydrogen in aluminium and its alloys.

6.1 HYDROGEN IN METALS

It is difficult to establish a theoretical framework with which to interpret information from manufacturing operations on the nature of hydrogen in metals.

There are models (60) which represent hydrogen solutions in liquid metals reasonably well, and to a great degree depend on assuming that hydrogen is accommodated in solution, as non-interacting atoms, all occupying equivalent interstitial sites.

The concept of true interstitial solution in solid metals presupposes a degree of perfection in structure difficult to achieve experimentally and certainly untypical of industrially produced metals where generally hydrogen is distributed hetrogeneously (60).

In establishing a satisfactory theoretical framework by which to interpret information from manufacturing operations it is necessary to examine the nature of hydrogen occlusion in metals.

The following analysis is applicable to metals which do not form hydrides.

6.2 HYDROGEN SOLUTIONS

Size factors determine that diatomic gas must dissociate on dissolution :

$$H_2(\text{gas}) \rightleftarrows 2H \text{ (solution)} \qquad (44)$$

The hydrogen in interstitial solution is assumed to exist as non-interacting atoms, all occupying equivalent sites.

For dilute solutions, Henry's law applies and if ideal behaviour is assumed for the gas, equilibrium is given by :-

$$K = \frac{a_{H}2}{aH_2} = \frac{N^2 p\theta}{P} \qquad (45)$$

where a_H is the activity of the solute referred to the atomic fraction at infinite dilution as the standard state, a_{H_2} is the

activity of the gas referred to the pure gas at a pressure p^{θ}, and N is the atomic fraction of solute in equilibrium with a gas pressure p.

Equation 46 yields (60) 'Sieverts Law' :

$$\frac{N}{N^{\theta}} = \left(\frac{p}{p^{\theta}}\right)^{0.5} \qquad (47)$$

where N^{θ} is the atomic fraction of solute in equilibrium with standard pressure p^{θ}, assuming N^{θ} lies within the range of composition for which Henry's law applies.

Variation of solute concentration at constant pressure with temperature is expressed by the van't Hoff isobar, substituting for K from equation 45 is given by :

$$\frac{\partial}{\partial T}(\ell n\ K)_p = 2\frac{\partial}{\partial T}(\ell n\ N)_p = \frac{\Delta H^{\theta}}{RT^2} \qquad (48)$$

and since, for a restricted temperature range, the standard enthalpy of solution can be considered constant, integration yields

$$\ell n\ N = -\frac{\Delta H^{\theta}}{2RT} + \text{constant} \qquad (49)$$

A solute comprising non-interacting atoms in a single phase diffuses according to Fick's Law.

$$\frac{\partial c}{\partial t} = DA\frac{\partial c}{\partial x} \qquad (50)$$

where under steady state conditions, the amount of matter flowing through a transverse cross-section of $A(m^2)$ in time, t, along a concentration gradient, $\partial c/\partial x$, and where D, the diffusion coefficient is seen to vary with temperature, according to an Arrhenius-type relation

$$D = D_o \exp -\frac{\Delta G^*}{RT} \qquad (51)$$

where ΔG^* is the activation energy for diffusion and D_o is a constant for the system.

Physical and Chemical Traps for Hydrogen

It is suggested that absorbed hydrogen (60) must be partitioned in the metal between the gas being in solution and any hydrogen trap sites such as voids and cracks.

Several kinds of traps for both atomic and molecular hydrogen have been identified. There is evidence for atomic traps due to the association of interstitial solutes with lattice defects as the binding enthalpy between the solute atoms and defects is negative,due to relief of lattice strain. Albrecht et al (146) have provided evidence for hydrogen transport in aluminium by dislocation transport. The question as to whether grain boundaries act as atomic traps for hydrogen is still unresolved.

Two kinds of molecular traps are known. The first comprises defects in which the gas accumulates until its pressure reaches the value required for equilibrium with solute hydrogen in the metal (60). The other is the result of spontaneous precipitation of hydrogen referred to as secondary porosity (147).

In certain alloys, additional hydrogen may also be absorbed in the form of chemical traps(such as Zirconium hydride)when these alloys are permitted to absorb hydrogen.

The concentration of dissolved hydrogen in metals is expressed in terms of $cm^3/100g$ of metal measured under standard temperature and pressure. Although it is important to realise that the total gas content is the sum of the quantities in true solution and in occluded forms. These can be represented as :

$$0.5H_2 \rightleftarrows H \text{ (solution)} \rightleftarrows H \text{ (trap sites)} \qquad (52)$$

6.2.1 Hydrogen in Aluminium and its Alloys

When aluminium is cast it retains virtually all of the dissolved hydrogen it contains (58, 59, 60) but because the solubility of hydrogen is less in the solid than in the liquid metal, some of the gas is rejected from solution and entrapped in the solid structure. The rejected gas can be nucleated both in the liquid during solidification and in the solid immediately afterwards, generating two forms of porosity distinguished as primary porosity and secondary porosity (147).

Both can have important effects on the cast metal and on the wrought products manufactured from it.

6.2.2 Hydrogen Sources During Melting and Casting

Molten aluminium readily absorbs hydrogen when reacting with water or its vapour.

$$2Al + 3H_2O \rightleftarrows Al_2O_3 + 3H_2 \qquad (53)$$

It is suggested that sources of hydrogen for absorption in melts are hydrated corrosion products, water and oil on the surfaces of virgin metal stored under unsatisfactory conditions (60) and on

scrap returned for remelting, although there is little direct experimental evidence for these observations.

The hydrogen content of the melt may also be augmented by reaction with water vapour in the atmosphere, and seasonal variations in the incidence of hydrogen generated defects, such as blistering, have been attributed to variation in humidity over the melts (148).

Another source of hydrogen is steam evaporated from residual moisture in the linings of launders, moulds and their accessories over which the molten metal passes during transfer from the furnace in the casting operations.

6.2.3 *Hydrogen Sources During Solid Metal Manufacture*

Solid metal can absorb hydrogen when heat-treated (60). The surface condition of the material is a factor. In Eborall and Ransley's experiments (61), corroded thin sheets of Al - 5Mg alloy evolved four times as much hydrogen as material which first had the corroded surface removed. Talbot and Granger (147) showed how hot-rolled plates of aluminium had their hydrogen contents doubled during an industrial anneal at 500°C for 8 hours.

Eborall and Ransley (61) and Swain (62) showed Al - Mg alloys readily absorb hydrogen from water vapour at 400°C - 500°C; the gas rapidly penetrating thin sections. The absorption is catalysed by sulphur which is present in industrial furnaces and this effect is inhibited by the vapour from volatile fluorides placed in the furnace atmosphere (60).

There is a considerable amount of work published on the distribution of hydrogen in castings and ingots of aluminium and its alloys and further information can be found in references 58, 59 and 60.

Interdendritic porosity in ingots cast for fabrication does not weld up completely in working operations but is flattened into planar discontinuities (58, 59, 60, 123). The presence of hydrogen gas in such voids inhibits healing on subsequent working and is responsible for effects such as blisters on annealed or solution-treated materials (58, 59).

Surface blistering is a common form of damage to wrought aluminium and its alloy products. The basic cause is the inflation of internal defects by hydrogen when the overlying material is soft during annealing or solution-treatment prior to ageing.

Blisters can be induced in otherwise sound metals if faults are introduced in the course of mechanical working. The metal needs to spend some time at a relatively high temperature to allow hydrogen to accumulate by diffusion to the defects as it is virtually immobile in aluminium at room temperature (60).

The most effective sources of blisters are defects formed as a

consequence of the extrusion process and areas of poor adhesion between cladding and core in roll-bonded clad products, as those observed by Kostron (149) in Al - Cu - Mg sheet. He also suggested that inclusions and hard intermetallic compounds can become partly detached from the matrix during deformation and hence provide blister sites.

When there is marked hydrogen absorption in solid aluminium alloys, as can happen during solution-treatment in air furnaces preparatory to age-hardening (150), spherical cavities grow near the surface and coalesce to form so-called 'diffusion' or 'reaction' blisters (149).

There is a body of evidence which accounts for the presence of hydrogen in aluminium and its alloys. What is yet unclear is the effect different conditions of Hot Isostatic Pressing would have on the hydrogen present in porosity in the metal.

The basic theory for removal of a pore containing gas under HIP has been reviewed in Chapter 5, but a simple analogy can be used to show the benefits of using higher pressures.

The internal pressure P_i to stabilise a pore of radius r is given by $P_i = 2\gamma/r$ where γ is the surface energy. If the pore exists without internal gas then $2\gamma/r$ causes a driving force for closure. As for most metals, γ is typically around $2Jm^{-2}$, a pore of radius 0.1mm gives a value of $2\gamma/r$ of ~ 4×10^4 Nm^{-2}. The maximum HIP pressures obtainable commercially are up to 200 MPa and comparing the two values shows how beneficial a HIP treatment can be.

If gas is present within the pore, increased HIP pressure P_H would be expected to reduce the radius of the pore, raising the internal pressure within the pore. It has been suggested (42) that an increase in external pressure causes increases in solubility of the gas, allowing it to diffuse away to permit pore closure.

Much of the published work shows the beneficial effects of HIP on the mechanical properties of materials (34, 47), yet very little is available on the behaviour of hydrogen gas present in metal porosity when subject to a HIP treatment.

Recent work by Rooy (47) has shown the improvement of properties undergone by cast aluminium parts after HIP. He suggests that the process success is a consequence of the combined effect of pressure and temperature which causes collapse of internal voids through plastic deformation. The hydrogen is assumed to be redistributed by going into solution at the increased pressure allowing

pore closure. A reheat treatment in casting with higher levels of hydrogen caused the gas to diffuse to lattice discontinuities and porosity is seen to appear at locations such as grain boundaries.

CHAPTER 7 - MATERIAL AND EXPERIMENTAL TECHNIQUES

7.1 AS-RECEIVED MATERIAL

The material under investigation is SUPRAL 150 (clad 2004) and has a nominal composition by weight of 93.5% Aluminium, 6% Copper and 0.5% Zirconium, with pure aluminium cladding on both faces of the sheet material.

The alloy was provided by Superform Metals Ltd., in the form of cold-rolled 4mm thick sheet (virgin or zero strain material) and as superplastically formed (SPF) discs cut from 'top hats' themselves, produced by Superform.

A material thickness profile of the whole top hat was measured and the true thickness strain ε_3, defined as $\ell n\ (t_f/t_o)$ was calculated.

Density measurements were carried out on $25mm^2$ samples cut from the discs in an attempt to relate the deformation to the cavitation present in the material, and to check the uniformity of the superplastic deformation within a disc.

7.2 ISOTHERMAL ANNEALS

In order to determine the recrystallisation and grain growth characteristics of the supplied materials, coupons (10mm x 20mm) were cut from the virgin and SPF material and annealed between temperatures of 200°C - 530°C for periods of time ranging from 30 minutes to 24 hours in an air-circulation furnace controlled to ± 1°C.

The densities of the coupons were taken before and after annealing, to determine the effects of increasing temperature and time on the cavitation present in the alloy.

The annealed coupons were mounted so as to expose the T-ST directions, as indicated in Figure 33, from which grain sizes were determined.

7.3 METALLOGRAPHIC EXAMINATION

Metallographic techniques were used to determine the effects of HIP, heat-treatment and other processes described later, on the composition, structure and cavitation present in the formed and unformed alloy.

7.3.1 Grain Size Determination

The Mean Linear Intercept (MLI) parameter was used to give values for the grain size. MLI values were obtained by observing a suitably etched specimen under the optical microscope and counting the number of grain boundary intersections along a line (of known length) which was superimposed on the specimen surface.

Dividing the line length by the mean number of intersections gave the MLI in microns. This process was repeated ten times at each location and the mean value recorded. Rotation of the specimen or graticule allowed the MLI to be determined in the T and ST directions.

7.3.2 Scanning Electron Microscopy

Cavitated and virgin specimens were examined in a Cambridge Instruments Stereoscan 2A, to observe the nature of cavitation and identify the precipitates present in the alloy by use of the analysis facilities.

An attempt was also made, by mapping, to determine the distribution of copper and zirconium in the material and relate this to the grain size.

Fracture surfaces of the room temperature tensile test specimens were also viewed under the SEM.

7.3.3 Transmission Electron Microscopy

Thin foils for the TEM were prepared by cutting 3mm diameter discs from the as-received and cavitated material by spark erosion machining to reduce deformation. The specimens were then mechanically ground to 0.15mm and subsequently jet polished using a Struers Tenupol on 20V and 0.2A. The electrolyte mixture contained ethanol, perchloric acid and glycerol in the proportions 7 : 2 : 2.

A photoelectric cell terminated polishing when a small perforation appeared in the foil. After washing in ethanol, the foils were placed in a hot stage and viewed in a Jeol 200 kV TEM.

The temperature of the hot stage was raised in 50°C increments up to 530°C, to see the effect on dislocation movement and the behaviour of precipitates (mainly $CuAl_2$) with increasing temperature.

A major problem in using this technique is the difficulty of obtaining photographs because of specimen movement in the hot stage during heating. At higher temperatures, oxidation of the specimens was another problem.

7.3.4 Hot Stage Microscopy

The polished and etched edge sections of both formed and virgin specimens of Supral 150 were viewed under a light microscope whilst being heated in a Leitz hot stage.

An atmosphere of high-purity Argon was used to minimise surface oxidation. The specimens were heated up in the hot stage in an attempt to view the behaviour of internal gases in the material with increasing temperature. Using this method, surface oxidation was minimised up to 400°C.

A high vacuum (> 10^{-6} torr) by the use of both a rotary pump and

a diffusion pump was achieved in the Hot Stage. This ensured no surface oxidation of the specimens up to 550°C and was used to study the behaviour of the intermetallics ($CuAl_2$ and $ZrAl_3$) with increasing temperature in the alloy.

7.4 *CAVITATION DETERMINATION*

Cavitation in the alloy was studied using two techniques :-

(a) Hydrostatic weighing

(b) Quantimet Image Analysis

7.4.1 *Hydrostatic Weighing*

Many variations of this technique exist for the measurement of density. It is often used to quantify the extent of cavitation during superplastic deformation (34, 35, 125, 126) or void-volume fraction during creep (38).

A commonly used method is that originally described by Ratcliffe (155) for the measurement of relative densities and the basis of this technique is to weigh the specimen against a dummy (standard) in air and liquid, before and after the specimen has been subjected to a treatment, which changes its density.

An alternative method is to measure the absolute density as described by Cawthorne and Sinclair (156).

The density of the sample is given by :-

$$\rho_s = \frac{(A - N)}{(A - W)} (\rho_{water} - \rho_{air}) + \rho_{air} \qquad (54)$$

where N is the empty weighing system, A is the specimen weight in air and W the specimen weight in water, see Figure 34. ρ_{air} is the density of air and ρ_{water}, the density of water.

7.4.2 *Apparatus and Procedure*

The apparatus, shown in Figure 34, uses an analytical, self-calibrating specific gravity Sartorious balance (with the pan inside a draught proof enclosure) reading to 10^{-5} grams.

Water with a few drops of wetting agent is used for the immersion liquid. The use of heavy organic liquids, which should, in theory, lead to improved accuracy, has been found (156) to lead to poor standards of reproducibility; the high coefficients of expansion of these organic liquids lead to strong convection currents. The vapours from such liquids are unpleasant, particularly since vigorous ventilation is precluded for reasons of balance stability. Water is innocuous, has a density well-characterised over the ambient temperature range and has a low coefficient of thermal expansion.

The repeatability of the technique may be adjudged from Figures

51 and 51a which give the results of density determinations on the same coupons of virgin and formed Supral 150 over a period of time.

7.5 *QUANTIMET IMAGE ANALYSIS*

The Imco Quantimet 720 analyser was used to give the area fraction and mean size of cavities in the T - ST plane of the unetched mounted specimens. Between five and ten areas were taken for each sample.

7.5.1 *Area Fraction*

The area fraction (a_f) of cavities was given by :-

$$a_f = \frac{X_c}{X_t} \tag{55}$$

where X_c = Number of picture points covering cavities

X_t = Total number of picture points on the screen, which is 500,000

Calibration of the screen area gives a value for each picture point, Table 5.

7.5.2 *Cavity Size Distribution*

The cavity size distribution can be obtained by several methods.

Firstly, the total number of cavities displayed (N_f) is divided into the total void area, X_a, to give the number of picture points per cavity, A_c

$$A_c = \frac{X_a}{N_f} \tag{56}$$

Assuming a distribution of spherical cavities, then each cavity area equals πr^2, and hence the mean cavity radius r, is given by :-

$$r = \left(\frac{A_c}{\pi}\right)^{\frac{1}{2}} \tag{57}$$

The radius can also be obtained from the perimeter values, as the perimeter is given by πd, where d is cavity diameter.

7.5.3 *Cavity Separation*

Using the 'intercept' mode on the Quantimet 720 enables the mean horizontal chord length (P_H) between cavities to be determined. The

cavity separation (ℓ) from this data is calculated by :-

$$\ell = \frac{X_t - X_a}{P_H} \qquad (58)$$

Some of the specimens used in the image analyser were photographed and printed for a manual image analysis.

A grid placed over the photograph enlarged to a suitable size allowed manual determination of the cavity size distribution.

7.6 HOT ISOSTATIC PRESSING

7.6.1 Equipment

Hot Isostatic Pressing was carried out in an internally-heated vessel of the type shown in Figure 35. The vessel is capable of safely operating at pressures up to 60 MPa (8000 psi) at 850°C.

Pressures up to 60 MPa can be achieved independently of temperature.

The pressure vessel consists of an EN24 high tensile Ni - Cr - Mo steel, Figure 35. A 4 t.p.i. buttress thread is machined in each end to accommodate the hollow nuts which retain the end-closures. These are cylindrical plugs separated from the hollow nuts by slip rings to prevent turning of the plugs. Sealing of each end closure is effected by rubber 'O' rings, set in a recess in the plug supported by two further rings to prevent extrusion of the 'O' ring under pressure. The plugs and hollow nuts are made from EN8, a medium-tensile carbon steel. The end plugs are thermally insulated from a double-wound helical heating element by ceramic fibre, heat shields and 'Sindanyo'.

The vessel is pressurised from a standard, high-purity argon holding (up to 17 MPa). Higher pressures are obtained by the use of an air-driven booster pump, Figure 36.

Temperature control is achieved by stainless steel sheathed chromel-alumel thermocouples in thermal contact with the specimen in the heating coil.

There are five other thermocouples located around the vessel; each has a preset temperature which, when exceeded, cuts the power to the vessel. The temperature is continuously monitored on a chart recorder. Pressure sensing and release devices are incorporated into the pressure circuit, to provide warnings in the event of over-pressurisation.

A fuller description of the vessel is given in reference 157.

7.6.2 Procedure

The specimens are placed inside the vessel which is then

evacuated using a rotary pump and flushed several times with high-purity argon. Charles Law was then used to calculate the initial vessel pressure required to give the desired final pressure at the temperature of HIPping.

The temperature was raised in 50°C stages to the desired value, a procedure which took between 5 and 15 minutes depending on the pressure and temperature required and the mass of metal to be HIPped. The temperature control is better than ± 2°C.

In later experiments the vessel was evacuated at temperature (~ 400°C) to ensure that any adsorbed gases and moisture in the vessel were removed. The Argon gas was then introduced and HIPping proceeded as described earlier.

7.7 EFFECT OF HIP ON CAVITATION IN SUPRAL 150

25mm^2 coupons were cut from the discs of the superplastically formed top hats and classified in terms of initial density and thickness strain.

Three coupons of differing thickness strains, containing different levels of initial cavitation were used for each HIP test. In order to determine the conditions which closed cavitation in the formed material, the following range of temperatures and pressures were used, all for a half-hour HIPping period.

Pressure (MPa)	Temperature (°C)
35)	
28)	
21)	300, 325, 350, 375, 400, 450
14)	
7)	

The density of each coupon was remeasured after HIPping and compared to the density of the undeformed virgin sheet material.

Once HIP conditions which closed cavitation in the deformed alloy were determined, these were used to show the effect of HIP time (between 30 seconds and 10 hours) on cavity closure and sealing.

The effect of heat-treatment on the HIPped SPF Supral 150 was also investigated to ascertain whether cavitation had closed or sealed during the HIP process.

7.7.1 Mechanical Property Improvement by HIP. Tensile Testing

25mm gauge-length tensile test specimens were cut from the discs of the formed top hats and from the undeformed cold-rolled sheet material in both at 0° and 90° to a chosen direction and tested at room temperature to give basic mechanical property data.

Before tensile testing, the specimens were subjected to a range

of HIPping conditions known to close cavitation, followed by the appropriate heat treatment recommended for the Supral 150, shown in Table 6.

Further work attempted to determine the effects of internal gases in cavity closure and sealing. Specimens were vacuum-degassed (as shown in Section 7.8) before being HIPped and heat-treated as before.

A fuller description of the conditions that each set of tensile test specimens has been subjected to is present in the table of results for each set, shown in Chapter 8.

7.8 VACUUM DE-GASSING

An attempt was made to determine the effect of internal gases on cavity closure and sealing in the alloy. To do this, tensile speciment were vacuum de-gassed before HIPping under conditions known to close cavitation.

The conditions used were 500^{o}C , under a vacuum of 10^{-6} torr for one hour. These are conditions used when analysing for hydrogen in the alloy and ensure little gas is left left within the alloy. (164)

The equipment used for the vacuum degassing process is shown in Figure 38.

8. RESULTS

8.1 AS-RECEIVED MATERIAL

Energy-dispersive X-ray analysis on the SEM shows that the heavily cold-rolled structure of the Supral 150 undeformed sheet material (Figure 39) consists of two phases : the aluminium rich matrix and copper rich ($CuAl_2$) θ precipitates of varying sizes. The presence of large $ZrAl_3$ precipitates, Figure 39, suggests that not all the Zr has been utilised to form a fine dispersion of cubic $ZrAl_3$ particles (< 0.2 μm) needed for grain boundary pinning.

The effect of static annealing at various temperatures and times on the grain size is shown in Table 7 and the change in structure is depicted in Figures 40a, 40b and 40c. It is clear that the material does not recrystallise easily below 450°C. At 530°C, recrystallisation and grain growth is rapid, Figure 41, with a grain size of approximately 30 μm after one hour, rising to over 75 μm in 15 hours. Figure 42 plots the variation of the grain size with time in log-log form.

8.1.2 Superplastically-Formed Material

Figure 43 gives the profile of a SPF 'top hat' which shows the variation of thickness strain, ε_3, ($\ell n\ t_f/t_o$), (where t_f is final thickness and t_o is the initial thickness) with increasing superplastic deformation.

The level of cavitation, as measured by densitometry, is seen to increase with increasing thickness strain, Figure 43[a].

Figures 45 and 46 give an example of the uniformity of superplastic deformation across the disc cut from a 'top hat' and the variation of cavitation (measured through densitometry), with strain across the disc.

The nature of the cavitation present in the SPF material is shown in Figure 47. The optical micrographs are taken from sections through the thickness of the sheet at a strain of 1.1.

Figure 47a shows the grain structure present after superplastic deformation of the sheet to a strain of 1.1 and Figure 47b confirms the complete bonding of the aluminium cladding to the matrix. Figure 47c shows a micrograph of the material grain size after a static anneal at 450°C for 1 day. The edge section shows a wide range of grain sizes across it. Figure 47d shows the mixed grain structure observed in cavitated Supral 150 (in T-ST section) after the recommended T6 heat treatment.

Cavitation is seen to be associated largely with the θ $CuAl_2$ precipitates and to a lesser extent with the larger $ZrAl_3$ precipitates (Figures 47e and 47f).

8.1.3 Isothermal Anneals

The effect of static annealing at different temperatures for times up to 15 hours on the cavitation and grain size present in SPF material was studied using densitometry and the MLI concept discussed in the last chapter.

Plotting the grain linear intercept ($d_{m\ell i}$) in the T and ST directions versus time, Figure 48, shows that for static annealing of a material with an initial grain size of between 5 - 7 μm, grain growth occurs above temperatures of 400°C. For a period of 15 hours, the majority of the grain growth is seen to take place in the first 3 hours.

Replotting the results for 400°C and 530°C in ℓn d vs ℓn t form, Figure 49, produces straight line plots for both the T and ST directions. The gradients of these lines shows that the initial growth rate increases with increasing annealing temperature.

Figure 50 shows the effect of grain size at different annealing temperatures for set times.

It can be seen that the grain size of the material remains constant at 200°C, irrespective of whether it has been annealed for one hour or fifteen hours. There is a greater time dependence on the grain growth above temperatures of 400°C.

8.1.4 Measurement of Cavitation by Hydrostatic Weighing

The hydrostatic weighing technique used for measuring the density (and hence cavitation) in the material is that of Cawthorne and Sinclair (156), in which they claim to achieve a precision of ± 0.04% for 30 mg specimens, using an electrobalance with a 0.1 μg sensitivity and water as the weighing liquid.

For the present investigation, a similar method was used. The weighing liquid was water and the balance used read to 10^{-5}g. An indication of the reproducibility of this method is given in Figures 51 and 51a. Figure 51 shows the variation in density of the same specimen of as-received Supral 150, taken over twenty five readings in a period of time. Figure 51a shows the same for a specimen of SPF Supral 150.

A maximum variation in the density for the virgin material is seen to be ~ 0.17% and for the SPF material of around 0.21%. When the results have been plotted as fractional density changes, the following formula has been used :-

$$\left(\frac{\Delta\rho}{\rho_o}\right) = \left(\frac{\rho_o - \rho_c}{\rho_o}\right) \qquad (59)$$

where ρ_c is the density of the SPF cavitated specimen and ρ_o is the density of the virgin material.

The value of ρ_o used in this investigation is 2.8086 g cm^{-3} and is the average of over 100 density readings taken on as-received Supral 150 from various batches of the material.

8.1.5 *Effect of Isothermal Anneals on Cavitation in Formed Supral 150*

Figure 52 shows the effect of time and temperature on the cavitation present in SPF Supral 150. The rate of sintering is seen to increase initially rapidly with time, becoming stable at longer times. For fixed times, Figure 53, the extent of cavity sintering, as indicated by density change values, increases with higher temperatures.

Figure 54 gives a logarithmic plot of the sintering rate, $\partial/\partial_t(\Delta\rho/\rho_o)$ versus the recipricol of the temperature for a fixed sintering time at atmospheric pressure (38).

8.2 *EFFECT OF HIP ON CAVITATION IN SUPRAL 150*

Figures 45 and 46 quantify the extent of initial cavitation in a disc of SPF Supral 150. This exercise was repeated for other discs and from the results three regions of initial cavitation levels in the specimens were identified. In region A the specimens contained between 3.42% and 2.88% cavitation; in region B between 2.88% and 2.59% and in region C between 2.17% and 1.81%.

For each HIP test, there were three specimens of differing initial density and hence cavitation. After HIP, the density of the specimens was remeasured.

Figures 55 - 64 show the results in graphical form, for coupons taken from regions A and C. The change in cavitation levels in the specimens have been represented by the density values and in terms of a fractional density change using equation 59.

The difference in fractional density change of a specimen before and after the HIP treatment is also plotted and given by :

$$\left(\frac{\Delta\rho}{\rho}\right)_f = \left(\frac{\rho_{CT} - \rho_o}{\rho_o}\right) - \left(\frac{\rho_C - \rho_o}{\rho_o}\right)$$

or

$$\left(\frac{\Delta\rho}{\rho}\right)_f = \left(\frac{\rho_{CT} - \rho_C}{\rho_o}\right) \qquad (60)$$

where ρ_o is the virgin (zero strain) material density,
ρ_C is the density of the SPF cavitated material
and ρ_{CT} is the density of the same coupon after treatment.

Figures 55a - 64a show the results in this form. Figures 65, 66 and 67 give composite plots of all the HIP results. They show that, generally, the rate of change in the density increases with increasing hydrostatic pressure. For the set HIP time of 30 minutes, combinations of the pressure and temperature required to return cavitated material to virgin material density, irrespective of the initial level of

cavitation, can be obtained from these plots, Figure 68. It is seen that as the temperature of HIP rises, lower external pressures are needed to close the cavitation.

Figure 69 shows the pressure/temperature combinations for successfully closing cavities in Supral (from Figure 68) on a plot giving the variation of flow stress, with temperature (at different strain-rates) for uniaxially tested Supral 150 from the work of Bricknell and Bentley (158). From the data available it is seen that those conditions of pressure and temperature required for cavity closure are similar to the variation of the flow stress with temperature change for Supral 100 at a strain-rate of around $5 \times 10^{-4} sec^{-1}$.

Assuming that there are no gases present in the cavities during HIP, the material will flow to fill the hole if the external pressure is greater than the flow stress of the material at the particular temperature and strain-rate. Figure 70 is an Arrhenius plot using the data from Figure 68 to determine the activation energy at a constant strain rate, ($Q_{\dot{\varepsilon}}$) by plotting ℓn(stress) against 1/T. The value of $Q_{\dot{\varepsilon}}$ from this graph was found to be 53.54 KJ mol^{-1} and may be used to determine the deformation mechanism operating during the HIP process. All the HIP tests have been conducted for 30 minutes duration. The effect of shorter times on cavity closure using conditions known to close porosity was also investigated. Figure 71 shows that under conditions of 28 MPa at 360°C and 450°C, cavitation in formed Supral 150 is eliminated after twenty and five minutes respectively, the rate of cavity sintering initially being high and decreasing with longer HIP times.

Figure 72 is a micrograph of SPF Supral 150, which has been HIPped back to virgin material density and Figure 72a shows the grain structure of the same specimen after etching.

The results presented in this section show the conditions of pressure, temperature and time needed to close cavitation in SPF Supral 150 components, but do not reflect the extent of cavity sealing due to the HIP process. Incomplete cavity sealing may be detected through the effect it may have on the mechanical properties of the material, as indicated in tensile test data. Alternatively, a post-HIP static anneal or the solution treatment described for the alloy may cause the partially sealed cavities to reopen.

8.3 EFFECT OF HEAT-TREATMENT ON PRE- AND POST- HIP MICROSTRUCTURE

When SPF Supral 150 is subjected to its heat-treatment detailed in Table 6, the level of cavitation is seen to decrease, Figure 73. The extent of the fall is dependent on the superplastic strain that the material has been subjected to.

If cavitation in the material is closed by suitable HIPping conditions (chosen from Figure 68) and then subjected to post-HIP annealing treatment (such as the heat treatment detailed in Table 6), cavitation is presumed to develop as indicated by a drop in the density of the material, Table 18. Figures 74, 75 and 76 show the nature of this cavitation, which appears to be more homogeneously

distributed through the material in comparison with that present after superplastic deformation.

This suggests that incomplete cavity sealing may be occurring. Increasing the HIPping time (up to ten hours) seems not to affect drastically the extent of cavity sealing, Table 8, which shows that solution treatment of material which has been HIPped for up to 10 hours still produces a drop in the density of the material, Figure 77.

It was thought that this effect may be due to the presence of dissolved gases, largely hydrogen, in the metal. Four specimens, taken from the flange region of 'top hats' were analysed, Table 9, and showed hydrogen levels ranging from 0.53 - 0.86ppm.

8.4 VACUUM DEGASSING OF SUPRAL 150

To ascertain whether the high level of dissolved hydrogen in the material was responsible for the reappearance of porosity during a post-HIP heat treatment, specimens of the cavitated material were vacuum annealed at 500°C under a vacuum of 10^{-6} torr for one hour, which ensured removal of the hydrogen gas from the alloy, as these are the conditions used in determining the levels of hydrogen in the material given in Table 9 (164).

The influence of using higher HIP temperatures (on as-received cavitated and vacuum degassed cavitated material) on cavity sealing as indicated by the extent of cavity reappearance on heat-treatment, is shown in Figures 74 and 75.

For the non-degassed material, Figure 74, HIPping under a pressure of 28 MPa for half an hour at 400°, 450°C and 500°C increases the density of the cavitated specimens to virgin material density. The post-HIP heat treatment decreases the density of the specimens with the lowest temperature HIP group suffering the greatest density change.

Similar results for vacuum degassed material are presented in Figure 75, although the decrease in the density on heat-treatment after HIP is less than that encountered for the non-degassed material.

At a HIP temperature of 530°C for the stated HIP conditions, the density of the specimens remains constant on heat-treatment, suggesting that no cavitation has reformed. These observations suggest that either the higher HIP temperatures cause better cavity sealing or the hydrogen gas removal is facilitated at elevated temperatures.

8.5 EFFECT OF HIP AND HEAT-TREATMENTS ON CAVITY MORPHOLOGY AND GRAIN SIZE

8.5.1 SPF Material

Figure 78 shows the nature of the cavitation present in SPF material after the T6 heat-treatment, which has a more rounded appearance than that present after superplastic deformation.

Figure 76 shows the change in morphology and distribution of cavities which reappear on heat-treatment after HIP at 450°C under a pressure of 28 MPa for ½ hour. The sections show less cavitation than that observed in the original SPF material, it is smaller and more homogeneously distributed, as the cavitation in SPF material seems to have a greater concentration along the centre of the edge section (Figure 47).

When the SPF material is HIP'ped at 500°C, 28 MPa, ½ hour, cavitation is eliminated giving a micrograph such as that in Figure 72. On subsequent heat treatment (T6), the cavitation that reappears takes the form shown in Figure 79. This is fine and rounded in appearance and homogeneously distributed. Some seems to be associated with the $CuAl_2$ precipitates and other inclusions present in the material.

Figure 80 shows the extent of cavity reappearance on solution treatment after HIPping SPF material at 100 MPa, 500°C for 3 hours. The specimen contained less cavitation in comparison to those already discussed in this section.

8.5.2 Vacuum Degassed SPF Material

Figures 81 and 82 show the effect that vacuum degassing has on the cavitation present in the alloy.

If the material is vacuum degassed (as described in section 8.4) and then heat-treated, the nature of the cavitation is shown in Figure 81.

Figure 82 shows that little cavitation reappears after a post-HIP heat treatment (HIP under 28 MPa, 450°C, ½ hour) if the material has been subjected to a vacuum degas before HIPping. The cavitation present is similar to that in Figures 79 and 80.

Quantimet Image Analysis results of T-ST sections containing cavitation of as-formed, as-formed and heat-treated (T6) and as-formed, HIPped (28 MPa, 450°C, ½ hour) and heat-treated specimens, are given in Figures 83 to 85 respectively. These consist of plots giving the number of cavities per mm^2 for set cavity lengths. Each figure represents a specimen, which is cut into sections, giving a plot for each section. The results confirm the effect HIP and heat-treatments have on cavitation in this alloy, as shown in the earlier micrographs in Sections 8.4 and 8.5.

The individual plots for each specimen show that when SPF material is heat-treated, the level of cavitation is seen to decrease. A comparison of the area fraction of cavitation in SPF and SPF + T6 material, Figures 82 and 83, shows that the cavitation level has decreased from 8.36% to 6.24%. These values represent the cavitation in polished T-ST sections. Experience has shown that continued polishing of these specimens gives varying levels of cavitation as the material is removed. The figures thus are being used to enable a comparison of the effects of heat-treatment and HIP on the extent of cavitation and cavity distributions.

Figures 82 and 83 also indicate that there is a decrease in number of the larger cavities (> 42 μm), but the figures are not greatly different, as the composite plots show.

When SPF material is HIPped (450°C, 28 MPa, ½ hour), metallography (Figure 72) and density measurements, Figure 68, indicate the closure of the cavities. Subsequent heat-treatment (T6) causes this cavitation to reappear, Figure 76. Q.I.A. of this cavitation, Figure 84, when compared to the cavitation present in SPF material (Figure 82) confirms that less cavitation reappears on heat-treatment after HIP.

8.5.3 Effect on Grain Size

The vacuum degas, HIP and heat-treatments subjected to this material, also affect its grain stability. The micrographs of etched edge (T-ST) sections of cavitated Supral 150 in Figures 86 and 87, give an example of the range of grain sizes that occur as a consequence of the treatments.

Figure 86 is a micrograph of cavitated Supral 150 which has been vacuum degassed (500°C, 10^{-6} torr, 1 hour) and then subjected to a T6 heat treatment, and shows a range of grain sizes in the section.

The specimens shown in Figures 87, 87a and 87b have undergone the vacuum degas treatment and then HIPped at 450°C, 28 MPa, for ½ hour; before HIPping commenced, the pressure vessel was also vacuum degassed at 450°C, 10^{-1} torr for ½ hour. After HIP the materials were subjected to the T6 treatment. The figures again verify the development of abnormal grain growth in this material giving a range of grain sizes.

Figures 48 and 50 and Tables 29 and 30 show the extent of grain size variation in the SPF Supral alloy when subjected to static anneals and various HIP and heat-treatments. The abnormal grain growth may have been attributed to an inhomogeneous distribution of precipitates in the alloy.

Wavelength and X-ray dispersive analysis facilities on the SEM were used to detect the presence of copper, zirconium, iron and silicon in the alloy and their distribution was found by using the mapping facilities.

Figure 88a is an SEM micrograph of as-formed material which has been heat-treated (T6).

Figures 88b - 88d give the distribution of the various elements and show the presence of copper and iron. Many of the cavities are seen to be associated with the copper containing particles. Zirconium is present in the alloy as $ZrAl_3$ in two sizes, as fine sub-micron sized precipitates (159) and larger sized particles, Figures 89 and 89a. Figure 89 shows how the larger zirconium precipitates can be detected by mapping. Unfortunately, mapping for the distribution of the finer $ZrAl_3$ precipitates, Figure 90 , shows less conclusive results, because of the small amount of zirconium in the alloy (~ 0.5%).

Silicon containing particles are also present in the alloy, Figure 88d.

Figure 90a shows an SEM micrograph of the range of grain sizes encountered in the T-ST section of AF Supral after HIP (500°C, 28 MPa, ½ hour) and T6 treatments.

Distribution maps of zirconium (using both energy dispersive and wavelength dispersive analysis facilities) fail to show any conclusive proof of the distribution of fine $ZrAl_3$ in the alloy.

Figures 90b and 90c seem to suggest a homogeneous distribution of Zr (using wavelength dispersive analysis) in both the large and small grain sized areas of the specimen - yet this result may just be showing the background levels, as Zr (being of sub-micron size) may not even be detected. However, the counts accumulated in ten seconds during spot analysis for zirconium, across the thickness of the specimen, Figure 91, in 0.01mm stages (Figure 92), show that no zirconium exists in the cladding, and seems to confirm its homogentous distribution in the matrix. The few high counts registered are probably due to the spot being positioned on the larger $ZrAl_3$ particles.

Finally, X-ray analysis of the cladding in heat-treated as-formed material, Figure 93, shows the presence of a small amount of copper, Fig.93a. This is confirmed by the line scan, Figure 93b, for copper across the matrix and cladding.

8.6 HOT STAGE MICROSCOPY

8.6.1 Transmission Electron Microscopy (TEM)

Hot stage TEM was used in an attempt to follow the changes in the microstructure (dislocations and precipitates) with increasing temperature. Thin foil TEM specimens of as-rolled Supral 150, Figure 94, showed a structure containing a high dislocation density. Raising the temperature of the hot stage showed the progressive elimination of the dislocation tangles, until at around 400°C, the formation of dislocation-free grains occurs, Figure 94c.

8.6.2 Optical Hot Stage Microscopy

This was used to try to observe the reformation of porosity in SPF material which had its cavitation closed by a suitable HIP treatment. Observations of the polished surfaces were made in a hot stage under high purity argon and in a vacuum which was better than 10^{-3} torr.

Figure 95 shows the surface of SPF Supral 150 after HIPping at 450°C, 28 MPa for ½ hour.

Figure 95a shows the same specimen after ½ hour at 530°C under a vacuum of > 10^{-3} torr in the Leitz hot stage, which registers no change.

A specimen which has undergone a similar treatment as above is then heated to 530°C in an atmosphere of high purity argon. The grain

size is indicated by the fine layer of oxide appearing on the surface. The porosity is also seen to increase with time, Figures 96b and c.

Figure 97 again shows the surface of HIPped SPF Supral 150. At 530°C it remains unchanged, Figure 97a, when under a vacuum (> 10^{-3} torr). Yet when the vacuum is lost, Figures 97b and 97c, oxidation of the surface again indicates the grain structure as well as the porosity.

These observations may suggest that hydrogen leaves the metal by a different mechanism when in a vacuum, as compared to atmospheric pressure.

8.7 THE MECHANICAL PROPERTIES OF SUPRAL 150

The effects of HIP and heat treatment on the microstructure and cavitation present in the alloy were followed by changes in the mechanical properties indicated by use of room temperature tensile tests.

The results, presented in Tables 10 - 34, show the tensile properties (UTS, 0.2%proof-stress and elongation) as well as the treatment which the specimens have undergone and also indicate the change in density of the material after each treatment.

As formed (AF) SPF material properties remain virtually unaltered when subjected to a static anneal at 450°C for thirty minutes.

The average values indicate a slight rise in the 0.2% proof stress (PS) and elongation percent for the annealed material, but the difference is insignificant.

Table 12 shows how solution-treatment of SPF material drastically improves the 0.2% PS and UTS with a smaller increase in the elongation percent. Subsequent ageing, Table 13, raises the material strength values but causes a slight reduction in the ductility. The densities of the specimens in Tables 12 and 13 increase as a consequence of the heat treatments.

HIPping the AF material under different conditions, all of which close cavitation (as indicated by a return to virgin material density), Tables 14 - 16 show little change in the 0.2%PS and UTS, but an increase in the ductility when compared with the figures for the AF material, Table 10.

The extent of initial cavitation in the material affects the ductility. For example, in Table 10 for the AF material, the ductility increases with higher initial specimen density, i.e. specimen L5 (ρ = 2.6750 gcm^{-3}) has a lower elongation present than specimen ET2 (ρ = 2.7490 gcm^{-3}). This effect is seen to prevail in the AF and T6 specimens (Table 13). In the AF and HIPped results presented in Tables 14 - 16, although the ductility values are, on average, higher when compared to the AF material, the influence of initial cavitation is less pronounced.

When cavitated material which has been HIPped (at 28 MPa , 450°C, ½ hour) and subsequently solution-treated (ST), Table 17, and ST and aged (T6), Table 18, is tensile tested, the effect of initial cavitation level on the post-treatment ductility is removed.

The densities of the specimen have reached virgin material density due to HIP, and decreased on subsequent solution-treatment, Table 17. Ageing the material produces no change on the solution-treated density, Table 18. The 0.2% and UTS values have also increased, but on average are slightly lower when compared to material which has undergone a similar heat-treatment without the HIP (Tables 12 and 13).

HIPping specimens of the cavitated material at 500°C, 28 MPa for ½ hour, followed by solution-heat treatment (T6), Table 23, produces 0.2% PS and UTS values similar to those attained by specimens HIPped at 450°C, 28 MPa for ½ hour and SHT, Table 18, but an increase in the ductility values are recorded by the former. There is also less of a density decrease on applying the T6 treatment after HIP for the specimens HIPped at the higher temperature, suggesting that less cavitation reappears after heat-treatment when HIPping at a higher temperature (at constant pressure and time).

This observation is strengthened by the results tabulated in Table 25, which show that using a HIP temperature of 530°C (at 28 MPa, for ½ hour) returns SPF material to virgin material density. Subsequent heat-treatment (T6) produces a smaller fall in density than encountered for material HIPped and heat-treated at the lower temperatures (of 450°C and 500°C), Tables 18 and 23. However, comparison of the mechanical properties in these tables shows a drop for the material HIPped at 530°C, Table 25.

Tensile test specimens of the SPF material were also HIPped under a pressure of 100 MPa for three hours at a temperature of 505°C. The results show (Table 27) that the post-HIP T6 treatment produces no change in the density of the material. The values for the mechanical property data are all higher than those recorded when the material has been HIPped at lower pressures for the same temperature and subjected to the T6 heat treatment (Tables 13, 18, 23 and 25).

8.7.1 Mechanical Properties of Vacuum-Degassed Material

As the material was analysed to contain a high level of hydrogen gas, Table 9, vacuum degassing of the tensile specimens (at 500°C, 10^{-7} torr for 1 hour, the conditions used when analysing for hydrogen), in a vacuum furnace was employed to ensure the removal of the hydrogen. A vacuum circuit was also fitted to the experimental HIP apparatus enabling the evacuation of the HIP pressure vessel so that before HIPping the vessel was subjected to a vacuum of 10^{-1} torr at 450°C for thirty minutes.

Table 19 shows the effect vacuum degassing (at 500°C, 10^{-7} torr 1 hour) SPF Supral 150 (prior to the T6 treatment) has on the mechanical properties which can be compared to the non-degassed material, Table 13. Looking at the average values, the 0.2% PS and ductility are slightly lower for the degassed material, but the UTS value is

marginally higher. The differences in these average values may not be significant, as inspection of any of the mechanical property tables will show similar differences between specimens which have undergone the same treatment.

The final values of the T6 density for the degassed material, Table 19, are similar to those of the non-degassed specimen, Table 13.

Table 20 shows that if before HIP the pressure vessel is vacuum degassed (at 10^{-1} torr, 450°C, ½ hour), and the specimens then HIPped (28 MPa, ½ hour, 450°C), followed by the T6 SHT, the resulting properties are slightly higher than those from material HIPped under the same conditions but without the vessel degas, Table 18. Although the drop in density produced in the latter is greater than that for the pressure vessel degassed specimens.

The same observations are true for SPF tensile specimens, Table 21, which have been vacuum degassed (500°C, 10^{-7} torr, 1 hour) and HIPped and heat-treated as those in Table 20 above.

If, however, the temperature of HIP for these degassed specimens is raised to 500°C, Table 24, there is less drop in density on SHT than that encountered for the degassed material HIPped at the lower temperatures. This effect is highlighted by the higher ductility values encountered in Table 24. The 0.2% PS and UTS figures show a slight drop when compared to those obtained at the lower HIP temperatures (Tables 18, 20 and 21). When the HIP temperature is raised again to 530°C, Table 26, very little cavitation reappears in the degassed material as the SHT density values are the same as the HIPped densities. The mechanical properties, however, all show a fall in their values when compared to those obtained by degassed material which has been HIPped at the lower temperatures (Tables 18, 20, 21 and 24).

Table 28 shows that under HIP conditions of 28 MPa, 450°C, a HIPping time of five minutes is required to return SPF cavitated material to virgin material density.

Tables 29 and 30 show the average values for the mechanical properties of non-degassed and degassed specimens, along with examples of the grain sizes induced in the material due to the different conditions.

8.7.2 Mechanical Properties of Cold-Rolled Virgin Supral 150

Table 31 gives the mechanical properties of as received cold-rolled 4mm sheet Supral 150. Subsequent annealing of this material (at 450°C for ½ hour) causes a reduction in the 0.2% PS and UTS but an increase in the ductility (Table 32).

If this material is HIPped (at 450°C, 28 MPa, ½ hour) and solution-treated (Table 33), all the mechanical properties show an increase. Subsequent ageing of this material, Table 34, again raises the 0.2% PS and UTS but a lower level of ductility is recorded.

HIPping cold-rolled sheet Supral 150, Table 34, produces a small but consistent increase in the density. Heat-treating the material results in a decrease in the density.

8.8 EFFECT OF VACUUM DEGASSING ON DUCTILITY IN SUPRAL 150

Figure 105 shows how the initial level of cavitation in SPF material can affect the ductility. For as-received SPF material, the ductility increases with higher initial density levels. Heat-treating this material raises the elongation values obtained, but there is still an effect from the initial cavity levels present.

If the SPF material is HIPped (450°C, 28 MPa, ½ hour) and solution-heat-treated (T6), there is a marked increase in the ductility with less influence from the extent of initial cavitation.

Raising the temperature of HIP to 500°C (at 28 MPa, ½ hour) followed by the T6 treatment, again raises the elongation percents recorded, but now there is virtually no effect on ductility from the initial cavitation levels present in the tensile test specimens. When the material is HIPped at 530°C (at 28 MPa, ½ hour) and heat-treated (T6), the ductility values are seen to fall.

Figure 107 shows how the initial cavity levels and subsequent treatments affect the ductility for SPF material which has been vacuum degassed (500°C, 10^{-7} torr, 1 hour). Vacuum degassing SPF material followed by the T6 treatment gives similar ductilities as those obtained by non-degassed (or as received) SPF material (Figure 105. Figure 107 also shows that the HIP treatments employed on the vacuum degassed material remove the influence that initial cavitation levels have on the ductility of the material.

The effect of HIPping temperature (at 28 MPa, ½ hour) on ductility for both non-degassed and degassed SPF materials is shown in Figures 106 and 108 The HIP elongations are higher than the as-received material ductilities in both cases, and the ductilities increase with increasing HIP temperature reaching a maximum at 500°C.

A fall in ductility is recorded when HIPping at 530°C for both cases, Figures 106 and 108.

9. DISCUSSION

9.1 AS-RECEIVED SUPRAL 150

The cold-rolled structure of the as-received (virgin) material is shown in Figure 39, and consists of an aluminium-rich matrix containing within it a distribution of $CuAl_2$ precipitates of varying sizes which are elongated in the rolling direction, and some large flakes, ~ 5 μm in diameter, which were found to be an intimate two-phase mixture of aluminium and the metastable $ZrAl_3$ phase (122). The as-received structure is also characterised by the appearance of a dispersion of small spherical $ZrAl_3$ particles (~ 4 - 10 nm), (153), which are very effective pinners for grain boundaries. The Supral 150 is also found to contain traces of iron and silicon containing impurities (Figures 88c and 88d).

The presence of copper in the alloy serves primarily to encourage recrystallisation and depress recovery by a lowering of the stacking fault energy (152), but the fine-grained structure produced in, for example, Al - 5Cu alloys (119), is unstable at temperatures above 400°C, as a large proportion of the copper returns to solution and is not available in aiding grain growth restriction.

Zirconium is added to the alloy to inhibit grain coarsening at elevated temperatures. It can be uniformly precipitated, but because of its low solubility in aluminium, it is necessary to chill the melt rapidly in order to retain a high supersaturation of the zirconium (121). The volume fraction of zirconium which gives rise to fine-scale precipitation is strongly dependent on the solidification rate which is slower in the central region of the casting. The proportion of large $ZrAl_3$ particles such as those seen in Figure 39, increases as the freezing rate decreases, leaving less in solid solution to provide for the fine $ZrAl_3$ dispersion used for grain boundary pinning (121, 152).

9.1.1 Static Recrystallisation of Virgin Supral 150

Static annealing of the virgin material produces recrystallisation and grain growth at temperatures above 400°C. Below this temperature, partial recrystallisation of the banded structure occurs, Table 7.

The recrystallised grain size is seen to increase with annealing time (Figures 40a and 40b) and with higher annealing temperatures, Figure 40c. Figure 41 and Table 7 show how the grain size increases with time at 450°C and 530°C. Re-plotting this data in log-log form for both the T- and ST- directions clearly illustrates an equation of the form :-

$$\ell n\, d_{m\ell i} = A \log t + C \qquad (61)$$

The rate of change of grain size in the T- and ST- directions is seen to be approximately equal at the two temperatures, although much greater growth occurs at the higher temperature, Figure 42.

The grain aspect ratio (AR) |T/ST| is always greater than unity at both temperatures, although as the AR suggests, at 530°C the structure is becoming more equiaxed.

The rate of grain growth decreases as the grain size increases, Figure 41, and is also implied by the fact that the empirical time exponent, A, (in equation 61), is always less than unity (118). The values of A from Figure 42 for the 450°C and 530°C plots are 0.40 and 0.39 respectively, which suggest that the rate of grain growth at the two temperatures is similar, for the times studied. Inspection of Figure 41 would indicate that the rate of recrystallisation and growth within the first thirty minutes would be higher at 530°C because of the larger grain size indicated after that time.

Increasing grain size also leads to a decrease in the grain boundary area and hence the corresponding decrease in grain boundary interfacial energy. As the latter provides the driving force for grain growth, larger grains reduce the residual driving force for further growth, at a particular temperature (118). In addition to this, grain growth in the alloy is also inhibited by the presence of second phase particles, probably $ZrAl_3$ (121, 152), as some of the copper will have gone back into solution at these temperatures and not be available for restricting grain boundary mobility (152).

The results also show that the grain size attained by the material through normal grain growth for the times studied, increases as the annealing temperature is increased. This arises since generally, the grain boundary mobility increases as the temperature increases (118). The larger grain sizes observed at 530°C (Figure 41) may also be caused because the copper is completely in solution at this temperature and not available in any form for restricting grain growth (119, 121).

The results in Figure 41 show the stability of the grain size at 450°C for up to 2 hours, and confirm the observations made by Watts et al (122) in their work on the Supral 150.

The microstructural changes undergone by cold-rolled as-received Supral on static annealing are well documented (121, 122, 159).

Christodulu (159) shows, through TEM work, how the heavy dislocation density in virgin Supral changes with increasing temperature, forming subgrains at 300°C. Upon further annealing at 400°C, the highly mobile dislocations are impeded (by particles identified by Watts (121, 122) as spherical $ZrAl_3$ and fine θ and θ' precipitates, leading to a suppressing of grain boundary migration and hence recrystallisation.

Further annealing at 460°C is shown to produce a recrystallised grain structure, and also contains regions transformed from a uniformly dislocated state to a network of polygonised cells (122). Increasing the annealing time at this temperature (for 3 hours) indicates that new grains form at the expense of the polygonised regions and appear to be produced by the migration of high-angle boundaries through the structure (122). The observations are in agreement with the results

of hot-stage TEM work presented in Figures 94a - 94c, which shows the production of a recrystallised grain structure at 460°C, in wrought Supral 150.

The dislocation-free grains seen in Figure 94c were produced by the movement of high angle boundaries through the material, as the temperature was raised.

9.2 *SUPERPLASTICALLY FORMED SUPRAL 150*

The initial role of copper in this alloy is to inhibit recrystallisation up to the superplastic forming temperature for the material. During static annealing, the $\theta(CuAl_2)$ and the finer θ' particles can act as recrystallisation nuclei for static recrystallisation (153). As Figure 48 shows, the grain structure of statically-annealed Supral is stable at 450°C for several hours.

The optimum superplastic forming conditions for Supral 150 have been established as 460°C at a strain-rate of ~ 3×10^{-3} sec^{-1} (121, 122), at which the highest value of m (= 0.5) is recorded.

Figure 47a shows the fine grain-size achieved by dynamic recrystallistation during the early part of superplastic deformation, up to 50% strain (122). The presence of copper serves to reduce the high stacking-fault-energy of aluminium, encouraging dynamic recrystallisation, in which new grains continually replace work-hardened ones. The fine grain size is stabilised by the dispersion of fine metastable $ZrAl_3$ and remains even after extensive deformation (122). The importance of copper in making the material superplastic was confirmed when an alloy of Al - 0.5% Cr (which was processed to contain very similar fine scale $ZrAl_3$ precipitates as in Supral) failed to show any superplastic response (120).

The dynamically-recrystallised grain size in SPF Supral seems to be more stable after a post-forming anneal than statically recrystallised grain size obtained in wrought Supral (Figures 48 and 41). At 530°C, for instance, a 15 hours annealing time gives a grain size of ~ 17 μm for SPF material as compared to ~70 μm for the as-received Supral.

This may be due to :-

(a) The behaviour of copper in the alloy at higher temperature.

(b) The differences in recrystallisation during static annealing and under superplastic deformation.

Static recrystallisation of the virgin cold-rolled alloy occurs at temperatures above 450°C, the copper-containing particles (θ, θ') act as nuclei for static recrystallisation (153). The grain size is larger than that produced in SPF material.

The SPF grain size is stable at temperatures below 300°C for times up to 15 hours. Grain growth in this material only occurs at 400°C after an anneal of 5 hours (Figure 48). The grain size in the virgin

material at 5 hours for 450°C, Figure 41, is over double that of the SPF material above. Allowing for the larger initial grain size of the wrought material, the results suggest that the grain size in the SPF alloy has greater stability on annealing than that found in the virgin material.

The results also suggest that copper may be playing a part in stabilising the recrystallised grain size, especially in areas depleted on fine $ZrAl_3$ precipitates.

At temperatures above 400°C, a large proportion of the copper is known to return into solution (119, 121) and at 530°C, all of it is in solution and is thus unavailable for grain growth restriction; as Figure 48 shows, the grain size of SPF formed Supral increases at annealing temperatures above 400°C.

The ℓnd vs ℓnt plot in Figure 49 shows that grain growth in SPF material statically annealed at 400°C and 530°C for various times behaves in a similar manner to grain growth in wrought material (at 450°C and 530°C), following a relationship of the form given by equation 61.

The growth rate at 530°C (0.149) is slightly higher than at 400°C (0.118) as expected, but this is not significant. It is a lower growth rate than that experienced by the wrought material (Figure 42), which at 530°C has a value of 0.4. Higgins (160), has collated the variation of A values (taken from equation 61) with temperature from 16 different metals. The values quoted range from 0.05 to 0.5. Generally, the data shows that A tends to 0.5 as the annealing temperature is increased (for a given metal) or as the impurity content is decreased.

The high value of A obtained for wrought material in comparison to the SPF material may suggest that there are fewer precipitates (of suitable size) present in the former for restriction of grain growth.

Figure 50 shows how the grain size of SPF material increases with time at temperature, indicating that there is virtually no effect of annealing times up to 15 hours at temperatures below 300°C.

9.3 CAVITATION IN SPF SUPRAL 150

9.3.1 Nucleation

It is generally accepted that during superplastic deformation, incomplete accommodation of grain boundary sliding (GBS) leads to stress concentrations at grain-boundary irregularities, triple points and/or second phase particles, leading to cavity nucleation (55,125, 69, 73).

Following nucleation, cavities will grow by various mechanisms, as described in Chapter 4.

The causes of cavity nucleation in Supral alloys (and fine

particle stabilised alloys in general) are well documented (61, 69, 73, 55).

Sohal(125) has stated that cavitation occurs during superplastic deformation in Supral 150 because of incomplete accommodation of GBS, leading to stress concentrations at $CuAl_2$/Al-matrix interfaces. The $CuAl_2$ particles are also harder than the matrix under the deformation conditions leading to their decohesion from the matrix. These well bonded particles are approximately four, three and five times as hard as the matrix at room temperature, 300°C and 500°C respectively (108).

Metallography indicates that large $ZrAl_3$ precipitates are sites for the largest cavities, Figure 89a. It is unclear from the observations whether these cavities were nucleated during the production of the wrought sheet or after superplastic deformation. However, the total number of cavities greatly exceeds the total number of large $ZrAl_3$ precipitates.

In addition to the above effect, the formation of large $ZrAl_3$ precipitates during casting depletes the Zr in supersaturated solution, which in turn effects the homogeneous distribution of fine $ZrAl_3$ required for grain size control.

Cavitation is also seen to be associated with $CuAl_2$ particles, Figures 47e and 47f. It tends to be confined to the central region of the sheet, Figure 47, and is non-uniform in size and distribution.

The clad layer, Figure 47b, appears to be uniform in thickness, cavity free and firmly attached to the matrix.

9.3.2 Cavity Growth

There are many cavity growth analyses that can be used to fit the behaviour of cavitation in this alloy, see Section 4.2.2.

Generally, cavity growth can be assisted by either diffusion or deformation-controlled mechanisms, or by a combination of both (29, 30, 39, 77, 125, 128, 133, 161), depending on the cavity size.

In the present investigation, density measurements show the increase on cavitation with increasing thickness strain in the top hats, Figure 43a. These results were replotted using the analysis developed by Stowell (69) (given in equation 18), for plasticity-controlled growth of cavities, where

$$\phi = \phi_o \ln (n\varepsilon)$$

where ϕ_o is the level of cavitation at zero strain and n is a parameter which usually has a value in the range 2 to 3, but is dependent on the alloy, and on strain-rate, temperature and grain size.

The logarithmic cavity percentage volume against natural strain gives a linear relationship, as would be expected from theory, Figure 98. Ridley (113) and Stowell (161) have both tested this model and

obtained good agreement between calculated and experimentally obtained results, despite simplified assumptions, i.e. that all voids are of the same initial size; they all pre-exist at zero strain and no nucleation occurs during deformation.

In the present work, the zero strain (or virgin) material is assumed to be cavity-free, thus the line in Figure 98 should emanate from zero cavity volume. The origin of the plot in fact corresponds to $\phi_o \simeq 0.11\%$ volume, which may suggest the existence of cavitation in the virgin material. In this model, the value of ϕ_o depends on how many of the pre-existing cavities are stable under SPF conditions, as following Hancock (130) voids with a critical radius, $r_c > 3\gamma/2\sigma$ where γ is the surface energy, would grow under the action of an applied stress, whilst cavities smaller than this radius would shrink. It is difficult to validate completely the Stowell model (and the others presented in the literature, Section 4.2.2), especially at low strains, because of the difficulty in precisely detecting and measuring the extent of the cavitation.

The model can, however, be used to compare the cavitation data for different material. The values of ϕ_o can give an indication of the initial levels of cavitation in the material at zero strain.

Ridley et al (113) have used the Stowell model and found varying values of ϕ_o for microduplex $\alpha - \beta$ nickel/silver alloys and conclude that the volume of pre-existing voids is different, possibly due to the purity of the material or to different thermomechanical treatments.

Despite the fact that some of the assumptions used in constructing the model are oversimplified, much data can be fitted to the Stowell model (133).

9.3.3 Variation of Cavitation in SPF 'Top Hats'

Figure 43a shows the increase in cavitation with increasing thickness strain in a SPF Supral 150 'top hat' supplied by Superform Metals Ltd. The numbers represent equal-sized specimens that were cut from the hat, and had their density measured.

Figure 45 shows the non-uniformity of the cavitation in a disc cut from a top hat. The cavitation is seen to vary between 3.0% and 1.8% in the same disc, as Figure 46 confirms, which shows how the densities (and hence cavitation) of the coupons vary with location in the disc.

It was for this reason that for the HIP tests, top hats were cut into equal sized specimens, which were each labelled, and had their initial density recorded, and then classified into three categories. For each HIP test, one coupon was used from each category.

The reproducibility of the density measurement technique is given in Figure 51, and shows the variation in density of the same coupons of virgin and SPF cavitated over 25 readings is 0.21% and 0.17% respectively. Each reading represents five density determinations.

This accuracy was considered sufficient for the present set of experiments.

9.3.4 *Activation Energies Associated with the Sintering Process in Supral 150*

SPF coupons of Supral 150 containing similar levels of initial cavitation (~ 3%), were statically annealed at different temperatures for up to 15 hours and were found to increase in density due to cavities closing under the action of surface tension forces.

Figure 52 shows density increasing continuously with time at temperatures above 400°C, but the sintering rate drops off very rapidly, after the first hour.

Increasing the temperature of anneal causes the sintering rate to increase, but even at the highest temperature (530°C), complete densification does not occur; the density change is only 1.5%.

The sintering rates are seen to increase with temperature, Figure 54, going from 5.4×10^{-9} s^{-1} at 300°C to 6.4×10^{-8} s^{-1} at 450°C for the same sintering time. Substituting the sintering rates in the equation of Beere and Greenwood (39)

$$Q = \frac{RT_1T_2}{(T_1 - T_2)} \quad \ell n \left(\frac{T_1S_1}{T_2S_2}\right) \qquad (62)$$

where Q is the activation energy for the diffusion process assumed to be rate controlling, R the gas constant, T the absolute temperature, S the sintering rate and the suffixes 1 and 2 refer to the two sets of conditions, the activation energy is found to be 61.93 KJ mol^{-1}.

The activation energy for lattice self-diffusion in pure aluminium is quoted as 141 KJ mol^{-1} (158). Unfortunately, the situation with regard to grain-boundary self diffusion in aluminium is not as well defined and no reported activation energy exists. Mukherjee (106) and Sohal (125) suggest the adoption of a value approximately half the lattice diffusion activation energy, i.e. around 70.5 KJ mol^{-1}. Following this suggestion, the rate-controlling process for the sintering of cavities in this alloy has an activation energy close to that of grain boundary diffusion, which would be expected as most of the cavitation is located on grain boundaries, Figure 44.

A similar conclusion was reached by Beere and Greenwood (39), who found that creep cavities situated on grain boundaries closed by a grain-boundary diffusion mechanism during sintering.

9.4 *EFFECT OF HOT ISOSTATIC PRESSING ON SPF CAVITATION*

Figures 55 to 64 show the effect of pressure sintering on cavity closure in the material, under a set HIP time of thirty minutes for different combinations of pressure and temperature.

The figures show the original cavitation levels and the post-HIP levels as indicated by density measurements. Also plotted against each figure is the change in the cavitation levels experienced by the specimens after undergoing various HIP treatments.

Figure 55 indicates that (for specimens containing an initial cavitation level of ~ 3%, (Region A)), a HIP pressure of 7 MPa has no effect on the extent of cavity closure below temperatures of 350°C, for a thirty minute HIP period, a result which is similar to that expected when annealing at atmospheric pressure for the same temperatures, Figure 52.

The rate of sintering increases with temperatures above 350°C, Figure 55a, (for a pressure of 7 MPa), although the material does not return to virgin material density (or better) until a temperature of 450°C is reached.

Comparing the density changes for pressureless sintering (Figure 52 and 55a) in specimens of similar initial densities, with those for pressure sintered specimens , clearly shows that the latter process enhances cavity closure, for example at 400°C and 450°C, a thirty-minute anneal at atmospheric pressure gives density changes of ~ 0.08% and ~ 0.36% respectively, compared to ~ 1.75% and ~ 3% for the same temperatures with a HIP pressure of 7 MPa, Figure 55.

There is also a difference in the sintering behaviour of material containing a lower level of initial cavitation than above, (material from Region C). Figures 60 and 60a show how complete cavity closure only occurs above 450°C at 7 MPa pressure, lower temperatures having no effect on the cavitation present in the material.

This may suggest either that cavities below a certain size which may be present in greater numbers in material from region A are sintered to closure at HIP temperatures above 350°C, Figures 55 and 55a, producing the increases in density described above, or larger cavities present in this material (initial cavitation level ~ 3%) decrease in size due to diffusional processes, which are seen to be enhanced by the external pressure.

The cavities present in material from Region C, Figures 60 and 60a, seem not to be altered by the diffusional processes. Complete cavity closure occurs at 450°C for a 7 MPa pressure, in both cases, suggesting closure occurs under these conditions by plastic flow.

Raising the HIP pressure to 14 MPa, the results show that diffusional processes are enhanced in specimens taken from both Regions A and C, (Figures 56 and 56a and 61 and 61a respectively), when compared to those HIPped at 7 MPa. The increases in density of specimens at temperatures above 325°C are all greater than those HIPped at 7 MPa. Complete densification is seen to occur at 400°C.

Increasing the pressure again to 21 MPa, for the same temperature and time, Figures 57, 57a and Figures 62 and 62a, indicates that for the two initial cavity levels, a temperature of 375°C has to be exceeded to close cavitation. It is difficult to say whether the

cavity closure mechanism is due to the increased(pressure enhanced) diffusion processes as seen when HIPping at 14 MPa, or because the flow stress of the material has been exceeded by the external pressure at the temperature (375°C) of HIP.

At HIP pressures of 28 MPa and 35 MPa, the material is shown to return to virgin material density (or better) at temperatures of 350°C and 330°C, regardless of the varying levels of initial cavitation, (Figures 58, 59, 63 and 64), present in the alloy.

Figures 65 and 67 show the composition of the HIP graphs given in Figures 55 - 64, and Figure 66 shows the composite HIP graph for material with an initial cavitation level of ~ 2.0% (Region B).

They all confirm that the rate of cavity sintering increases with higher temperatures and with higher HIP pressures, as indicated by the increases in the slope of the density versus temperature curves.

The graphs also suggest that complete cavity closure closure may result because the flow stress of the material is exceeded by the external pressure.

If the temperature and pressure combinations which return the cavitated material to virgin material density (or better) are taken from Figures 65, 66 and 67, and their average values plotted, the resulting plot given in Figure 68 shows the combinations of pressure and temperature which will return cavitated material to virgin material density regardless of the initial level of cavitation present, for a thirty minute HIP period.

Bricknell and Bentley (158) show how the flow stress of Supral 100 varies with temperature and strain-rate during uniaxial tensile deformation. Their results are shown in Figure 69, along with the external HIP pressure/temperature plot taken from Figure 68. Assuming that the flow stress of the material is exceeded at each pressure/temperature combination which leads to virgin material density, and cavity closure is predominantly by a plastic yielding mechanism (and there is no gas in the cavities), then from Figure 69, the strain-rate at which cavities close under the experimental conditions for this investigation is approximately 5×10^{-4} sec^{-1}.

It may also be possible, from the above results, to obtain a value for the activation energy associated with the plastic flow of the material to determine the deformation mechanism.

9.4.1 Activation Energy Associated with Flow During HIP

A value for the activation energy associated with the flow of the material during HIP can be obtained from the results in Figure 68, assuming that the external pressures which lead to hole closure are equal to or greater than the flow stress of the material, and that the material flows at a constant strain-rate.

The ability to define an activation energy depends on the deformation following an empirical equation of the form :-

$$\sigma = K\ \dot{\varepsilon}^{m}\ \exp\ (\frac{Q}{RT}) \qquad (63)$$

where σ is the flow stress, $\dot{\varepsilon}$ the strain rate, m, the strain-rate sensitivity, R, the gas constant, T the absolute temperature and Q the activation energy.

The activation energy at constant $\dot{\varepsilon}$, $Q_{\dot{\varepsilon}}$, was obtained by plotting ℓn (stress) against 1/T (from the results in Figure 68) and the linear plot obtained is shown in Figure 70. The gradient of this plot gives a value for the activation energy, found to be 53.54 KJ mol^{-1}. Padmanahban and Davies (72) have shown that the activation energies derived at constant stress (Q_σ) and constant strain-rate ($Q_{\dot{\varepsilon}}$) will be different and suggest that the discrepancies in the literature , where both lattice and grain boundary control have been reported, was due to a failure to distinguish between them. They showed that

$$m\ Q_\sigma = Q_{\dot{\varepsilon}} \qquad (64)$$

and as m ~ 0.5, which is usually also the measured ratio of grain boundary to lattice diffusion energies, such an argument is appealing. However, this factor cannot account for all the published data, and the question remains unresolved.

They also suggest that the true activation energy can be identified with that measured at constant stress, (Q_σ).

Bricknell and Bentley (158) found an activation energy ($Q_{\dot{\varepsilon}}$) of 48 KJ mol^{-1} for a constant strain-rate of 1×10^{-4} sec^{-1} and a corresponding Q_σ of 146 KJ mol^{-1} for superplastic flow in Supral 100. The ratio of the two ($m = Q_{\dot{\varepsilon}}/Q_\sigma$) was found to be ~ 0.36; the value of m was confirmed by step-change rate tests. The value of Q_σ (146 KJ mol^{-1}) was close to that reported for bulk diffusion (141 KJ mol^{-1}) in the literature (158).

In the present investigation, the experimental results indicate cavity closure occurs by plastic flow of the material. Assuming that the external pressure (at each temperature) which causes a return to virgin material density is equal to or greater than the flow stress of the material, then a plot of $\ell n\sigma$ vs 1/T would yield an activation energy ($Q_{\dot{\varepsilon}}$) for the flow process, Figure 70, which occurs during cavity closure.

The magnitude of $Q_{\dot{\varepsilon}}$ obtained from Figure 70 is 53.54 KJ mol^{-1}, which is close to the value of $Q_{\dot{\varepsilon}}$ obtained by Bricknell and Bentley (158) (48 KJ mol^{-1}), who concluded that the activation energy obtained under these deformation conditions ($\dot{\varepsilon} \sim 1 \times 10^{-4}$ sec^{-1}) is that expected for lattice diffusion. This observation suggests that the activation energy associated with cavity closure by plastic flow during HIP is similar to that expected for lattice diffusion.

Experimental evaluation of activation energies for flow is a

topic of controversy and for the same system depending on composition, stress and temperature, the activation energy can be of the order of either lattice diffusion or grain boundary diffusion (72, 158). For instance, the activation energy, Q_σ, during superplastic deformation in regions II and III for the 430°C to 490°C range studied in Supral 100 (158), corresponds to that expected for boundary diffusion, rising in region I to that measured for bulk diffusion.

It is apparent from the review of this phenomenon given by Padmanabhan and Davies (72) that when comparing activation energies, it is important to be aware of the experimental conditions and methods involved in its determination.

9.5 MECHANISMS OF HOT ISOSTATIC PRESSING

There are a host of theories present in the literature which can be used to explain pore removal by pressure sintering, section 5.3. In the present investigation, the level of cavitation in the material, and the imposed experimental conditions used to eliminate this, suggest that material flow mechanisms, and as the specimen densifies, diffusional mechanisms, are responsible for densification.

9.5.1 Densification by Plastic Flow

The results in section 9.3.4 indicate that during pressureless sintering, cavity closure occurs predominantly by a grain boundary diffusion process, which is observed experimentally to be enhanced by the imposition of pressure. However, complete cavity closure only occurs when the external pressure is greater than the published values of the flow stress given for Supral 100, at the HIP temperature and strain-rate, suggesting that closure is by plastic flow of the material.

In this section, an attempt is made to compare the experimental results with the model for plastic yielding of Ashby et al (135, 136) reviewed in section 5.3.3.

Figure 99 shows how HIPping at various combinations of pressure and temperature for 30 minutes affect SPF cavities in Supral 150 specimens with the same initial level of cavitation, as measured by the density method.

The values of the density (ρ) attained by these specimens under the corresponding conditions of HIP can be plotted (see section 5.3.3) in terms of the empirical relationship proposed by Heckel (143) :-

$$\ln\left(\frac{1}{1 - \left(\frac{\rho}{\rho_o}\right)}\right) = k_1 \frac{P_e}{\sigma_y} + k_2$$

which provides a convenient framework in which experiment and theory can be compared. The model for plastic yielding given by Ashby (135) is :-

$$P_3 > -\frac{2}{3}\sigma_y \ln\left(1 - \frac{\rho}{\rho_o}\right)$$

where $P_3 = P_e - P_i + \frac{2\gamma s}{z}$

P_3 = external pressure, P_i = internal gas pressure (assumed to be zero); γ_s = surface energy, z = pore radius; σ_y is the flow stress, ρ_o is the virgin material density (2.8060 gcm) and K_1 and K_2 are constants.

The values of external pressure and density (ρ) can be obtained from Figure 99. The flow stress (σ_y) of the material at the HIP temperature is found by extrapolating the flow stress versus temperature data for Supral 100 (from the work of Bricknell and Bentley (158) at a strain rate of 1×10^{-4} sec^{-1}. This data is plotted in Figure 100.

The plots of $\ell n\ (1/1 - (\rho/\rho_o))$ versus the normalised pressure (P_e/σ_y) for the different HIP temperatures are given in Figure 101, along with the plot given by Ashby's model (135) for plastic yielding. It is assumed that complete cavity closure occurs when the density of the specimen (ρ) is equal to that of the virgin material (ρ_o).

In the analyses used above, as $\rho \rightarrow \rho_o$ then

$$\ell n\left(\frac{1}{1 - \left(\frac{\rho}{\rho_o}\right)}\right) \rightarrow \infty$$

which is indicated on Figure 101 as the specimens reach virgin material density. The results also show that at 300°C, there is virtually no material flow regardless of the pressure (in the range tested), whereas at 450°C, complete closure has occurred at 7 MPa.

The value of the normalised pressure (P_e/σ_y) needed to close cavitation is seen to increase with falling temperature. Figure 102 shows how at 450°C, to achieve cavity closure, the external pressure needs to be twice the flow stress of the material at that temperature and strain-rate, yet at 350°C, the same process required the external pressure to be eight times as high as the flow stress. A possible explanation for this effect may be that any gases present in the material are more mobile at the higher temperatures, leading to lower internal gas pressures in the cavities.

It seems from the results that the simplified theory of Ashby et al (135) does not completely account for the experimental data. The analysis does, however, show the contribution of material flow during pore closure in Supral 150.

Under the conditions of HIP which close porosity, densification of the alloy may also be aided by creep processes (such as temperature dependent dislocation creep), although further work is needed to confirm this for the present system.

Wilkinson and Ashby (137) have developed models to account for power law creep (see section 5.3.5) during pressure sintering, yet critical tests of the theories have been hindered by the lack of both

experimental and accurate materials data.

A great deal of the work in determining the dominant mechanisms during HIP has been undertaken by Ashby et al (135, 136, 137, 142) who have produced pressure sintering diagrams for the densification of a variety of powder metals.

Generally, their results show the complexity of pressure sintering, for example, in consolidating silver powder, at a single temperature, any one of five different mechanisms can control the rate of sintering, depending on the applied pressure and density. A typical diagram is shown in Figure 26, for the consolidation of tool steel from powder. It is clear that hole closure occurs initially by plastic yielding under the high external pressures, followed by the time dependent process of power-law creep, where the material flow rate is dependent on some exponent of the pressure. As final density is approached (< 1% cavitation), complete densification occurs, with diffusional processes predominating. This mechanism is also operative under pressureless sintering, but under HIP conditions its value is accelerated from a value determined by $2(\gamma/r)$ to a much more rapid rate of $2(\gamma/r) + P_H$, where P_H is the external pressure, γ the surface energy and r the pore radius.

9.5.2 Densification by Diffusional Processes

The results in Figure 71 show the density change encountered in cavitated specimens (with an initial cavity level of 3%) when subjected to a HIP pressure of 28 MPa for various times at two different HIP temperatures ($350^{o}C$ and $450^{o}C$).

The rate of cavity closure is seen to be greater at $450^{o}C$ than at $360^{o}C$, the values being 7.833×10^{-5} sec^{-1} and 2.042×10^{-5} sec^{-1} respectively at a fixed sintering time.

A value for the activation energy, Q, associated with this process, is obtained by using the equation suggested by Beere and Greenwood (39)

$$Q = \frac{RT_1T_2}{(T_1 - T_2)} \ln \left(\frac{T_1S_1}{T_2S_2}\right) \qquad (62)$$

where S_1 and S_2 are the two sintering rates at temperatures T_1 ($450^{o}C$) and T_2 ($360^{o}C$).

The activation energy is found to be 62.42 KJ mol^{-1}, which is very close to that observed for grain boundary diffusion in aluminium (71 KJ mol^{-1}) (106, 125), suggesting that final densification is also aided by diffusional processes along grain boundary paths.

9.5.3 Sintering of Grain Boundary Cavitation

Although various analyses are present to describe the sintering characteristics of powder compacts (6, 38, 39, 52), and casting porosity, they fail to represent fully the distinct type of cavitation

present in SPF materials, which consists of cavities with a range of different sizes and morphology, found frequently on grain boundaries, Figure 44.

This situation is similar to the creep cavitation found in polycrystalline materials (38, 39). The diffusional growth of such cavities has been described by Hull and Rimmer (129),and Ashby (135) has modified this equation and applied it to cavity shrinkage (see Section 5.4.1), showing that the rate at which a spherical cavity, situated on a grain boundary sinters, is given by :-

$$\frac{dr}{dt} = \frac{D_b \delta \Omega}{4r^2 kT} \left\{\frac{2\gamma}{r} - P_i\left(+\frac{r_i}{r}\right)^3 + P_e\right\} \left\{\frac{1}{\ell n\left(\frac{x}{r}\right) - \frac{3}{4}}\right\} \qquad (42)$$

Integration of equation 42 leads to the change of cavity size with sintering time.

The above equation is also readily evaluated by applying Simpsons rule, and a computer programme (Appendix A) was utilised to show how the cavity size is expected to decrease with sintering time for this alloy under a HIP pressure of 28 MPa at two different temperatures of 450°C and 360°C in an attempt to compare with the experimental results shown in Figure 71, for densification of this material under these conditions.

Taking typical values for aluminium as $\Omega = 1.23 \times 10^{-25} m^3$, $\delta = 5 \times 10^{-10}$ m, $\gamma = 0.55 Jm^{-2}$, $k = 1.35 \times 10^{-23}$ JK^{-1} and an applied pressure, P_e of 28 MPa.

Assuming that there are no gases in the cavities (i.e. $P_i = 0$) and taking the boundary diffusion coefficients as $6.18 \times 10^{-22} m^2 s^{-1}$ at 450°C & $7.04 \times 10^{-22} m^2 s^{-1}$ at 360°C, then for an initial cavity radius of 40 μm with a spacing of 100 μm, the time for cavity closure at the two temperatures is shown in Figure 103. The time taken for the radius to fall to zero at the two temperatures is similar to the time shown in Figure 71 , for cavitation (as measured by density values) to be eliminated. These results have to be viewed with caution, as the times for cavity closure predicted by Ashby's equation are extremely sensitive to the values of initial cavity radius and spacing, and Figure 104 shows that adjusting these produces large changes in the times needed for sintering.

More work has to be done in characterising the cavity size, distribution and separation in the material, before any conclusions can be drawn from the data. The effect of internal gas pressure has also been ignored; Beere and Greenwood (39) suggest creep cavities in copper contain a pressure of up to 10 MPa developed by diffusion of gas along grain boundaries and bulk diffusion of interstitial gas atoms, although they show that complete pressure sintering does occur because of gas diffusion away from the cavity. However, the problem is complicated and is another area for possible further work.

There is a considerable amount of data to support the diffusional

sintering mechanism for cavities in a range of materials.

Walker and Evans (162) have shown the sintering of grain boundary creep cavities occurred with an activation energy equal to that for grain boundary diffusion. Beere and Greenwood (39), working on creep cavitation in copper and magnesium, and Stevens and Flewitt (38), investigating a Nickel-Chromium alloy, have all looked at the contribution of hydrostatic pressure on sintering of cavities in these materials and conclude that the decrease in sintering rate with time and the increase in rate with higher hydrostatic pressures were consistent with a model of cavity closure by grain boundary diffusion.

The activation energies calculated in the present work on SPF cavitation in the Supral alloy indicate that the mechanism for cavity sintering occurs by a grain boundary diffusion process at both atmospheric and higher external pressures.

Increasing the pressure and temperature also brings into operation processes (such as material flow) which have a higher activation energy, as discussed in Section 9.4.1.

9.5.4 Effect of Heat-Treatments

As discussed earlier, components formed from Supral 150 are solution-treated and aged to give them peak mechanical properties.

Solution-treating at 530°C reduces the level of cavitation by a sintering process as depicted in Figure 73. The cavities on solution-treatment also take on a more rounded appearance, indicative of sintering by diffusive mechanisms, Figure 78, confirming the earlier results for the annealing of Supral 150 in Section 9.3.4.

Another effect of the heat-treatment is the production of surface blistering (34, 58, 59), which was sometimes observed in the Supral 150; recent work by Daly (163) on Supral 220 showed extensive surface blistering : the problem being heightened at the solution-treatment temperature.

There is much evidence in the literature to connect blistering with the evolution of gases, particularly hydrogen from metals (60), during heat-treatment. In aluminium and its alloys the occurrence of blistering due to hydrogen has been reported in both the cast and wrought states (34, 58, 59, 60, 61, 123).

Hess and Turnbull (58) and Talbot and Granger (147) suggest that the major part of the hydrogen is introduced into the metal during casting and emphasize the need for good in-line degassing procedures to reduce this. They also point out that at the solidification temperature, the solubility of hydrogen in the liquid to that in the solid is ~ 20 : 1, providing the driving force for the gas to come out of solution. Its presence in the voids inhibits complete healing on subsequent working leading to the appearance of defects such as blistering during solution treatment.

In the present investigation, the Supral 150 used blistered during solution-treatment.

A further indication of the presence of gas in this alloy was given when SPF material, originally containing around 3% cavitation which had been HIPped to give complete cavity closure, showed on average, the reappearance of ~ 0.5% cavitation, Figure 76, on solution-treatment. The average cavity size is smaller and appears more rounded than SPF cavitation. Its distribution is also more uniform when viewed along an edge section, unlike SPF cavitation which shows larger cavities in the centre.

Quantimet Image Analysis results on edge sections of as formed (AF), AF and T6, and AF, HIPped and T6 specimens shown in Figures 83, 84 and 85, confirm the results of the optical metallography, although many more sections would need to be looked at to provide an accurate measure of the volume of cavitation. Specimens of wrought Supral 150, taken from the flange region of several top hats, were sent for hydrogen analysis by the vacuum extraction method (164); the results given in Table 9 show up to 0.86 ppm of hydrogen present.

Talbot (60, 147), has stated that aluminium sheet with hydrogen levels greater than 0.2 ppm is prone to blistering during heat treatments.

Hess and Turnbull (58), found that annealing an aluminium alloy containing different levels of hydrogen at 525°C, produced severe blistering for specimens with levels greater than 0.29 ppm. The extent of blistering was seen also to increase with the thickness of the sheet, and they suggest that during annealing the diffusing hydrogen atoms are more likely to escape from the surface of the thinner material than to combine to form molecular hydrogen and hence cause blistering. They also observed less blistering (for all the thicknesses investigated) as the hydrogen content decreased.

In the present investigation, the results suggest that hydrogen is the cause of cavity reappearance on solution-treating the alloy after HIPping. The effect of increasing the HIPping temperature (for the same pressure and time), Figure 74, shows that less cavitation reappears on a post-HIP heat treatment. This may be because at the higher HIP temperatures, the increased rate of diffusional processes may be providing far better cavity sealing, or because the increased mobility of the hydrogen in the material makes it less likely to form molecular hydrogen in the cavities, thus eliminating the effect that internal gas pressure has on preventing cavity sealing.

Increasing the HIPping time to 10 hours for HIP conditions of 360°C, 28 MPa, Figure 77, shows a slight improvement in cavity sealing at the higher times as indicated by a lower drop in the density after a post-HIP heat treatment.

So far, it has been assumed that hydrogen is present in Supral 150 as a consequence of the casting and rolling schedules involved in producing the sheet material (60, 147), see Section 6.2.2. Work

by Eborall and Ransley (61) and Swain (62) has shown that Al - Mg alloys readily absorb hydrogen from water vapour at temperatures between 400°C - 500°C; this absorption is inhibited by the addition of slightly volatile fluorides which act by forming a protective film, leading to a decrease in the tendency of the alloy to blister during heat treatment, especially in industrial furnaces where hydrogen absorption is catalysed by the presence of sulphur.

If the hydrogen level in SPF Supral specimens is reduced (by vacuum degassing under conditions that are used for hydrogen analysis in the vacuum extraction test (164)), and the material HIPped under 28 MPa for ½ hour at three temperatures (450°C, 500°C and 530°C), cavity closure occurs, Figure 75. Subsequent heat-treatment shows that the greatest fall in the density occurs at the lower HIP temperature (450°C); at 500°C and 530°C, there is virtually no change. Nevertheless, the extent of cavity reappearance on SHT is less for vacuum degassed specimens than for the as-received SPF alloy, Figure 74.

9.5.5 Effect of HIP and Heat-Treatment on Cavity Morphology

Figure 78 shows the nature of cavitation in SPF Supral 150 after the T6 treatment. It differs from SPF cavitation in the fact that the cavities have changed from a craggy morphology to a more spherical shape.

Heat-treating vacuum degassed (500°C, 10^{-6} torr, 1 hour) material produces a similar effect on the cavitation as described above; a comparison of the edge sections, Figures 78 and 81, and density measurements, Tables 13 and 14, indicate that vacuum degassed material, in general, attains a slightly higher density on solution-heat treatment, when compared to non-degassed specimens of similar initial cavity levels. This suggests that hydrogen out-gassing during SHT may be causing pore enlargement.

Bampton et al (34) have seen a similar effect in heating experiments with the 7475 alloy. They found that at temperatures above 500°C, for times of one hour (or more), out-gassing of hydrogen trapped in the material (from the casting stage) occurred, producing internal pores and/or surface blisters, but longer times at temperature eventually lead to pore shrinkage. They also found some evidence of internal gas pores forming preferentially at inclusions.

Earlier results have shown that increasing the HIP temperature (for a given time and pressure) or vacuum degassing the material, before HIPping (Figures 74 and 75), show the reappearance of a smaller amount of porosity on heat-treatment.

Figure 82 shows these pores (~ 2 - 4μm in size) are evenly distributed throughout the specimen.

Talbot and Granger (147) have observed similar sized pores on heating aluminium alloys, and describe them as "secondary porosity", which may be present at low hydrogen content,< 0.15ppm, as distinct from the larger porosity caused at higher gas concentrations. They

suggest that this porosity is nucleated immediately after solidification, on imperfections or minute inclusions, and persists through both hot and cold working. The gas is regenerated by heating the worked metal.

Rooy (47) has concluded that casting porosity in aluminium is eliminated at high temperatures and pressures (500°C, 100 MPa), by the plastic collapse of the voids, aided by the tendency of any hydrogen to go back into solution, as its solubility (which is related to the square root of the pressure) increases with pressure and temperature (147). They also observe , however, that subsequent heat treatments result in hydrogen diffusion to inclusions or lattice discontinuities, where porosity is observed to reappear, although they fail to characterise its shape, size and distribution. Similar observations are made in the present work, where cavity closure occurred in specimens which were HIPped (by HIP Metals, Chesterfield) at 505°C, 100 MPa for 3 hours. Subsequent heat treatment resulted in no appreciable fall in density, Table 27, but as Figure 80 shows, there is a reappearance of the fine secondary porosity discussed earlier.

Optical hot stage microscopy results, Figures 95 - 97, failed to determine conclusively whether precipitates and inclusions were sites for the reappearance of porosity during heat treatment.

These results did indicate, however, that hydrogen escape from the material occurs by a different mechanism at atmospheric pressure than under a vacuum; as Figure 95 indicates, thirty minutes at 530°C under 10^{-3} torr produces virtually no difference in the surface of the specimen, yet the same time at atmospheric pressure (under high purity argon) produces increasing levels of porosity with time.

It is suggested that in the presence of a vacuum, there is a sufficient driving force for hydrogen atom diffusion out of the metal. Under atmospheric pressure, this force is insufficient and these atoms migrate to lattice discontinuities (such as precipitates and inclusions), form molecular hydrogen, and this expands under an increasing temperature, causing porosity.

9.5.6 Effect on Grain Size

Figures 47d, 72b, 86 and 87 give examples of the range of grain sizes formed after various heat treatments. For instance, Figure 87b shows grain sizes ranging from 157 μm to 9.8 μm.

This form of abnormal grain growth has been reviewed by Cotterill and Mould (118), who give examples of its existence in a range of metals and alloys. Generally,

(a) Abnormal grain growth will only begin at the completion of the normal growth process. Large grains are not freshly nucleated, but particular grains of the initial structure which have enlarged.

(b) Abnormal grain growth increases with time and temperature as normal growth discussed in Section 9.1.1.

(c) In alloys where grain growth is inhibited by dispersions of second phase particles, an increase in temperature, which affects this dispersion, can lead to the onset of abnormal grain growth. Examples of metals in which particle-induced grain growth has been reported include steels, iron-silicon alloys (associated with dispersions of silica, manganese sulphide and aluminium nitride) and aluminium alloys (with particles containing copper, iron and manganese), all of which are reviewed in reference 118. From the work by Ahlborn (119) on the Al-6Cu alloys, it is evident that grain coarsening occurs in the material because of the dissolution of the restraining θ and θ' particles in the 350°C - 500°C temperature range.

The Supral 150 essentially retains its small grain size due to the fine dispersion of $ZrAl_3$ particles, although Watts et al (121, 122) suggest that in areas denuded of the $ZrAl_3$, θ and θ' particles of critical size may aid in grain growth restriction. Dissolution of these particles at higher temperature may free grain boundaries, leading to abnormal grain growth.

In the present results, abnormal growth is seen to occur either under high temperatures (500 - 530°C for up to 2 hours), Figures 86 and 87, or at lower temperatures, 450°C, but appreciably longer times (greater than 15 hours), Figure 47c. To ascertain whether this behaviour was due to the inhomogeneous distribution of precipitates, particularly $ZrAl_3$, in the alloy, distribution maps (Figure 88a - 88d), using the wavelength dispersive facilities on the SEM, were produced and show clearly the distributions of copper, iron and traces of silicon in a formed and heat treated specimen, but the results for zirconium are not as conclusive.

Energy dispersive facilities on the SEM, used at higher magnifications, also failed to show conclusively the distribution of the fine $ZrAl_3$ in the fine grained AF material, Figures 89 and 89a, although the coarse $ZrAl_3$ particle is identified.

Further use of wavelength dispersive facilities at higher magnification on a material containing a range of grain sizes, (Figures 90 and 91) failed to show any correlation between the distribution of fine $ZrAl_3$ particles and the abnormal grain growth. Spot analysis across the section, Figure 91 and 92 , for zirconium, indicates an even distribution with none present in the cladding. It has been suggested that the high beam current needed in order to detect the fine $ZrAl_3$ particles produces excessive background levels which may mask detection of the zirconium.

In summary, the results fail to determine whether inhomogeneous distribution of the fine $ZrAl_3$ is responsible for the abnormal grain growth. Yet, comparing the characteristics of this alloy with the results of Ahlborn (119) and Watts (121, 122) discussed earlier, suggests that there may be regions in which $ZrAl_3$ is not available for grain boundary pinning; in these, the homogeneously distributed θ and θ' precipitates end in restricting growth, yet their dissolution occurs at higher temperatures leading to abnormal growth in particular grains.

9.6 EFFECT OF 'HIP' ON MECHANICAL PROPERTIES OF SUPRAL

Room temperature tensile tests were employed to see the effect of various HIP and heat treatments on the mechanical properties of Supral 150.

9.6.1 Effect of HIP and Heat Treatment on Ductility

The ductility of the as-received (AR) material rises from 9.4% (Table 10) to 12.8% on solution treatment (ST) and falls again to 9.1% on ageing (T6), indicating the importance of cavities formed around $CuAl_2$ precipitates on the ductility in the material during ambient temperature deformation.

The increase in ductility on solution treatment may be because the high temperature causes a fall in the cavity levels, due to sintering effects, and also puts all the copper in solution and thus it is not available for the θ and θ' precipitate formation, which is frequently associated with sites for cavity initiation and growth during deformation. The ageing process precipitates the θ and θ', leading to the fall in ductility and increase in 0.2% PS and UTS values observed in Table 13.

HIPping the AR material under various conditions (Tables 14, 15 and 16), raises the ductility, but as expected, has no appreciable effect on the 0.2% PS and UTS values.

Solution treating (ST), Table 17, and ST and ageing (T6), Table 18, AR material which has been HIPped (at 28 MPa, 450°C, ½ hr), Table 16, produces increases in the 0.2% PS and UTS values; solution treatment renders an elongation of 15% which falls to 12.4% on the T6 treatment.

Raising the HIP temperature to 500°C, Table 23, followed by the T6 treatment, increases the ductility again to 14.2%, although it is seen to fall if the HIP temperature is raised again to 530°C, Table 25. This reduction in ductility may be due to excessive grain growth in the material at the higher temperature.

The discussion has so far used the average values of the mechanical properties.

Figure 105 shows the effect of both HIP and heat treatments on ductility and whether the initial levels of cavitation influence the elongation percent even after the HIP and heat treatments. The ductility is influenced by the initial levels of cavitation for AR and AR + T6 material, higher initial densities leading to greater ductilities.

HIPping the material(for 28MPa,½hr)at 450°C, followed by the T6 treatment, gives higher ductilities (than above), Figure 106, and shows virtually no effect of the initial level of cavitation, Figure 105.

Raising the HIP temperature to 500°C, offers the best ductility,

and there is no effect from the initial cavity levels. Yet increasing the HIP temperature to 530°C leads to a drop in ductility and the effect of the initial level of cavitation is less clear. Similar observations are made on the vacuum-degassed material for the same HIP and heat treatment conditions, Figures 107 and 108, although the corresponding ductility values are slightly lower.

The following conclusions can be made from the results :-

(a) Ductility is affected by the initial level of cavitation in AF and AF + T6 material, although elongation values are greater in the latter.

(b) HIPping the SPF material under conditions which close cavitation nullifies the influence of the level of initial cavitation on ductility, higher temperatures of HIP (up to 500°C under the same pressure and time) followed by the T6 treatment increases the ductility by up to 36% over the AF + T6 material, although raising the HIP temperature to 530°C leads to a fall in the ductility. This effect may be attributed to the excessive grain growth of the material under the treatment conditions.

(c) The increase in ductility observed in degassed and non-degassed material, when HIPping at 28 MPa, ½ hour, for temperatures between 450°C and 500°C (Figures 106 and 108) (followed by the T6 treatment), corresponds to the lower levels of cavity reappearance under these conditions, Figures 74 and 75.

(d) Similar trends (as in a and b) are shown by AF material which has been vacuum degassed (as described in Section 9.5).

9.6.2 Effect of HIP and Heat Treatments on UTS and 0.2% PS in Supral

The T6 heat treatment on cavitated Supral 150 produces an increase in both the 0.2% PS and the UTS values by virtue of an age hardening mechanism, Tables 10 and 13, yet HIPping the specimens back to virgin material density has no effect on these properties, Table 14. Comparison of the average mechanical property data given in Table 29 shows that HIPped and heat treated specimens have slightly lower 0.2% PS and UTS values (Tables 18, 23 and 25) than the AR + T6 specimens, Table 13. This effect was at first thought to be attributed to excessive grain growth in the HIPped specimens, but grain size determinations, Table 29, indicate that there is very little to distinguish between the grain growth characteristics before and after HIP.

For vacuum degassed material, whose average property values are summarised in Table 30, there is still a drop in the 0.2% PS and UTS when HIPped at temperatures above 500°C. For example, the 0.2% PS has dropped by ~ 26% from that of AR + T6 material to that HIPped at 530°C, 28 MPa, for ½ hour and subsequently heat treated (T6).

The comparison of the mechanical properties has been made from the average values given in Tables 29 and 30, but inspection through Tables 10 - 28 will show that specimens given the same treatment can have large differences (sometimes ~ 20%, Table 13), in the 0.2% Proof Stress (PS). This may be because they are taken from different top

hats, which have varying material properties.

It is therefore clear from the results that HIP treatments have less of an effect on the 0.2% PS and UTS values, which are more sensitive to the heat treatments employed and to the original material properties.

However, the beneficial effect of HIP on ductility through the elimination of cavitation, is clearly shown from the results. HIP at lower pressures does not remove the scatter found in the 0.2% PS and UTS values of SPF material from different top hats.

Although the effect of increasing this HIP pressure to 100 MPa (at 500°C for 3 hours) on the mechanical properties of SPF material is given in Table 27 and shows improvements in all the 0.2% PS, UTS and ductility values over the AR material, the higher pressure has also reduced the scatter in the 0.2% PS values (which is ~ 9% for the worst case) for the specimens taken from different top hats.

The mechanical property values reported in the literature for heat treated (T6) Supral 150 (153) are 270 MPa for the 0.2% PS, which is lower than the average value obtained in this investigation, Table 13, a slightly higher UTS value of 390 MPa and a lower ductility,6%. The authors do not state the SPF strain in the specimens, as this affects the ductility and, to a lesser extent, the 0.2% PS and UTS (32).

9.6.3 Mechanical Properties of Wrought (Sheet) Supral 150

The cold rolled sheet tensile test specimens gave an average 0.2% PS value of 265 MPa and UTS of 273 MPa, Table 31, which are lower than those of AR and T6 specimens, Table 13. The heavily dislocated structure has recrystallised when the wrought alloy is annealed at 450°C for 30 minutes, leading to the drop in both the 0.2% PS and UTS values, Table 32, yet an increase in ductility is observed.

HIPping this material (at 450°C, 28 MPa, ½ hr), followed by solution treating, Table 33, shows a large increase in ductility, which falls on subsequent ageing, Table 34. The mechanical properties for this material are similar to those of SPF material which has undergone the same HIP treatment, Table 18.

Table 34 also shows the slight rise in density of wrought Supral on HIPping; subsequent solution heat treating indicates a small decrease, perhaps due to hydrogen outgassing as discussed in Section 9.5.

9.6.4 Fracture

Room temperature fracture of as-received Supral 150 is by a ductile shear process. The external fracture is characterised by a 45° shear surface and failures by cavity growth and coalescence, Figures 109a and 110.

The cavitated SPF material fails again by growth and coalescence of voids, although the external fracture surfaces have a jagged mor-

phology, as the material has tried to fail by shear but the cavitation in the material changes the crack propagation direction, Figure 109c.

The failure process again is characterised by the growth and interlinkage of cavities, Figure 110.

SPF material which has been HIPped back to theoreticel density fails in a manner similar to the as-received virgin material, Figure 109d.

10. CONCLUSIONS

1. Recrystallisation of as-received Supral 150 occurs at temperatures above 450°C and growth obeys a relationship of

$$\ell n\ d_{mli} = A\ \ell n\ t + c$$

2. The dynamically-recrystallised, fine-grain structure in SPF Supral 150 is stable under static annealing up to 400°C, after which growth follows the same relationship as above.

3. Cavity nucleation is associated with both $ZrAl_3$ and $CuAl_2$ precipitates under SPF. Cavities are largely located at grain and interphase boundaries and growth is predominantly plastic-deformation controlled and increases with increasing SP strains.

4. The activation energy associated with pressureless sintering of SPF cavities is found to be close to that for grain boundary diffusion in aluminium.

5. During HIP at pressures up to 35 MPa, complete cavity closure occurs when the external pressure is greater than the flow stress of the material at that temperature and strain-rate. The ratio of external pressure (P_e) to the flow stress (σ_f) needed to close cavitation increases with falling HIP temperature. The activation energy, ($Q_{\dot{\varepsilon}}$) associated with plastic flow was found to be 53.54 KJ mol^{-1}.

6. The activation energy associated with pressure sintering is found to be close to that of grain boundary diffusion in aluminium. Sintering of cavities is enhanced by the application of pressures greater than 7 MPa.

7. The material is shown to contain a high level of hydrogen (~ 0.8ppm) which manifests itself by causing blistering on heat treatment, and is also responsible for the reappearance of porosity in material returned to theoretical density by HIPping. On subsequent heat treatment, the extent to which porosity returns is decreased either by HIPping at higher temperatures, or pressures, or vacuum degassing the sheet material before HIP.

8. Hydrogen is thought to go into solution under HIP conditions allowing cavity closure. At high concentrations the hydrogen migrates to defects, (such as inclusions, precipitates), forms molecular hydrogen and causes porosity on subsequent heat-treatment (pore size > 20 μm). At lower concentrations, (< 0.1ppm) a post-HIP, high-temperature treatment yields smaller pores of 2 - 4 μm.

9. HIP and heat treatments lead to abnormal grain growth, indicating an inhomogeneous distribution of the fine $ZrAl_3$, used for grain boundary pinning and the importance of the finer θ and θ' precipitates restricting grain boundary migration.

10. Room temperature tensile ductility is enhanced by the HIP process, which also removes the influence of initial cavity levels on ductility observed in formed material.

A scatter in the 0.2% PS and UTS values is found in as-formed and heat-treated specimens, probably due to material variations. Low pressure HIPping does not reduce this effect, although higher pressures (100 MPa), do slightly enhance both the 0.2% PS and UTS whilst also drastically reducing the scatter.

Room temperature fracture of as-received Supral is by a 45^{o} ductile shear process. The external fracture characteristics of the cavitated SPF material has a jagged appearance, as the fracture process due to shear is changed by the presence of cavities.

SPF material which has been HIPped back to theoretical density fails in a similar manner to as-received material. All the specimens fail by a cavity growth and coalescence mechanism.

SUGGESTIONS FOR FURTHER WORK

The areas in which further work can be undertaken from the present investigations are :-

a. Characterising the SPF material variability and its effect on mechanical properties; more work is also needed on the dispersion characteristics of inclusions and precipitates and their relationship to grain growth.

b. Effect of post-forming HIP on other properties, i.e. fatigue, fracture toughness of superplastic alloys.

c. Effects that varying the parameters of t, T and P during HIP has on cavity-closure mechanisms, i.e. do longer times promote creep mechanisms which aid closure at lower external pressures (below the flow stress of the material at that temperature and strain-rate).

d. Vary the initial level of hydrogen in the material (during the casting stage) and see whether lower levels promote less porosity reappearance in SPF material HIPped to theoretical density on subsequent heat-treatment and also determine whether this porosity is caused by partially sealed cavities re-opening or if it is caused by the expansion of hydrogen gas which has collected at metal imperfections, such as precipitates and inclusions.

e. Determine the effects that external sources of gas (e.g. humid furnace atmospheres) have on hydrogen uptake into the alloy.

f. Ascertain the behaviour of hydrogen in the alloy during HIP, and how this varies under different HIP conditions.

REFERENCES

1. B.R. WARD, R.F. ASHTON, J.I. BENNETCH. Proc. International Conference - Superplasticity in Aerospace-Aluminium. Cranfield Institute of Technology, 12 - 15 July 1985. pp 326 - 352.

2. M.V. HYATT. Proc. of Int. Conf. on Al-Alloys. Torino, Italy. October 1976. pp 31 - 43.

3. C.T. POST. Iron Age, July 1980. pp 39 - 44.

4. Superplastic Forming - Conf. Proc. Ed. S.P. Agrawal ASM, Metals Park, OHIO 44073. March 1984.

5. Superplastic Forming of Structural Alloys. Eds. N.E. Paton and C.H. Hamilton. Held at San Diego, USA. June 1982.

6. Superplasticity in Aerospace-Aluminium-Int. Conf. Cranfield Institute of Technology. Eds. R. Pearce and L. Kelly. Cranfield July 1985.

7. T.G. NIEN and J. WADSWORTH Ibid. pp 194 - 214.

8. R. SAWLE. Chart. Mech. Eng., Dec. (1978). p 73.

9. R. SAWLE, Metallurgia, 46, (10), (1979). p 62.

10. J.A. WERT. J. Met. Sept., 35 (1982).

11. J.A. WERT, N.E. PATON, C.H. HAMILTON and M.W. MAHONEY. Metall. Trans. A. 12A (1981). p 1267.

12. Aluminium-Lithium Alloys. Eds. T.H. Sanders Jr. and E.A. Starke Jr. TMS-AIME, Warrendale, PA, 1981.

13. Aluminium-Lithium Alloys II. Eds. T.H. Sanders Jr. and E.A. Starke Jr. TMS-AIME, Warrendale, PA. 1981.

14. Aluminium-Lithium Alloys. Int. Conf. held at Oxford. July 1985, by the Metals Society.

15. R.J. LEDERICH, P.J. MESCHTER, S.M.L. SASTRY. Int. Conf. Superplasticity in Aerospace-Aluminium held at Cranfield Institute of Technology. July 1985. Eds. R. Pearce and L. Kelly pp 105 - 126.

16. L.G. KELLY. Superplastic Forming. Conf. Proc. Ed. S.P. Agrawal. ASM, Metals Park, OHIO, 44073, March 1974, pp 61 - 62.

17. D. ELGEE, S. JOHNSTON, B. GINTY. Int. Conf. Superplasticity in Aerospace-Aluminium. Held Cranfield Institute of Technology, July 1985. Eds. R. Pearce and L. Kelly pp 407 - 425.

18. R.B. VASTAVA, Ibid. pp 448.

19. A.J. BARNES, Ibid. pp 424 - 427.

20. U. KOCH and P.J. WINKLER. Ibid. pp 367 - 390.

21. A. ARIELI and R.B. VASTAVA. Conf. Proc. ASM. Superplastic Forming. Ed. S.P. Agrawal. ASM. Metals Park, OHIO, 44073. March 1984. pp 70 - 75.

22. C. BAMPTON, F. McQUILKIN, G. STACHER. Ibid. pp 76 - 83.

23. M.J. STOWELL. Superplastic Forming of Structural Alloys. Conf. Proc. AIME. Eds. N.E. Paton and C.H. Hamilton. San Diego, USA. June 1982. pp 321 - 338.

24. C.W. HUMPHRIES, N. RIDLEY, J. Mat. Sci. 9 (1974). p 1429.

25. M.J. STEWART. Met. Trans. 7A (1976) p 399.

26. G.L. DUNLOP, E. SHAPIRO, D.M.R. TAPLIN and J. CRANE. J. Met. Trans. 4 (1973) p 2039.

27. S. SAGAT, D.M.R. TAPLIN, Acta. Metall. 24 (1976) p 307.

28. A. ARIELI and A. MUKHERJEE. Mat. Sci. and Eng. 43 (1980) p 47.

29. D.M.R. TAPLIN, R.F. SMITH. 'Fracture 1977'. Vol. 2. Proc. ICF4, Waterloo, Canada, 1977.

30. J.P. PARTRIDGE. MSc Thesis. Cranfield Institute of Technology, (UK). 1982.

31. Superplastic Aluminium Evaluation - Report. AFWAL-TR-81-3051. June 1981.

32. A.J. SHAKESHEFF. Int. Conf. Superplasticity in Aerospace-Aluminium. Held at Cranfield, July 1985. Eds. R. Pearce and L. Kelly. pp 36 - 54.

33. S.P. AGRAWAL and J.M. TUSS. Ibid. pp 296 - 325.

34. C.C. BAMPTON, A.K. GHOSH, M.W. MAHONEY. Ibid. pp 1 - 35.

35. C.C. BAMPTON, A.K. GHOSH, M.W. MAHONEY and R. RAJ. Superplastic Aluminium Evaluation. AFWAL-TR-81-3051. June 1981. pp 123-169.

36. J. PILLING and N. RIDLEY. Int. Conf. on Superplasticity in Aerospace-Aluminium. Held at Cranfield Institute of Technology, July 1985. Eds. R. Pearce and L. Kelly. pp 136 - 145.

37. P.J. MESCHETER, P.S. PAO and R.J. LEDERICH. Scripta Met. 18 (1984) p 833.

38. R.A. STEVENS and P.E.J. FLEWITT, Acta Met. 27 (1979) p 67.

39. W. BEERE and G.W. GREENWOOD. Met Sci. 5 (1971) p 107.

40. E.I.J. PAPEN. 'Isostatic Pressing Technology'. Int. Conf. at Loughborough Univ. Sept. 1978. p 47.

41. S.J. PAPROCKI, E.S. HODGE, D.C. CARMICHAEL and P.J. GRIPSHOVER. BMI-1374, 28 August 1959.

42. G.W. GREENWOOD. Paper 11. 17th Annual BICTA Conf. held at Sheffield. September 1983.

43. R. WIDMER. Proc. 1st Int. Conf. Isostatic Pressing - Loughborough Univ. (1978).

44. R. STEVENS and P.E.J. FLEWITT. Mat. Sci. and Eng. 50 (1981) p 271.

45. Review - Foundry Trade Journal, Feb. 1983. pp 228 - 237.

46. H.D. HANES and J.M. McFADDEN. Met. Prog. (1983) pp 23 - 31.

47. E.L. ROOY - Modern Castings. Dec. 1983. pp 18 - 20.

48. J.K. TIEN, W.J. BOESCH, T.E. HOWSON, W.B. CASTLEDINE - Developments in and Understanding of Powder Superalloys. Powder Metallurgy Conference - Zurich. 1980.

49. F.D. LORDI, A.D. FOSTER, W.E. SCHILLING. Advanced Materials and Coatings. 1980 General Electric Co. GER-2182N.

50. J.R. PAUL. Carbon Fibre Composites, Design News 7-6 (1981) p 57.

51. D.J. ROBERTS, Mater. and Design. 6, 3 July 1985.

52. R.A. STEVENS and P.E.J. FLEWITT. Mater. in Eng. 3 June 1982. pp 461 - 469.

53. F.V. LENEL. Powder Metallurgy - Metal Powder Industries Federation, Princeton, New Jersey. 1980.

54. D. EYLON, F.H. FROES and R.W. GARDINER. Journal of Metals. February 1983. pp 35 - 45.

55. H. ZEITLER and W. SCHARFENBERGER. Aluminium 60 12 (1984) p 803.

56. G.V. SCARICH. 28th Nat. SAMPE Symp. April 1983. p 1329.

57. A. VARTOLEAUX and M. SUERY. Int. Conf. - Superplasticity in Aerospace. Cranfield July 1985. Eds. Pearce and Kelly. pp 55 - 66.

58. P.D. HESS and G.K. TURNBULL in 'Hydrogen in Metals'. ASM Conf. Proc. 23 - 27 September 1973. Eds. I.M. Bernstein and A.W. Thompson. p 277.

59. K.B. DAS, E.C. ROBERTS and R.G. BASSETT. Ibid. p 289.

60. D.E.J. TALBOT. Int. Met. Reviews. Review 201 1975. Vol. 20. pp 166 - 184.

61. R. EBORALL and C.E. RANSLEY. J. Inst. Metals, 71, 1945. p 525.

62. A.J. SWAIN. J. Inst. Metals, 46, 1931, p 187.

63. C.C. BAMPTON and J.W. EDINGTON - Metall. Trans. A. Vol. 13A (1982) p 1721.

64. C.E.J. PEARSON. J. Inst. Metals. 54 111 (1934).

65. T.G. LANGDON. Met. Trans. 13A May 1982 , p 689.

66. R.H. BRICKNELL and J.W. EDINGTON. Acta Met. Vol. 27 (1979), p 1303.

67. J.W. EDINGTON. Met. Trans. A Vol. 13A, May 1982. p 703.

68. J.W. EDINGTON, K.N. MELTON, C.P. CUTLER. Prog. Mat. Sci. 12, 61 (1976).

69. M.J. STOWELL. Metals Sci. Vol. 14, July 1980. p 267.

70. D.M.R. TAPLIN, G.L. DUNLOP, T.G. LANGDON. Ann. Rev. of Mat. Sci. 9 (1979) p 151.

71. T.G. LANGDON. Met. Sci. 16 (1982) p 175.

72. K.A. PADMANABHAN and G.J. DAVIES. 'Superplasticity' - MRE 2. Published by Springer-Verlag, 1980.

73. S.H. GOODS, L.M. BROWN. Acta Met. 27 (1979) pp 1 - 15.

74. R. RAJ and M.F. ASHBY. Acta Met. 23 (1975) p 653.

75. J.E. HARRIS. Trans. Met. Soc. AIME 23 (1965) p 1509.

76. C.H.M. JENKINS. J. Inst. Metals. 40 (1928) p 21.

77. I.R. BACKOFEN, I.R. TURNER and D.H. AVERY. Trans. ASM (1964) 57. p 980.

78. G.J. DAVIES, J.W. EDINGTON, K.N. CUTLER and K.A. PADMANABHAN. J. Mat. Sci. 5. (1970) p 1091.

79. W.R. KERR. J. Mat. Sci. 15 (1980) p 3104.

80. N.E. PATON. J. Eng. Mat. Tech. Trans ASME 97 (1975) p 313.

81. M.A. BURKE, W.D. NIX. Acta Met. 23 (1975) p 793.

82. W.B. MORRISON. ASM Trans. Quart. 61 (1968) p 423.

83. O.D. SHERBY, R.D. CALIGIURI, E.S. KAYALI and R.A. WHITE - Advances in Metal Processing. Eds. J.J. Burke and R. Mehrabian and V. Weiss. Plenus Press. 1981. p 133.

84. B.P. KASHYAP, A. ARIELI, A.K. MUKERJEE. J. Mat. Sci. 20 (1985) p 2661.

85. M. SUERY and B. BAUDELET. J. Mat. Sci. 10 (1975) p 22.

86. A. ARIELI and A. ROSEN. Met. Trans. 8A (1977) p 1591.

87. H.W. HAYDEN, S. FLOOREEN and P.D. GODDELL. Met. Trans. 3(1972) p 883.

88. B.P. KASHYAP and A.K. MUKERJEE. J. Mat. Sci. 18 (1983) p 3299.

89. M.A. CLARKE and T.H. ALDEN. Acta Met. 21 (1973) p 1195.

90. D.S. WILKINSON and C.H. CARCERES. J. Mat. Sci., Lett. 3 (1984) p 331.

91. R. RAJ and M.F. ASHY. Met. Trans 2 (1971) p 1113.

92. T. CHANDRA, J.J. JONAS and D.M.R. TAPLIN. J. Mat. Sci., 13, (1978) p 2380.

93. R.D. VASTAVA and T.G. LANGDON. Acta Met. 27 (1979) p 251.

94. P.M. HAZZELDINE and D.E. NEWBURY. 'Grain Boundary Structure and Properties'. Eds. G.A. Chadwick and D.A. Smith. Academic Press, London, 1975. p 235.

95. R.B. NICHOLSON - 'Electron Microscopy and Structure of Materials'. Eds. G. Thomas. Univ. of California Press, Berkeley, 1972. p 689.

96. D. LEE. Acta Met. 17 (1969) p 1057.

97. R.E. REED-HILL in 'Physical Metallurgy Principles'. Van Nostrand Co. Inc. Princetown, New Jersey. 1966. p 216.

98. W. BEERE. J. Mat. Sci. 12 (1977) p 2093.

99. W. BEERE. Phys. Status Solidi. 449, (1977) p 65.

100. H. NAZIRI, R. PEARCE, M. HENDERSON-BROWN and K.F. HALE. Acta. Met. 23 (1975) p 489.

101. P.M. HAZZELDINE and D.E. NEWBURY. Proc. of 3rd Int. Conf. on Strength of Metal and Alloys. Cambridge. 1973 Vol. 1. Pub. by Inst. of Metals, London, 1973. p 202.

102. L.C.A. SAMUELSSON, K.N. MELTON, J.W. EDINGTON. Acta Met. 24, (1976) p 1017.

103. G.L. DUNLOP and D.M.R. TAPLIN. J. Mat. Sci. 7 (1973) p 316.

104. D.A. WOODFORD, ASM Trans. Quart. 62 (1969) p 291.

105. A. BALL and M.M. HUTCHISON. Met. Sci. J. Vol. 13, (1969) p 1.

106. A.K. MUKHERJEE. Mat. Sci. Eng. Vol. 8, (1971) p 83.

107. R.C. GIFKFINS. Metall. Trans A. Vol. 7A, (1976). p 1225.

108. M.F. ASHBY and R.A. VERRALL. Acta Met. 21 (1973) p 149.

109. J.H. GITTUS. Trans ASME. J. Eng. Mat. and Tech. 99 (1977). p 244.

110. M.F. ASHBY, C. GANDHI and D.M.R. TAPLIN. Acta Metall. Vol. 27, (1979) p 669.

111. S. SAGAT, D.M.R. TAPLIN. Met. Sci. 10 (1976) p 94.

112. D.A. MILLER and T.G. LANGDON. Metall. Trans. A. 9A (1978) p 1688.

113. D.W. LIVESEY and N. RIDLEY. Metall. Trans. A. 9A (1978) p 519.

114. D.J. LLOYD and D.M. MOORE in 'Superplastic Forming of Structural Alloys'. Conf. Proc. San Diego. June 21 - 24 1982. Eds. N.E. Paton and C.H. Hamilton. p 148.

115. C. ZENER in 'Grains, Phases and Interfaces, an Interpretation of Microstructure' - C.S. Smith. Trans ASME. 175 (1948) p 15.

116. F.J. HUMPHREYS, 'The Nucleation of Recrystallisation of Second Phase Particles in Deformed Aluminium'. Acta Met. 25 (1977), pp 1323 - 1344.

117. D.S. WILKINSON and C.H. CACERES - Acta Metall. Vol. 32 No. 9, (1984) pp 1335 - 1345.

118. D. COTTERILL and P.R. MOULD, Recrystallisation and Grain Growth in Metals, Surrey University Press, London (1974) p 266.

119. H. AHLBORN, E. HORNBOGEN and U. KOSTER. J. Mat. Sci. (4) (1969) p 944.

120. N. RYUM, Jnl. of Inst. Metals. Vol. 94 (1966), p 191.

121. B.M. WATTS, M.J. STOWELL, B.L. BAKIE, D.G.E. OWEN. Metal Science, June 1976. pp 189 - 197.

122. Ibid. p 198.

123. A. CIBULA. Metall. Trans. 3 (1972) p 751.

124. K. MATUKI and M.J. YAMADA. Japan Inst. Metals 37 (1973) p 448.

125. G.S. SOHAL. PhD Thesis, Cranfield Institute of Technology, 1980.

126. C.I. SMITH, B. NORGATE and N. RIDLEY. Metal Science 10 (1976), p 182.

127. M.J. PAINTER, R. PEARCE and F. SHEHATA. Jnl. of Mech. Working Tech. ASM (1974) p 2004.

128. N. RIDLEY and D.W. LIVESEY. Res. Mechanica Lettres. 1 (1981) p 73.

129. D. HULL and D.E. RIMMER. Phil. Mag. 4 (1959) p 675.

130. J.W. HANCOCK, Met. Sci. 10 (1976) p 319.

131. I.W. CHEN and A.S. ARGON. Acta Metall. 29 (1981) p 1759.

132. L. MARTINEZ and W.D. NIX. Scripta Met. 15 (1982) p 757.

133. 1st Int. Conf. on Isostatic Pressing - 19th - 21st September 1978. Loughborough University of Technology.

134. 17th Ann. Conf. Proc. BICTA. Stratford-upon-Avon. Sept. 4 - 7, 1983.

135. M.F. ASHBY. Acta Met. Vol. 22. Mar 1974. p 275.

136. F.B. SWINKLES, D.S. WILKINSON, E. ARTZ and M.F. ASHBY. Acta Met. Vol. 31 (1983) p 1829.

137. D.S. WILKINSON, PhD Thesis. Univ. of Cambridge. (1978).

138. B.H. ALEXANDER and R.W. BALLUFI. Acta Met. 5 (1957) p 666.

139. G.W. GREENWOOD, H. JONES and J.H. WOODHEAD. Phil. Mag. 31 (2975) p 39.

140. J. BRETT and L. SEIGLE. Acta Met. 14 (1966), p 575.

141. P. MURRAY, D.T. LIVEY and J. WILLIAMS in 'Ceramic Fabrication Processes'. Ed. W.D. Kingery. 1958. p 147.

142. E. ARTZ, M.F. ASHBY and K. EASTERLING. Report Univ. of Cambridge. CUED/C/MATS/TR.88 Oct. 1981.

143. R.W. HECKEL. Trans. Am. Inst. Min. Eng. 221 (1961) p 1001.

144. K.H. WESTAMACOTT, R.E. SMALLMAN and P. DOBSON. Metall. Sci. J. 2 (1968) p 177.

145. G.W. GREENWOOD. 'Vacancies 76'. Eds. R.E. Smallman and J.E. Harris. p 141. Metals Society London (1977).

146. J. ALBRECHT, I.M. BERNSTEIN and A.W. THOMPSON. Met. Trans. A. Vol. 13A May 1982 p 811 -

147. D.E.J. TALBOT, D.V. GRANGER. Jnl. of Inst. of Metals, Vol. 92, 64 (1963).

148. L.W. EASTWOOD. 'Gas in Light Alloys' 1946 London. Chapman and Hall.

149. H. KOSTRON - Z. Metallkunde. 43 (1952) p 269.

150. H. CHADWICK. J. Inst. Metals. 83 (1954) p 513.

151. C.J. SMITHELLS and C.E. RANSLEY. Proc. Roy. Soc. A 152 (1935) p 706.

152. K.J. GARDNER and R. GRIMES. Met. Sci. March - April, 216 (1979).

153. I.J. POLMEAR. 'Light Alloys - Aluminium Alloys'. Published by Edward Arnold. (1981).

154. N.A. PRATTEN. Jnl. of Mat. Sci. 16 (1981) p 173.

155. R.T. RATCLIFFE. Brit. Jnl. App. Phys. Vol. 16 (1965) p 1193.

156. C. CAWTHORNE and W.D.J. SINCLAIR. J. Phys. E - Scientific Instruments. Vol. 5 (1972) pp 531 - 533.

157. B.D. CLAY and G.W. GREENWOOD. Journel of Physics E; Scientific Instruments. Vol. 3 (1970) p 573.

158. R.H. BRICKNELL, A.P. BENTLEY. Journal of Materials Science, 14 (1979) p 2547.

159. G. CHRISTODOULU. PhD Thesis. Cranfield Institute of Technology (1979).

160. G.T. HIGGINS. Met. Sci. J. 8 (1974) p 143.

161. M.J. STOWELL. Met. Sci. Vol. 17 Jan 1983. pp 1 - 11.

162. G.K. WALKER and H.E. EVANS. Metals Sci. J. 4 (1970) p 155.

163. J. DALY. MSc Thesis. 1985. School of Industrial Science, Cranfield Institute of Technology, England.

164. C.E. RANSLEY and D.E.J. TALBOT. J. Inst. Metals Vol. 84 (1955 - 56) p 445.

```
      IMPLICIT REAL *8 (A-H,O-Z)
      REAL PH(50)

1     continue

      print'('' Input gamma,A,Ri,X :- ''$)'
      READ(5,*) GAMMA,A,Ri,X
      print'('' Input new Pi :- ''$)'
      READ(5,*) Pi
      print'('' Are the values for Ph new :- ''$)'
      READ(5,*) I
      if(I.EQ.2) goto 2
        print'('' Input number of Ph values :- ''$)'
        read(5,*) N
        do 3 I=1,N
          print'('' Input Ph :- ''$)'
          read(5,*) PH(I)
3       continue
2     continue

      write(6,6) GAMMA,A,RI,X
6     format('Gamma=',F8.4,' A=',F8.4,' Ri=',F8.4,' X=',F8.4)
      do 4 I=1,N
        write(6,*) PH(I),PI
        CALL PLOT(GAMMA,A,RI,X,PH(I),PI)
4     continue
      write(6,*) ('----------------------------------------')

      print'('' To run again? :- ''$)'
      READ(5,*) M
      if(M.eq.1) goto 1
      STOP
      END

      SUBROUTINE PLOT(GAMMA,A,RI,X,PH,PI)
      implicit real (A-H,O-Z)
      REAL R(50),T(50)
      print'('' Are the values for R new :- ''$)'
      read(5,*) NEW
      if(NEW.EQ.2) go to 3
        print'('' Input number of values for R :- ''$)'
        read(5,*) M
        do 1 I=1,M
          print'('' Input R ''$)'
          read(5,*) R(I)
1     continue
3     continue
      write(6,*) (' ')
      do 2 I=1,M
        CALL INTEG(GAMMA,A,RI,X,PH,PI,R(I),T(I))
      WRITE(6,*) T(I)
2     continue
      DO 4 I=1,M
      WRITE(6,*) R(I)
4     CONTINUE
      write(6,*)
      return
      END

      SUBROUTINE INTEG(GAMMA,A,RI,X,PH,PI,R,T)
      implicit real (A-H,O-Z)

      GH=(R-RI)/20
      T=0.0
      RV=R
      CALL FUNCT(GAMMA,A,RI,X,PH,PI,RV,TV)
      T=T+TV
      RV=RI
      CALL FUNCT(GAMMA,A,RI,X,PH,PI,RV,TV)
      T=T+TV
      if(R.NE.RI) then
        do 74 I=1,19
          RV=RV+GH
          CALL FUNCT(GAMMA,A,RI,X,PH,PI,RV,TV)
          T=T+3.0*TV
74      continue
      endif
      GH=3.0*ABS(GH)/8
      T=T*GH
      return
      END

      SUBROUTINE FUNCT(GAMMA,A,RI,X,PH,PI,R,T)
      implicit real (A-H,O-Z)

      A1=R**2/A
      A2=2*GAMMA/R+PH-PI*(RI/R)**3
      A3=LOG(X/R)-0.75
      T=(A1/A2)*A3
      return
      END
```

Table 1 - CASTING ALLOYS CURRENTLY PROCESSED BY HIP (45)

Casting Alloy	Temperature
Stellite 21-Co superalloy	1.230°C
Rene 80-Ni superalloy	1.200°C
Rene 120-Ni superalloy	1.220°C
17-4PH-steel	1,180°C
Ti-6Al-4V-titanium	970°C
No. 903-tin bronze	760°C
A356-aluminium	540°C

Table 2 - STRAINS WHERE AN EQUIAXED STRUCTURE IS ACHIEVED FOR VARIOUS SUPERPLASTIC ALLOYS (84)

Alloy	Engineering strain (%)
Al–Cu–Zr	~ 50
60/40 Brass	< 30
Cu–P	< 30
Cu–Zn–Fe	< 40
IN-744	< 80
Al–Cu eutectic	~ 15
Pb–Sn eutectic	~ 5
Ti–6Al–4V	0*

*Static annealing at the test temperature.

Table 3 - SUMMARY SHOWING HOW THE VARIOUS THEORIES FOR SP DEFORMATION FIT THE EXPERIMENTALLY OBSERVED BEHAVIOUR OF SP MATERIALS

	Experimentally Required	Ashby-Verall	Ball-Hutchinson + Mukherjee	Mukherjee	Gifkins	Gittus
Microstructural						
Grain-boundary sliding	Yes	Yes	Yes	Yes	Yes	Yes
Grain-boundary migration	Yes	*	*	*	*	*
Equiaxed grain shape	Yes	Yes	Yes	Yes	Yes	Yes
Grain rotation	Yes	Yes	*	Yes	Yes	*
3-D grain rearrangement	Yes	*	*	*	Yes	*
Dislocation activity	Yes	*	Yes	Yes	*	*
Dislocation pile-ups	No	No	Yes	Yes	Yes	Yes
Grain-boundary structure related details	Yes	No	No	No	No	No

Table 4 - POSSIBLE MECHANISMS OF PRESSURE SINTERING (135)

Mechanism number	Mechanism	Transport path for matter From	To	Densifying Mechanisms	Stages Operative
0	Elastic adhesion			x	0
1	Plastic yielding	Neck region	Porosity surface	x	1-3
2	Power-law creep	Neck region	Porosity surface	x	1-3
3	Boundary diffusion	Grain boundary in neck	Porosity surface	x	1-3
4	Lattice diffusion	Grain boundary in neck	Porosity surface	x	1-3
5	Surface diffusion	Surface	Porosity surface		1
6	Lattice diffusion	Surface	Porosity surface		1
7	Evaporation-condensation	Surface	Porosity surface		1

Table 5 - QUANTIMET 720 ANALYSER CALIBRATION

OBJECTIVE	A X I S		AREA (mm^2)	RADIUS (pp)
	X	Y		
X5	1.49	1.15	1.713	1.85 µm
X10	0.76	0.61	0.463	1.08 µm
X40	0.18	0.15	0.027	0.262 µm

Table 6 - HEAT TREATMENT SCHEDULES FOR SUPRAL 100/150

T6 TREATMENT

SOLUTION TREATMENT

Solution treat by heating uniformly at a temperature of 530°C± 5°C for 60 minutes ± 10 minutes and quench rapidly in a 30 - 50% aqueous solution of Quindella at a temperature not exceeding 40°C.

ARTIFICIAL AGEING

Artificially age by heating uniformly at either :-

a) 165°C ± 5°C for 20 hours ± 1 hour or

b) 175°C ± 5°C for 10 hours ± 1 hour or

c) 185°C ± 5°C for 5 hours ± 1 hour.

Table 7 - VIRGIN MATERIAL - STATIC ANNEALS

200°C and 300°C - Partial Recrystallisation - Difficult to do Grain Sizes.

TEMPERATURE = 400°C			
TIME (Hours)	GRAIN SIZE ($d_{m\ell i}$) T (μm)	ST (μm)	AIR. (T/ST)
up to 2 hrs.	BANDED STRUCTURE		
5 hrs	16.12	15.92	1.012
TEMPERATURE = 450°C			
½	9.58	7.32	1.31
1	10.8	8.76	1.23
2	19.23	16.25	1.18
5	25.20	20.23	1.24
15	35.77	29.54	1.20
TEMPERATURE = 530°C			
½	20.87	15.37	1.32
1	35.7	30.23	1.18
2	40.32	38.54	1.05
5	54.05	42.67	1.26
15	75.32	64.54	1.16

Table 8 - DATA FOR S.P.F. SUPRAL 150 CAVITATED COUPONS, HIPped AT 360°C, 28 MPa, FOR VARIOUS TIMES AND SOLUTION-TREATED (530°C 1 HOUR, COLD-WATER-QUENCHED)

SPECIMEN	ε_3	A $\rho_{A.R.}$	B ρ_{HIP}	C $\rho_{HIP+S.T.}$	TIME (HOURS)
1	0.0503	2.7499	2.8172	2.7738	1
2	1.0532	2.74923	2.81288	2.78048	1
3	1.100	2.73978	2.80907	2.76476	1
AVERAGE		2.74630	2.81305	2.7730	
4	0.9457	2.7599	2.81058	2.77166	2
5	0.9407	2.76075	2.81136	2.77673	2
6	0.9528	2.75876	2.81035	2.77680	2
AVERAGE		2.75980	2.81076	2.7750	
7	1.0151	2.73805	2.80566	2.77270	5
8	1.0614	2.73016	2.80938	2.78201	5
9	1.0936	2.7347	2.80952	2.77934	5
AVERAGE		2.7343	2.8081	2.77801	
10	0.9431	2.76674	2.80796	2.78324	10
11	0.9578	2.75184	2.80991	2.78578	10
12	0.9507	2.7767	2.81010	2.78563	10
AVERAGE		2.7651	2.80932	2.7848	

Table 9 - RESULTS OF HYDROGEN CONTENT DETERMINATION OF Al - 6Cu - 0.5Zr ALLOY SHEET

SAMPLE	HYDROGEN CONTENT (ppm)
B13	0.80
A8	0.80
A5	0.53
C17	0.86

TABLE 10

Specimen	Treatment	ρ gcm^{-3}				DIR	0.2% P.S. MPa	UTS MPa	E1% on 25mm gl
		ρ .CAV	ρ HIP	ρ S.T.	ρ AGED				
L5	As received S.P.F. TOP HAT Supral 150.	2.6750				90°	88.9	162.48	8.6
13		2.6920				0°	106.59	180.78	9.0
J2		2.7170				0°	99.01	181.02	8.0
N2		2.730				90°	103.51	172.52	10.4
N5		2.7445				90°	103.51	172.52	10.40
ET2		2.7490				0°	92.47	187.82	10.0
AVERAGE							81.74	176.19	9.4

TABLE 11

Specimen	Treatment	ρgmc^{-3}				DIR	0.2% P.S. MPa	UTS MPa	E1% on 25mm gl
		ρ.CAV	ρHIP	ρS.T.	ρAGED				
04	Cavitated and annealed 450°C air cool. ½hr	2.7120				90°	95.6	133.84	8.2
F4		2.7215				0°	100.24	183.77	11.4
G3		2.7340				0°	101.23	186.65	11.8
AVERAGE							99.03	168.08	10.46

Table 12

Specimen	Treatment	ρgcm^{-3}				0.2% P.S. MPa	UTS MPa	E1% on 25mm gl	DIR
		ρCAV	ρHIP	ρS.T.	ρAGED				
02	Cavitated and Solution treated (530°C 1 hour) C.W.Q.	2.7130	-	2.7546	-	165.92	287.82	14.0	90°
G1		2.7405	-	2.76104	-	174.04	319.09	12.4	0°
N4		2.7315	-	2.75926	-	174.46	304.45	12.0	90°
AVERAGE						171.47	303.78	12.8	

Table 13

Specimen	Treatment	ρgcm^{-3}				0.2% P.S. MPa	UTS MPa	E1% on 25mm gl	DIR
		ρCAV	ρHIP	ρS.T.	ρAGED				
M4	Cavitated, Solution-treated and aged (T6)	2.7160	-	2.75627	2.75588	296.87	310.85	8.4	90°
H4		2.7325	-	2.76078	2.76312	262.32	357.02	10.0	0°
I4		2.700	-	2.7537	2.75269	295.90	315.46	6.0	0°
W1		2.70563	-	2.75403		326.30	385.30	9.24	0°
X4		2.73409	-	2.76763		339.05	367.73	10.42	0°
U2		2.76814	-	2.76813		282.53	328.52	8.8	0°
R3		2.74479	-	2.75438		274.73	341.89	10.26	90°
AVERAGE						293.95	343.82	9.01	

Table 14

Specimen	Treatment	ρgcm^{-3} ρ.CAV	ρHIP	ρS.T.	ρAGED	DIR	0.2% P.S. MPa	UTS MPa	E1% on 25mm gl
L3	Cavitated and HIPped (450°C 14MPa 1/2hr)	2.6585	2.80654			90°	74.67	120.30	7
DT10		2.697	2.81003			0°	90.09	172.75	12.4
K4		2.7130	2.80558			90°	80.83	171.77	16
F5		2.7210	2.81516			0°	85.91	175.13	15
AT13		2.749	2.81100			0°	92.05	191.78	16.0
BT9		2.761	2.81500			90°	84.75	177.66	16.5
AVERAGE							84.71	168.23	13.81

Table 15

Specimen	Treatment	ρgcm^{-3} ρ.CAV	ρ.HIP	ρS.T.	ρAGED	DIR	0.2% P.S. MPa	UTS MPa	E1% on 25mm gl
L4	Cavitated and HIPped (375°C 28 MPa 1/2 hr)	2.66478	2.80610			90°	82.63	144.6	7.4
I1		2.70123	2.81586			0°	95.55	160.78	9.2
05		2.70482	2.80788			90°	92.23	164.71	13.2
03		2.71386	2.80684			90°	95.55	168.00	11.2
AT7		2.741	2.81200			90°	85.0	182.09	12.0
AT5		2.741	2.80500			0°	97.99	158.78	14.0
AVERAGE							91.47	163.16	11.16

Table 16

Specimen	Treatment	ρ.CAV	ρHIP	ρS.T.	ρAGED	DIR	0.2% P.S. MPa	UTS MPa	E1% on 25mm g.l.
L2	Cavitated and	2.6585	2.80740	-	-	90°	84.32	143.35	5.2
DT19	HIP'ped (450°C	2.6930	2.80500	-	-	0°	86.67	156.60	10.6
DT3	28MPa, ½hr.)	2.6960	2.80900	-	-	0°	73.40	166.93	10.8
DT12		2.6990	2.80500	-	-	0°	86.94	150.81	11.0
H2		2.7210	2.80030	-	-	90°	104.93	193.46	14.8
G2		2.7410	2.80651	-	-	90°	103.26	193.62	16.0
AVERAGE							90.14	167.46	11.4

Table 17

Specimen	Treatment	ρCAV	ρgcm^{-3} ρHIP	ρS.T.	ρAGED	DIR	0.2% P.S. MPa	UTS MPa	E1% on 25mm gl
K2	Cavitated, HIPped (450°C 28 MPa and solution-treated (530°C 1 hr), C.W.Q.	2.70288	2.80660	2.76649		90°	129.01	278.98	16.0
K3		2.70528	2.80416	2.76570		90°	146.39	292.78	14.0
H1		2.72361	2.80988	2.76464		0°	148.37	290.42	16.2
CT4		2.73900	2.80200	2.78854		90°	140.01	295.87	15.6
ET8		2.74200	2.81300	2.76986		0°	126.34	294.72	15.8
AVERAGE							138.02	290.55	15.52

Table 18

Specimen	Treatment	ρ CAV	ρgcm^{-3} ρHIP	ρS.T.	ρAGED	0.2% P.S. MPa	UTS MPa	E1% on 25mm gl	DIR
P2	Cavitated, HIPped, 450°C 28 MPa ½ hour solution - treated and aged (T6)	2.7130	2.80671	2.77792	2.77918	240.34	330.0	11.5	0°
CT1		2.724	2.80910	-	-	220.37	314.35	12.4	90°
H5		2.7305	2.80943	2.77510	2.77567	240.10	342.0	11.8	0°
M5		2.7380	2.80943	2.78140	2.78085	247.30	356.0	12.8	90°
BT17		2.7630	2.81180	-	2.78019	207.8	313.05	13.0	90°
BT18		2.766	2.80970	-	2.78301	227.2	338.08	12.9	0°
AVERAGE						230.51	332.24	12.40	

Table 19 - CAVITATED, VAC. DEGASSED ($500^{o}C$ 10^{-6} TORR 1 HOUR) + T6

ρ/gcm^{-3}

Specimen	ρ_c	ρ_{VDGAS}	ρ_{ST}	ρ_{T6}	0.2% PS MPa	UTS MPa	E1%	DIR
2A	2.73283	2.74530	2.75064	2.75924	260.85	360.30	9.7	0^{o}
2B	2.71944	2.74210	2.75123	2.76034	295.30	343.10	9.0	0^{o}
2C	2.70933	2.73120	2.76034	2.75999	235.60	342.30	8.3	0^{o}
2D	2.74212	2.75321	2.76012	2.76014	244.0	350.45	8.6	90^{o}
2E	2.73312	2.75123	2.76315	2.76421	254.30	360.20	7.5	90^{o}
					———	———	———	
AVERAGE					258.01	351.27	8.54	
					———	———	———	

Table 20 - CAVITATED (VDGAS 450°C 10^{-1} TORR ½ HOUR IN PRESSURE VESSEL) + HIP (450°C 28MPa ½ HOUR) + T6

Specimen	ρ_c	ρ_{HIP}	ρ_{HIP+T6}	DIR	0.2% PS MPa	UTS Mpa	E1%
VT1	2.72134	2.80900	2.79481	0°	260.34	359.9	12.6
XT2	2.73995	2.81032	2.79441	90°	280.21	347.3	9.6
XT3	2.74080	2.80666	2.79375	90°	240.61	360.31	14.2
AVERAGE					260.38	355.83	11.13

Table 21

FORMED VDGAS (500°C 10^{-6} torr 1 hr) VESSEL VAC (10^{-1} torr ½ hr) + HIP (28 MPa, 450°C ½ hr) + T6

Specimen	ρ_c	ρ_{VDG}	ρ_{HIP}	ρ_{HIP+T6}	0.2% MPa	UTS MPa	E1%	DIR
	ρ/gcm^{-3}							
W3	2.6963	2.70789	2.80561	2.79340	259.3	331.86	10.0	0°
Y1	2.73537	2.75975	2.80570	2.79950	243.79	328.97	12.0	0°
V2	2.73063	2.75165	2.80249	2.79250	244.0	398.2	10.0	0°
P3	2.73167	2.74558	2.80904	2.79601	246.7	349.05	11.3	90°
Q4	2.72077	2.74935	2.80603	2.79532	242.4	326.31	10.1	90°
T4	2.74593	2.75064	2.80260	2.79583	261.00	375.83	12.0	90°
X1	2.74067	2.75528	2.81125	2.78988	295.60	397.30	11.2	0°
S5	2.74786	2.75656	2.81312	2.79117	298.30	396.2	10.4	90°
T2	2.74601	2.75686	2.81031	2.78520	275.94	378.62	10.5	90°
AVERAGE					262.91	363.59	10.07	

Table 22 -

FORMED VESSEL, VESSEL DEGAS (10^{-1} TORR, 450°C ½ HOUR) HIP (500°C 28MPa ½ HOUR + T6 (WATER QUENCH))

ρ/gcm^{-3}

Specimen	ρ_f	ρ_{VDGAS}	ρ_{ST}	ρ_{ST+AGE}	ρ_{HIP}	ρ_{HIP+T6}	0.2%PS (MPa)	UTS (MPa)	E1% on 25mm g.l.	DIR
R5	2.73207				2.80988	2.79239	279.84	293.84	12.0	90°
S1	2.72994				2.81172	2.79670	314.28	414.72	11.0	90°
P1	2.74367				2.81073	2.79192	313.31	417.74	12.3	90°
Q2	2.76904				2.80637	2.78744	301.37	396.54	12.0	90°
Y2	2.73217				2.81171	2.79313	307.52	416.25	14.0	0°
AVERAGE							303.26	407.8	12.26	

Table 23

AS FORMED, HIP (500°C 28 MPa ½ hr) + T6 (NO DEGAS)

Specimen	ρ_f	ρ_{f+ST}	ρ_{f+T6}	ρ_{HIP}	ρ_{HIP+ST}	ρ_{HIP+T6}	DIR	0.2% (MPa)	UTS (MPa)	E1%
T1	2.75895	-	-	2.81210	2.79346	2.79533	90°	229.56	325.69	14.5
X3	2.73718	-	-	2.80937	2.79346	2.79532	0°	238.42	336.95	14.0
P4	2.71736	-	-	2.81178	2.7926	2.79409	90°	238.42	336.95	14.3
AVERAGE								235.46	333.19	14.26

Table 24 - CAVITATED, VAC. DEGASSED (10^{-6} TORR, 1 HOUR 500°C), PRESSURE VESSEL DEGAS (10^{-1} TORR, ½ HOUR, 450°C) + HIP (500°C 28 MPa, ½ HOUR) + T6

Specimen	ρ_f	ρ_{VDGAS}	ρ_{ST}	ρ_{T6}	ρ_{HIP}	ρ_{HIP+T6}	DIR	0.2% PS MPa	UTS MPa	E1%
1A	2.74743	2.7722	-	-	2.81494	2.80485	0°	218.33	293.18	16.0
1B	2.70764	2.77038	-	-	2.81292	2.80547	0°	247.38	338.52	16.0
1C	2.74316	2.76593	-	-	2.81444	2.80571	90°	261.04	341.37	13.05
1D	2.69160	2.76751	-	-	2.81260	2.80495	90°	249.33	347.76	15.37
1E	2.75292	2.77131	-	-	2.81316	2.80662	0°	230.78	336.81	15.95
								———	———	———
AVERAGE								241.37	331.52	15.27
								———	———	———

Table 25 - CAVITATED, HIP (530°C, 28 MPa, ½ HOUR) + T6. NO DEGAS.

$\rho_{gcm^{-3}}$

Specimen	ρ_f	ρ_{HIP}	ρ_{HIP+T6}	0.2% (MPa)	UTS (MPa)	E1%	DIR
3A	2.70296	2.81080	2.79929	244.71	319.57	9.8	0°
3B	2.71481	2.81031	2.79867	168.90	272.90	10.7	0°
3C	2.72049	2.80894	2.80352	225.40	315.66	11.35	0°
3D	2.70713	2.80866	2.8003	222.50	310.25	8.30	90°
3E	2.71400	2.80887	2.79807	222.92	317.50	11.40	90°
AVERAGE				216.88	307.17	10.31	

Table 26 - CAVITATED, VAC. DEGASSED (500°C 10^{-6} TORR 1 HR) + PRESSURE VESSEL DEGASSED (10^{-1} TORR, 450°C, ½ HOUR) + HIP (530°C, 28 MPa, ½ HOUR) + T6

Specimen	ρ_f	$\rho_{f+VDGAS}$	ρ_{HIP}	ρ_{HIP+T6}	0.2%PS (MPa)	UTS (MPa)	0.2% E1%	DIR
5A	2.71526	2.74964	2.80901	2.80916	157.52	260.52	11.91	90°
5B	2.71893	2.751964	2.81012	2.80820	207.08	313.59	12.4	90°
5C	2.71063	2.75115	2.81089	2.80925	217.82	294.30	9.0	90°
5D	2.72009	2.75334	2.81077	2.810236	206.5	309.80	9.9	0°
5E	2.70942	2.75001	2.81154	2.81236	163.40	272.42	8.8	0°
AVERAGE					190.46	290.12	10.20	

Table 27 - HIP METALS (100 MPa 3 HOURS 505°C) + T6

ρ/gcm^{-3}

Specimen	ρ_f	ρ_{VDGAS}	ρ_{ST}	ρ_{ST+AGE}	ρ_{HIP}	ρ_{HIP+T6}	0.2% PS (MPa)	UTS (MPa)	E1% on 25mm g.l.	DIR
U4					2.81014	2.80826	282.02	368.36	10.0 (Blister)	0°
T3					2.81398	2.81364	301.88	412.57	12.0	90°
P2					2.81433	2.81592	304.33	410.85	16.0	90°
R1					2.81461	2.81582	310.07	408.97	14.0	90°
V5					2.81251	2.81230	306.09	414.13	14.0	0°
AVERAGE							300.87	402.97	13.2	

Table 28 - FORMED + HIP (28 MPa, 450°C VARIOUS TIMES) + T6

Density ρ/gm cm^{-3}

Time	Specimen	ρ_f	ρ_{VDGAS}	ρ_{ST}	ρ_{ST+AGE}	ρ_{HIP}	ρ_{HIP+T6}	0.2% PS (MPa)	UTS (MPa)	E1% on 25mm g.1	DIR
30 secs	W2	2.70419				2.78631	2.78923	247.78	371.77	12.78	0°
	V1	2.73975				2.79142	2.78946	274.21	346.53	10.12	0°
	Q1	2.72431				2.78889	2.78434	265.48	371.04	8.92	90°
5 mins	U5	2.72244				2.80866	2.79841	267.5	359.9	9.5	0°
	V4	2.73933				2.81022	2.79341	264.3	383.15	12.4	0°
	Y4	2.73869				2.80566	2.79675	243.8	365.04	14.2	0°

Table 29 - AVERAGE OF MECHANICAL PROPERTY VALUES FOR NON-DEGASSED SUPRAL 150

TREATMENT	TABLE NO.	NO. OF SPECS.	0.2 PS (MPa)	UTS MPa	E1%	SPECIMEN	GRAIN SIZE (μm)			COMMENTS
							T	ST	AR	
As received (A.R.)cavitated	10	6	81.74	176.19	9.4	7C	6.5	5.45	1.19	Stable grain structure
A.R.+450°C ½ hr.	11	3	99.03	168.08	10.46	-	-	-	-	-
A.R. + S.T.	12	3	171.47	303.78	12.8	G1	12.88 (210.2)	11.79 (200)	1.09 (1.05)	Fairly equiaxed, some large grains.
A.R. + T6	13	7	293.95	343.82	9.01	H4	9.09 (222)	10(100)	0.91 (2.2)	Mixture of grain sizes.
A.R.+HIP(14MPa 450°C, ½hr)	14	6	84.71	168.23	13.81	-	-	-	-	-
A.R.+HIP(28MPa 375°C ½hr)	15	6	91.47	163.16	11.16	-	-	-	-	-
A.R.&HIP(28MPa 450°C ½hr)	16	6	90.14	167.46	11.4	A2	7.22	6.51	1.10	Equiaxed and uniform.
As above + S.T.	17	5	138.02	290.55	15.52	3	9.46	8.8	1.08	Uniform
As above + T6	18	6	230.51	332.24	12.4	F2	10.08	9.56	1.05	Uniform
A.R.+HIP(500°C 28MPa, ½hr) + T6	23	3	235.46	333.19	14.26	P4	7.10 (48.6)	6.67 (34.8)	1.06 (1.39)	Uniform-larger grains sparodic along edges.
A.R.+HIP(530°C 28MPa, ½hr) + T6	25	5	216.88	307.17	10.31					
A.R.+HIP(100MPa, 3hrs, 500°C)+T6	27	5	300.87	402.97	13.2	S2	34.15	26.3	1.29	

Table 30 - AVERAGES OF MECHANICAL PROPERTY DATA FOR DEGASSED SUPRAL 150

TREATMENT	TABLE NO.	NO. OF SPECS.	0.2PS (MPa)	UTS (MPa)	E1%	SPEC	GRAIN SIZE (μm)			COMMENTS
							T	ST	A.R.	
A.R.cavitated VAC degas (500°C,10^{-6} torr 1 hour) + T6	19	5	258.01	351.27	81.54	R4	8.56(28.4)	8.52(25.3)	1.0(1.12)	Few larger grains, but all equiaxed
A.R. + Pressure vessel degas (450°C 10^{-1} torr ½hr + HIP(450°C 28MPa, ½hr) + T6	20	3	260.38	355.83	11.13	-	-	-	-	-
A.R. + VDGAS(500°C 10^{-6}torr, 1 hr) + Press.vessel degas (450°C,10^{-1}torr ½hr) + HIP(28MPa, 450°C, ½hr) + T6	21	9	262.19	363.15	10.07	V2	7.38(1000)	6.61(125)	1.11(8.0)	Larger grains mainly along edges
As above, but HIP (500°C 28MPa, ½ hr) + T6	24	5	241.37	331.52	15.27	-	-	-	-	-
As above but HIP (530°C 28 MPa, ½ hr) + T6	26	5	190.46	290.12	10.20					

Table 31 - SUPRAL 150 VIRGIN MATERIAL - TENSILE TEST RESULTS

SPECIMEN	DIR	0.2% P.S. (MPa)	UTS MPa	E1% on 25mm g.l.	CONDITIONS
VT1	90°	273.35	281.50	13.0	
VT2	90°	274.03	280.90	10.0	
VT3	90°	269.81	278.74	13.0	As received
VT4	0°	284.05	297.09	16.0	rolled 4mm sheet
VT5	0°	265.17	271.90	16.0	
VT6	0°	262.53	271.82	12.0	
VT7	90°	254.80	258.34	10.2	
VT8	90°	269.40	275.05	13.8	
VT9	0°	237.30	247.16	12.2	
AVERAGE		265.60	273.61	12.91	

Table 32 - SUPRAL 150 - VIRGIN MATERIAL - TENSILE TEST RESULTS

SPECIMEN	DIR	0.2% P.S. MPa	UTS MPa	E1% on 25mm g.l.	CONDITIONS
A	90°	126.14	238.8	16.36	
B	90°	129.51	242.5	20.0	
C	90°	117.88	228.5	16.3	As received
D	0°	116.38	242.47	16.36	annealed for
E	0°	123.38	236.80	12.7	½ hr at 460°C
F	0°	122.46	247.30	16.36	
AVERAGE		122.62	239.39	15.84	

Table 33 - SUPRAL 150 - VIRGIN MATERIAL - TENSILE TEST RESULTS

SPECIMEN	DIR	0.2% P.S. MPa	UTS MPa	E1% on 25mm g.l.	CONDITIONS
VT12	0°	135.7	303.92	24.07	As received,
VT11	0°	130.45	301.23	22.5	HIPped 450°C, 28 Mpa,
VT10	90°	154.43	306.49	22.2	½ hr., solution-treated
					(530°C 1 hour C.W.Q.)
AVERAGE		140.19	303.88	22.5	

Table 34 - SUPRAL 150 - VIRGIN MATERIAL - TENSILE TEST RESULTS

SPECIMEN	DIR	0.2% P.S. (MPa)	UTS (MPa)	E1% on 25mm g.l.	CONDITIONS
VT7	90°	247.80	342.65	11.11	As received, HIPped (28MPa, 450°C, ½hr)
VT8	90°	232.92	334.07	12.90	Solution-treated
VT9	0°	230.85	334.12	11.88	and aged (T6)
AVERAGE		237.19	336.94	11.96	

DENSITY CHANGES/ρgcm^{-3}

	ρ(A.R.)	ρ(HIP)	ρ(HIP+S.T.)	ρ(HIP+S.T.+AGE)
CT7	2.8020	2.80988	2.7920	2.79145
VT8	2.8000	2.81006	2.7971	2.78102
VT9	2.8009	2.80916	2.7971	2.77952

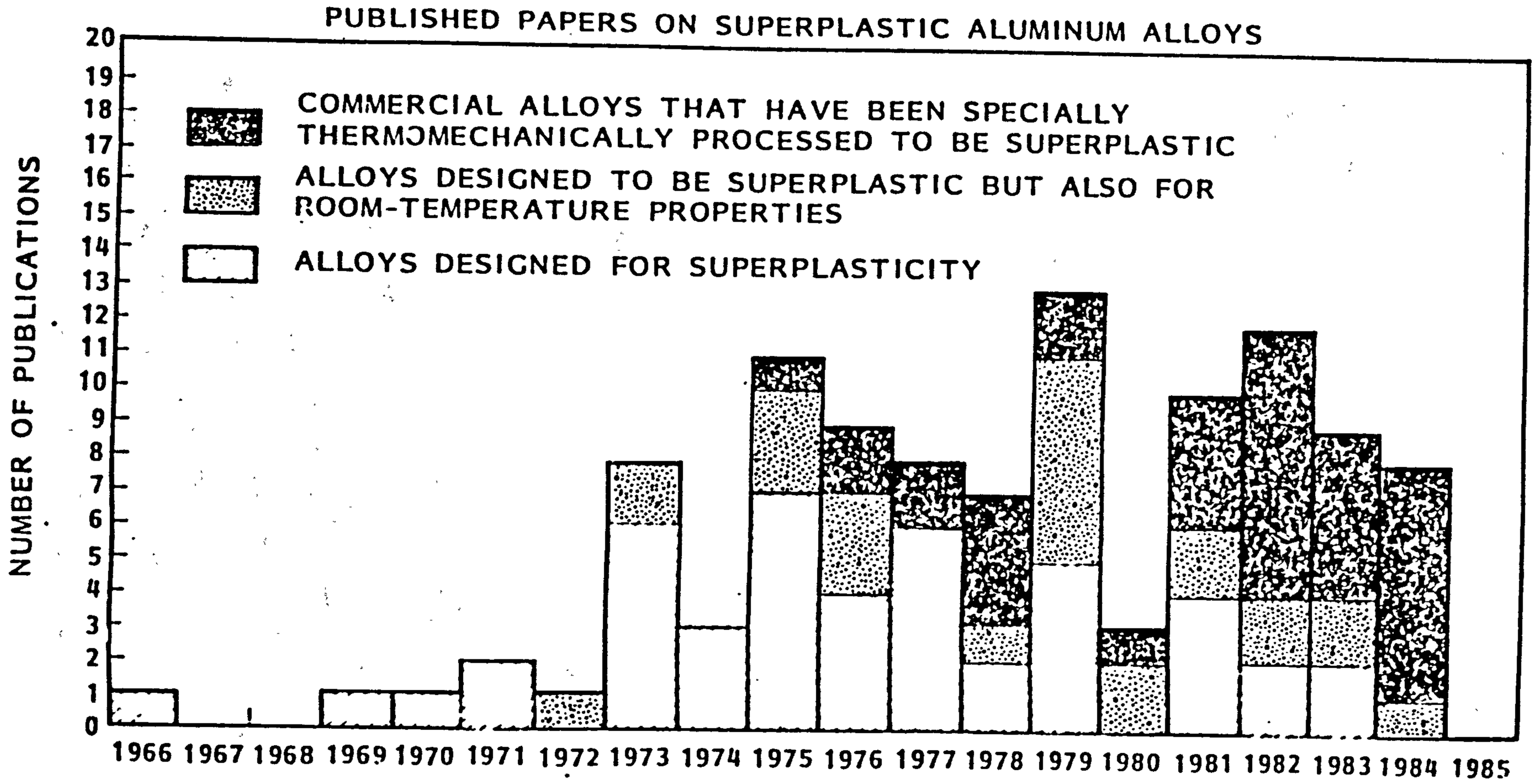

Figure 1 - Publications on superplastic aluminium alloys from 1960 - more emphasis on commercial alloy investigation in recent years (7).

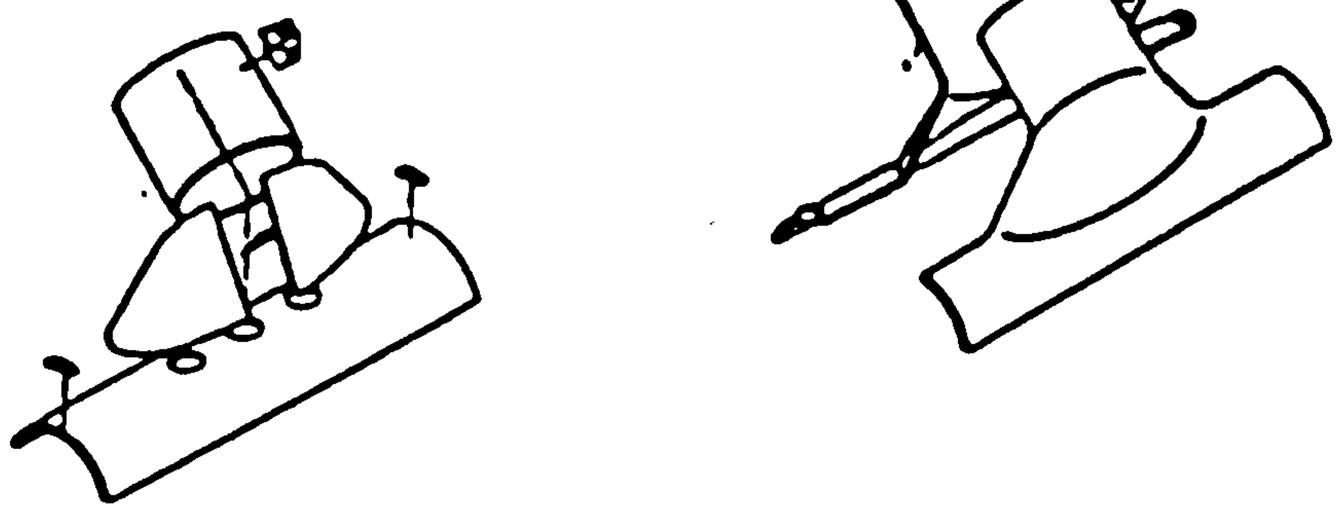

Figure 2 - Helicopter skid shoe, conventional design (ℓ) and SPF-Al design (r). (20).

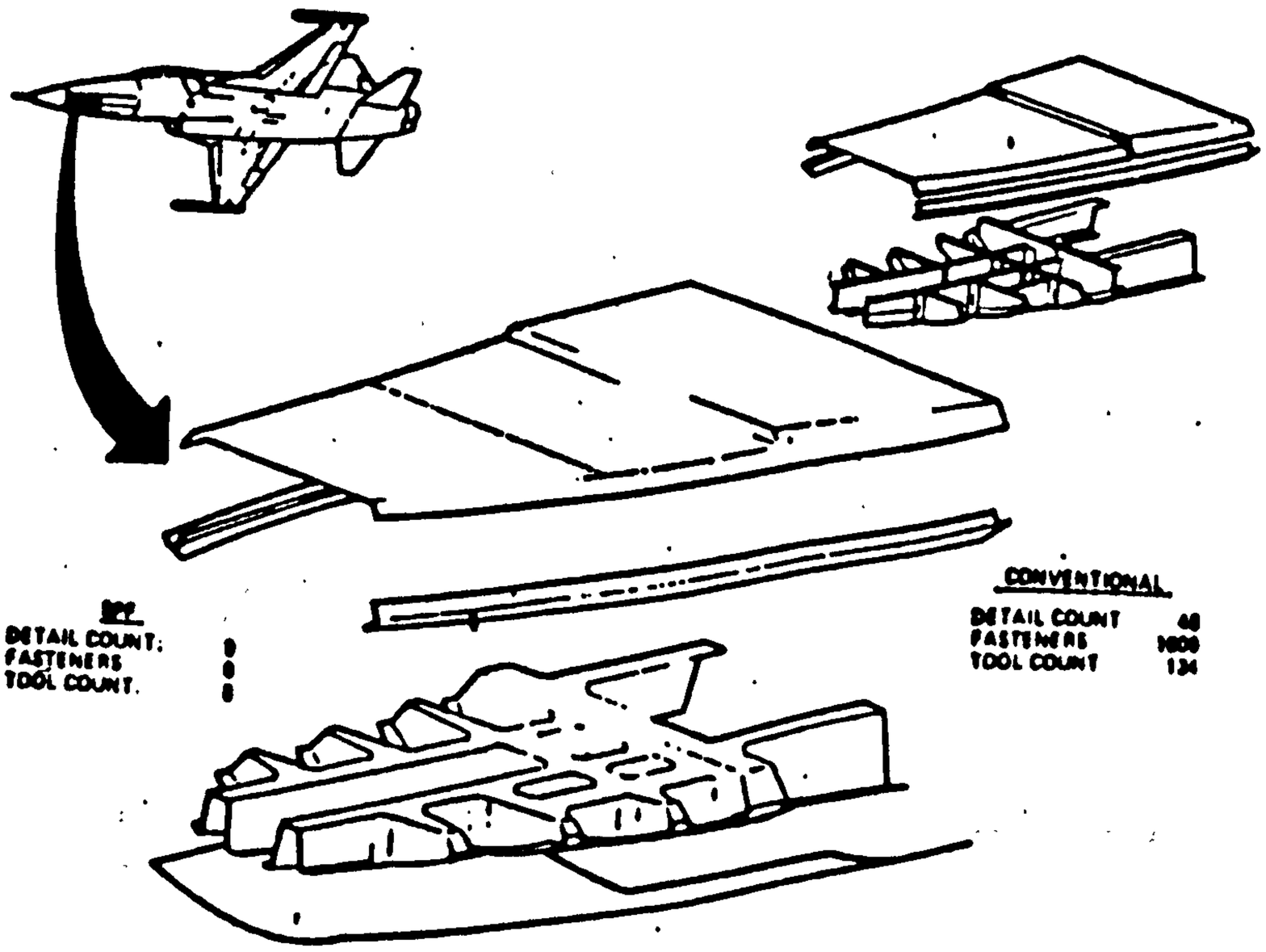

Figure 3 - Potential uses of SPF aluminium in avionics compartment (21).

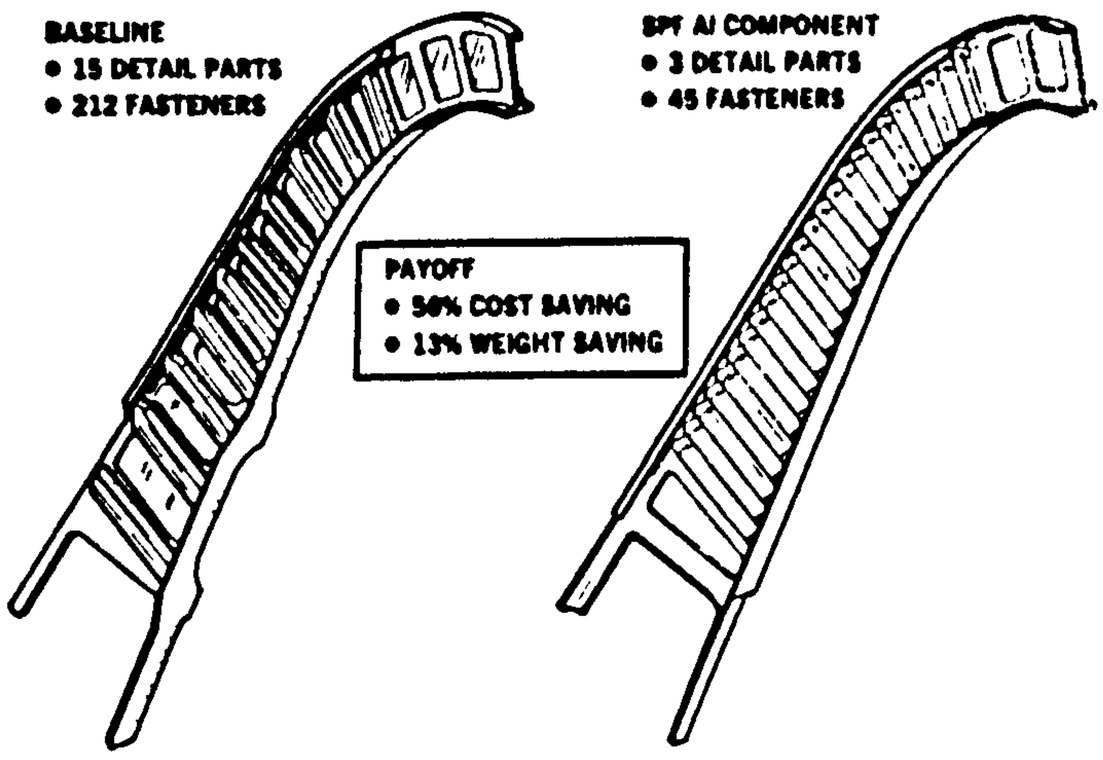

SPF/Al Fuselage Frame

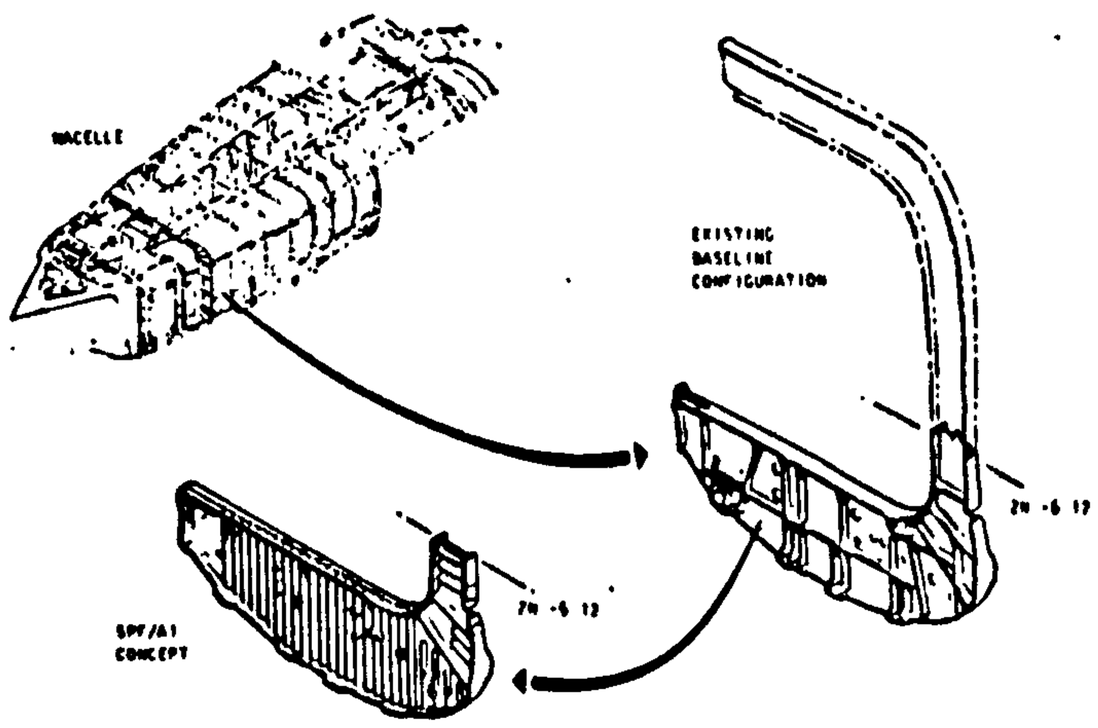

Forward Nacelle Frame - YN 200

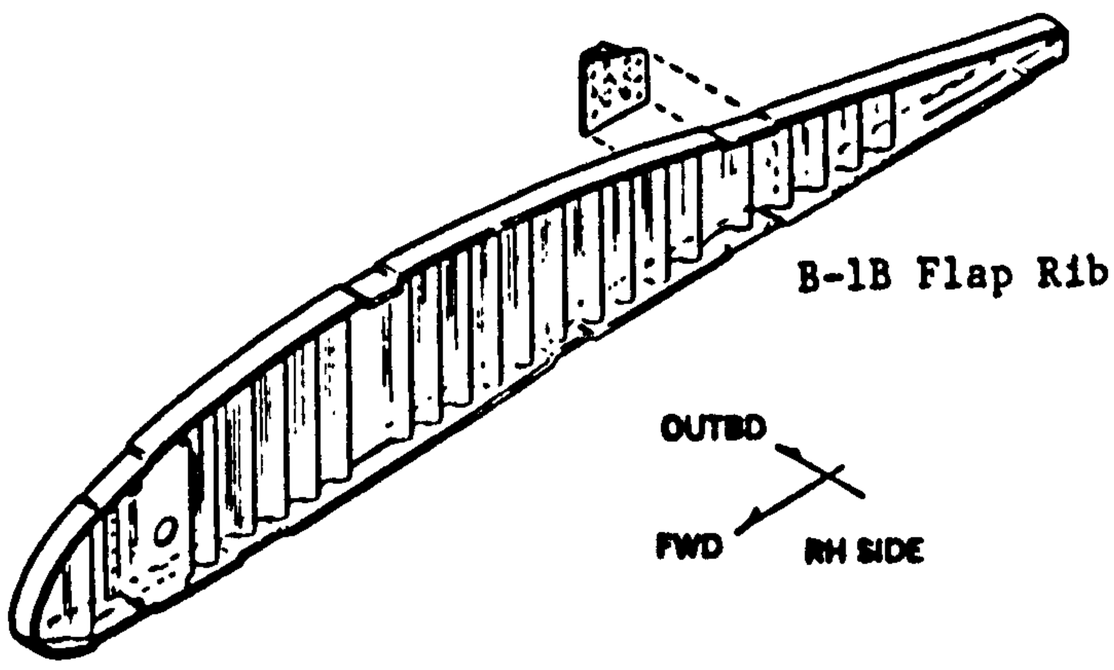

B-1B Flap Rib

Figure 4 - Studies showing the potential of SPF materials in structural applications (22).

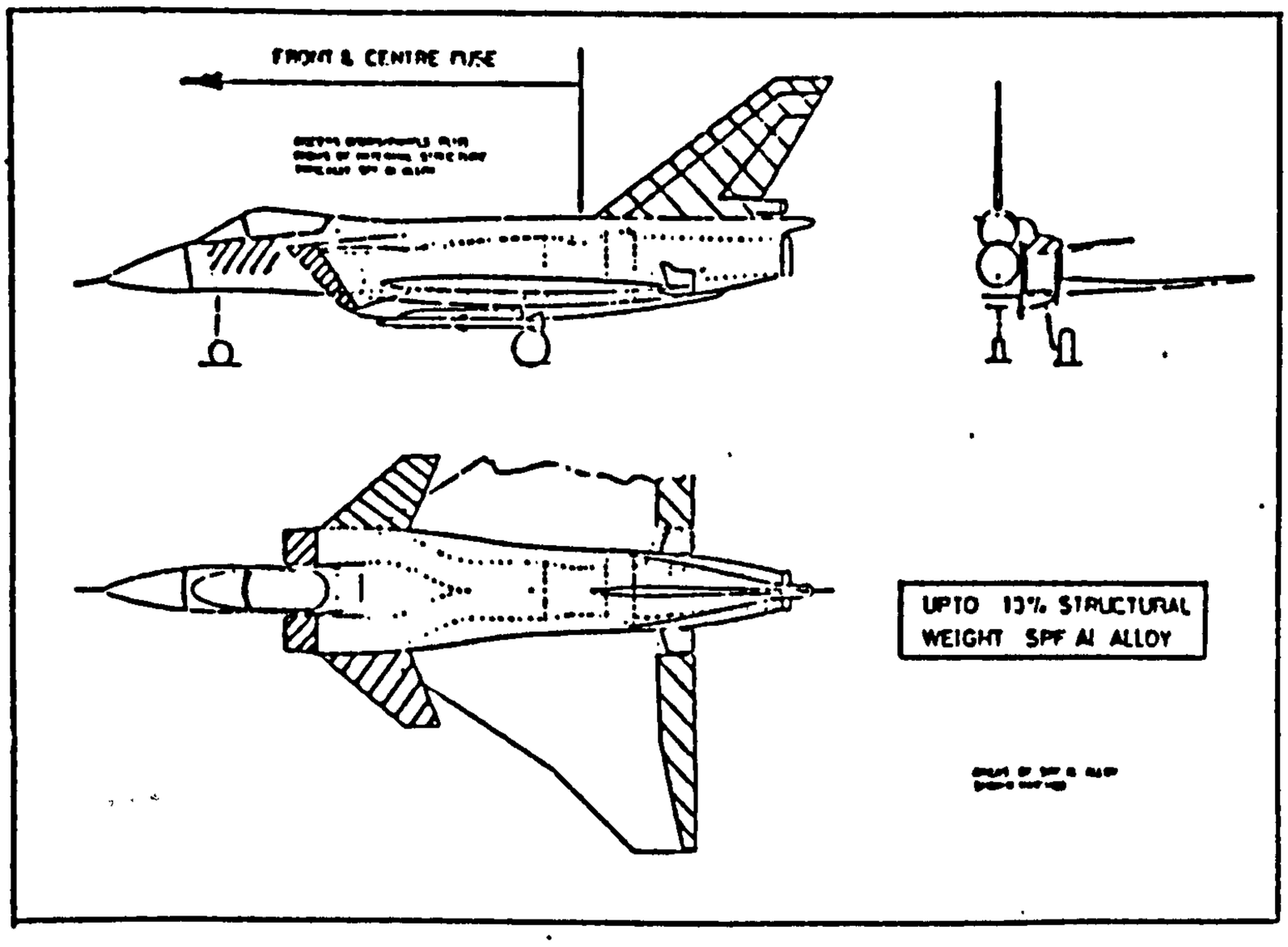

Figure 5 - Predicted areas of SPF usage in Tornado include fins, fore planes, air-intakes etc. (17).

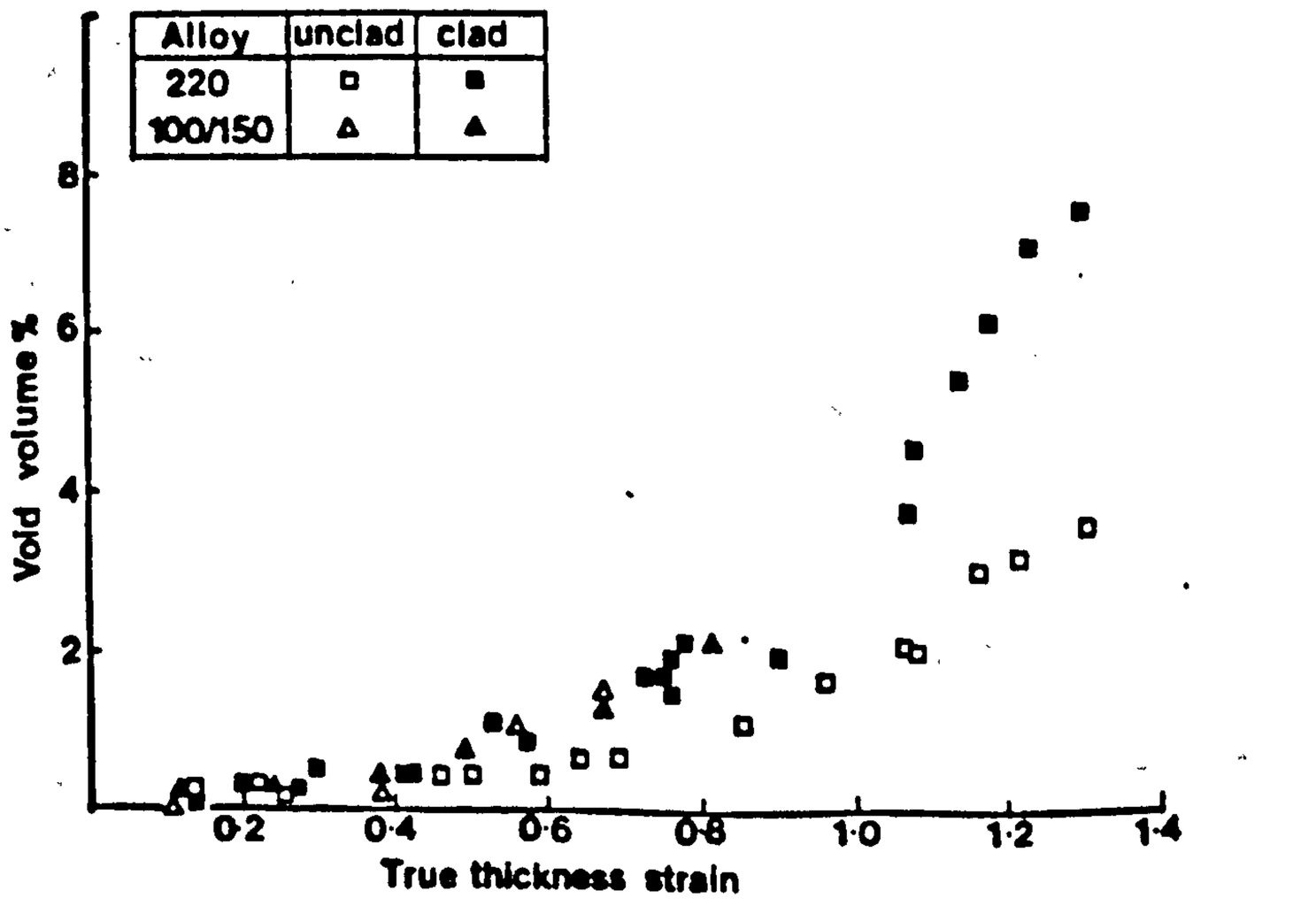

Figure 6 - Effect of superplastic strain on void volume in SUPRAL alloys (32).

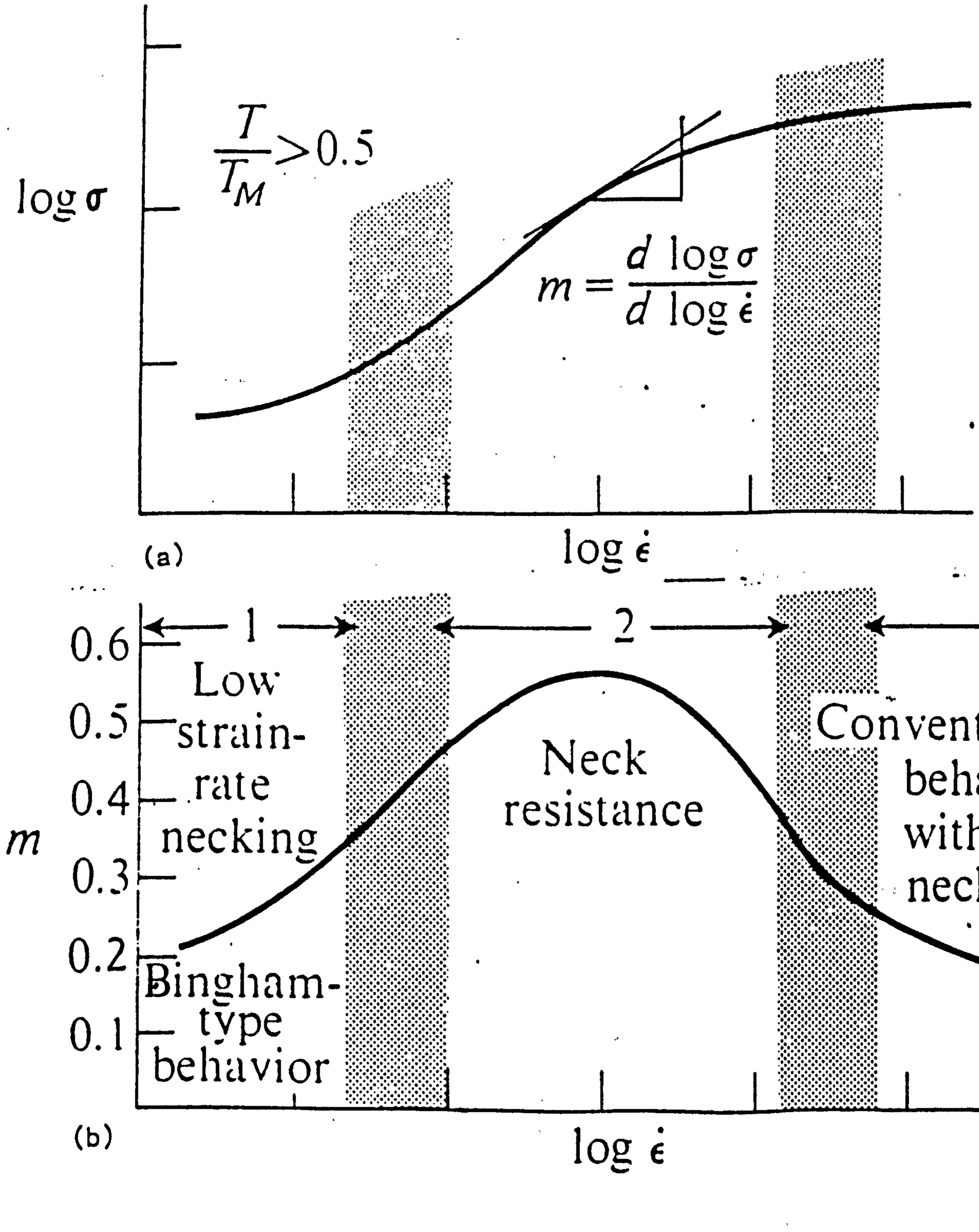

Figure 7(a) - Stress-strain behaviour of SP materials.

Figure 7(b) - Strain-rate sensitivity versus strain-rate for a SP material.

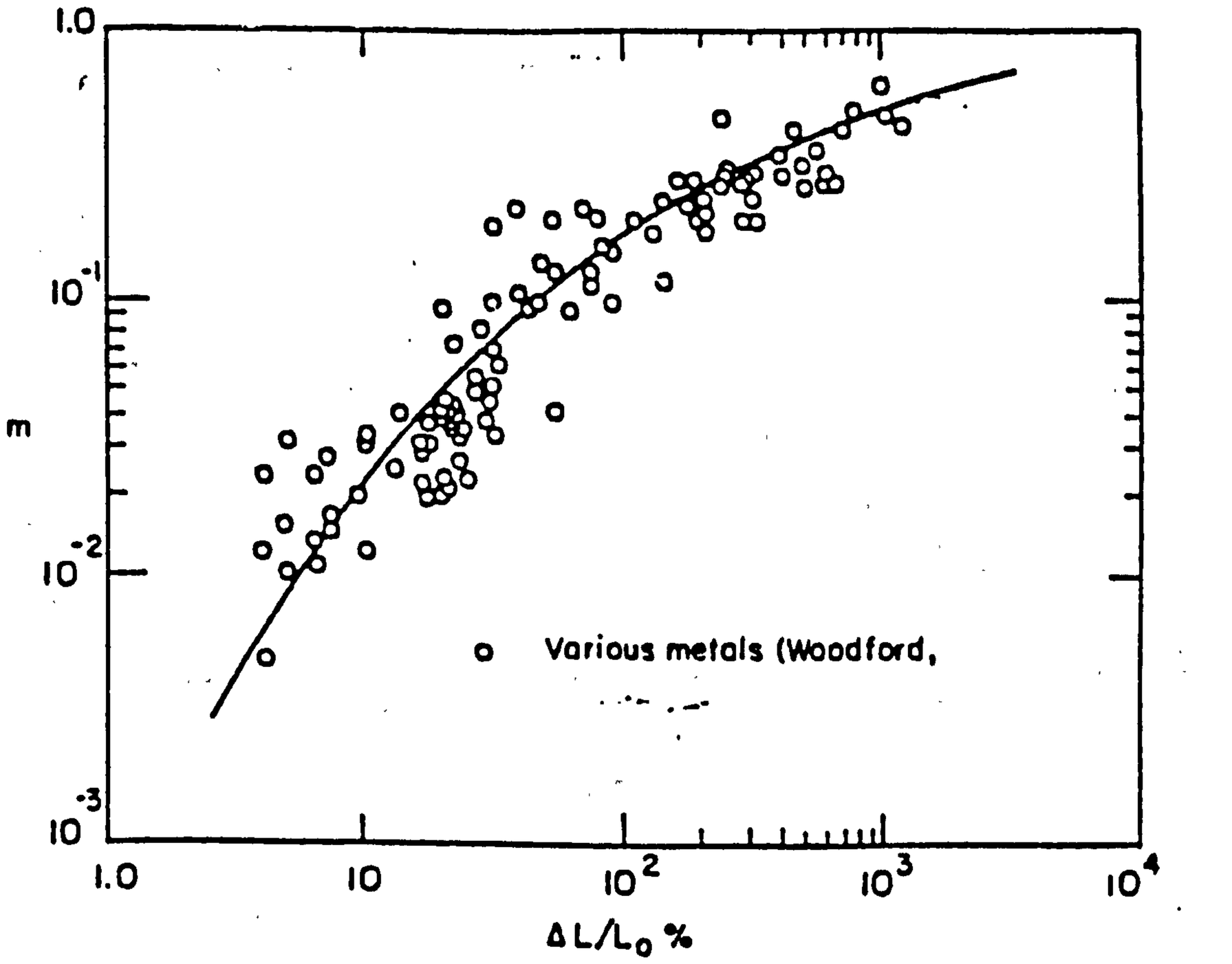

Figure 8 - Woodford's classic graph of m versus elongation for SP metals (80).

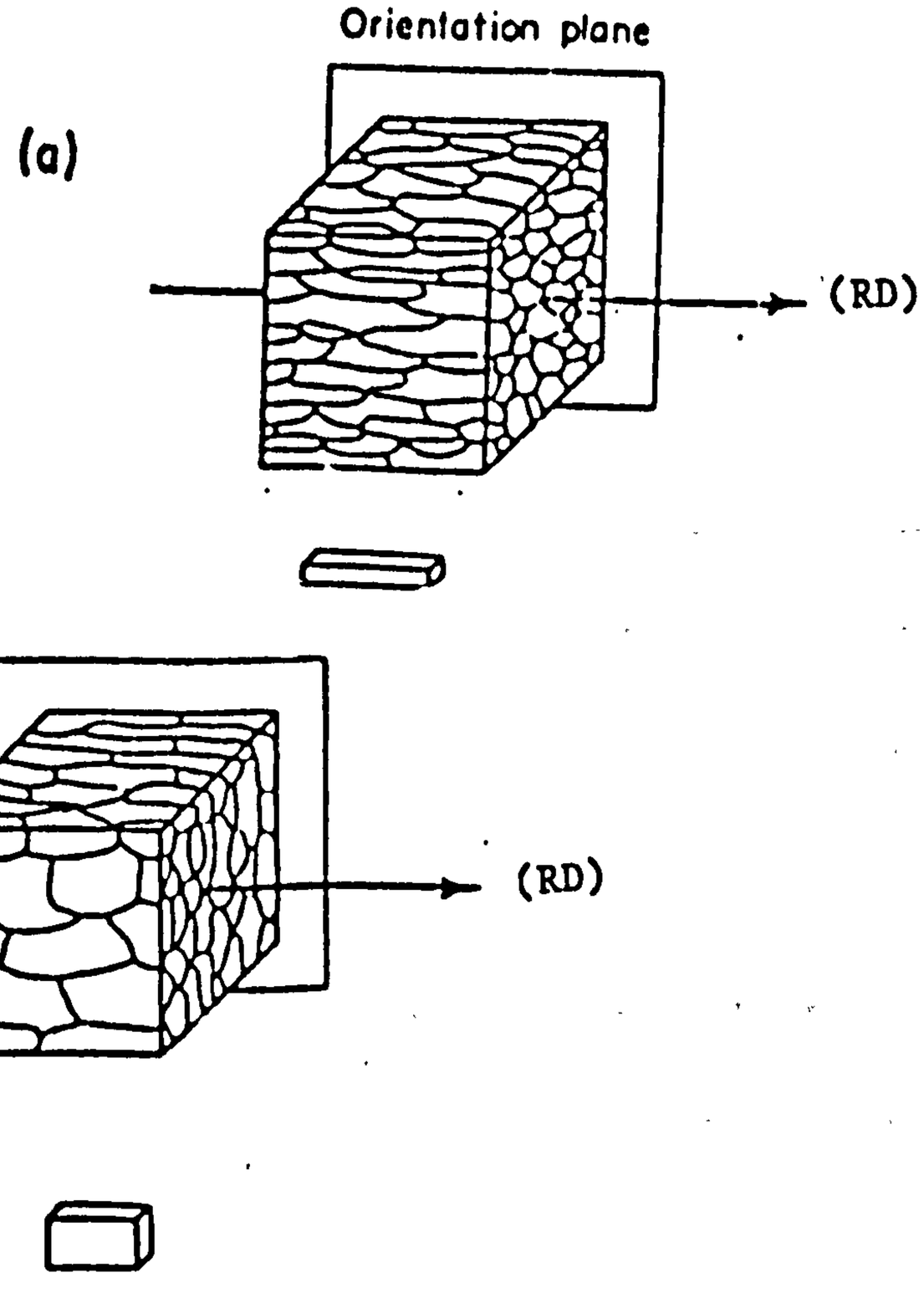

Figure 9 - Initial grain structures in worked materials; generally, 9a results from extrusion or swaging and 9b from rolling processes (84).

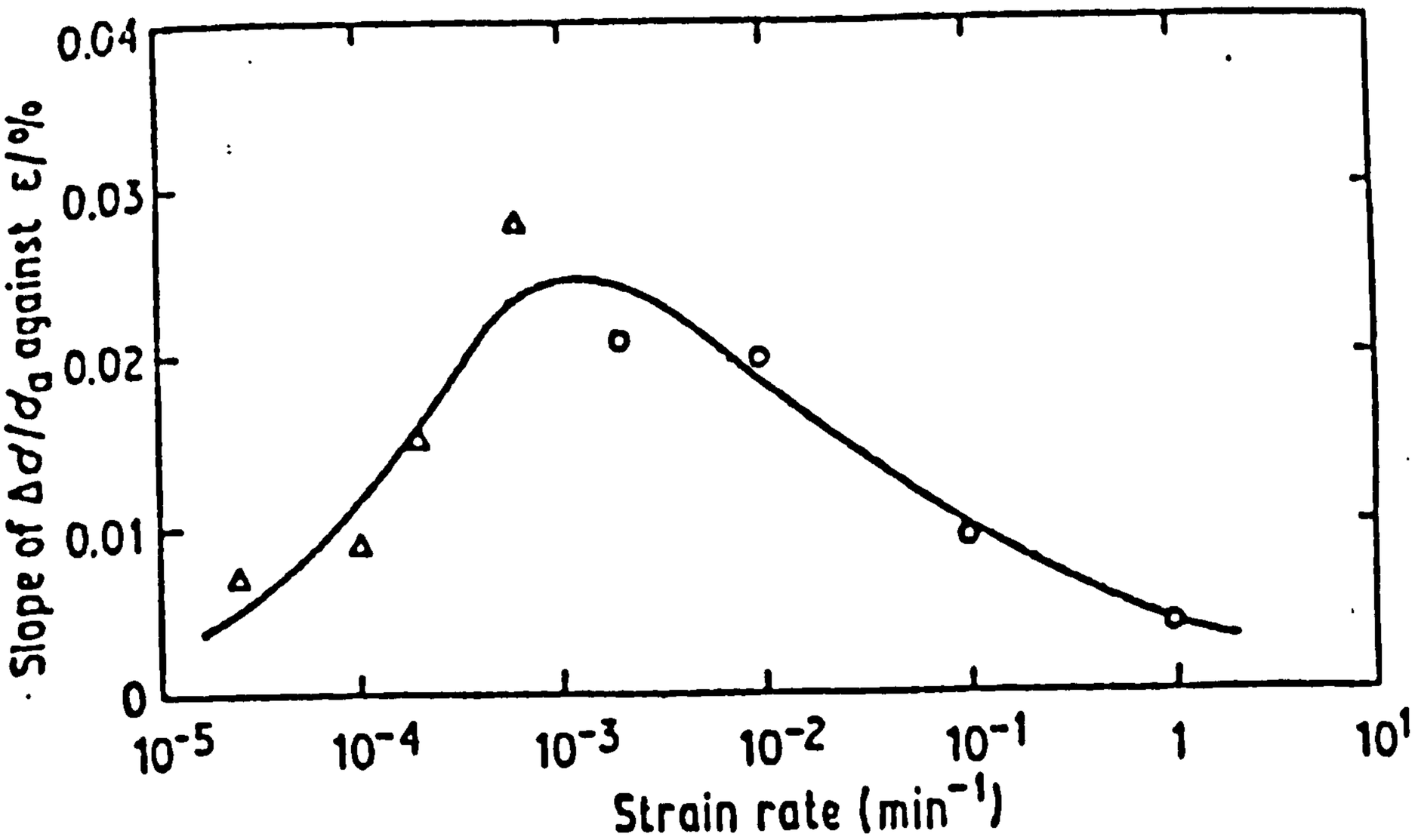

Figure 10 - The variation of the 'grain enhancement' parameter (ℓn Δd/da) increases with strain, reaching a maximum at intermediate strain-rates (89).

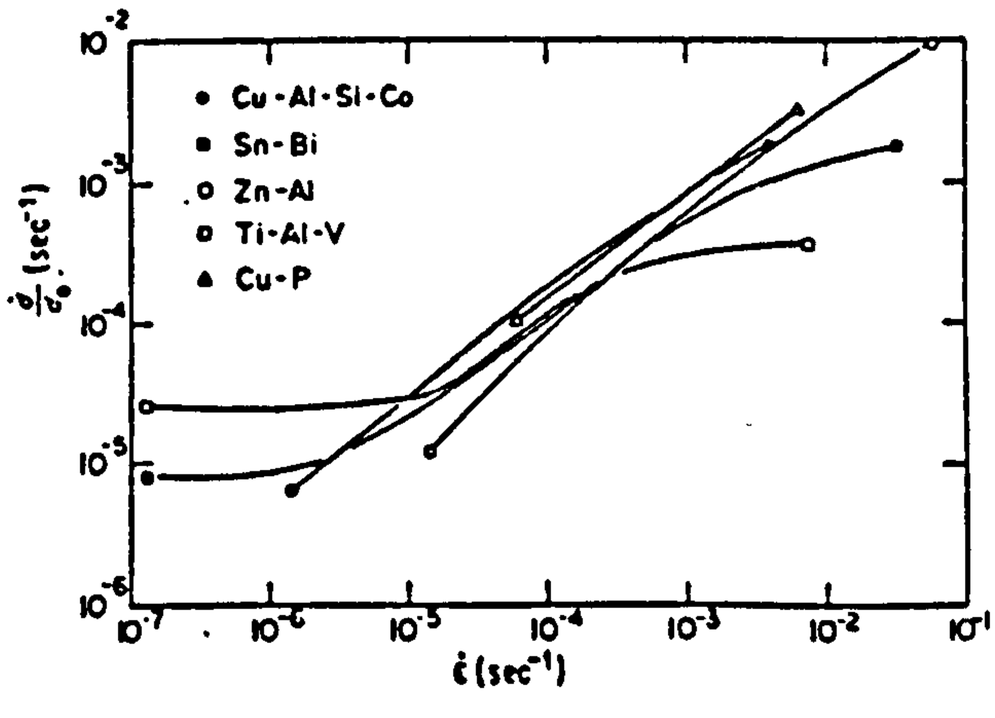

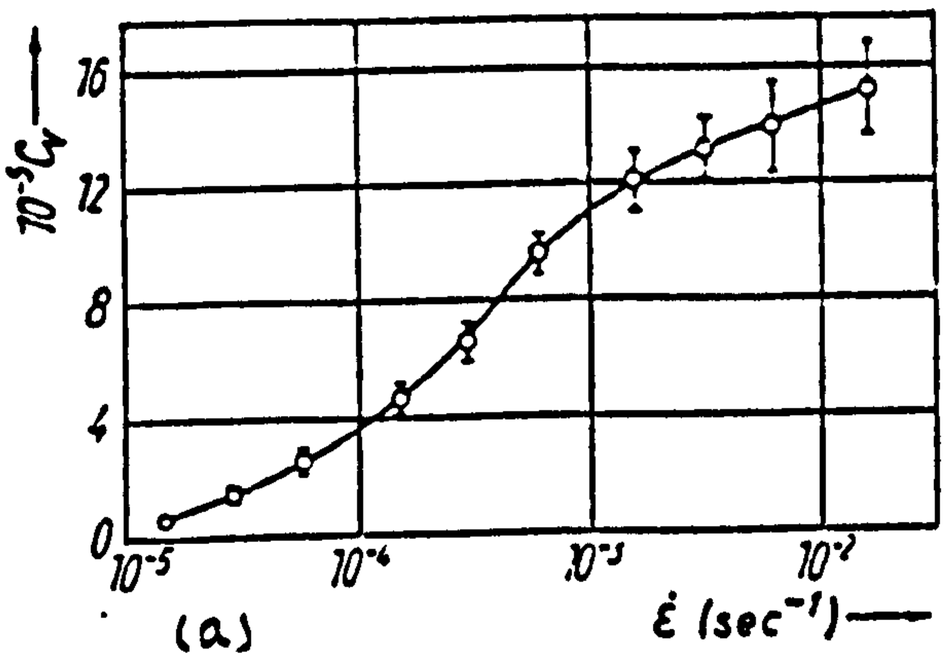

Figure 11 - Shows how the grain growth due to deformation increases with larger strain-rates for various materials (90).

Figure 11a- The strain-rate dependence of excess vacancies, ΔC_v in Zn - 0.4% Al alloy (90)

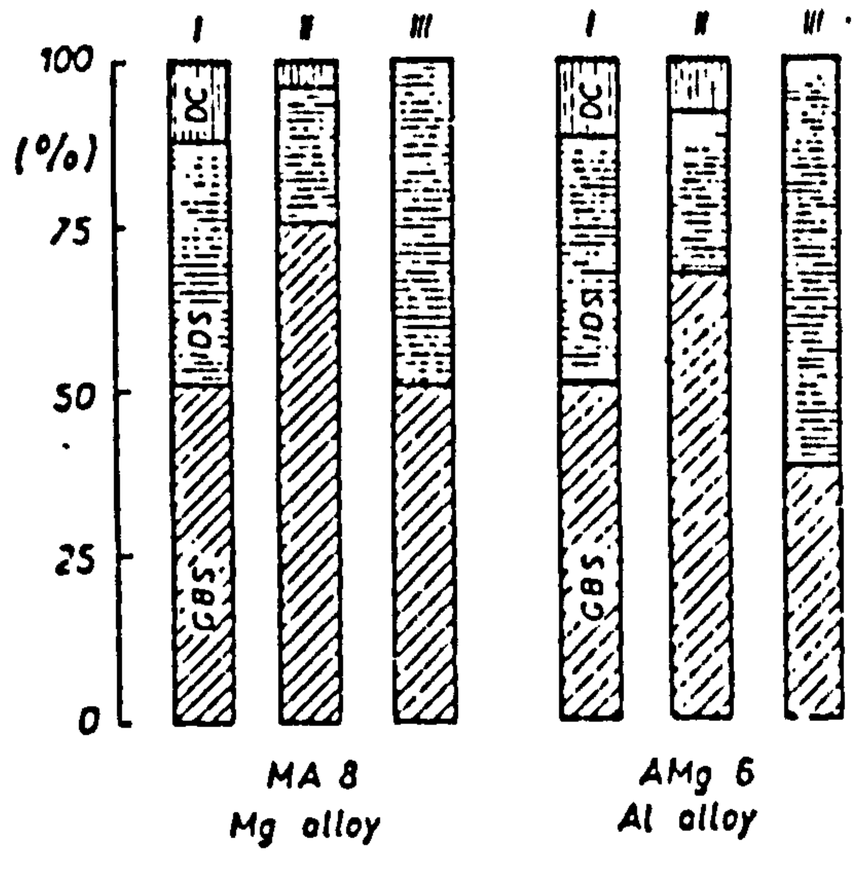

Figure 12 - Contributions of grain boundary sliding (GBS), intragranular dislocation slip (IDS) and diffusion creep(DC) to deformation of two alloys (84).

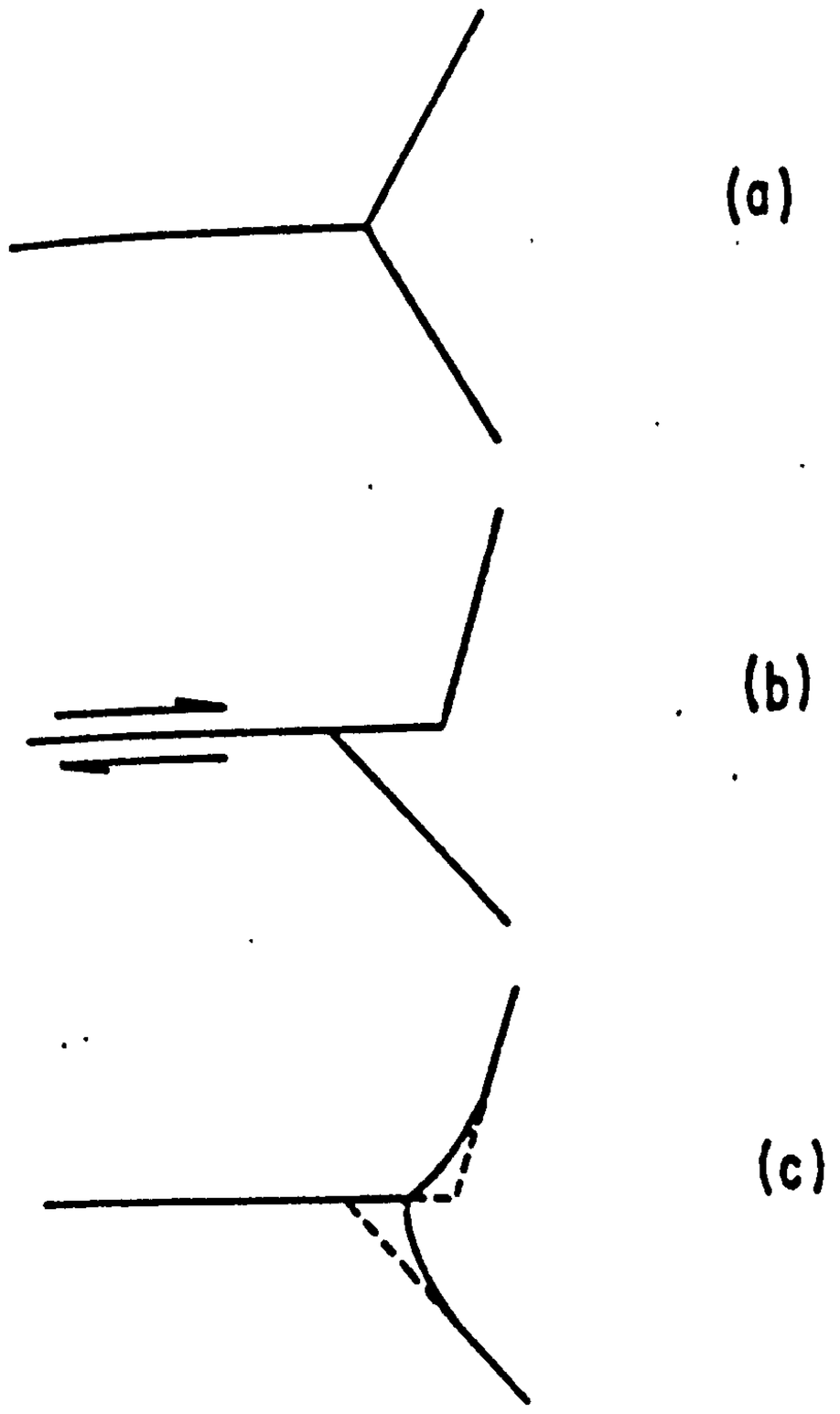

Figure 13 - Schematic diagram showing the mechanism by which the boundaries become curved; (a) initial state, (b) after sliding (c) after separation at triple points (96).

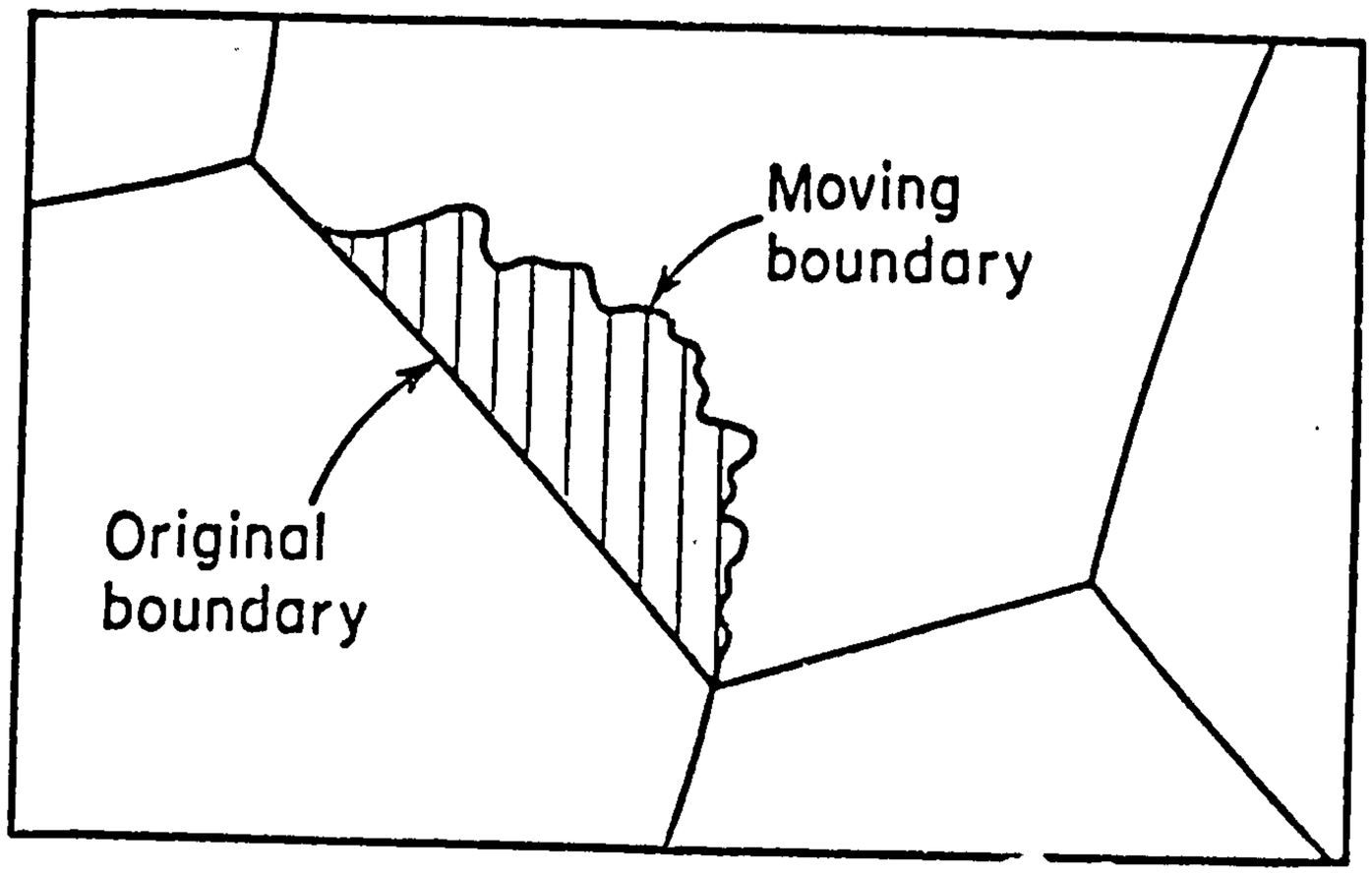

Figure 14 - Schematic representation of strain-induced boundary migration (97).

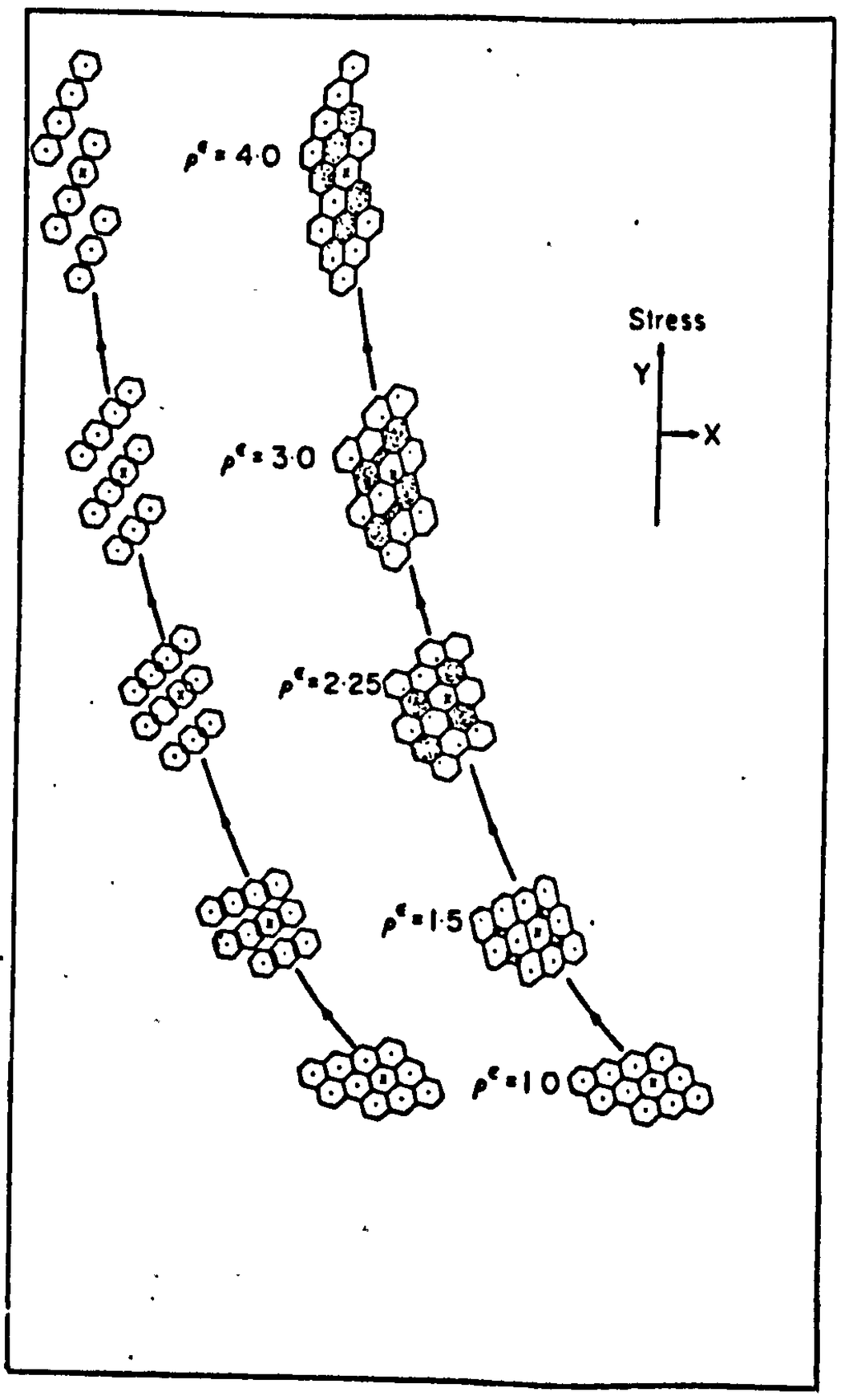

Figure 15 - Sequence for three dimensional grain re-arrangement (101).

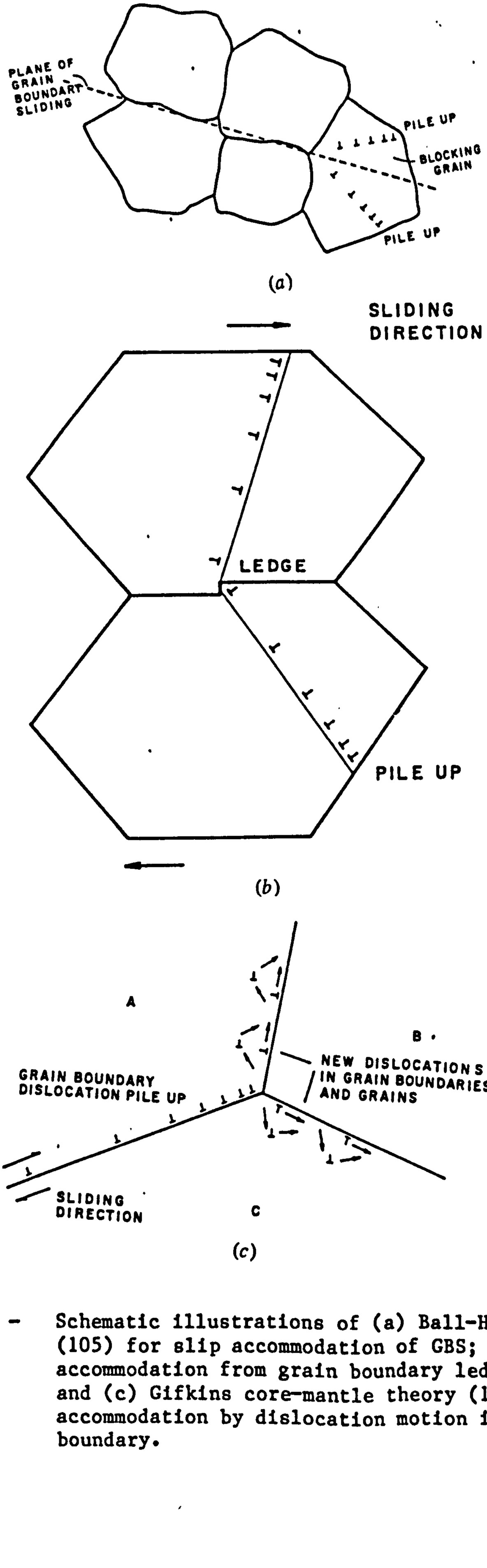

Figure 16 - Schematic illustrations of (a) Ball-Hutchison model (105) for slip accommodation of GBS; (b) Slip accommodation from grain boundary ledges, Mukerjee (106) and (c) Gifkins core-mantle theory (107) with accommodation by dislocation motion in and near grain boundary.

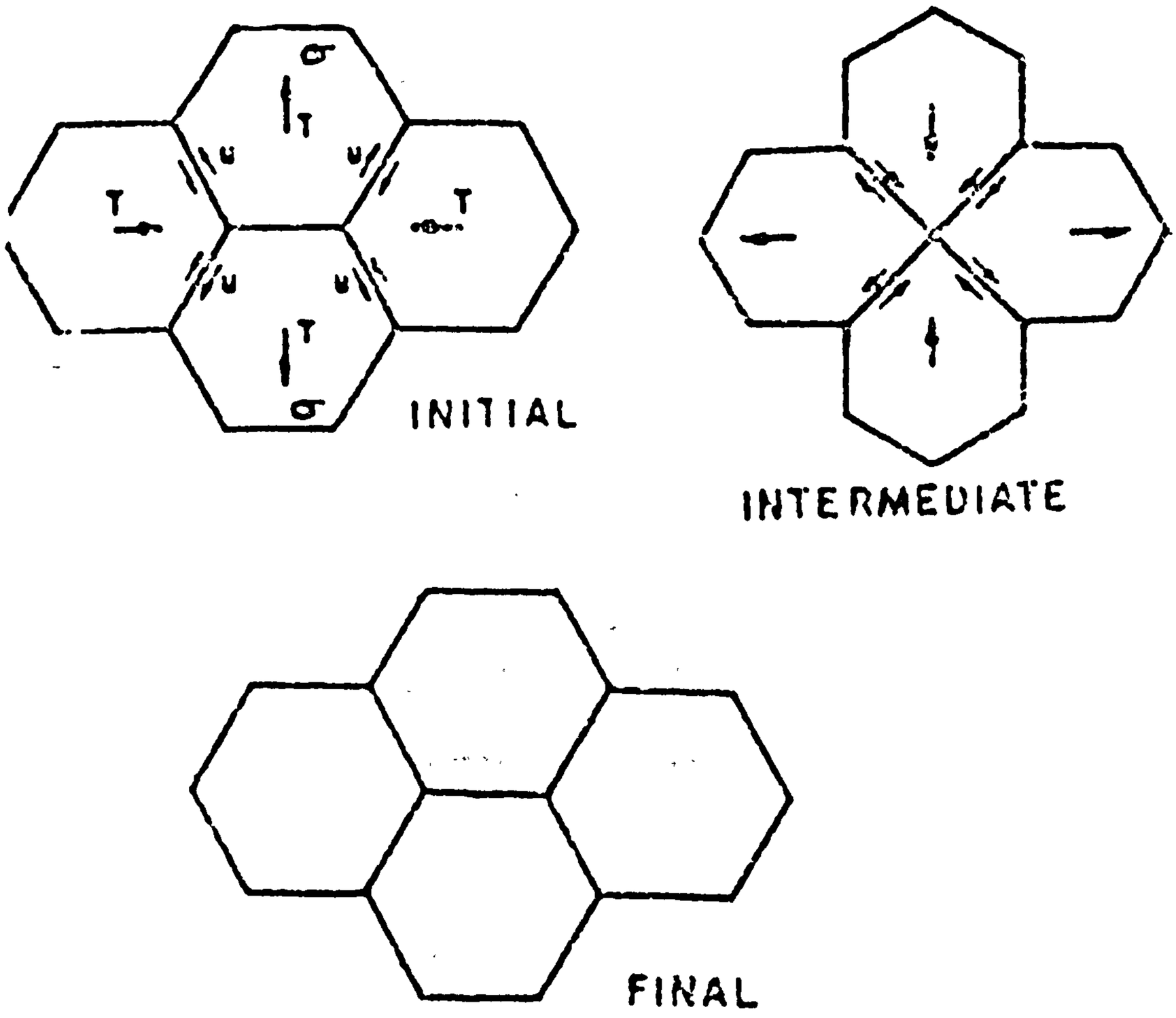

Figure 17 - Illustration of Ashby-Verrall (108) grain switching mechanism.

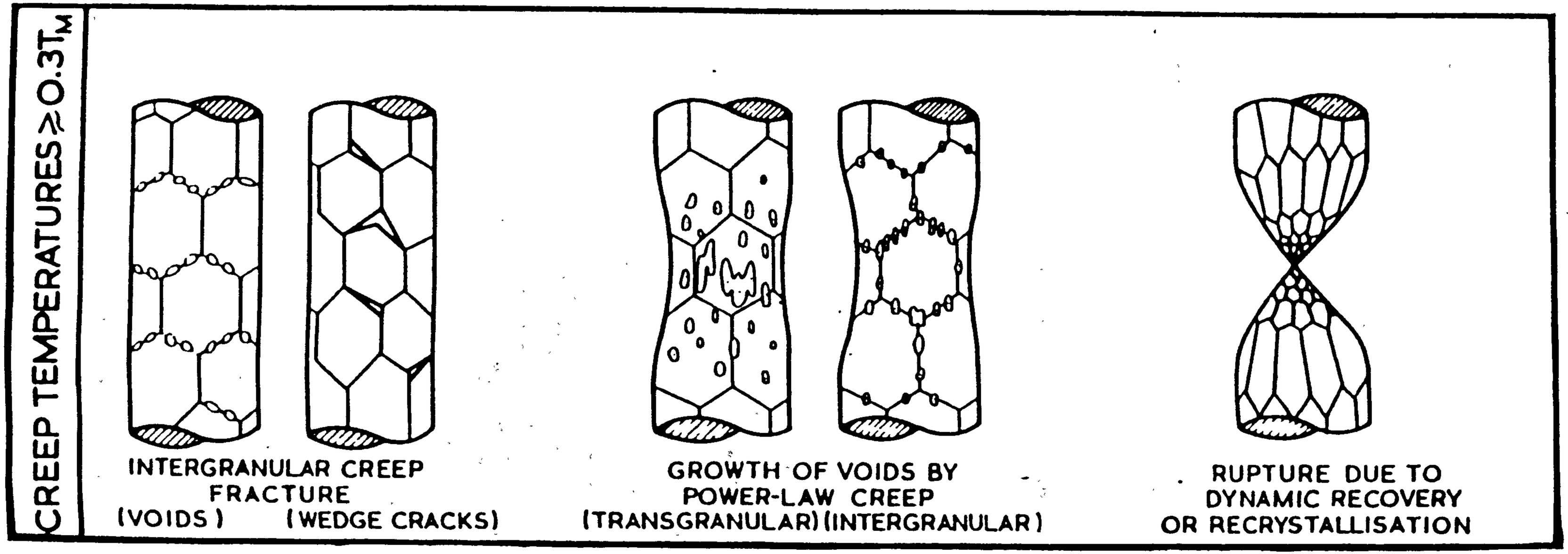

Figure 18 - Fracture mechanism classification at T > 0.3Tm (110).

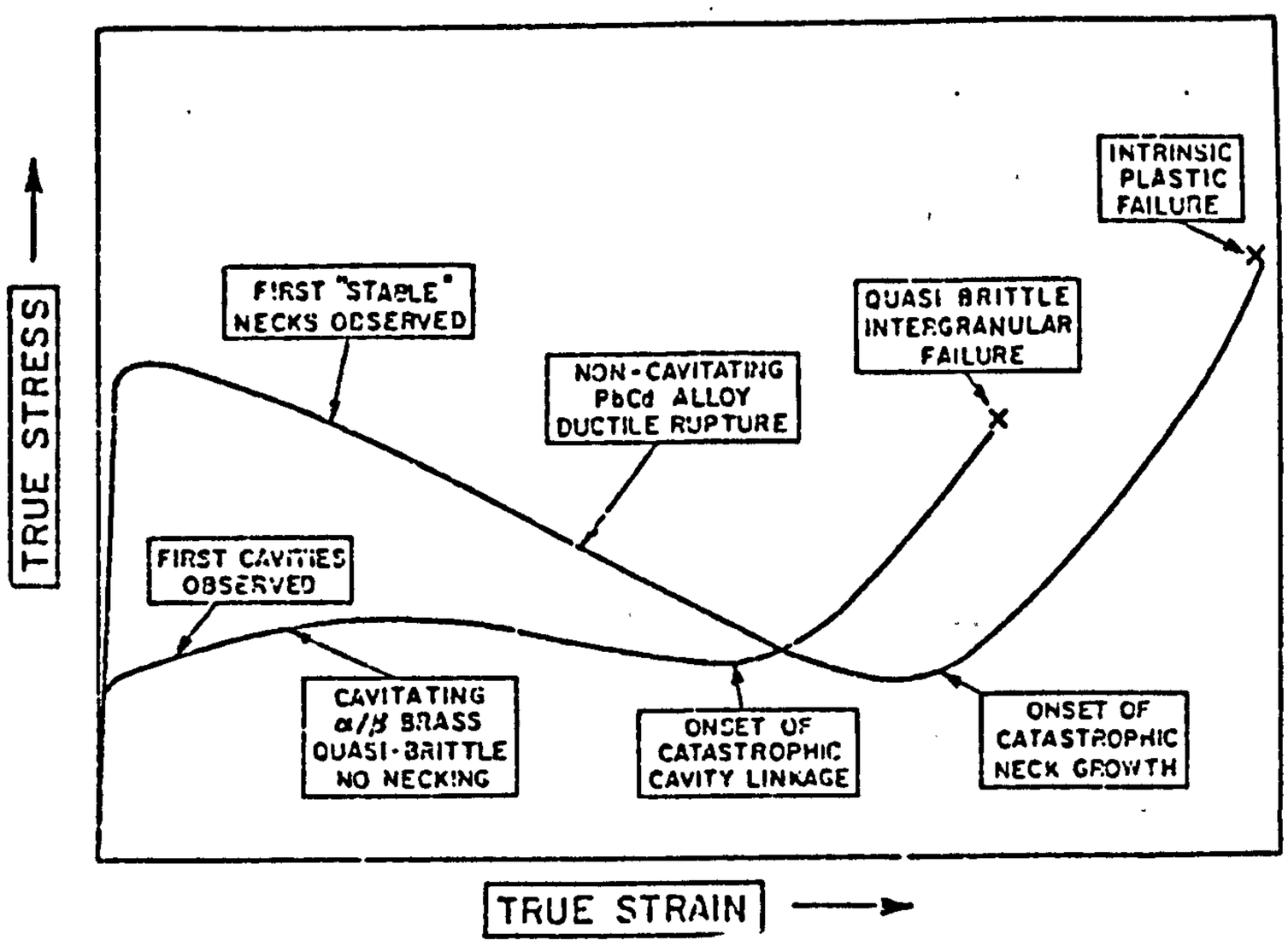

Figure 19 - Schematic stress-strain curves for two types of SP materials - a ductile PbCd and a quasi-brittle α/β brass.

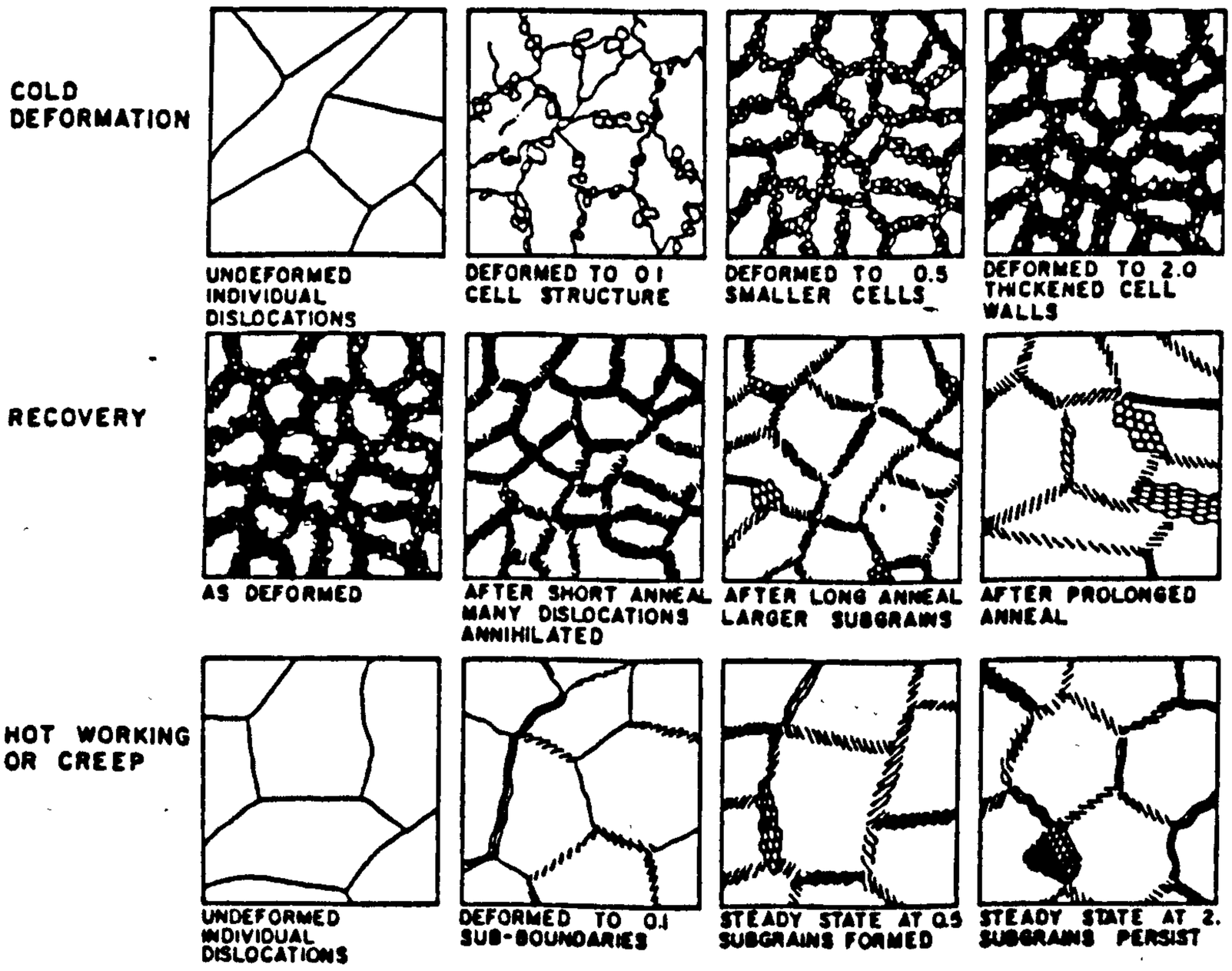

Figure 20 - Illustrations of the role of substructure under different conditions.

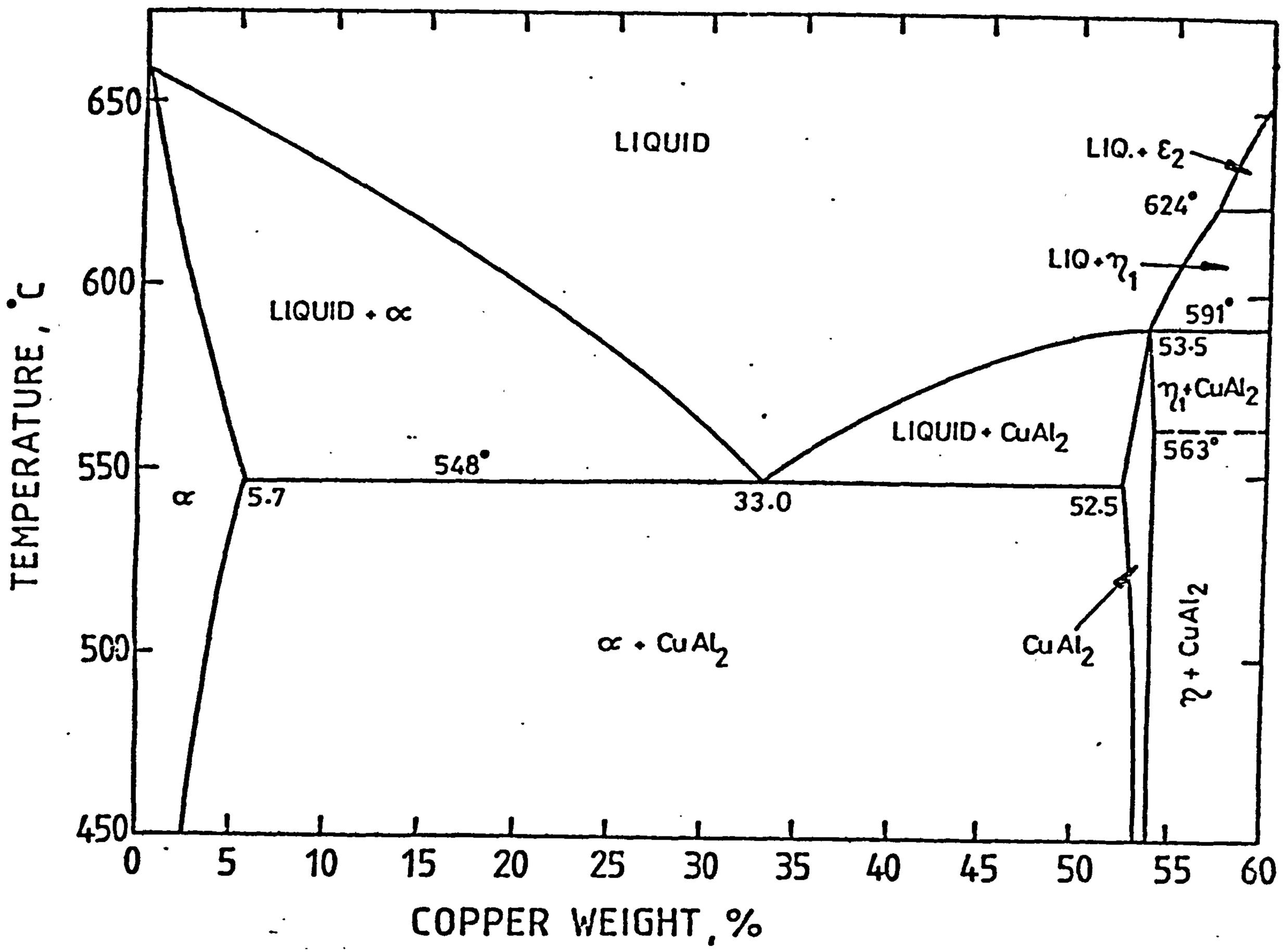

Figure 21 – The aluminium end of the Aluminium – Copper equilibrium diagram.

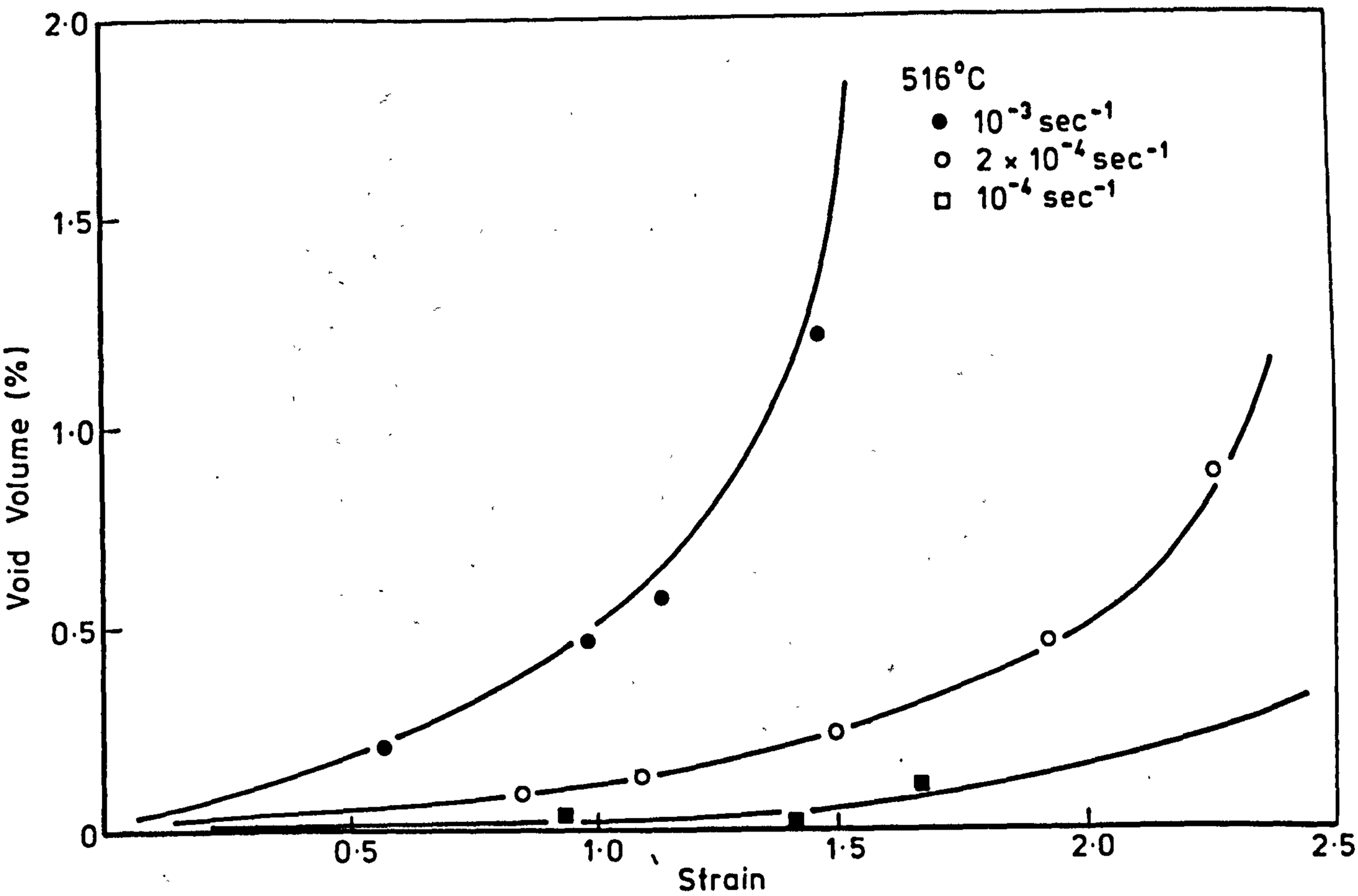

Figure 22 - Dependence of cavitation on strain as observed by Ghosh in reference 23.

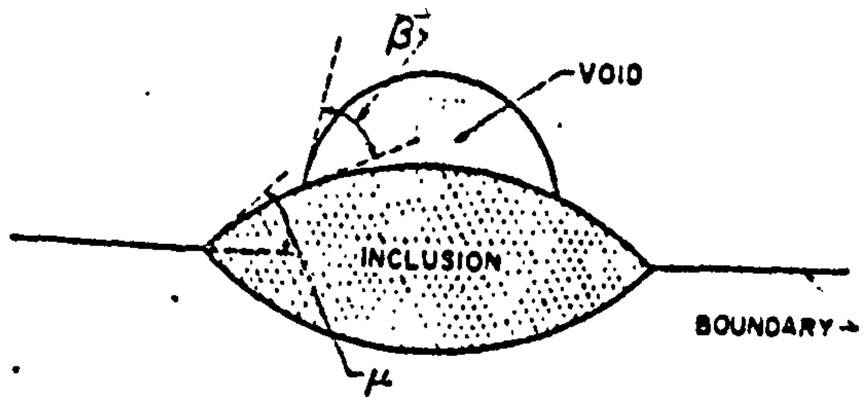

Figure 22(a)- Cavities nucleated at inclusions on a grain boundary after Raj and Ashby.

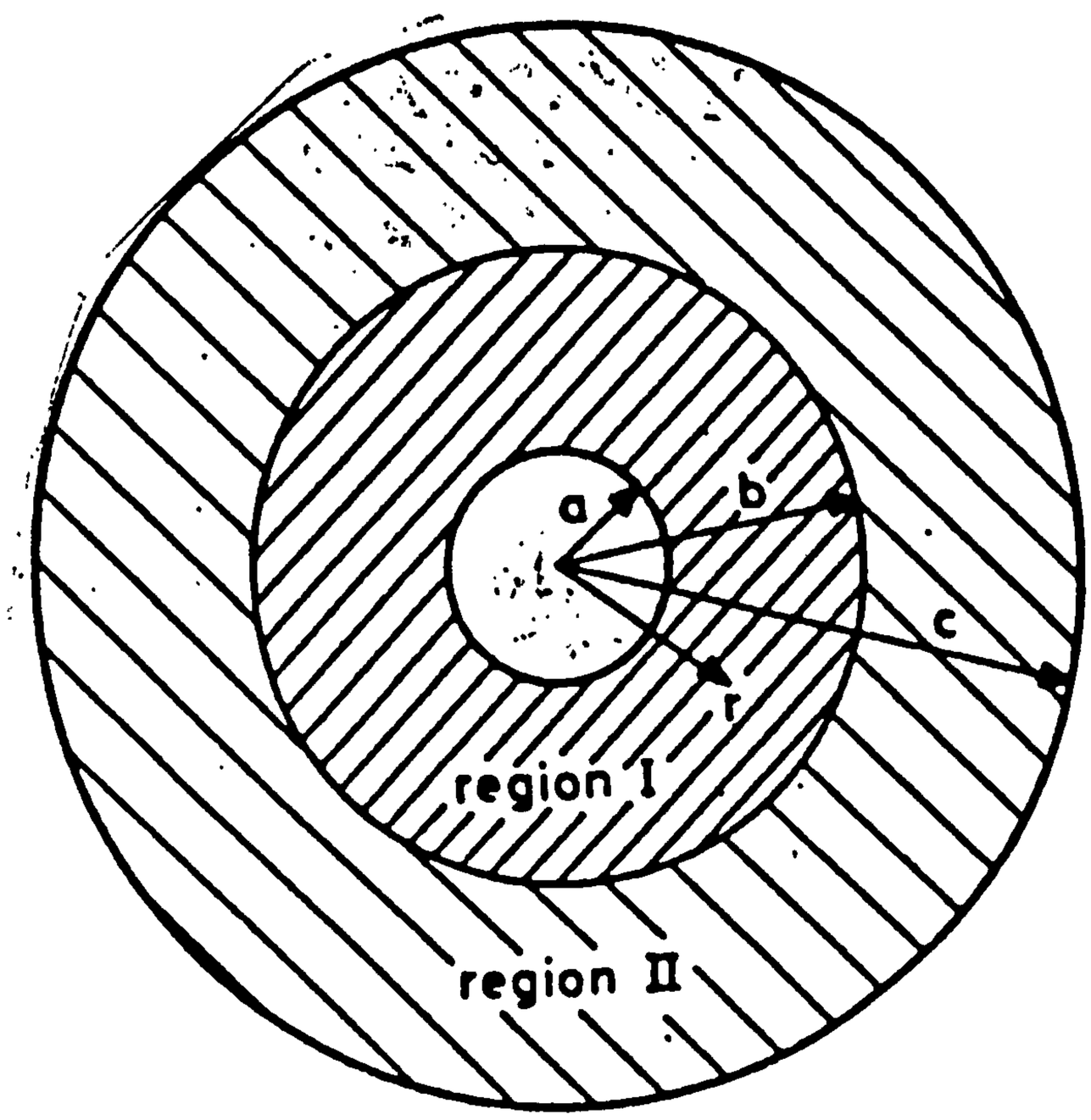

Figure 23 - Geometry of cavity radius a, residing on a grain boundary (viewed normal to the boundary). The mean cavity spacing in the boundary is 2c

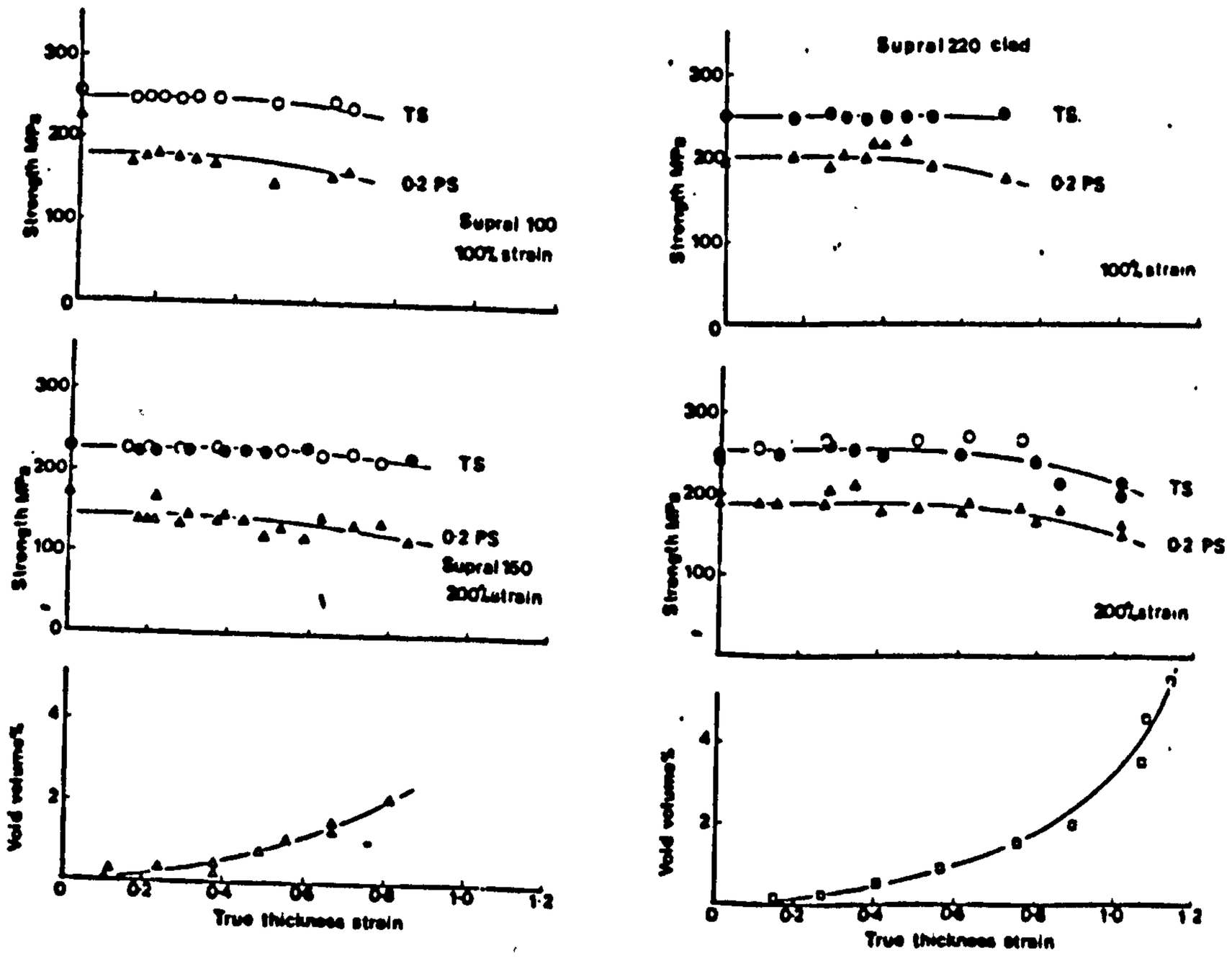

Figure 24 - Effect of SP strain and cavitation on the as-formed tensile properties of Supral 100, 150 and 220 (32). [Shaded L, unshaded T directions].

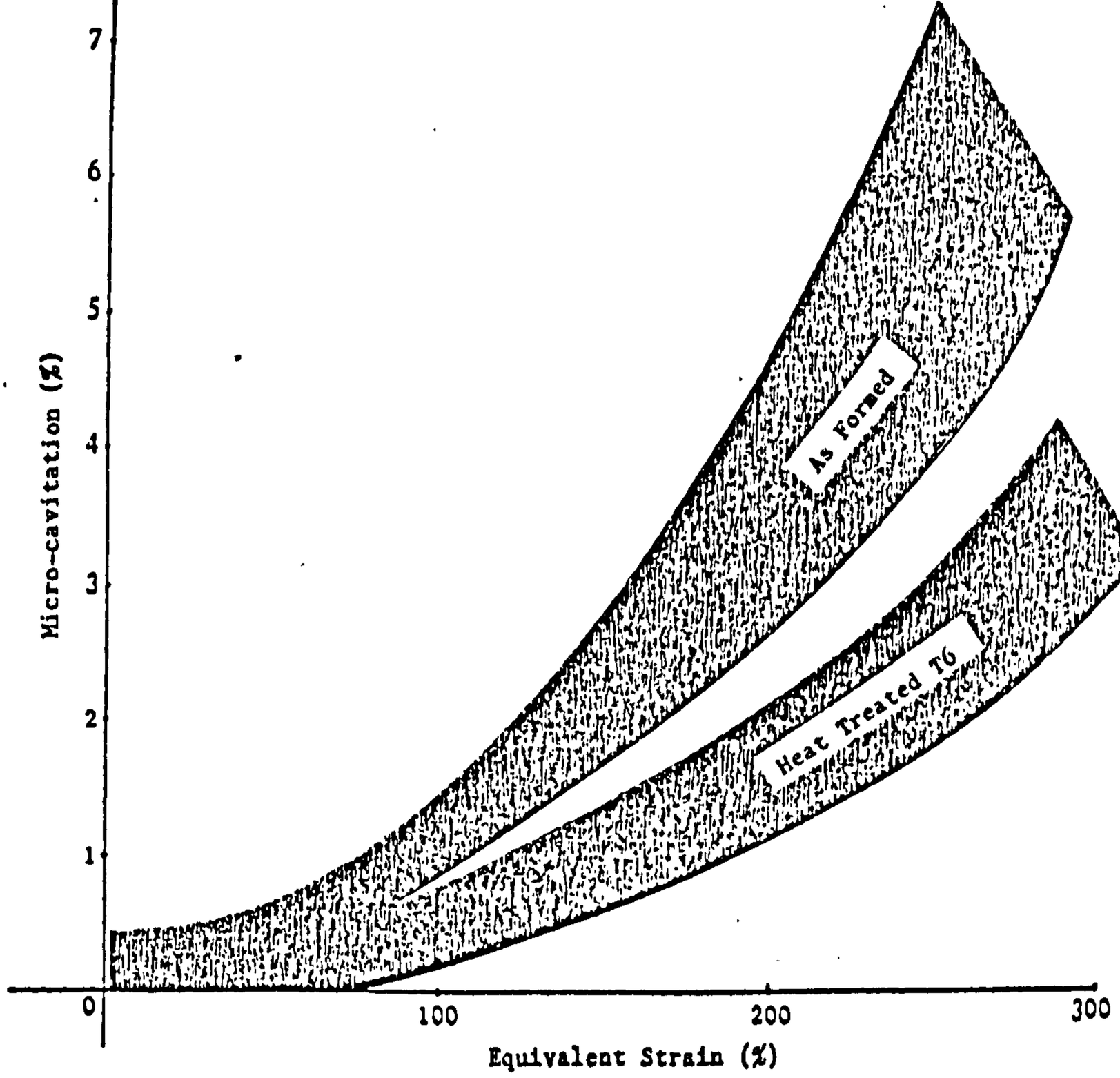

Figure 25 - The effect of heat treatment on micro-cavitation level in SUPRAL alloys (19).

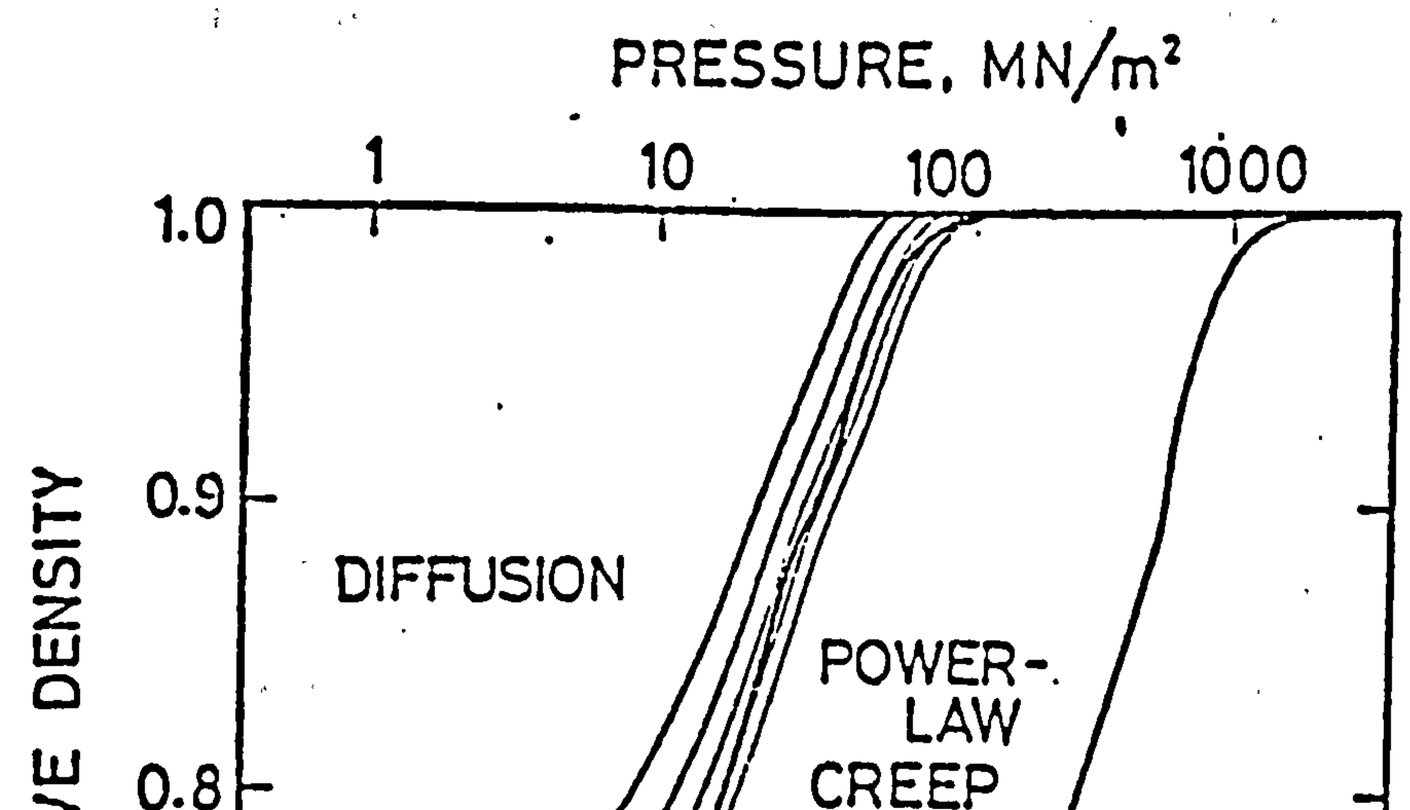

Figure 26 - Typical HIP densification diagram after Ashby (135).

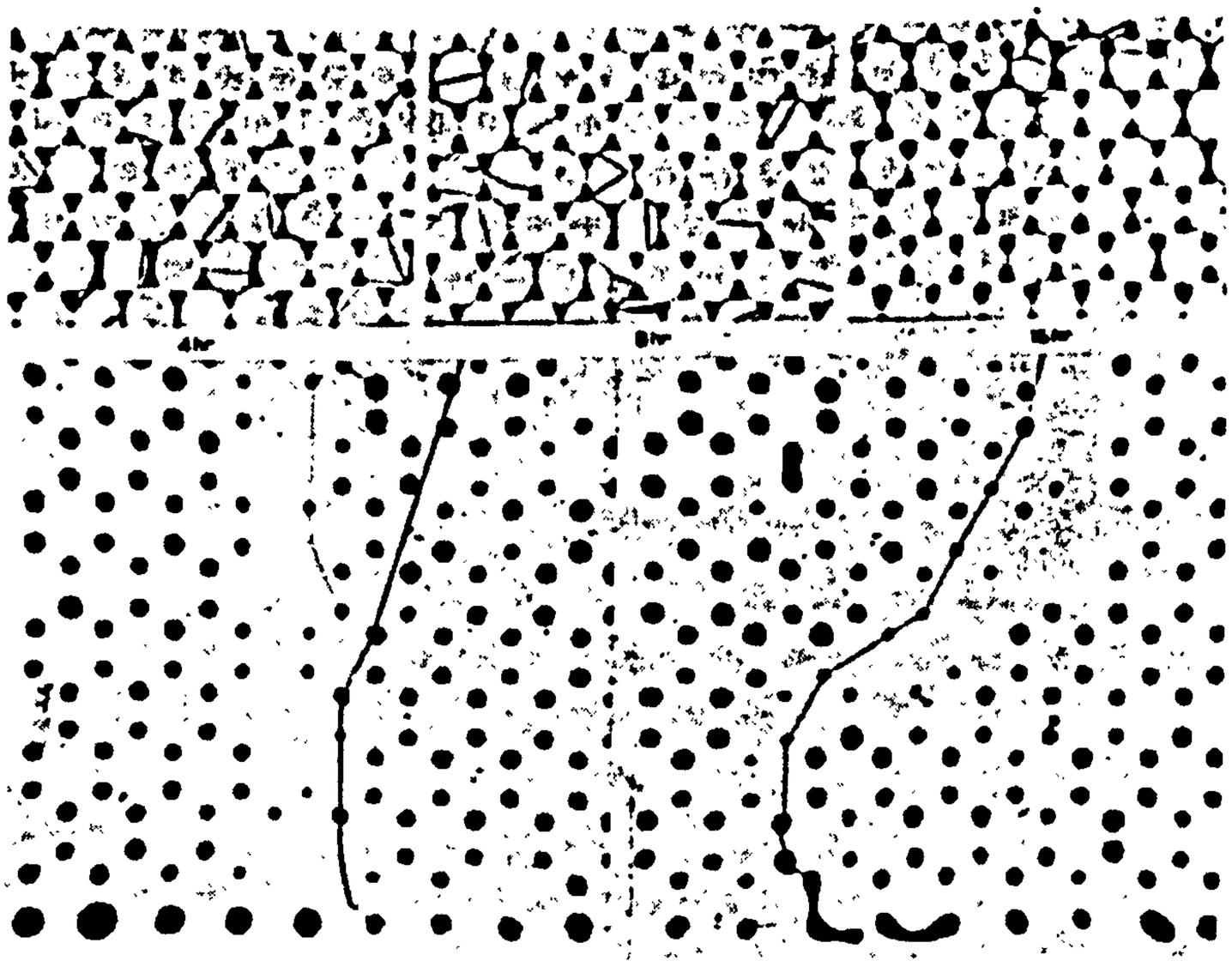

Figure 27 - The role of grain boundaries in pore shrinkage illustrated by studies of filling of interstices of fine copper wires. The lower figure illustrates less porosity around grain boundaries (138).

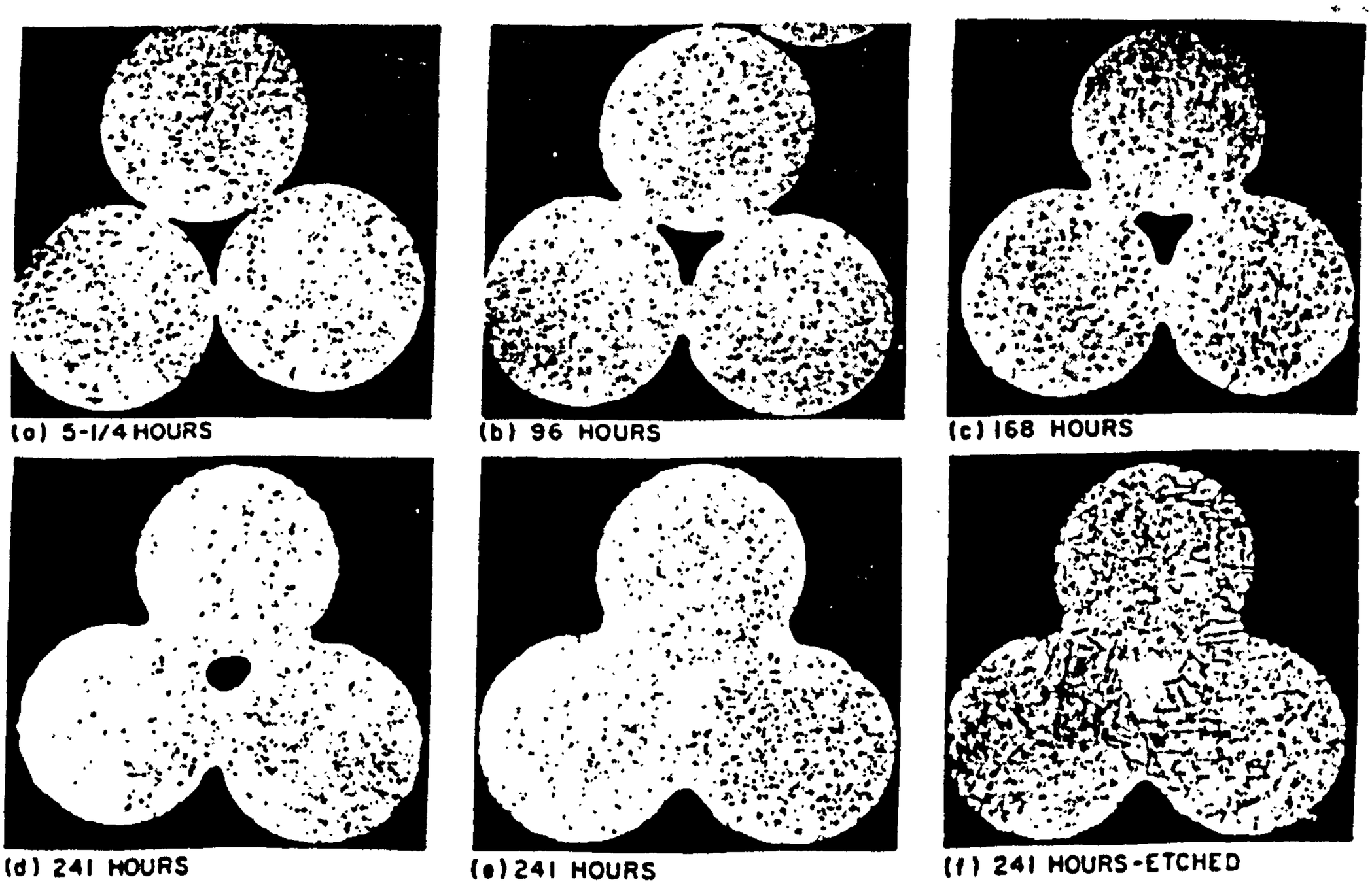

Figure 28 - The mechanism of sintering by diffusion processes in Ni - 2% Alumina alloy. Note how the original particle distribution is not preserved (140).

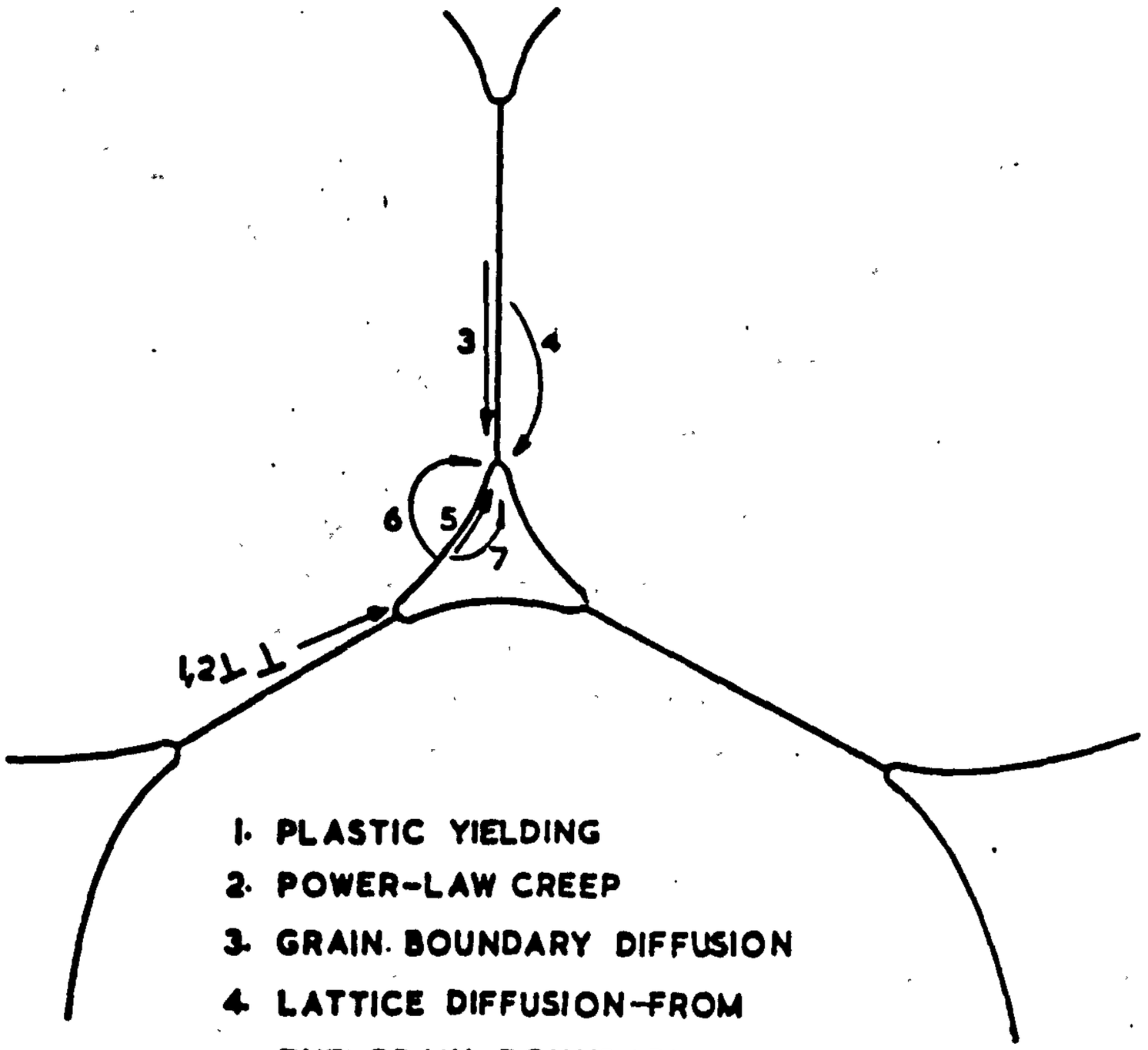

Figure 29 - Mechanisms which contribute to sintering during stage 1 densification in powder metallurgy (137).

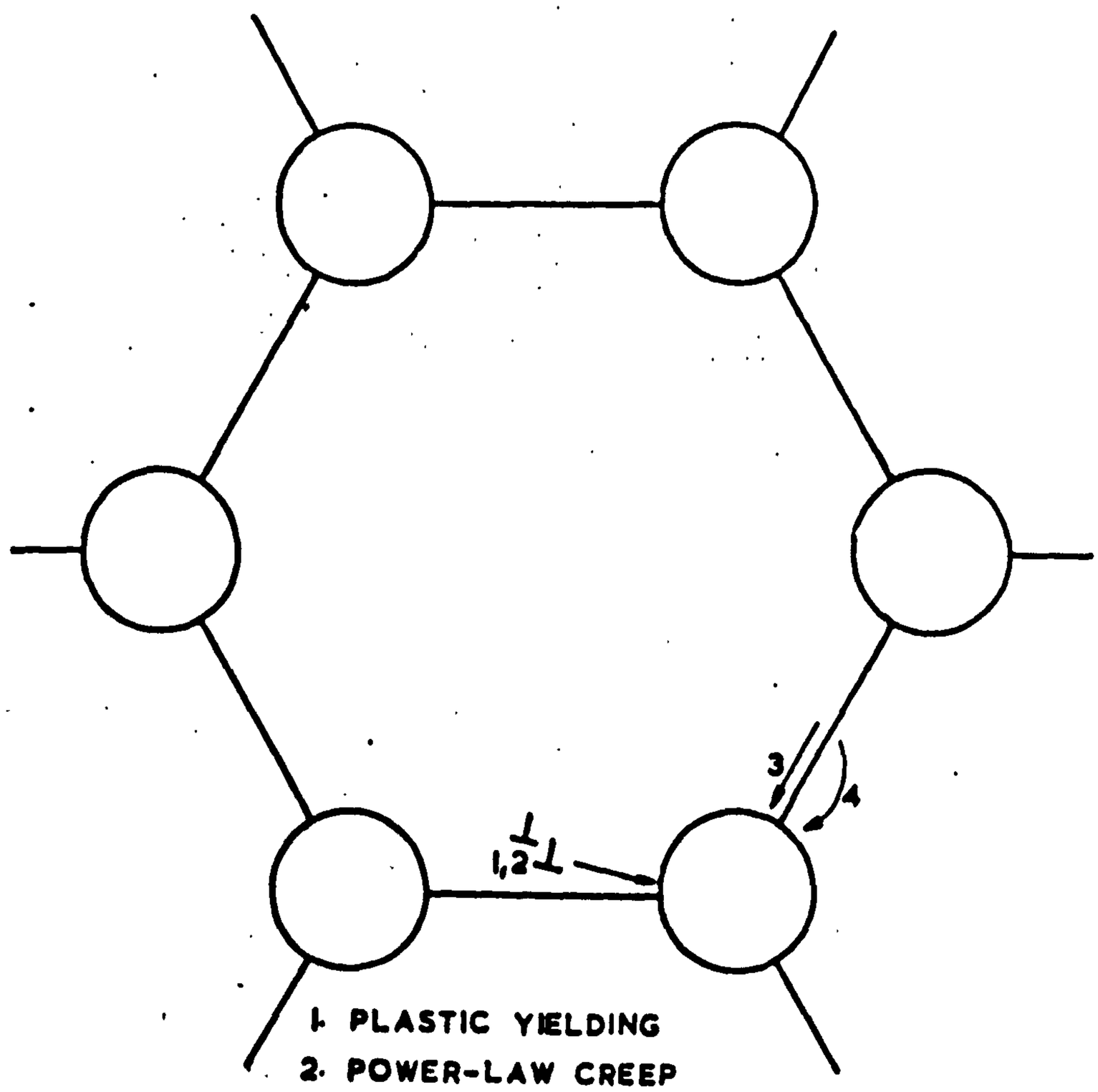

Figure 30 - Mechanisms operative during stage 2 and 3 densification (135).

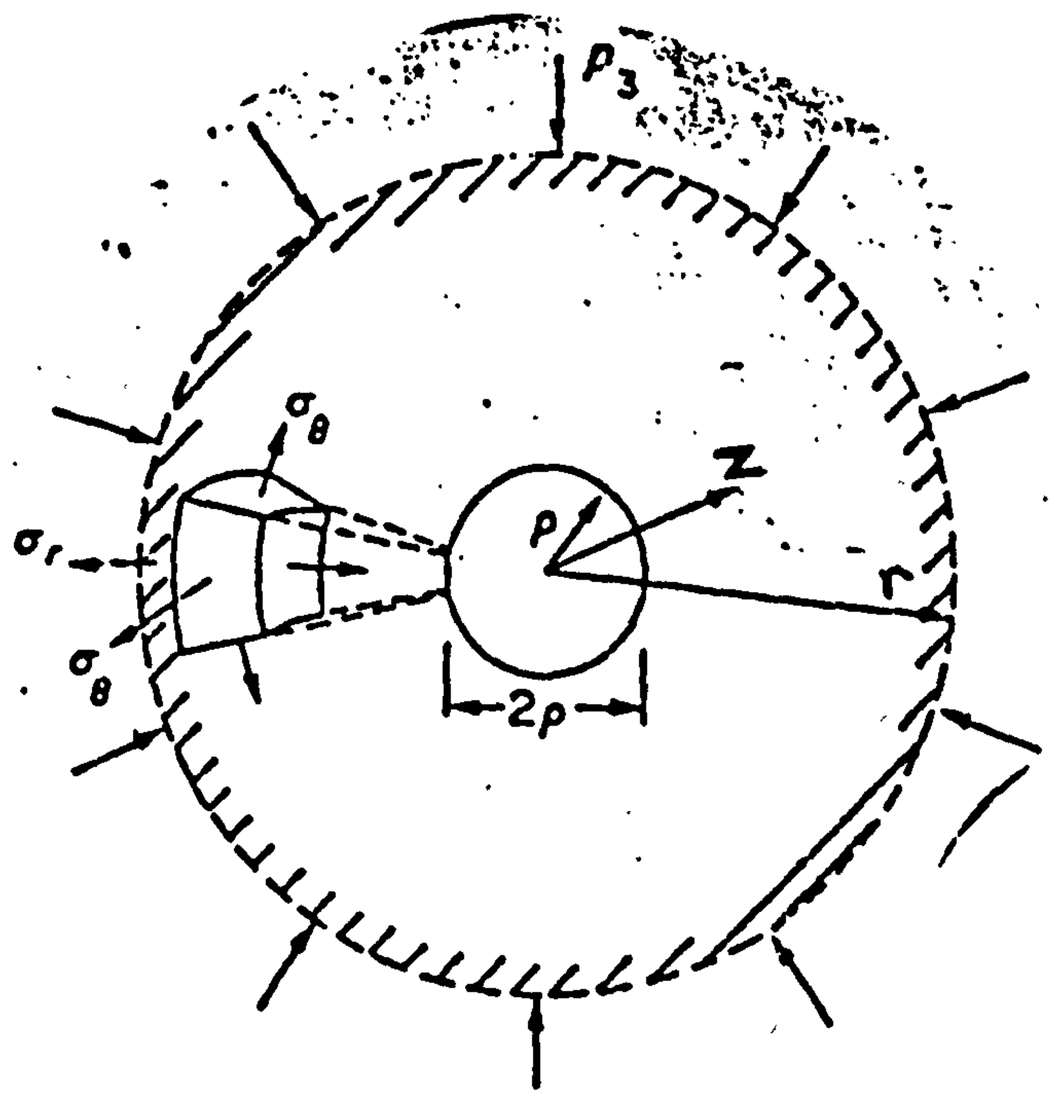

Figure 31 - Final stage densification for pressure sintering based on the collapse of a thick spherical shell of inner radius z and outer radius r.

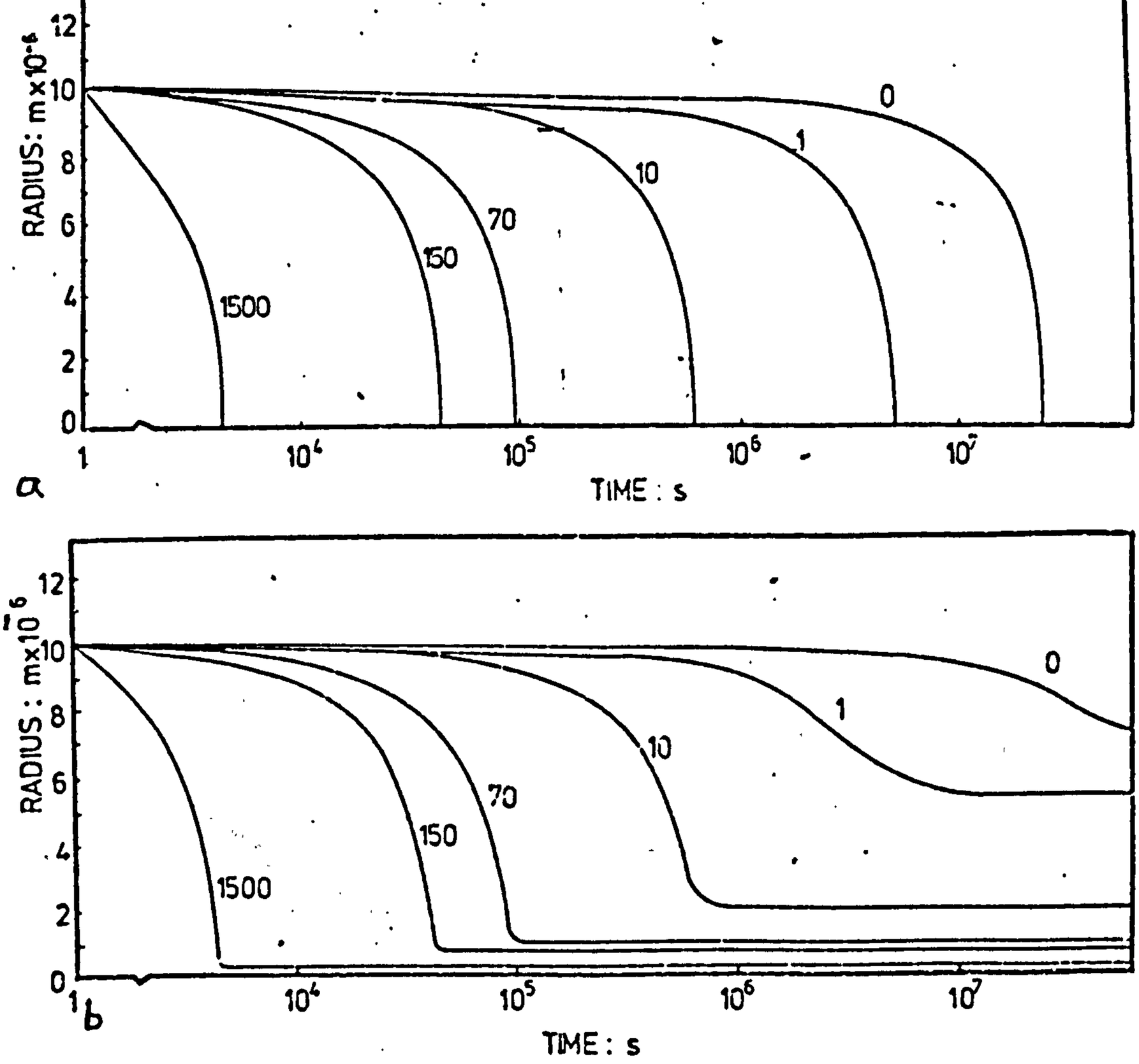

Figure 32 - Theoretical analysis for annealing of grain boundary cavities (38) showing increasing external pressure reduces time for cavity closure (b) presence of internal gas pressure prevents complete cavity closure.

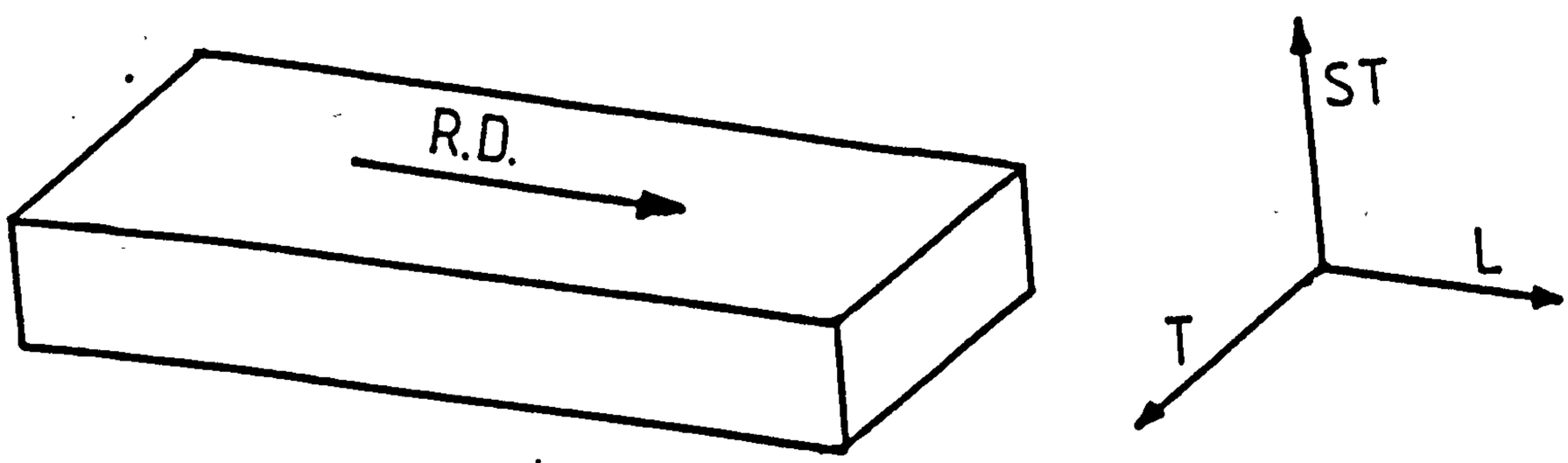

Figure 33 - T, ST and L directions with respect to the rolling direction (RD) in sheet Supral.

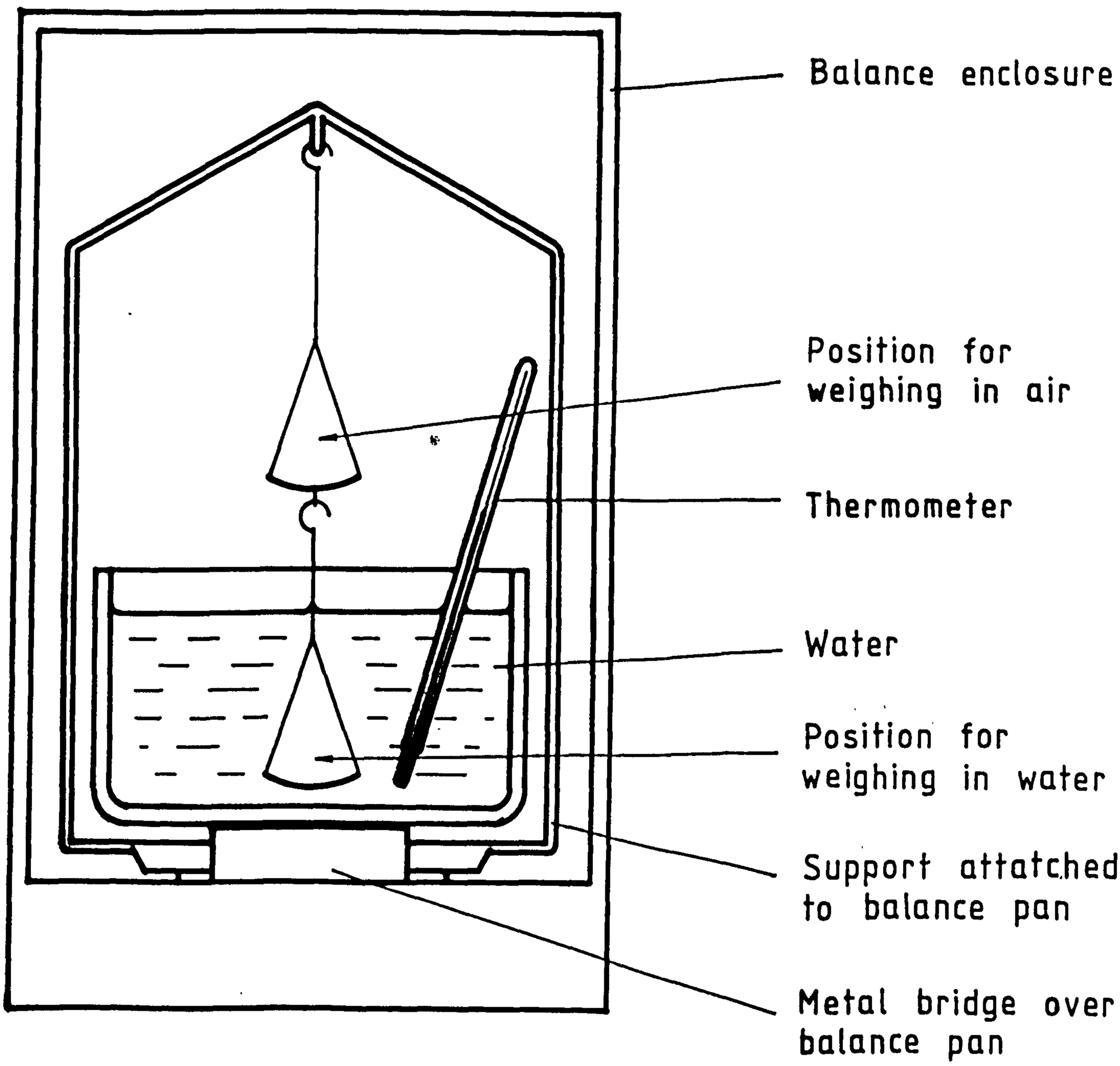

Figure 34 - Arrangement used for measurement of density in Supral.

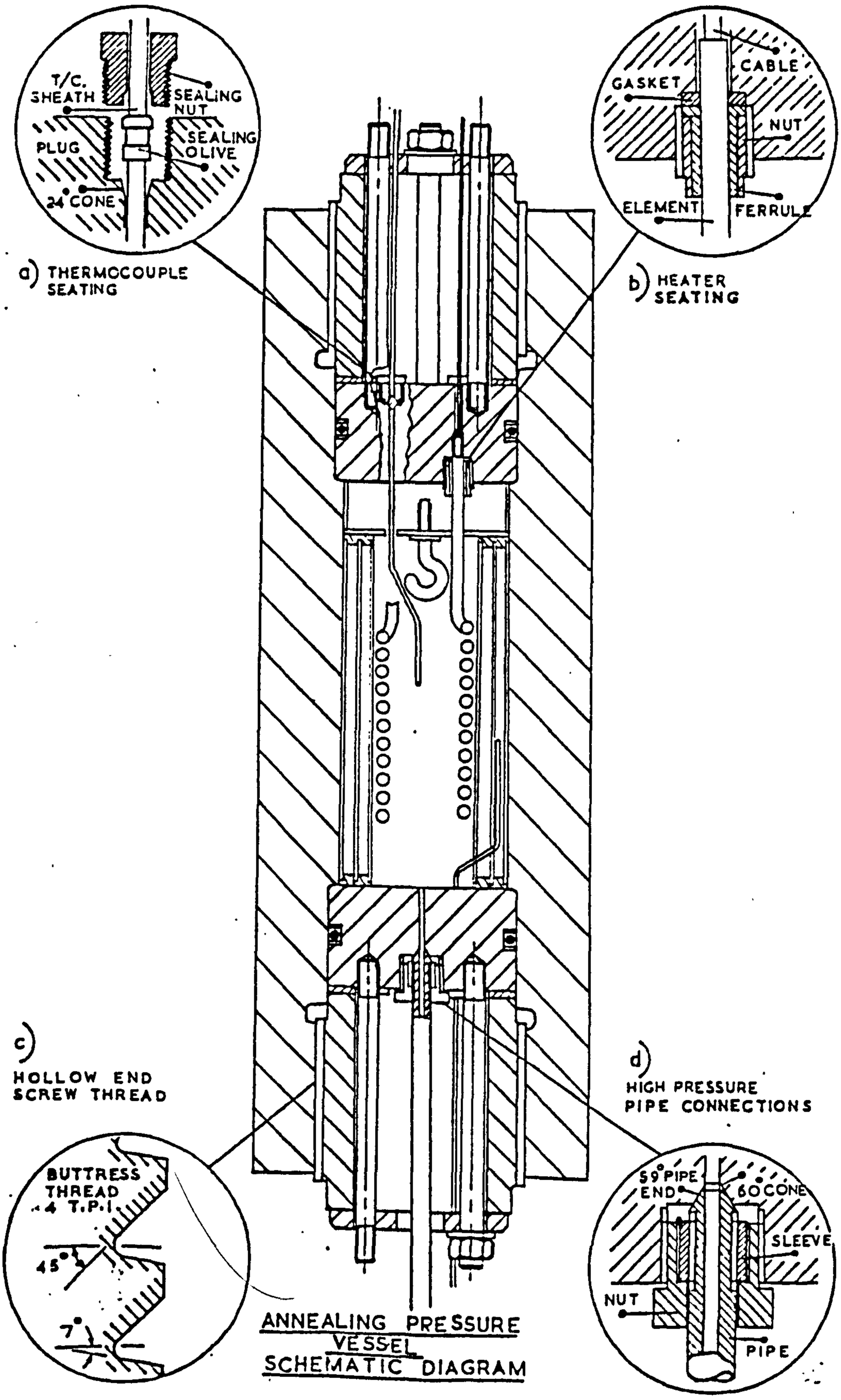

Figure 35 - Schematic diagram of HIP pressure vessel.

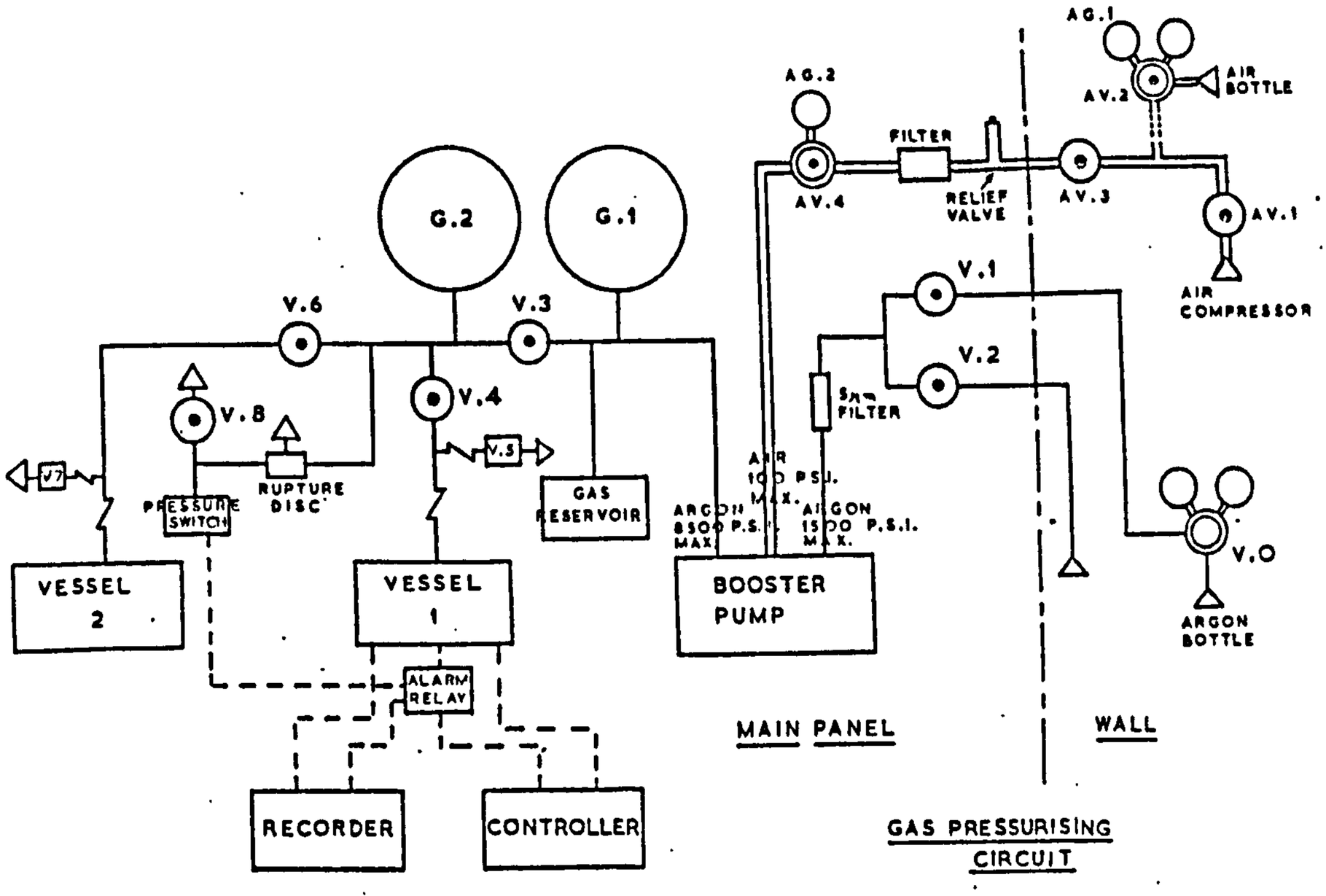

Figure 36 - Gas pressurising circuit for HIP unit.

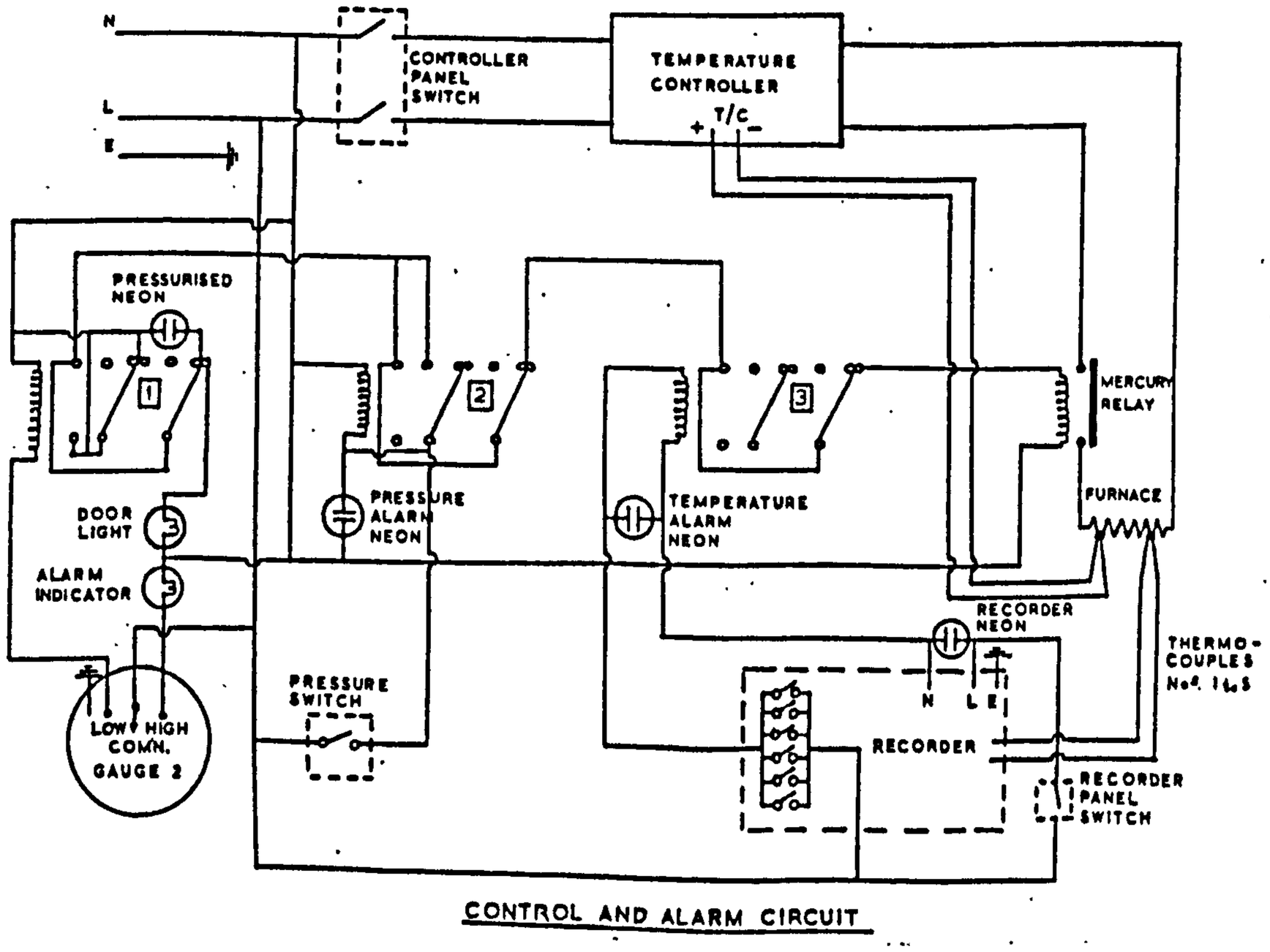

Figure 37 - Control and alarm circuit for HIP unit.

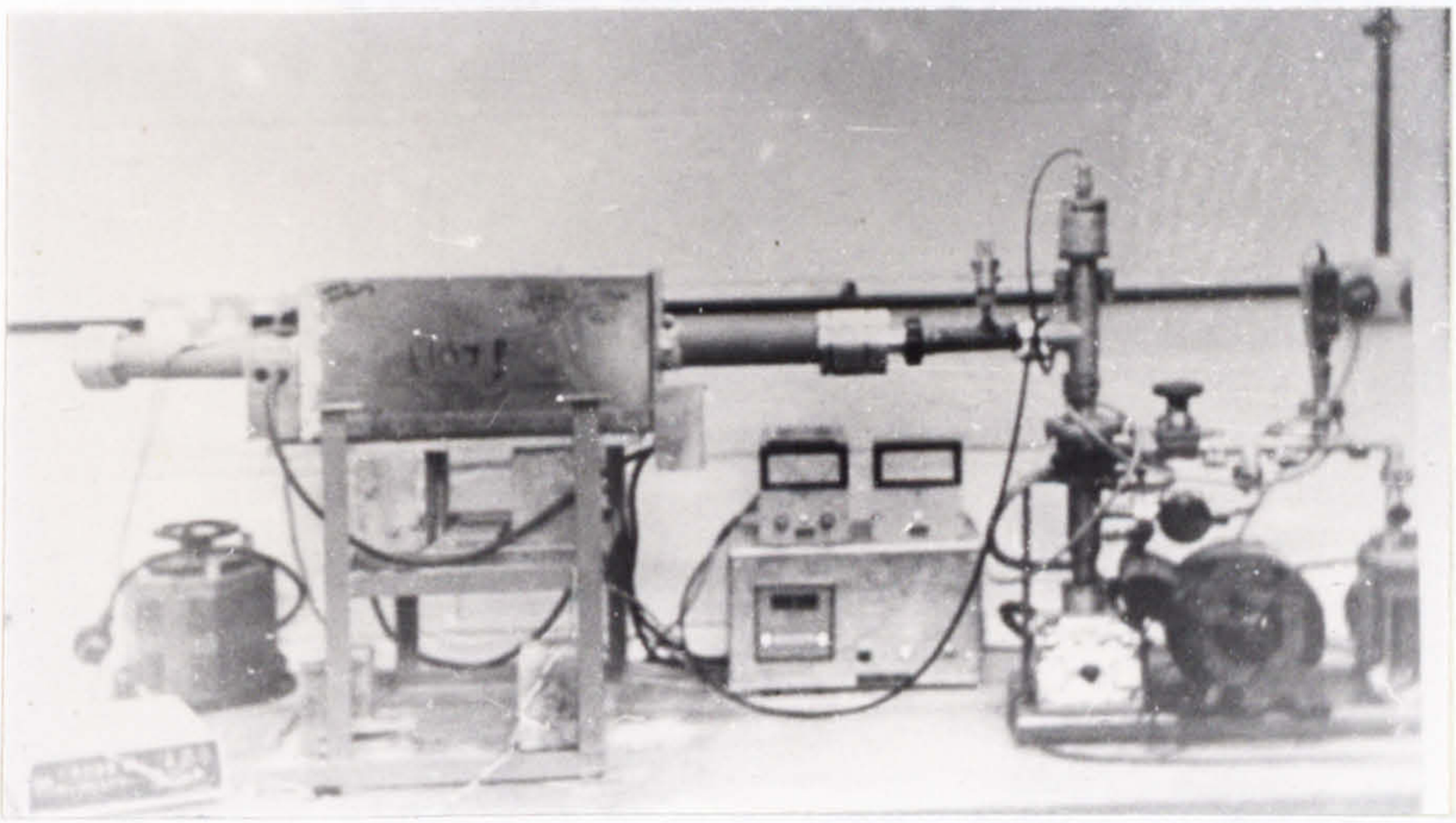

Figure 38 - General view of vacuum degassing facility.

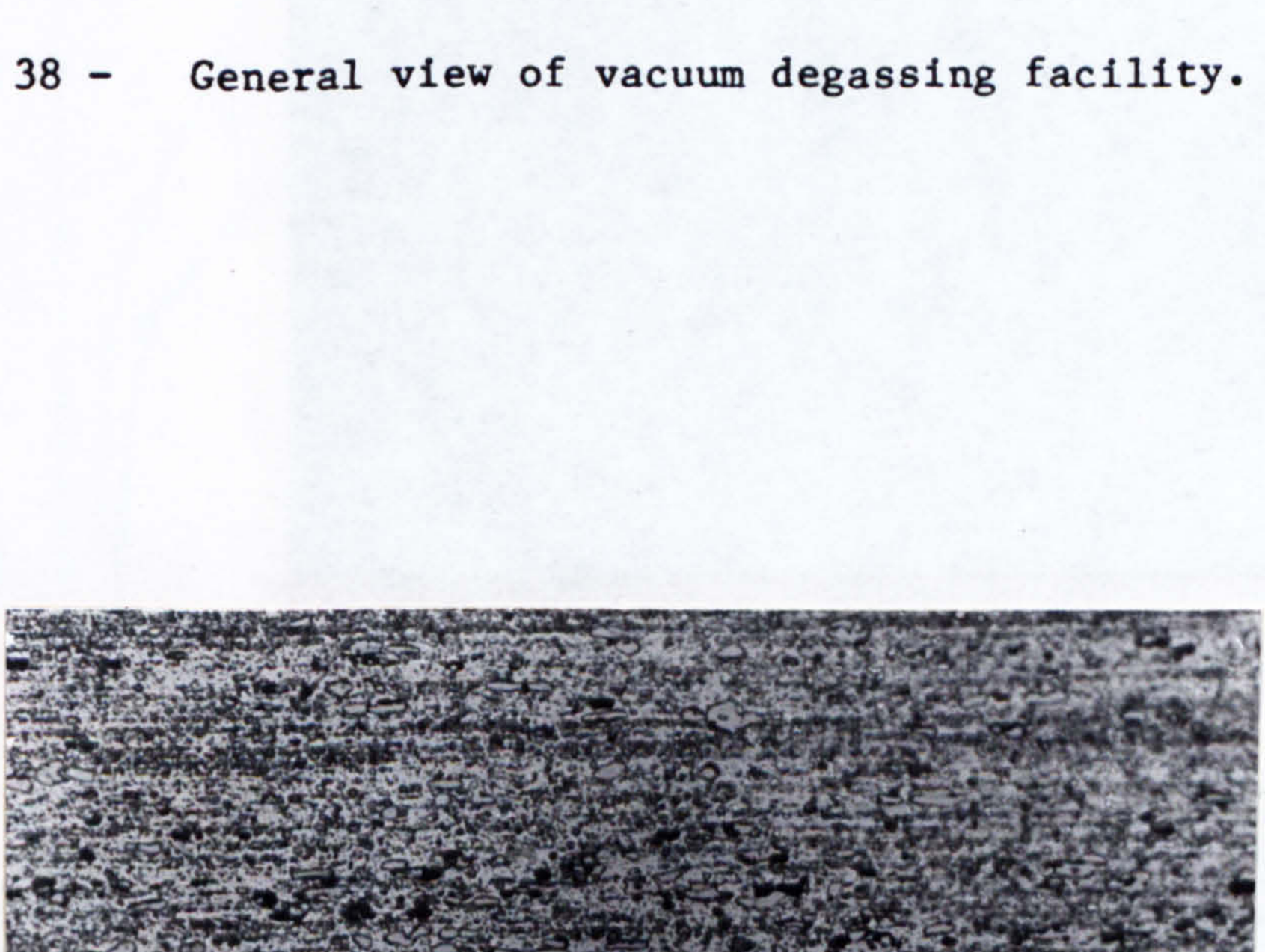

Figure 39 - Optical micrograph of as-received (virgin) SUPRAL 150 edge section banded structure and large $ZrAl_3$ particle. x 600.

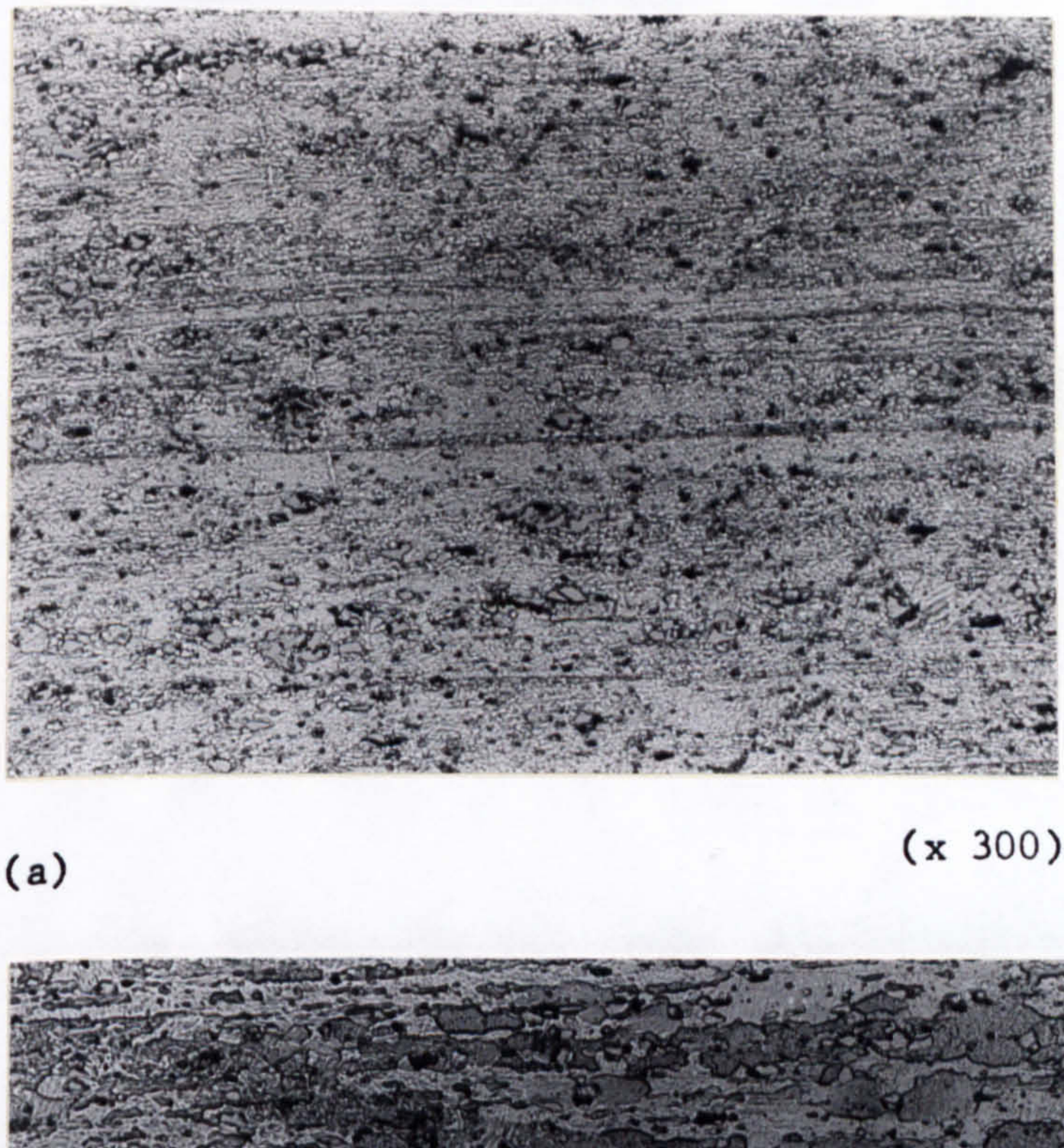

(a) (x 300)

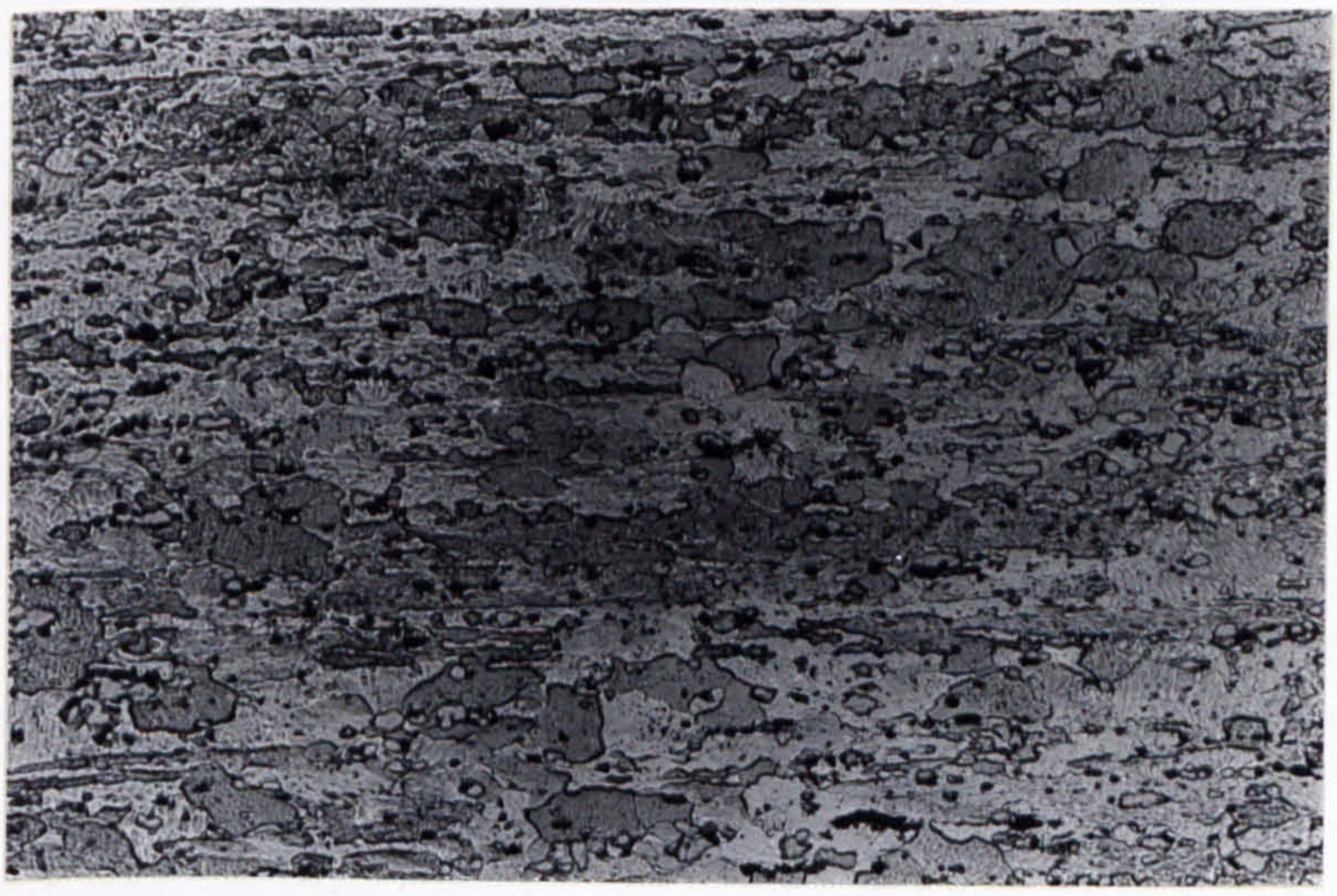

(b) (x 300)

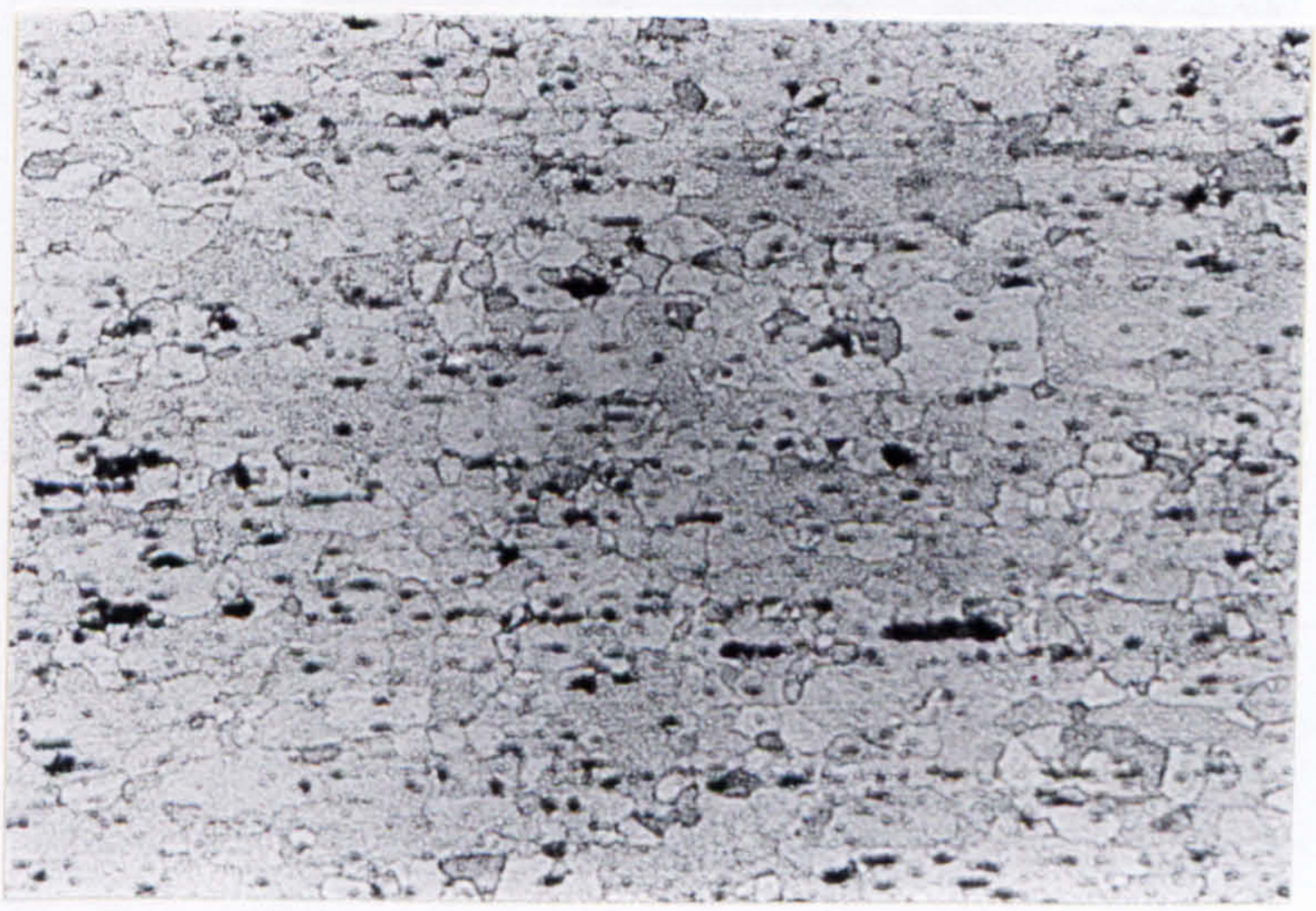

(c) (x 150)

Figure 40 - The influence of temperature and time on the recrystallisation behaviour of as-received SUPRAL 150 after (a) 2 hours at 400°C (x 300), (b) 1 day at 400°C (x 300) and (c) after solution-treatment (x 150).

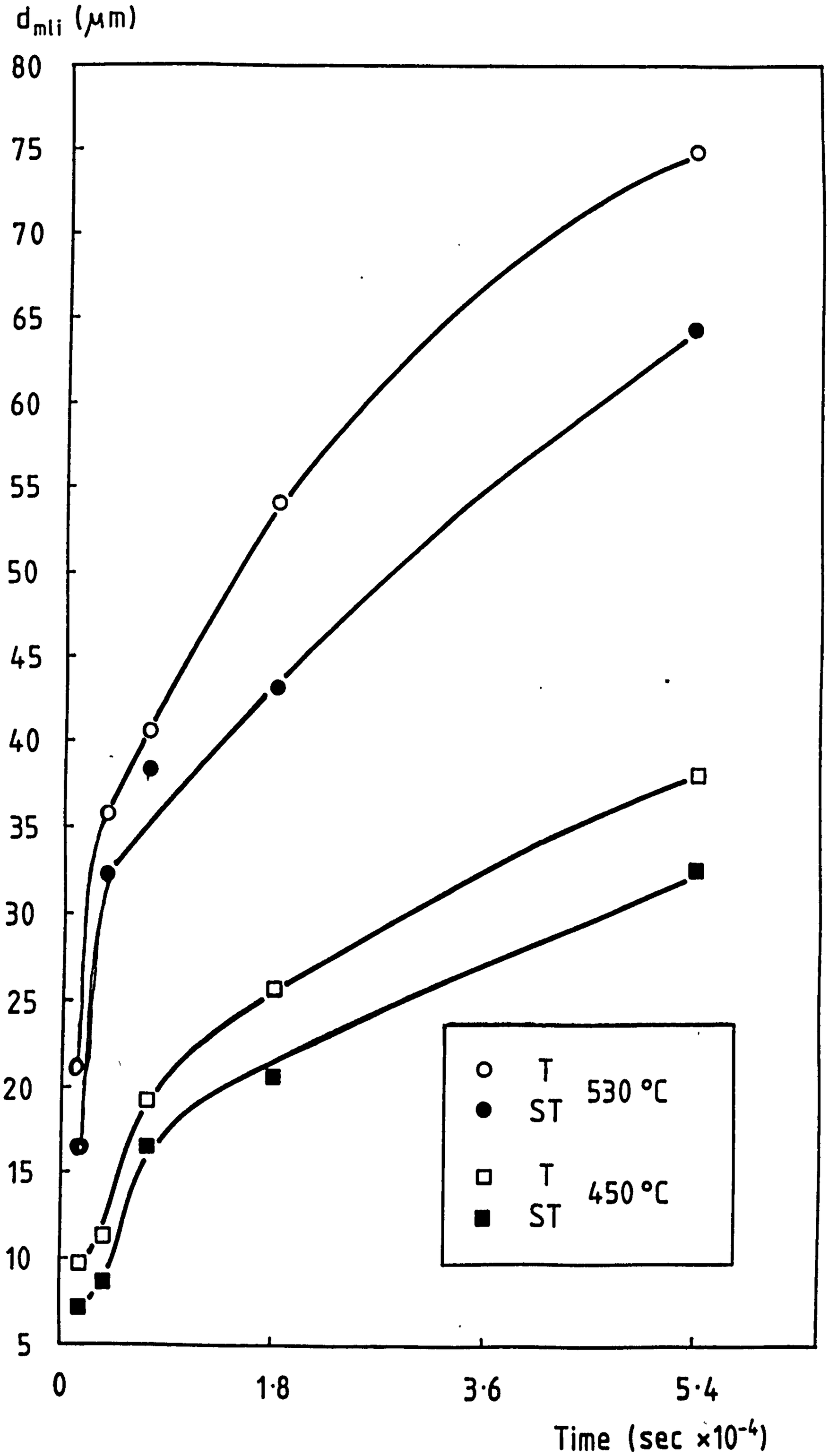

Figure 41 - Main Linear Intercept (d_{mli}) versus time (t) for as-received virgin Supral 150.

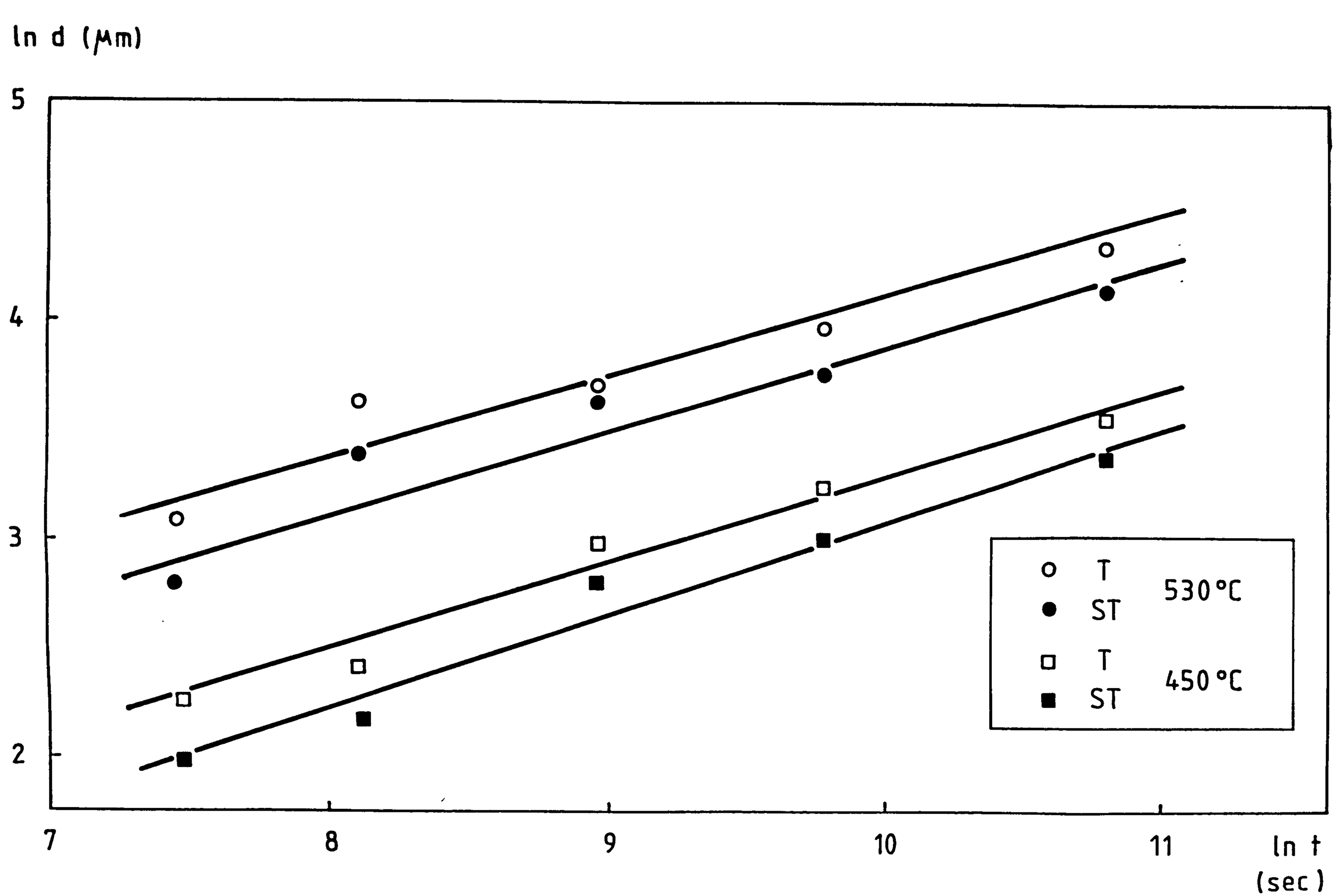

Figure 42 - Mean linear intercept grain size (d_{mli}) versus time (t) for as-received SUPRAL 150 at 450°C and 530°C on a log-log scale.

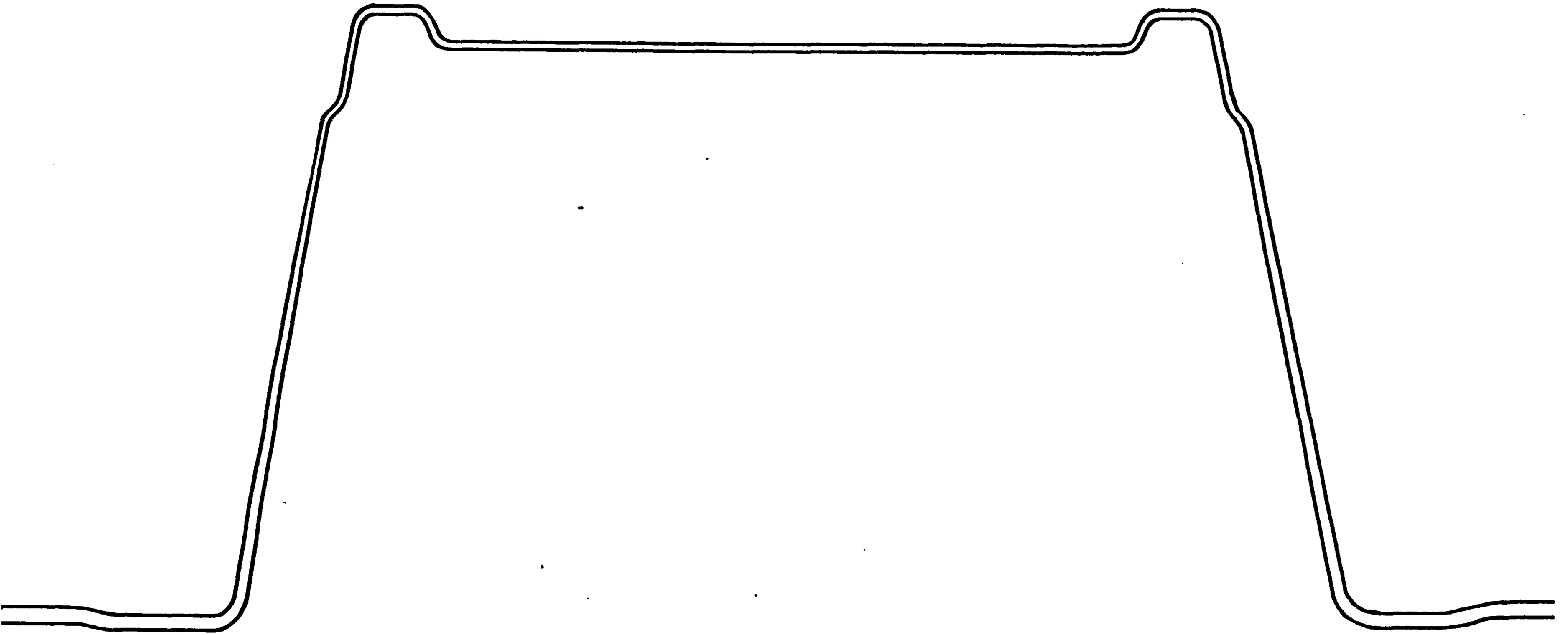

Figure 43 - Edge profile of SPF top hat in SUPRAL 150 showing variation in thickness.

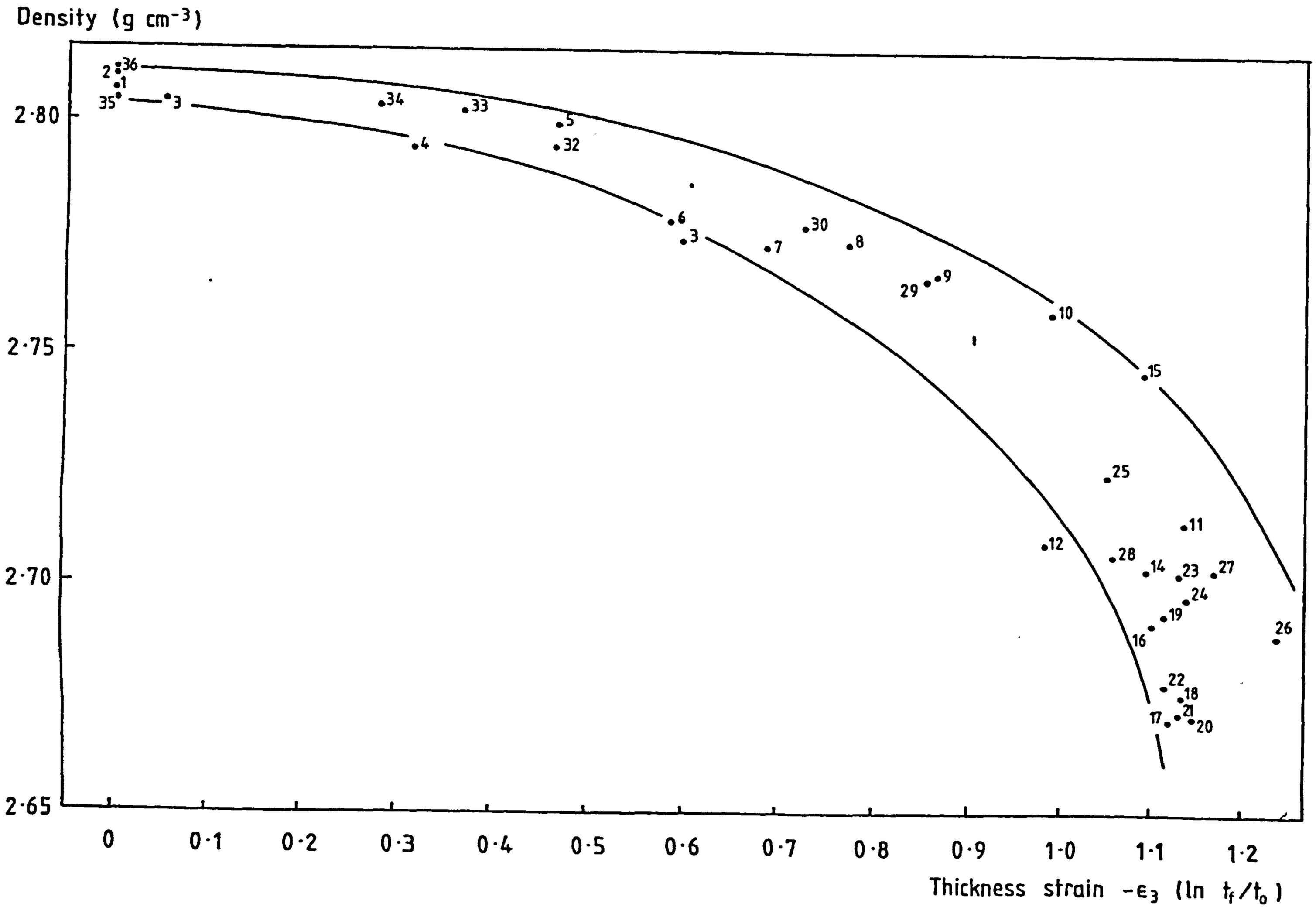

Figure 43a – Variation of density, indicating level of cavitation, with increasing thickness strain, (ε_3).

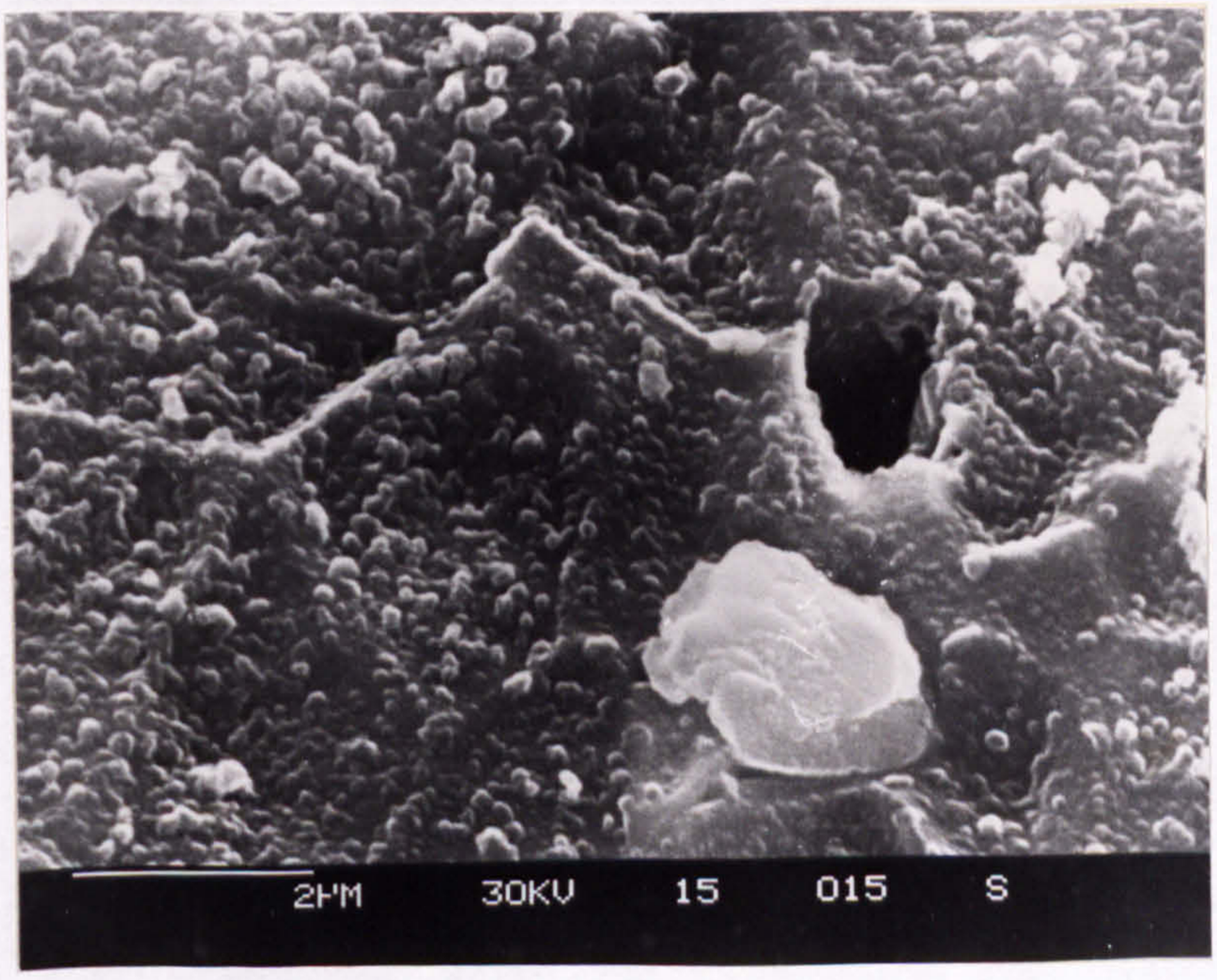

Figure 44 - Nature of grain boundary cavitation in SPF SUPRAL 150.

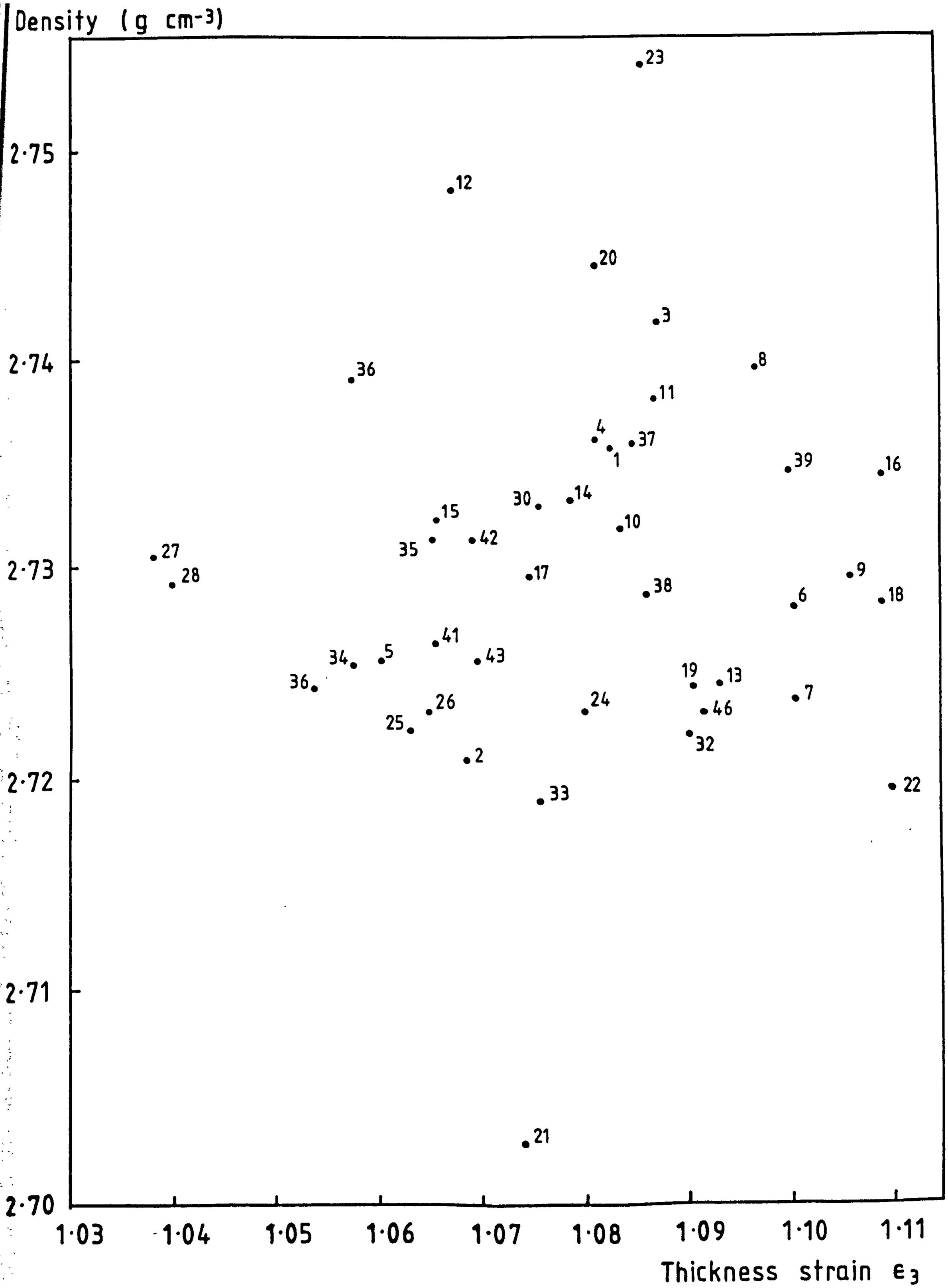

Figure 45 – Variation of cavitation with thickness strain in SPF disc of SUPRAL 150.

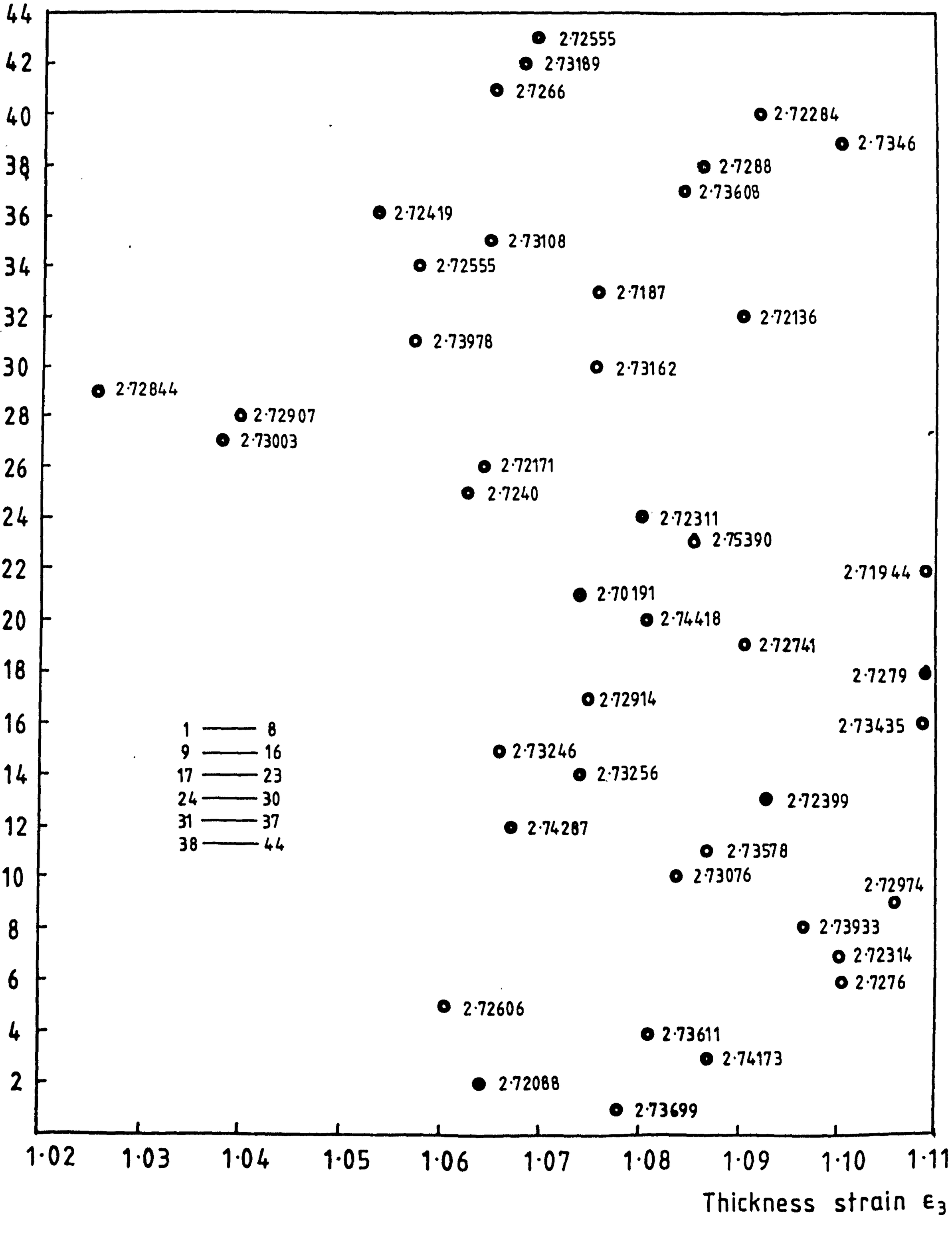

Figure 46 – The variation of thickness strain with specimen location in SPF 'top hat' disc.

(x 75)

Figure 47 - Micrographs of SPF Supral 150 edge sections showing as-received SPF cavity morphology (x 75).

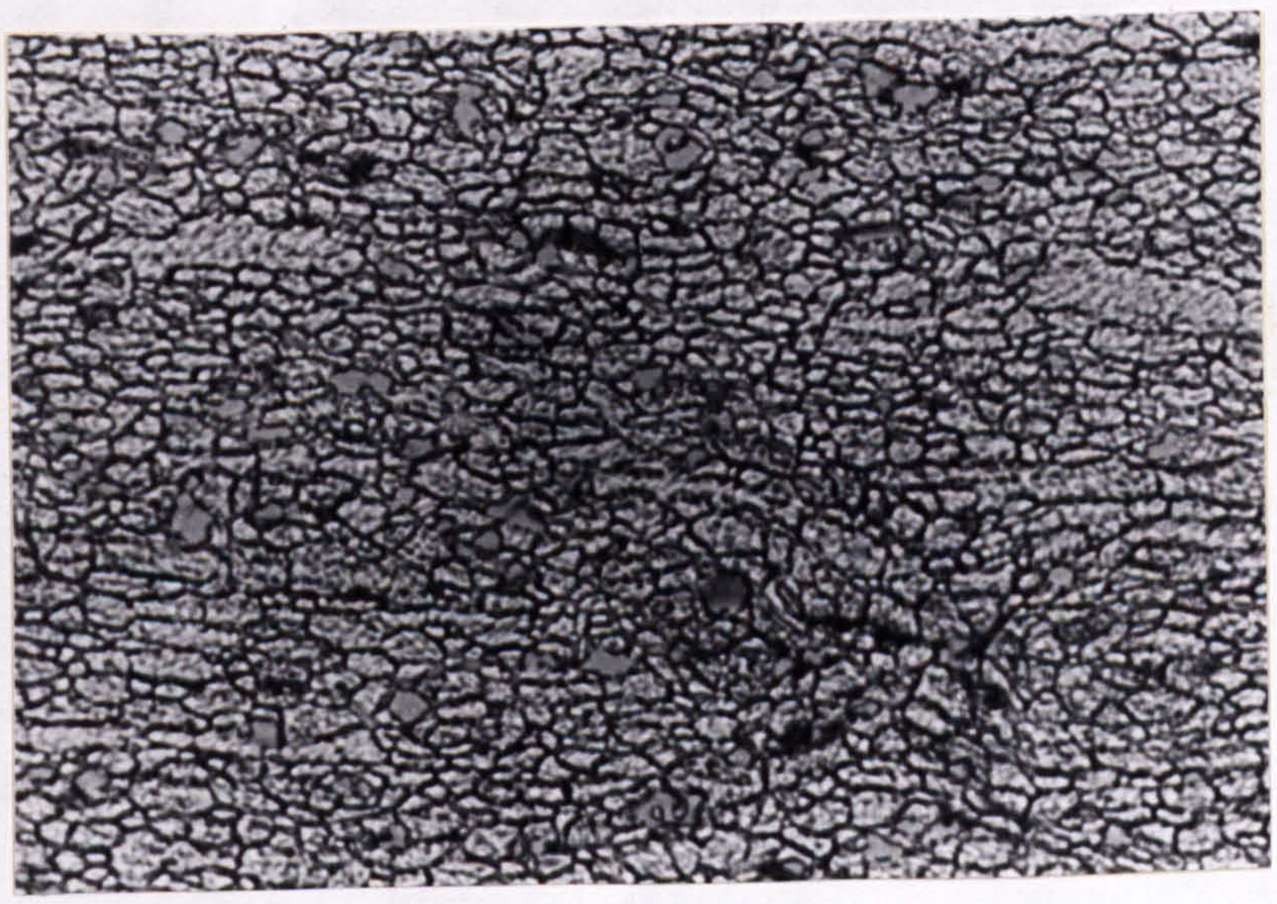

(x 300)

Figure 47a - SPF Supral 150 micrograph showing grain structure after forming (x 300).

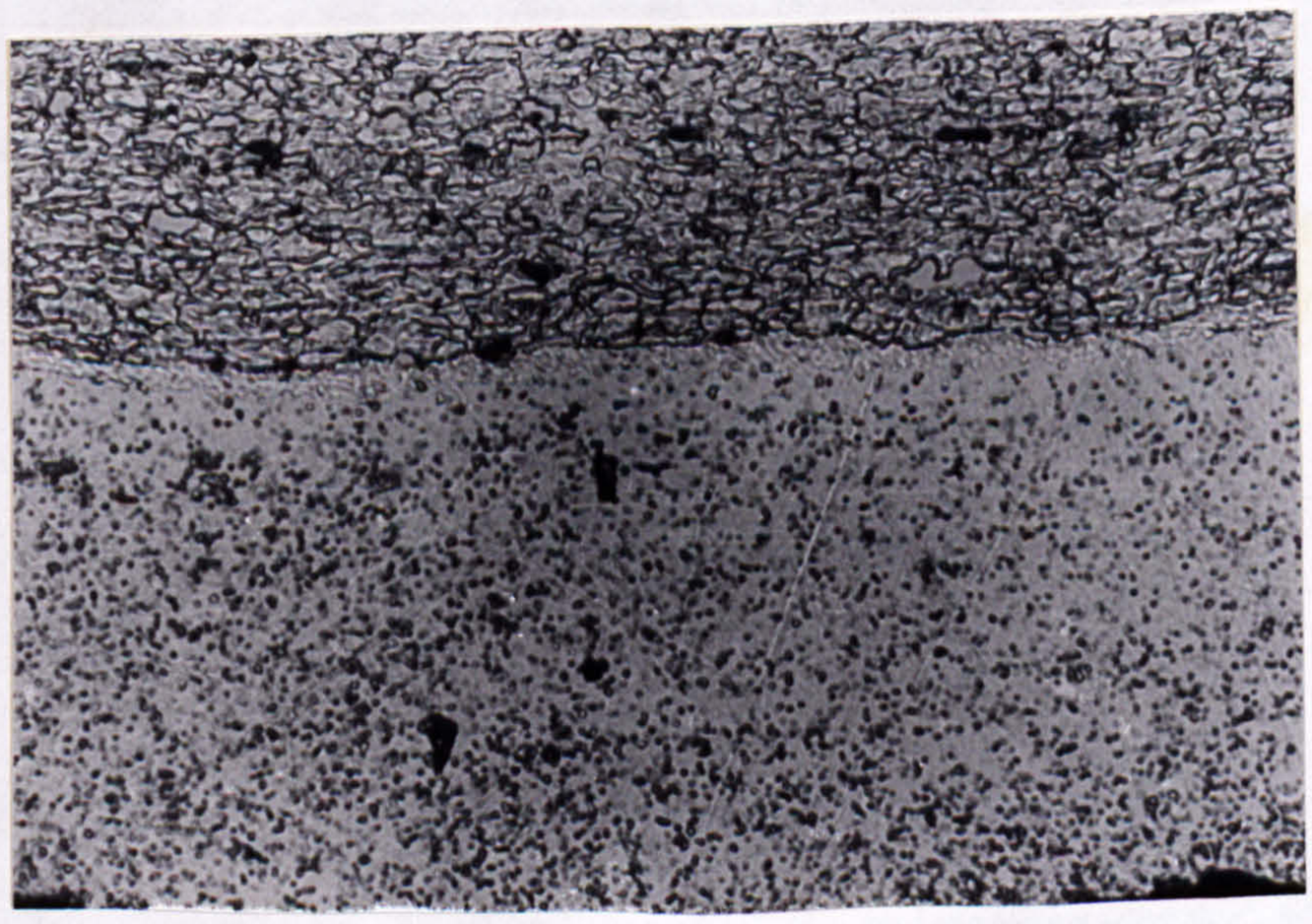

(x 300)

Figure 47b - Figure showing the complete adhesion of the aluminium cladding to the matrix (x 300).

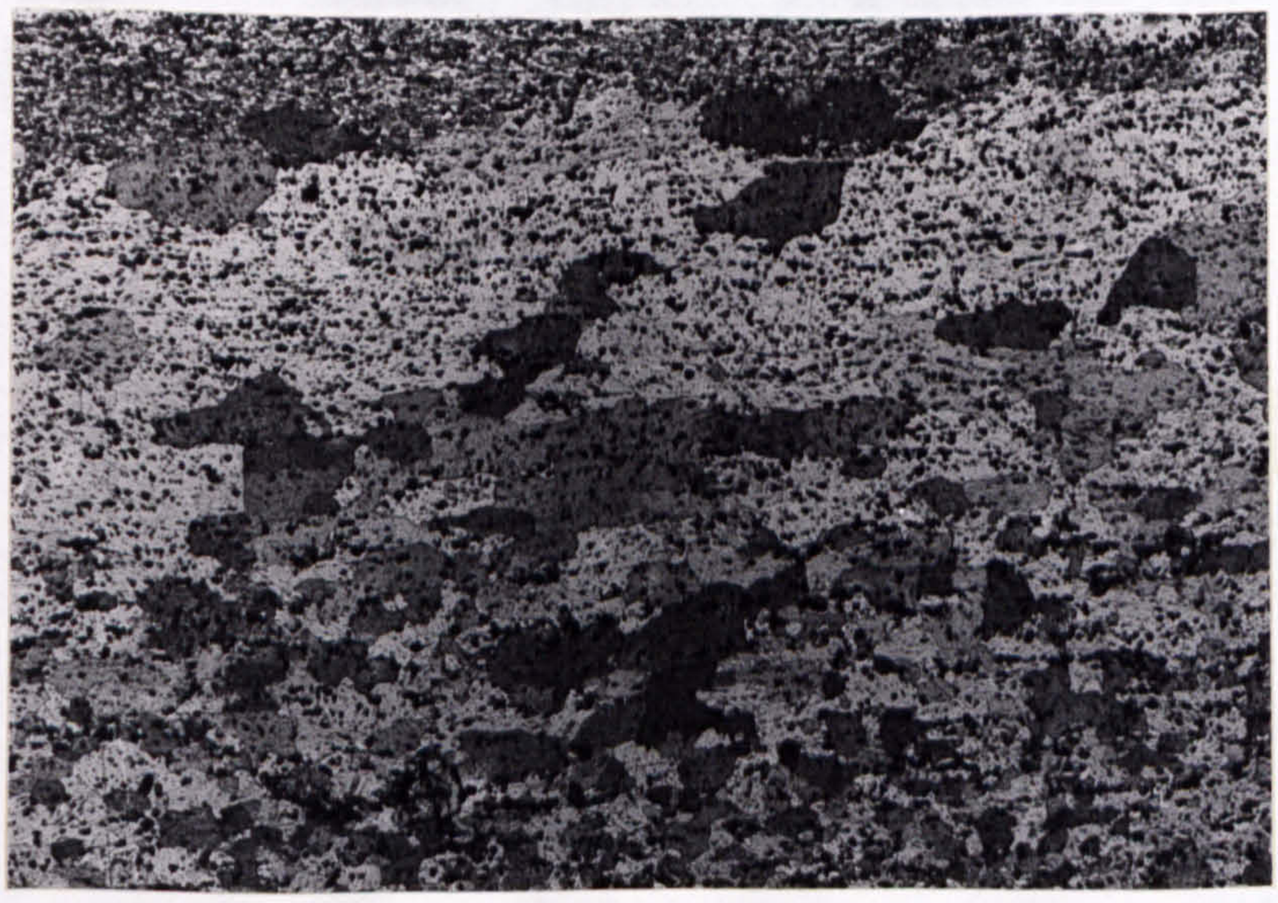

(x 75)

Figure 47c - Grain size in SPF Supral 150 after static anneal at 450°C for 1 day. Note range of grain sizes.

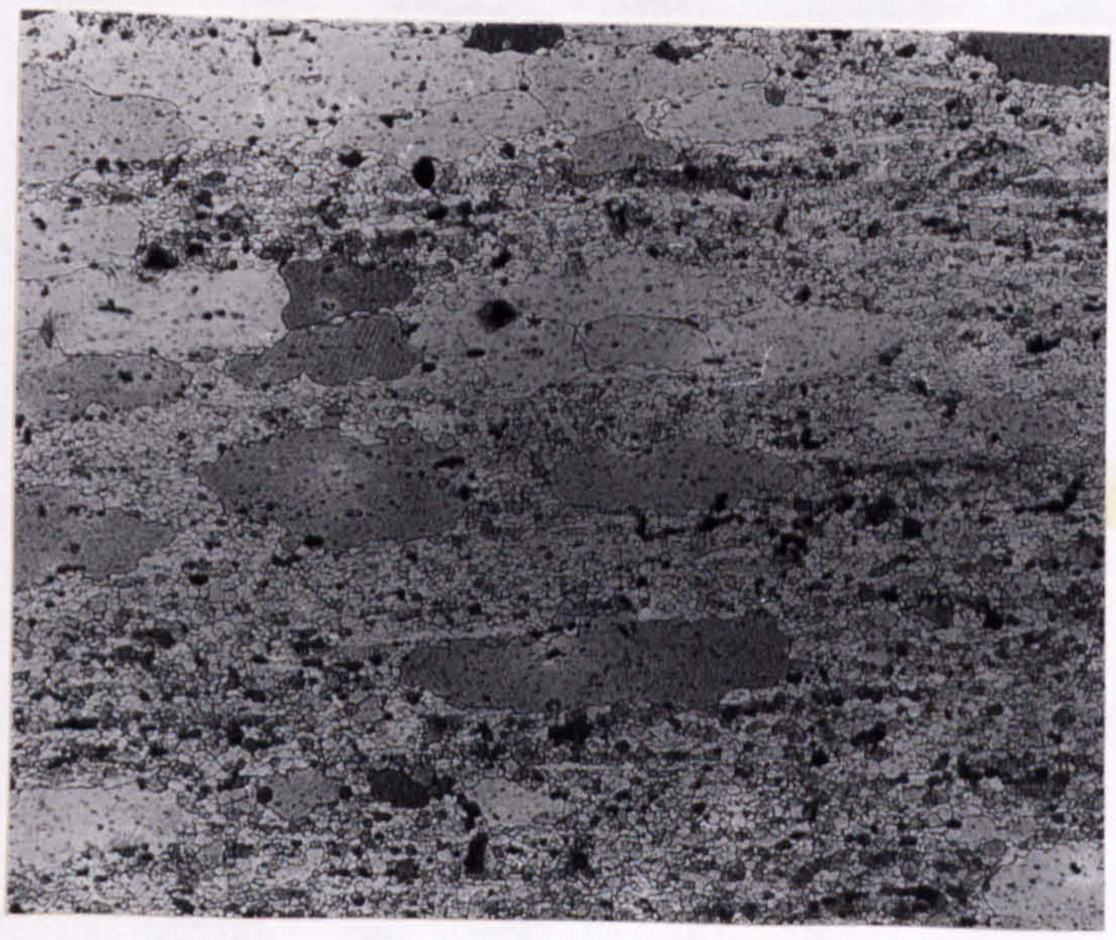

(x 75)

Figure 47d - Variable grain size in SPF Supral 150 after the T6 heat treatment.

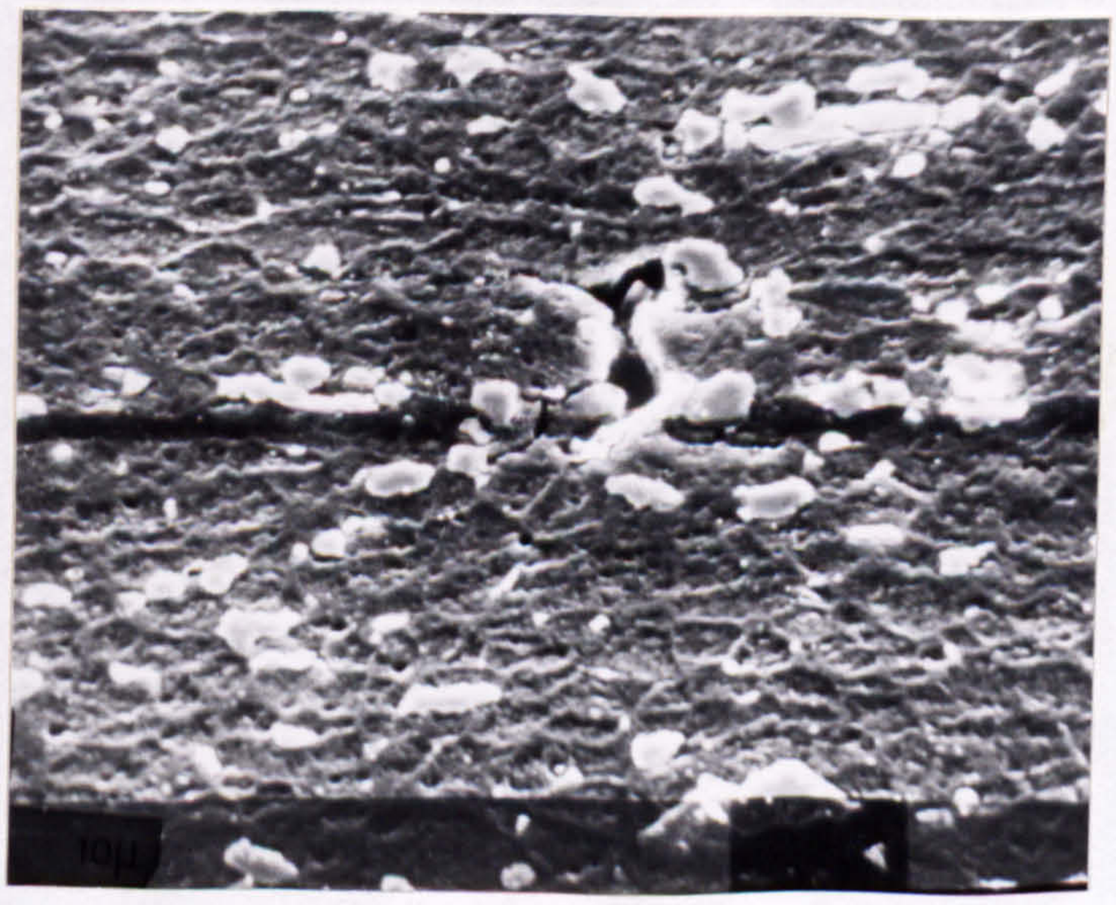

Figure 47e - SEM micrograph of SPF cavity showing its association with $CuAl_2$ precipitates.

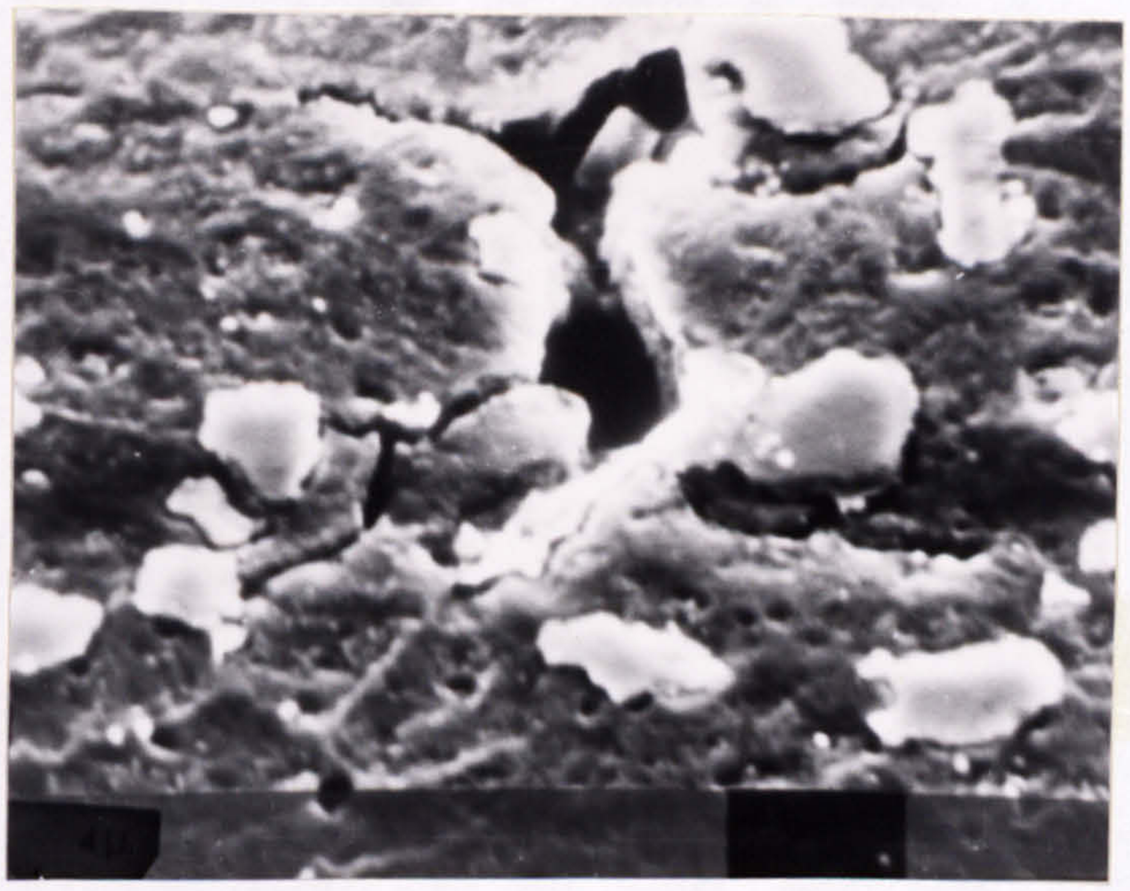

Figure 47f - Cavitation associated with $CuAl_2$ at higher magnification.

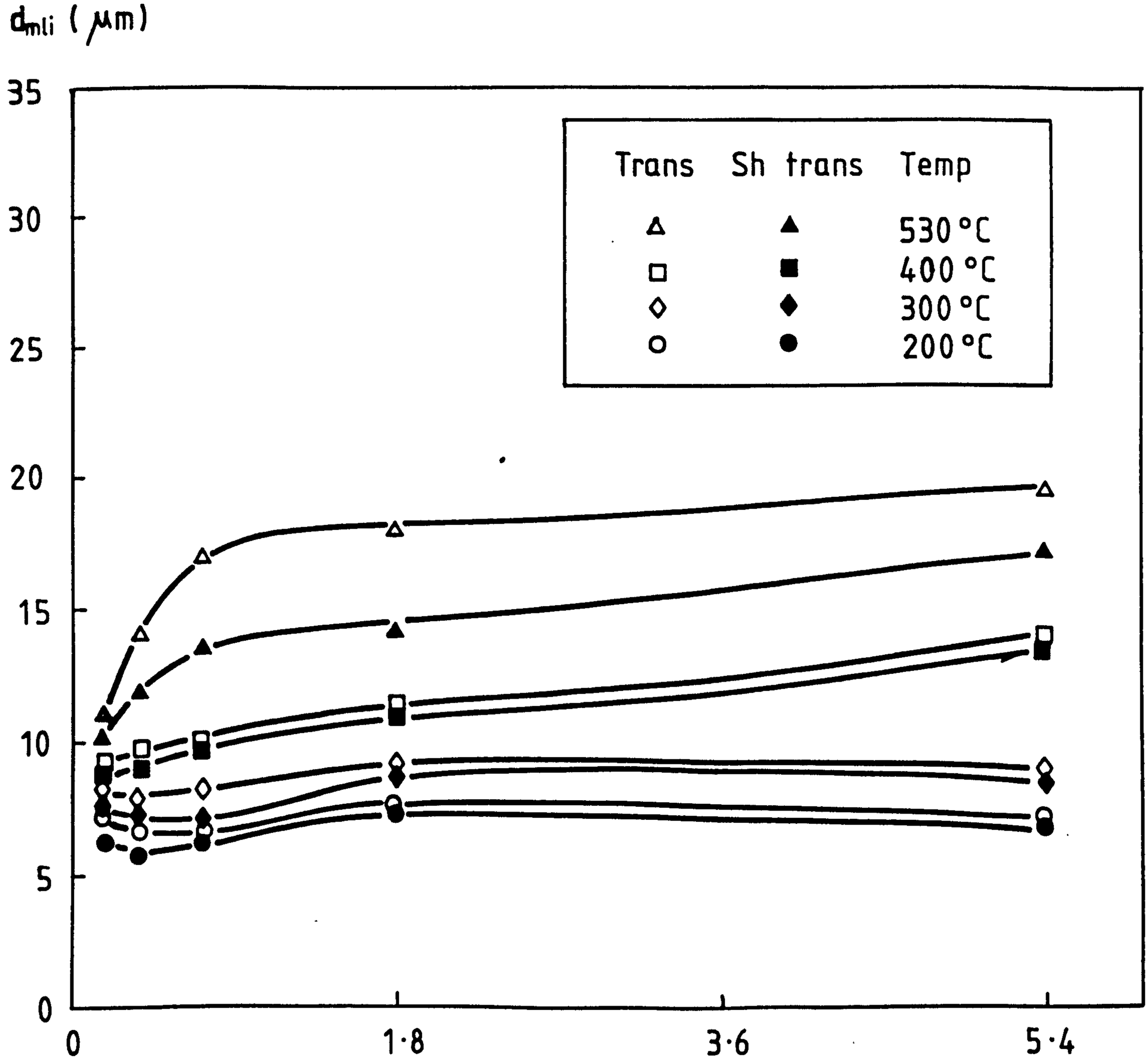

Figure 48 - The effect of annealing temperature and time on SPF grain size stability.

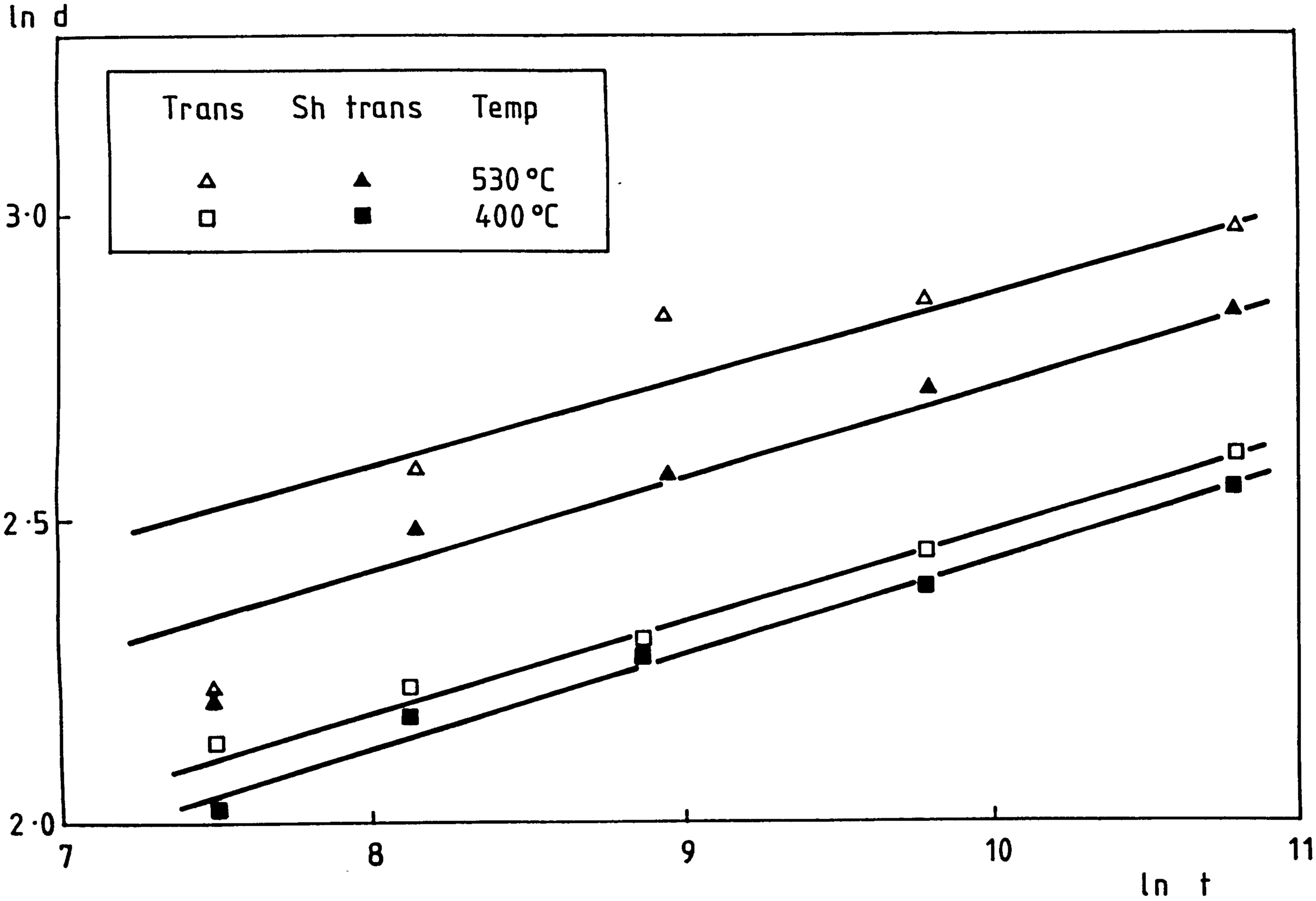

Figure 49 – Mean linear intercept (d_{mli}) versus time (t) for SPF Supral 150 at 400°C and 530°C plotted on a log-log scale.

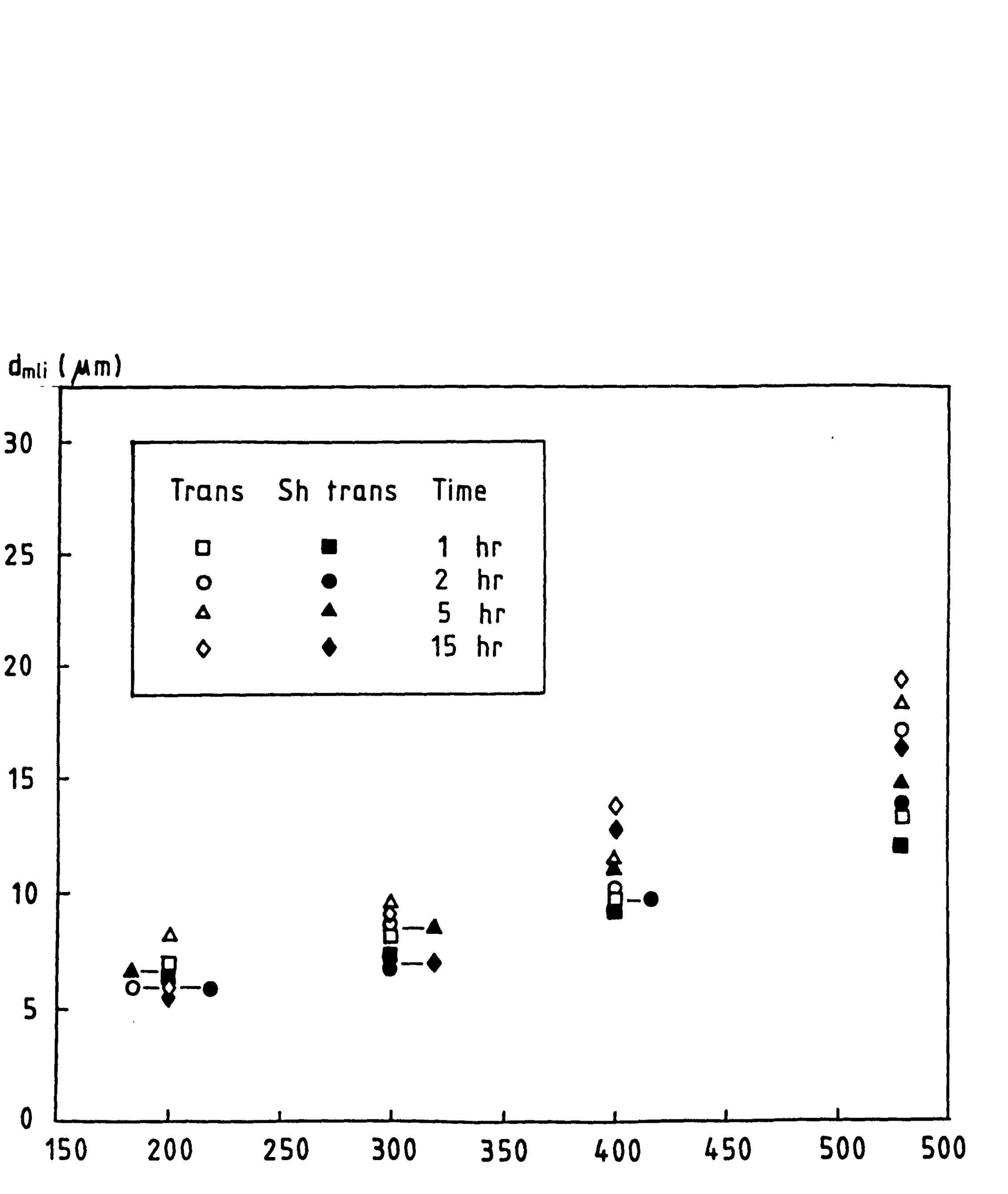

Figure 50 - The effect of time at various temperatures on grain growth on SPF Supral 150.

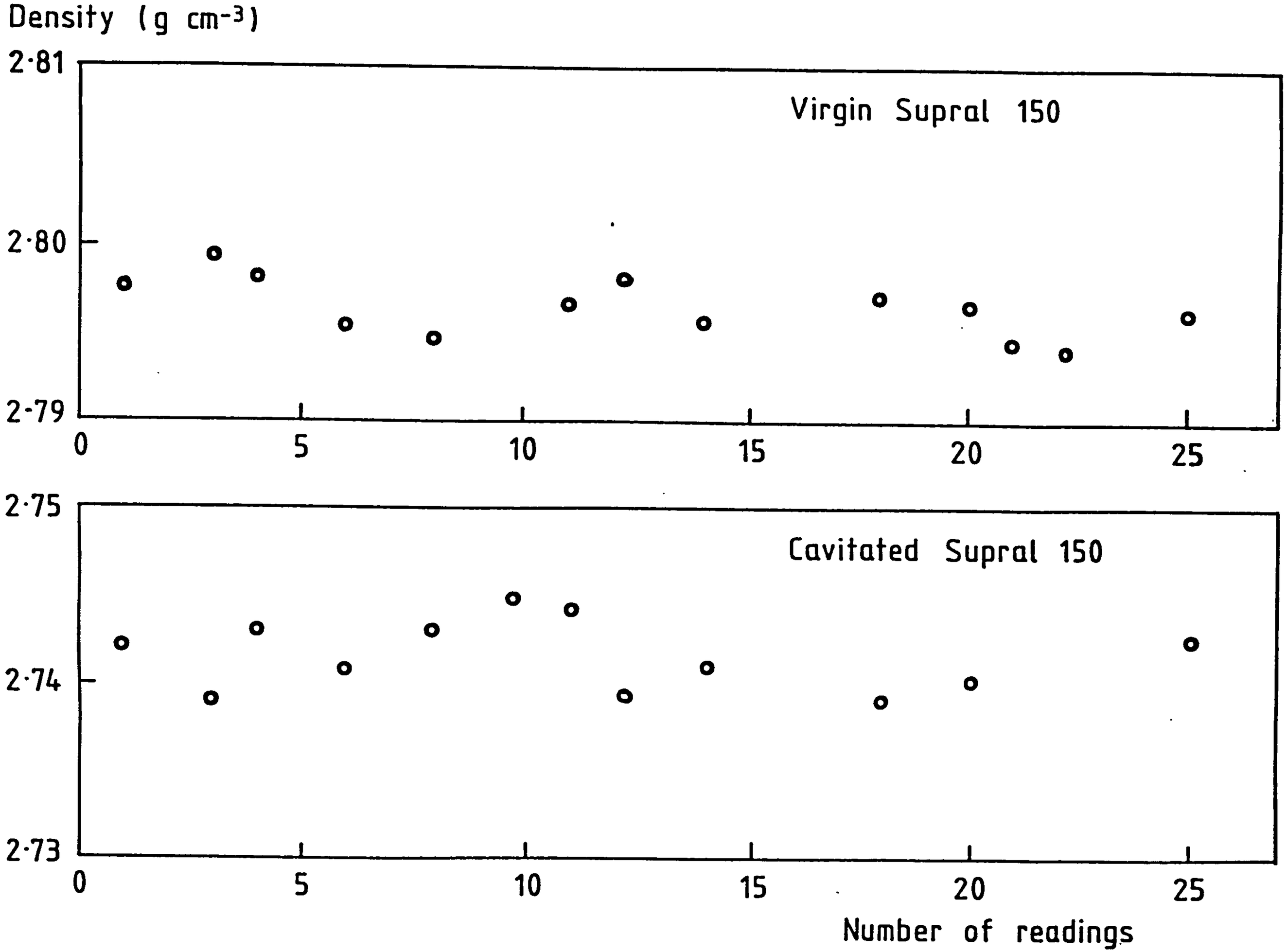

Figure 51 - The variation in density of the same specimens of Virgin Supral 150 and (a) SPF cavitated Supral 150, which shows good reproducibility of the technique.

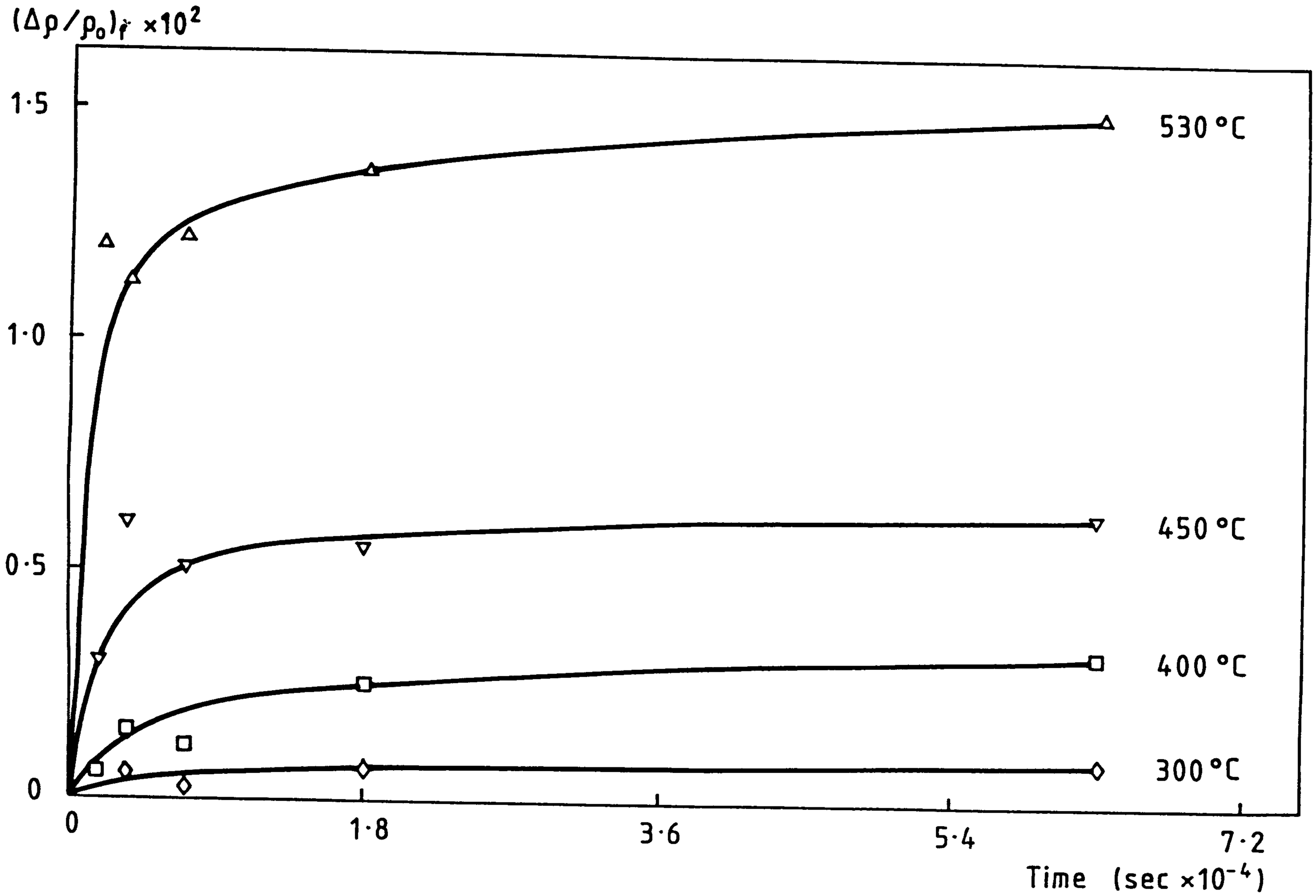

Figure 52 - Fractional density increase $(\Delta\rho/\rho_o)_f$ in SPF Supral 150 with time at different annealing temperatures.

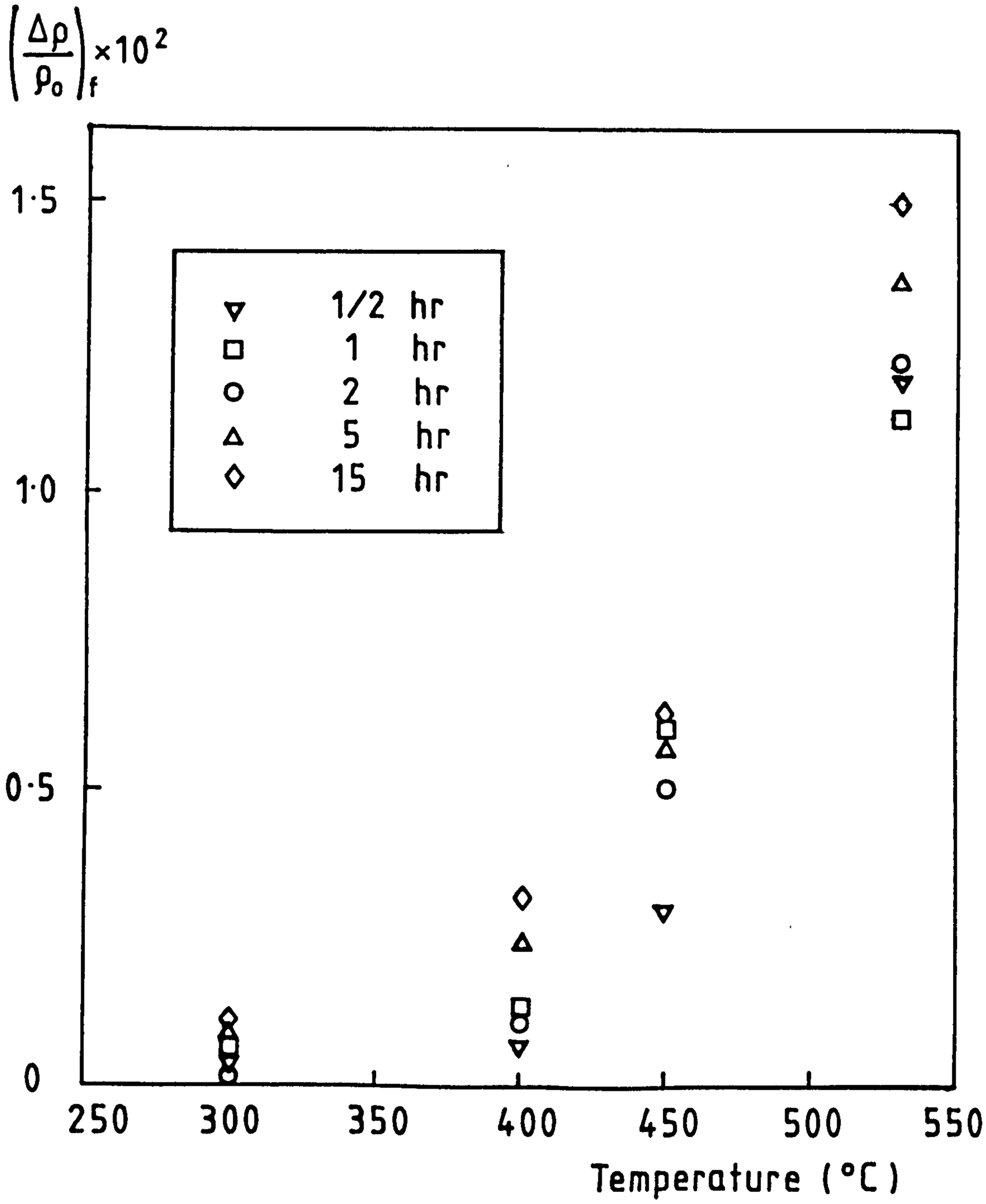

Figure 53 - Effect of annealing time on the sintering of cavities (given by $(\Delta\rho/\rho_o)_f$) at different temperatures.

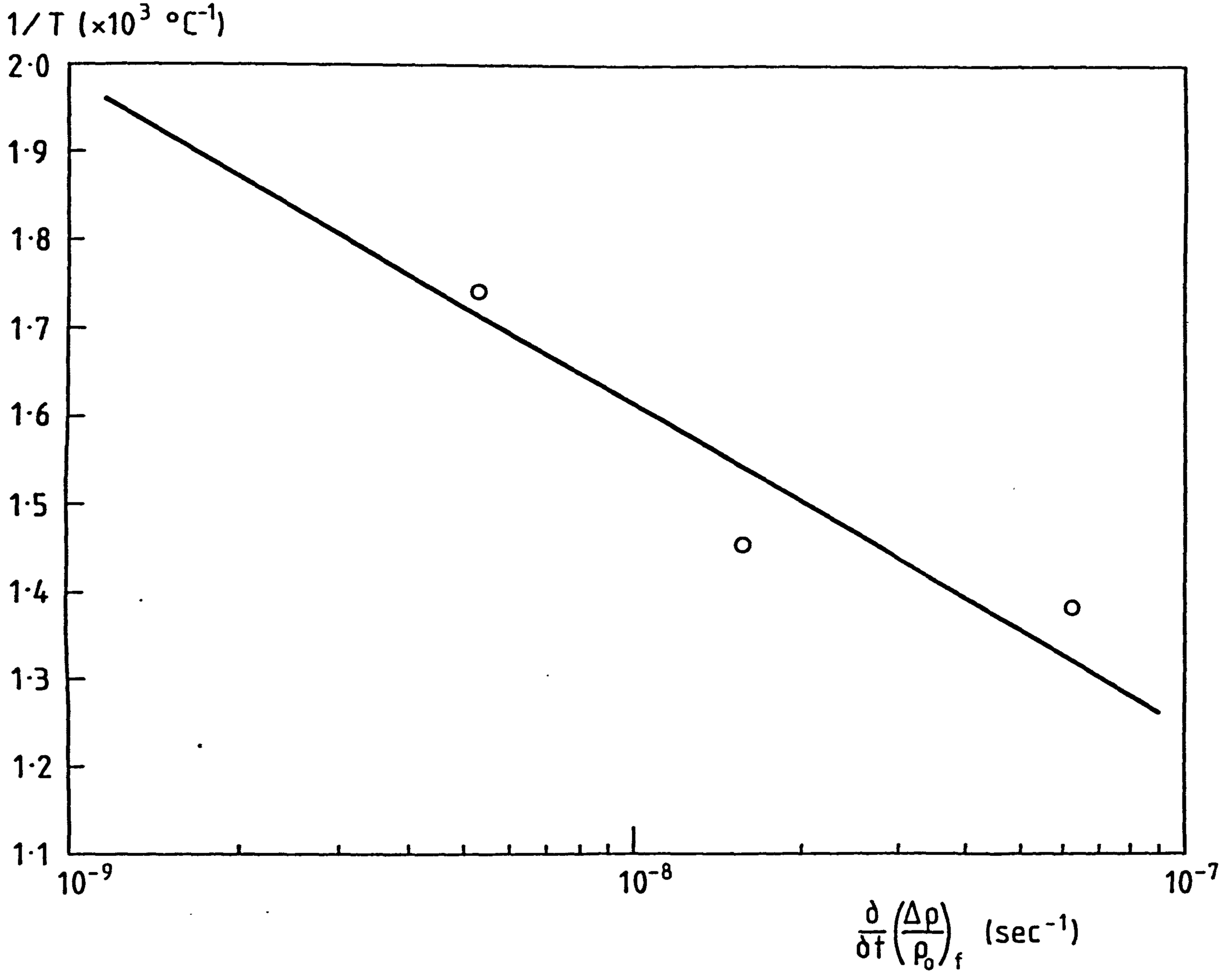

Figure 54 – Plot of sintering rate $d/dt(\Delta\rho/\rho_o)_f$ versus the reciprocal of the temperature for given sintering time. The gradient gives an activation energy for sintering of $Q = 61.93$ KJ mol^{-1}.

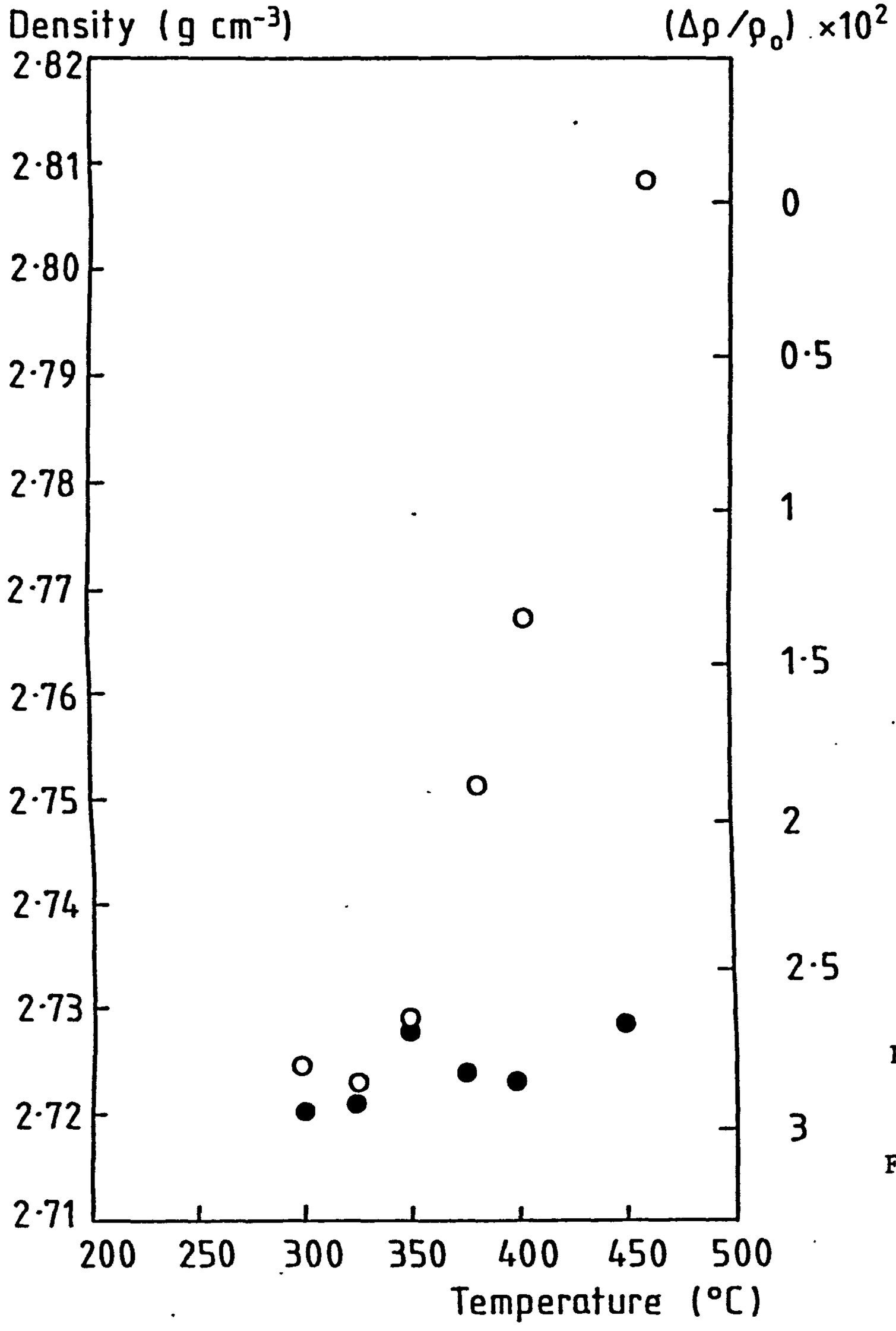

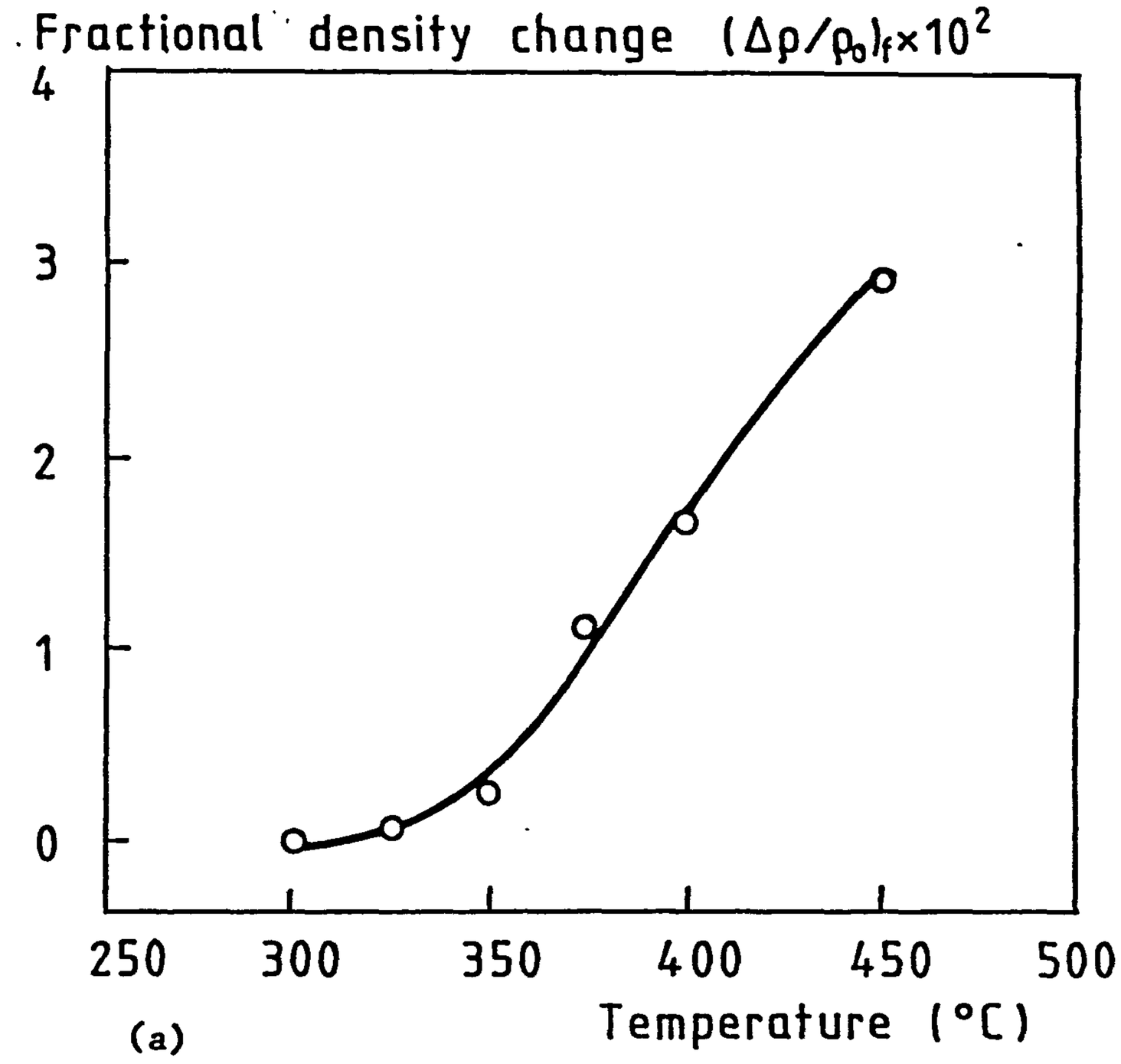

● Before HIP Region A

○ After HIP 7 MPa

Figure 55 – The effect of temperature on density (hence cavitation) in Supral 150 using 7 MPa HIP pressure.

Figure 55a – The fractional density change in as-received SPF Supral 150 after HIP at 7 MPa for various HIP temperatures.

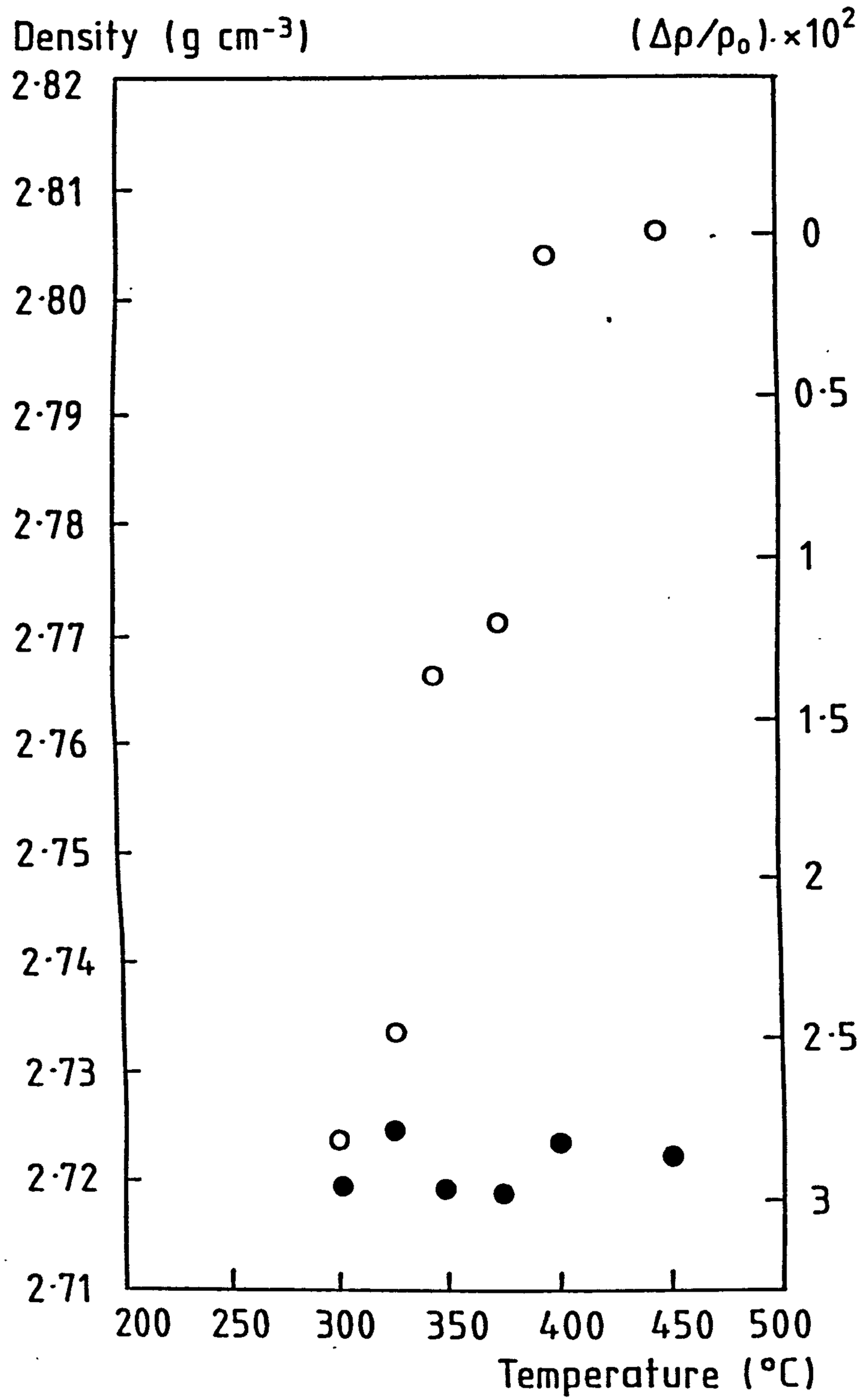

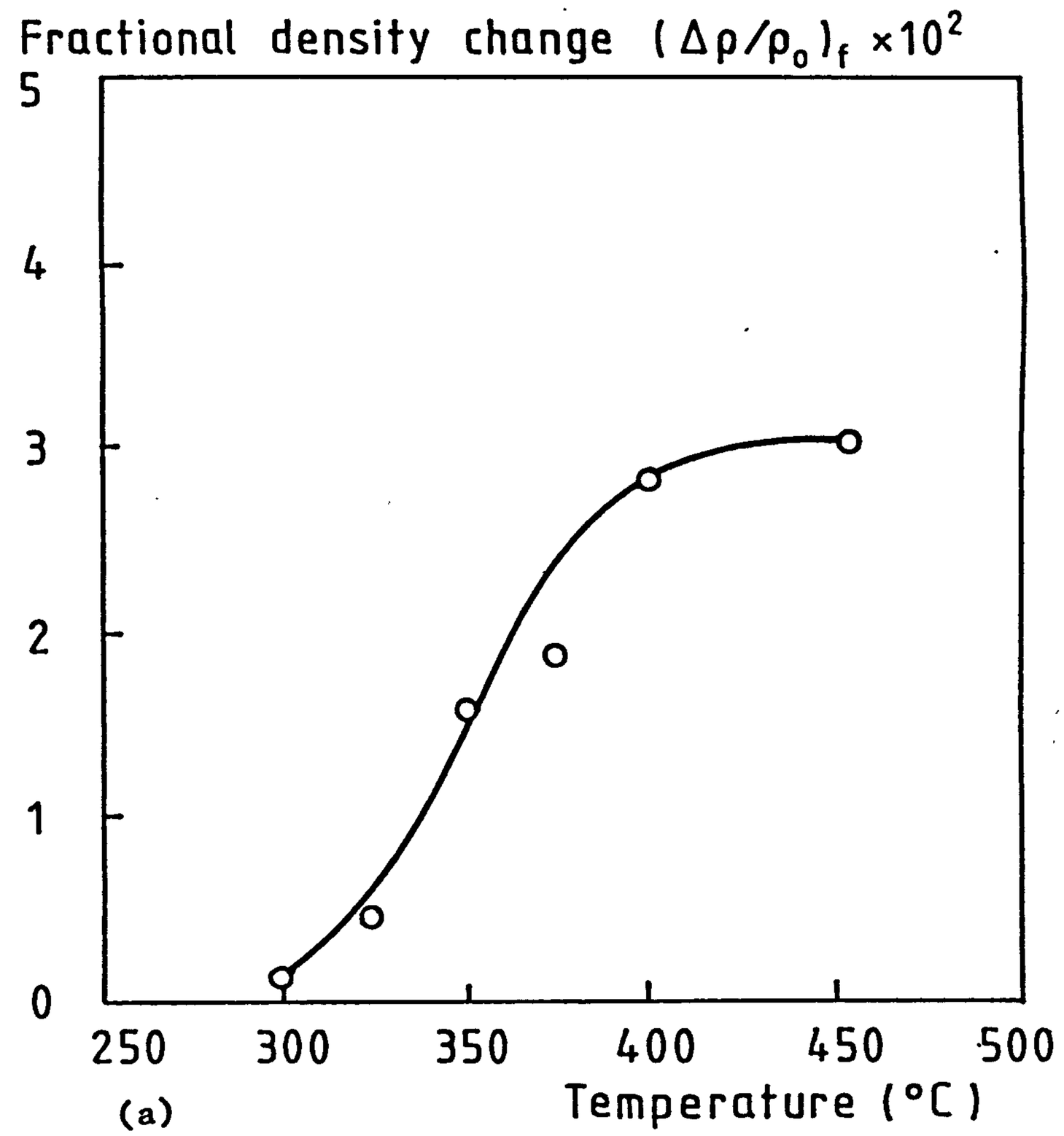

● Before HIP Region A

o After HIP 14 MPa

Figure 56 – The effect of temperature on density in SPF Supral 150 using 14 MPa HIP pressure.
(a) The fractional density change in SPF Supral 150 after HIP at various temperatures.

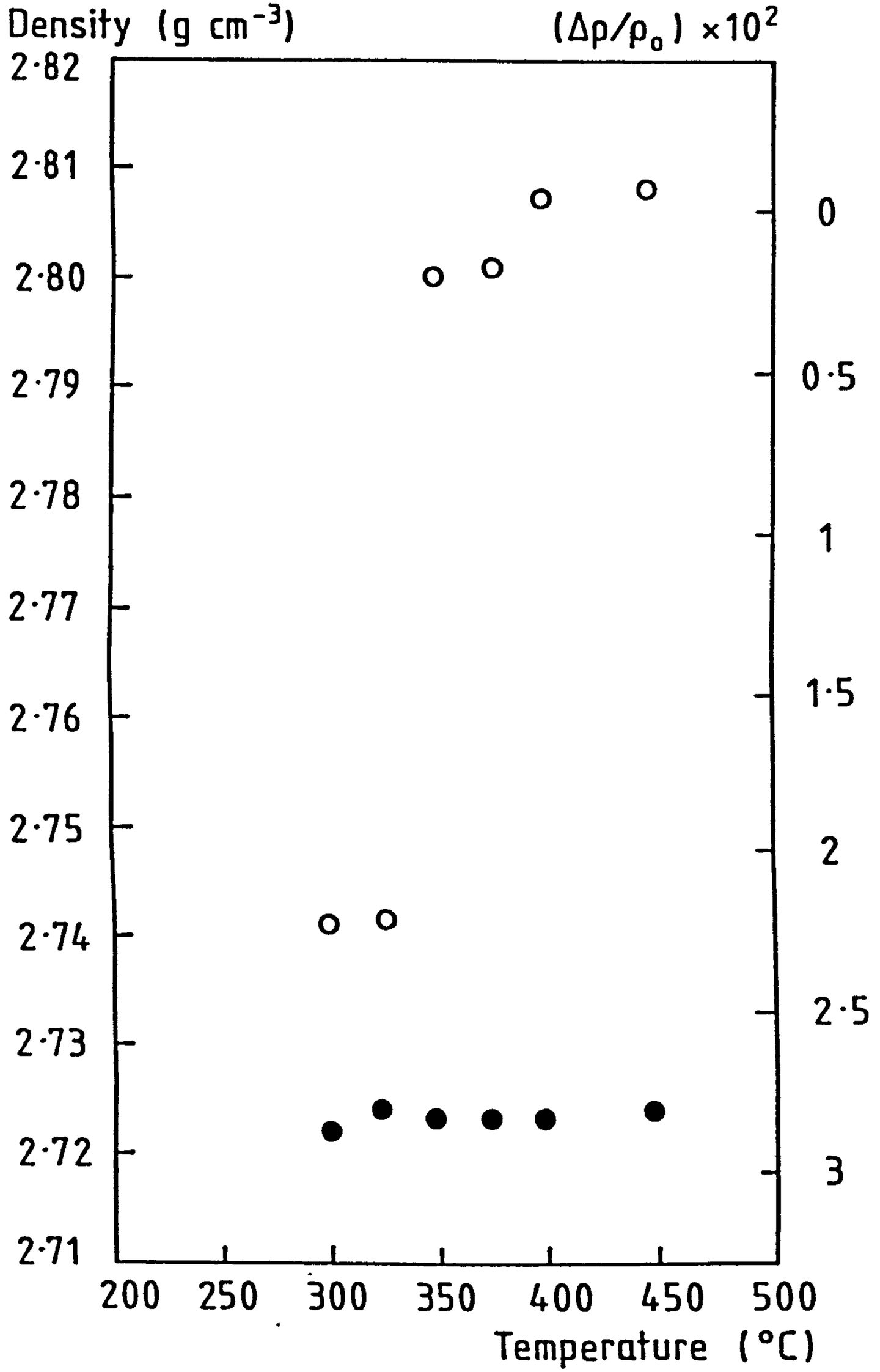

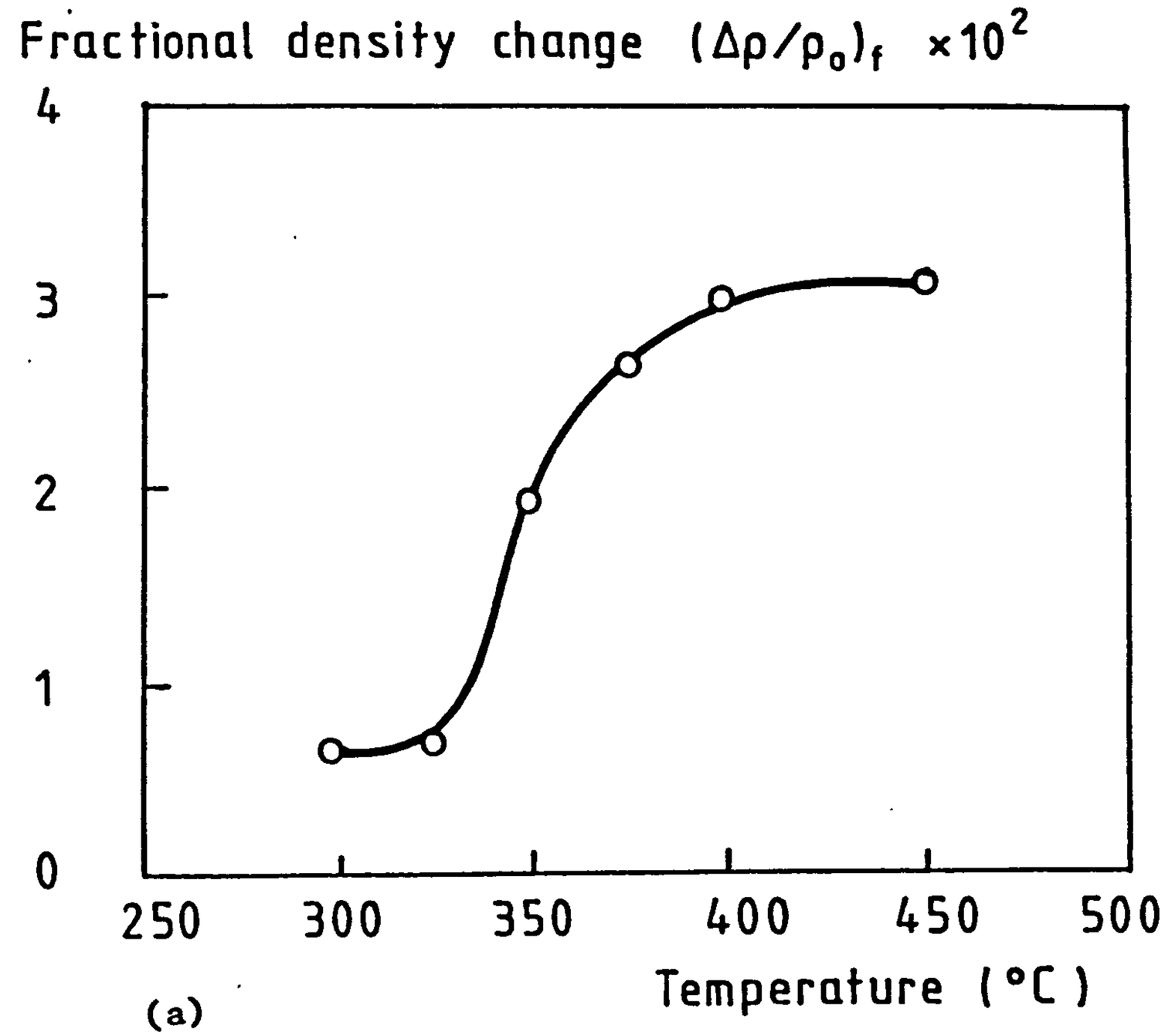

● Before HIP Region A

○ After HIP 21 MPa

Figure 57 – The effect of temperature on density in SPF Supral 150 using 21 MPa HIP pressure. (a) The fractional density change after HIP at various temperatures.

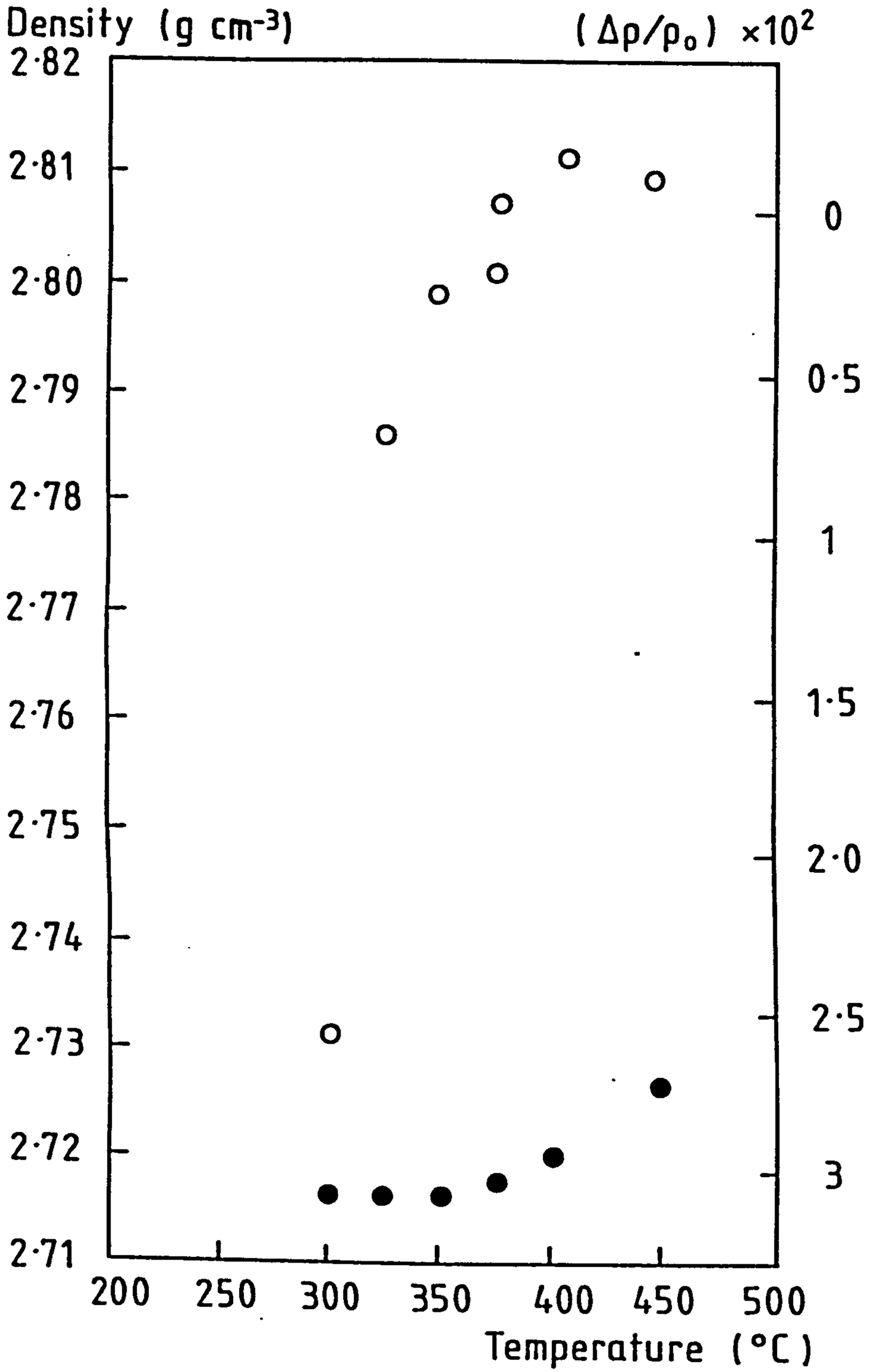

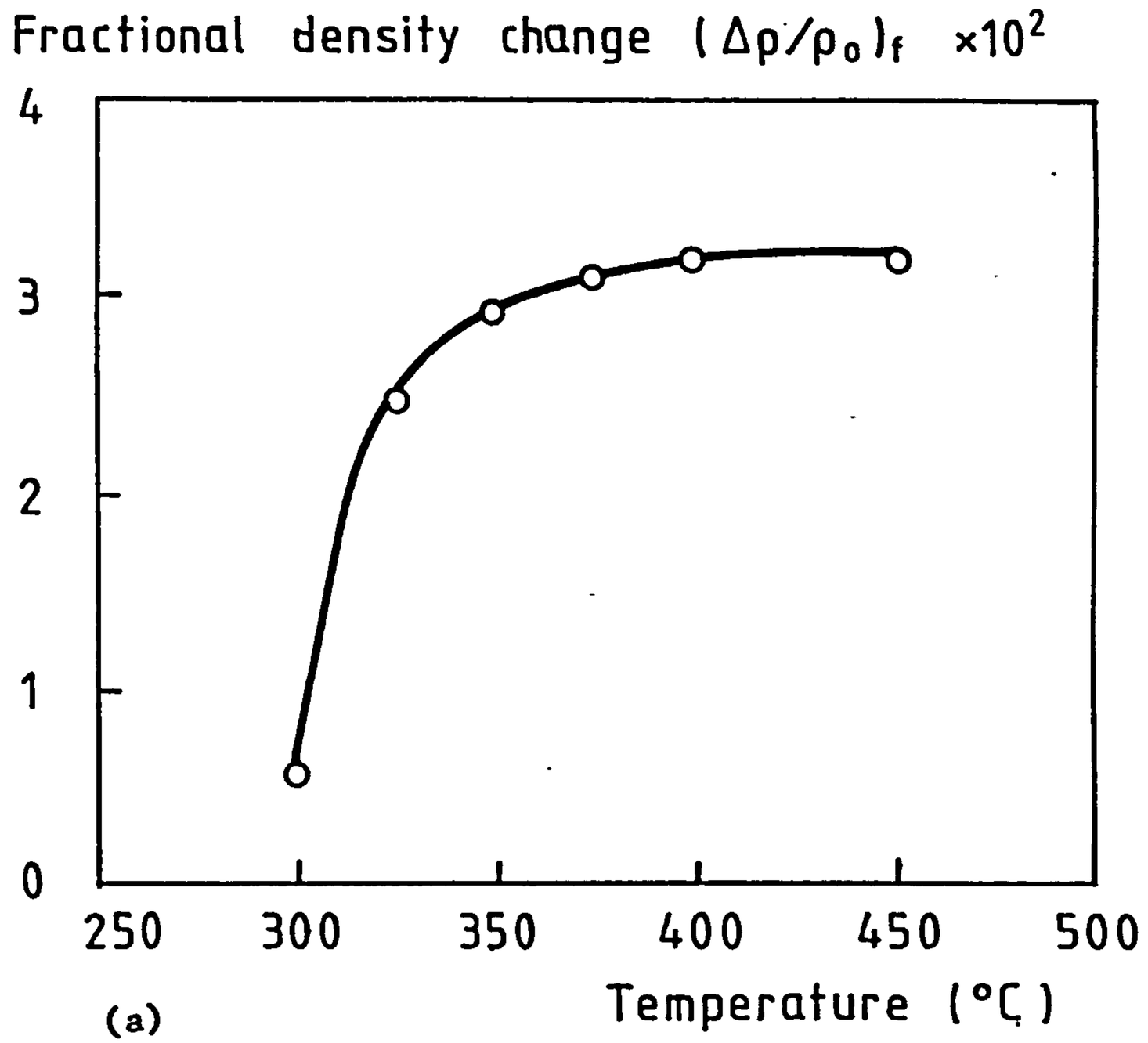

Figure 58 – The effect of temperature on density in SPF Supral 150 using 28 MPa HIP pressure. (a) The fractional density change after HIP at various temperatures.

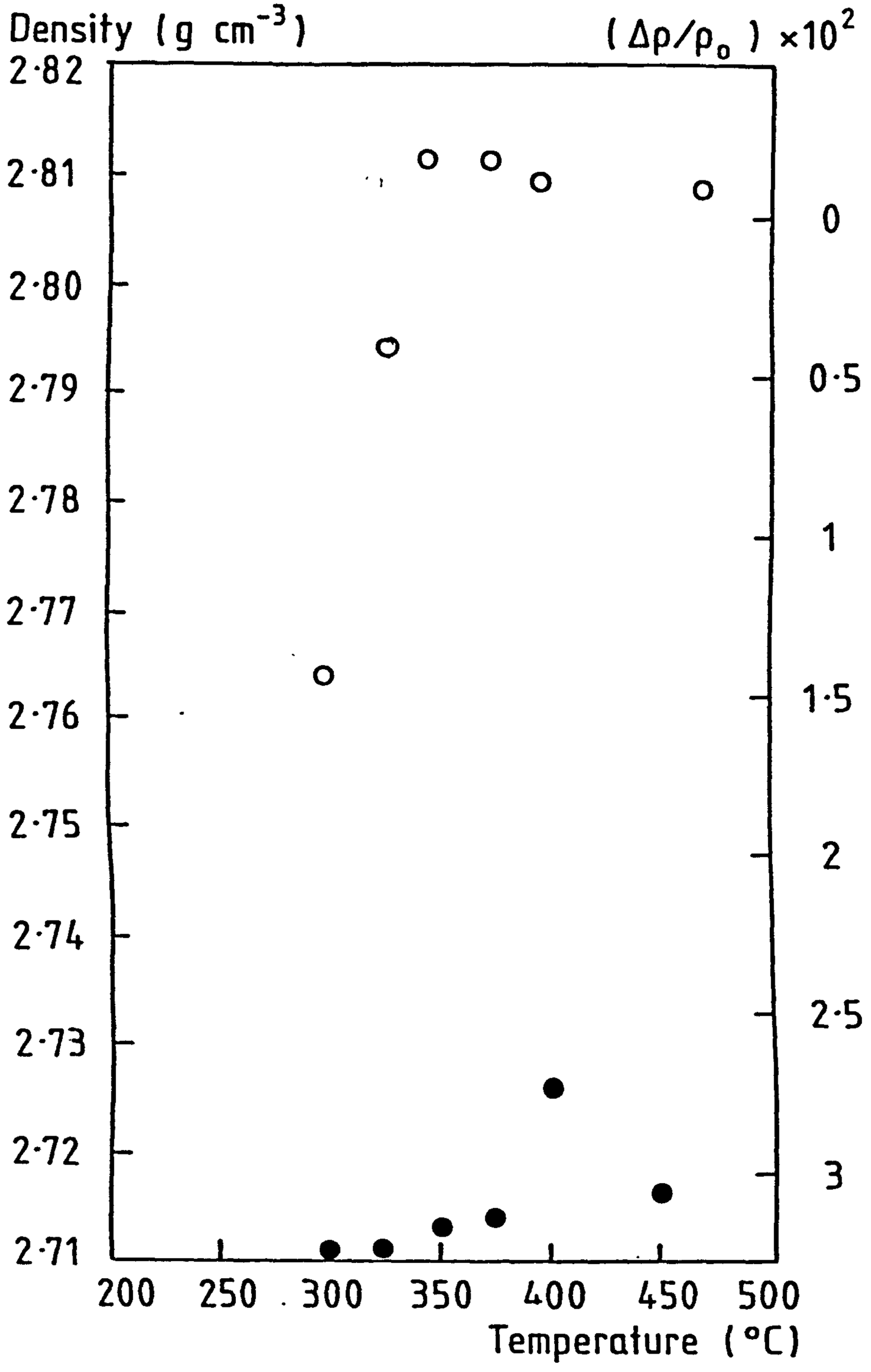

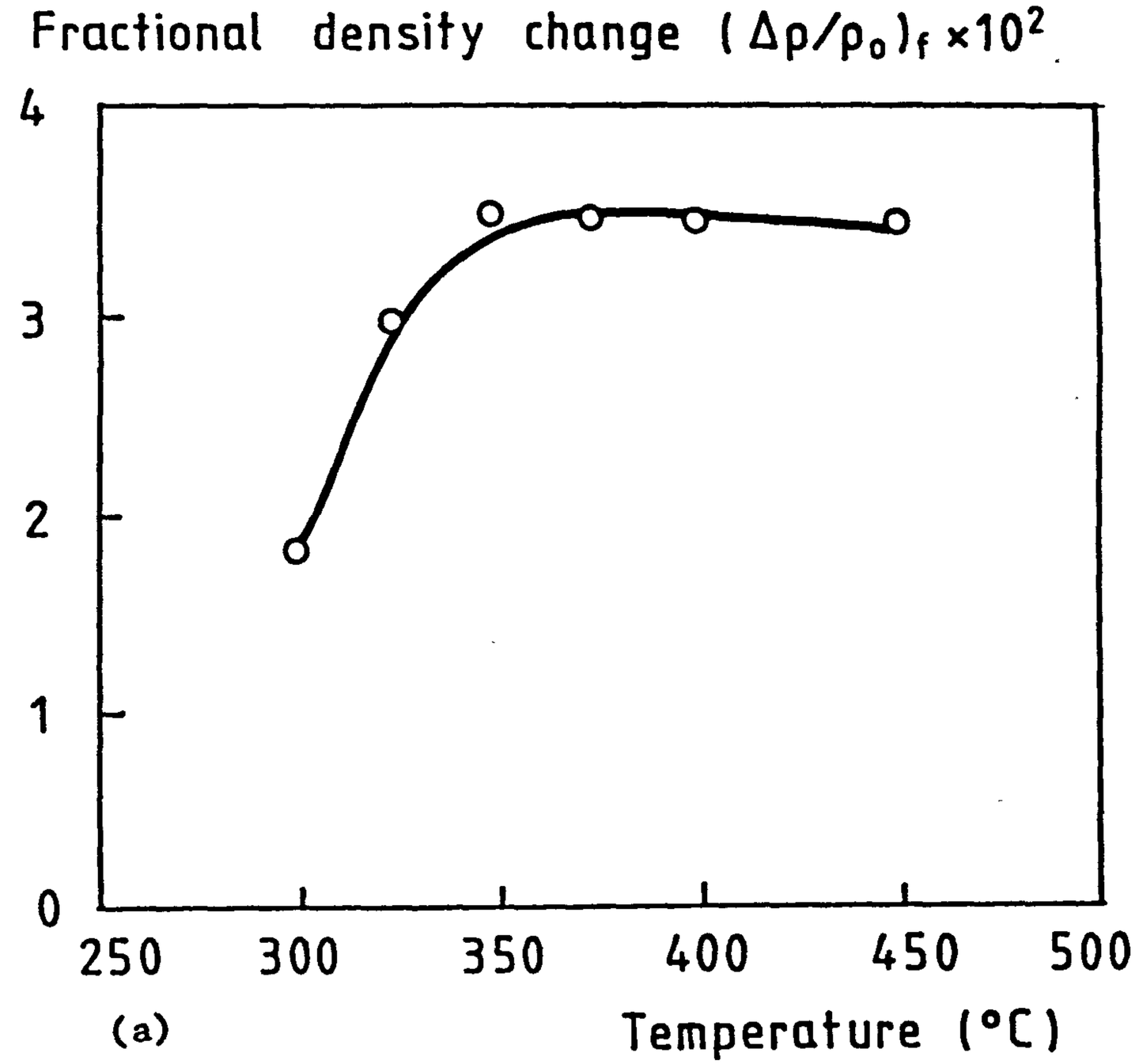

● Before HIP Region A

o After HIP 35 MPa

Figure 59 – The effect of temperature on density in SPF Supral 150 using 35 MPa HIP pressure. (a) The fractional density change after HIP at various temperatures.

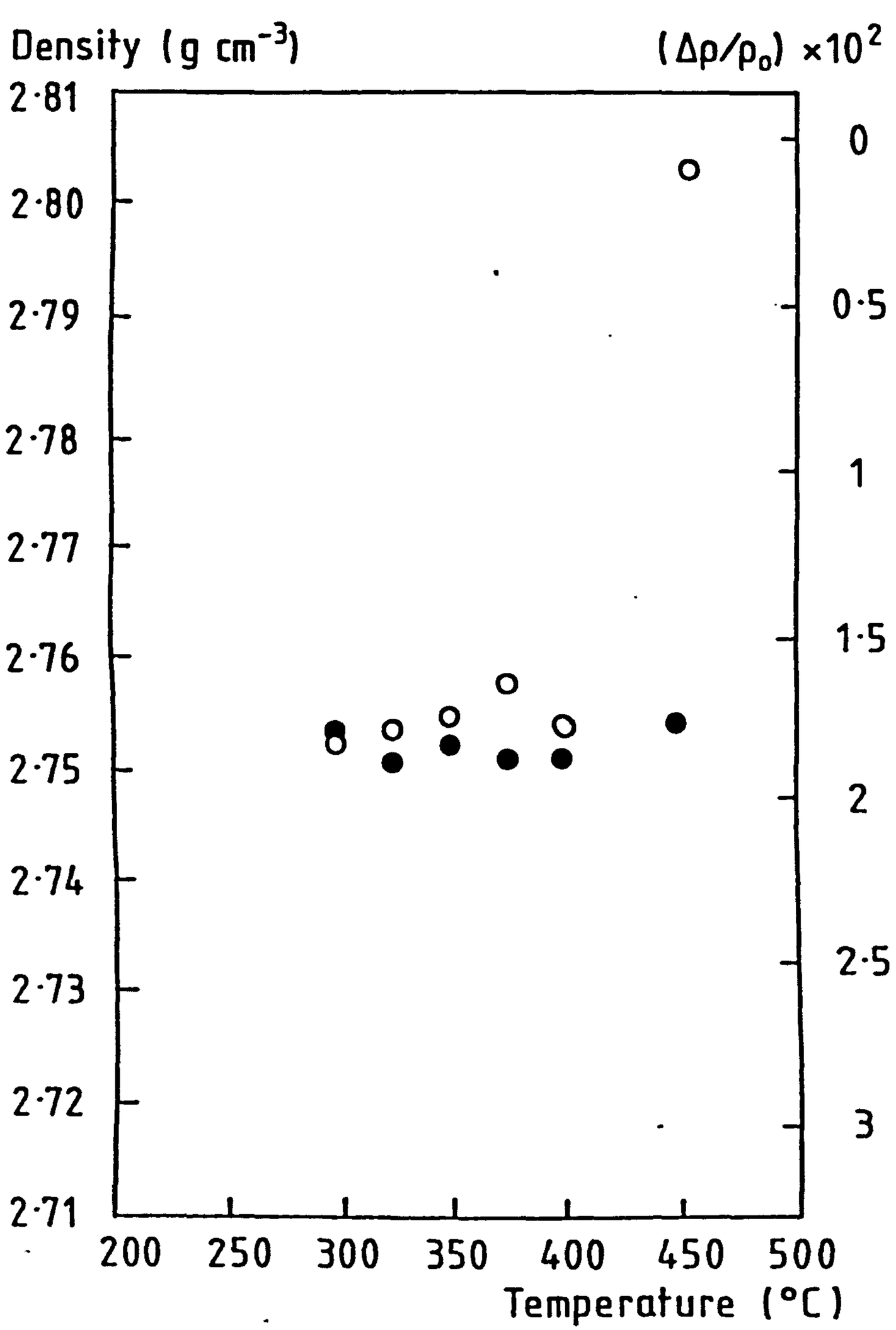

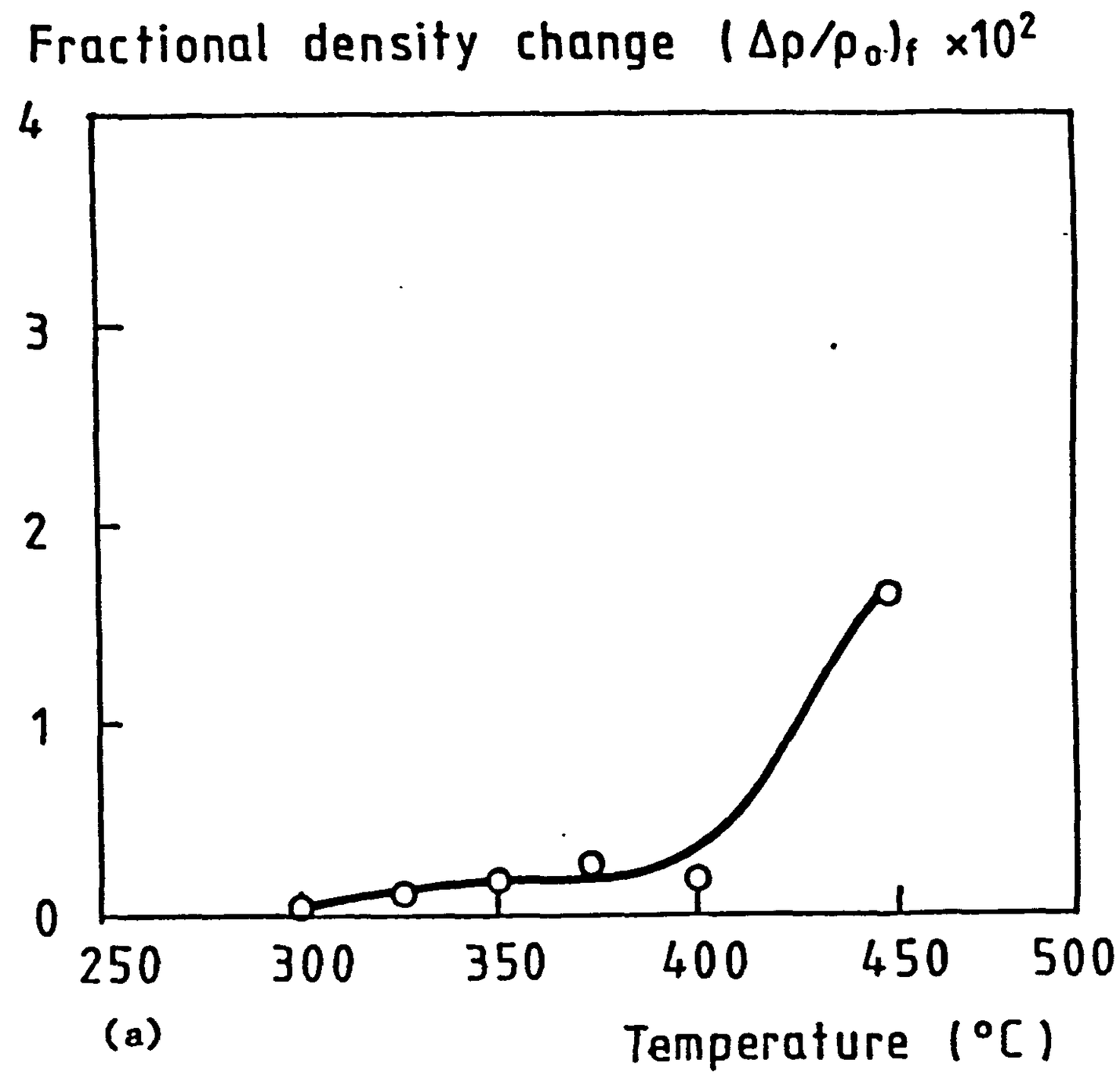

● Before HIP Region C

○ After HIP 7 MPa

Figure 60 – The effect of temperature on cavitation in SPF Supral 150 using 7 MPa HIP pressure. (a) The fractional density change in SPF Supral 150 after HIP at various temperatures.

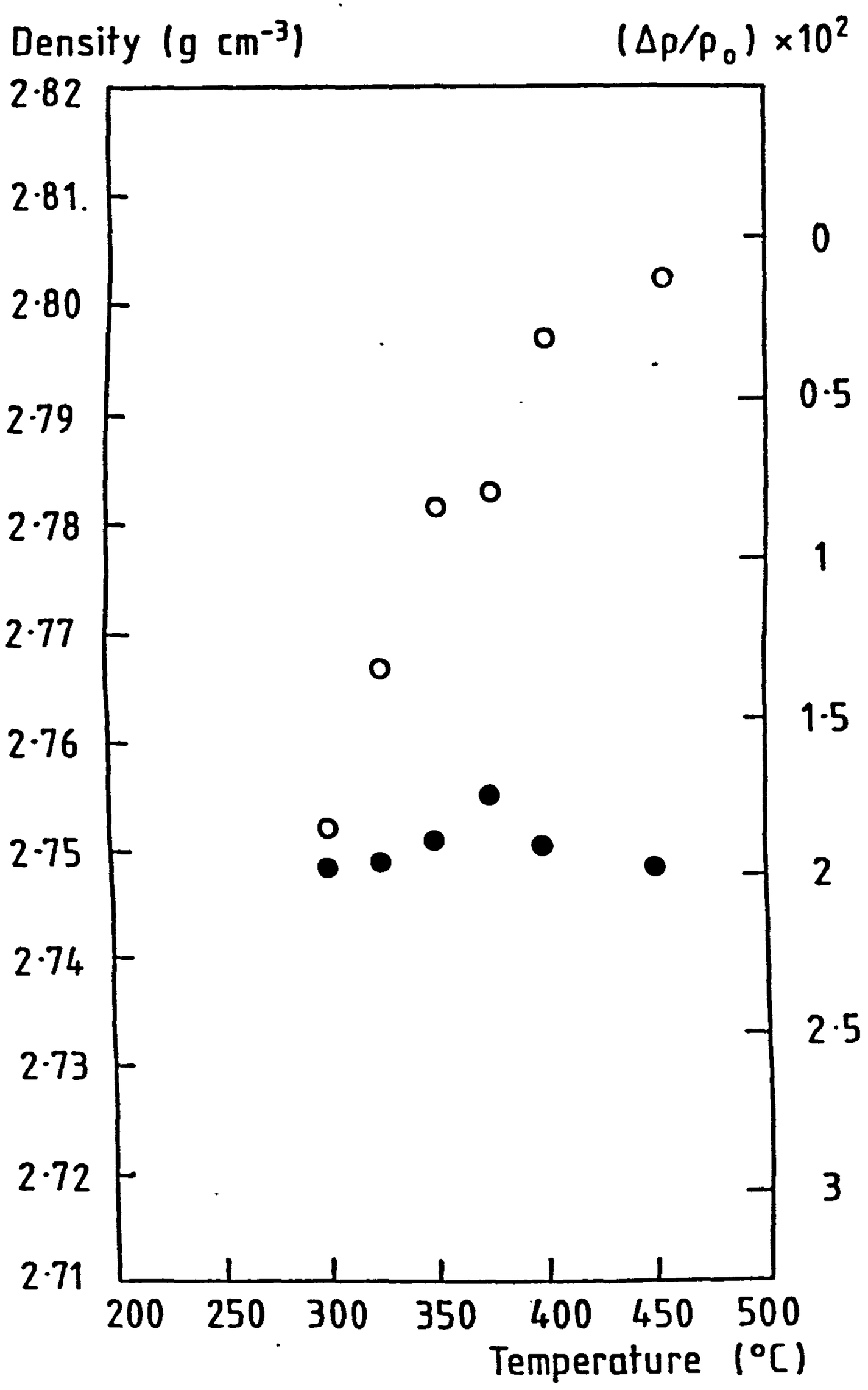

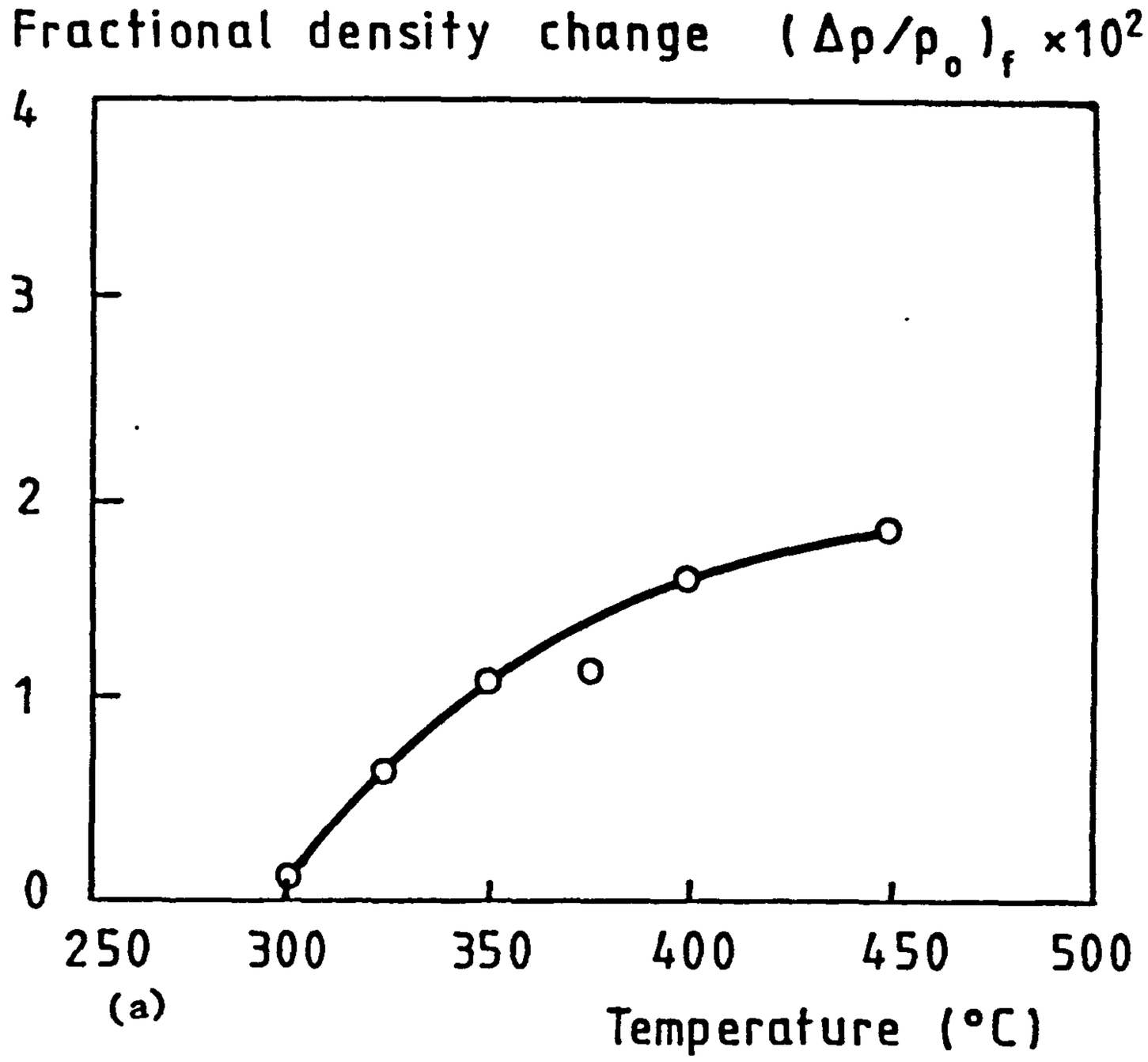

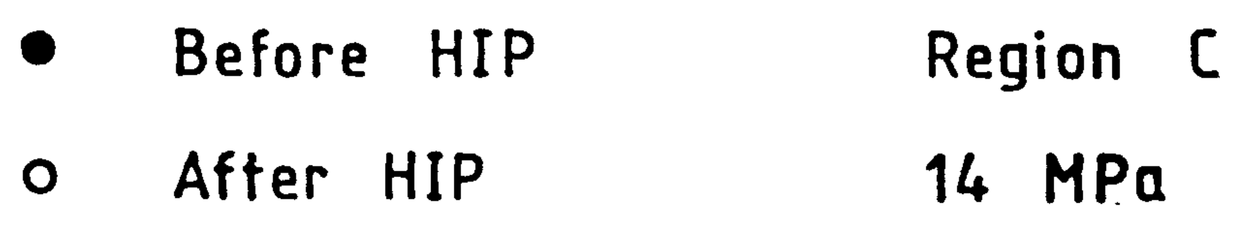

Figure 61 – The effect of temperature on cavitation in SPF Supral 150 using 14 MPa HIP pressure. (a) The fractional density change after HIP at various temperatures.

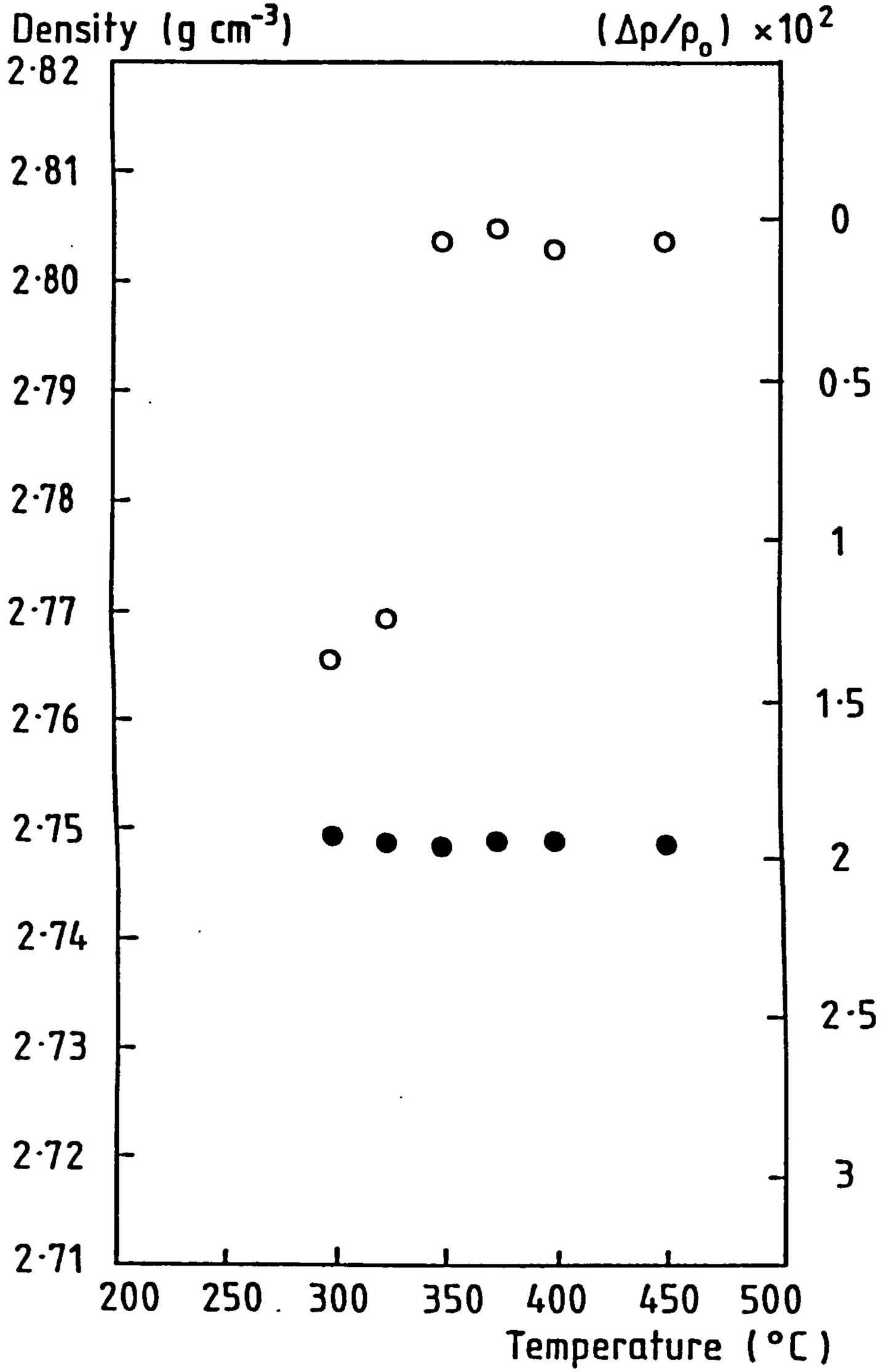

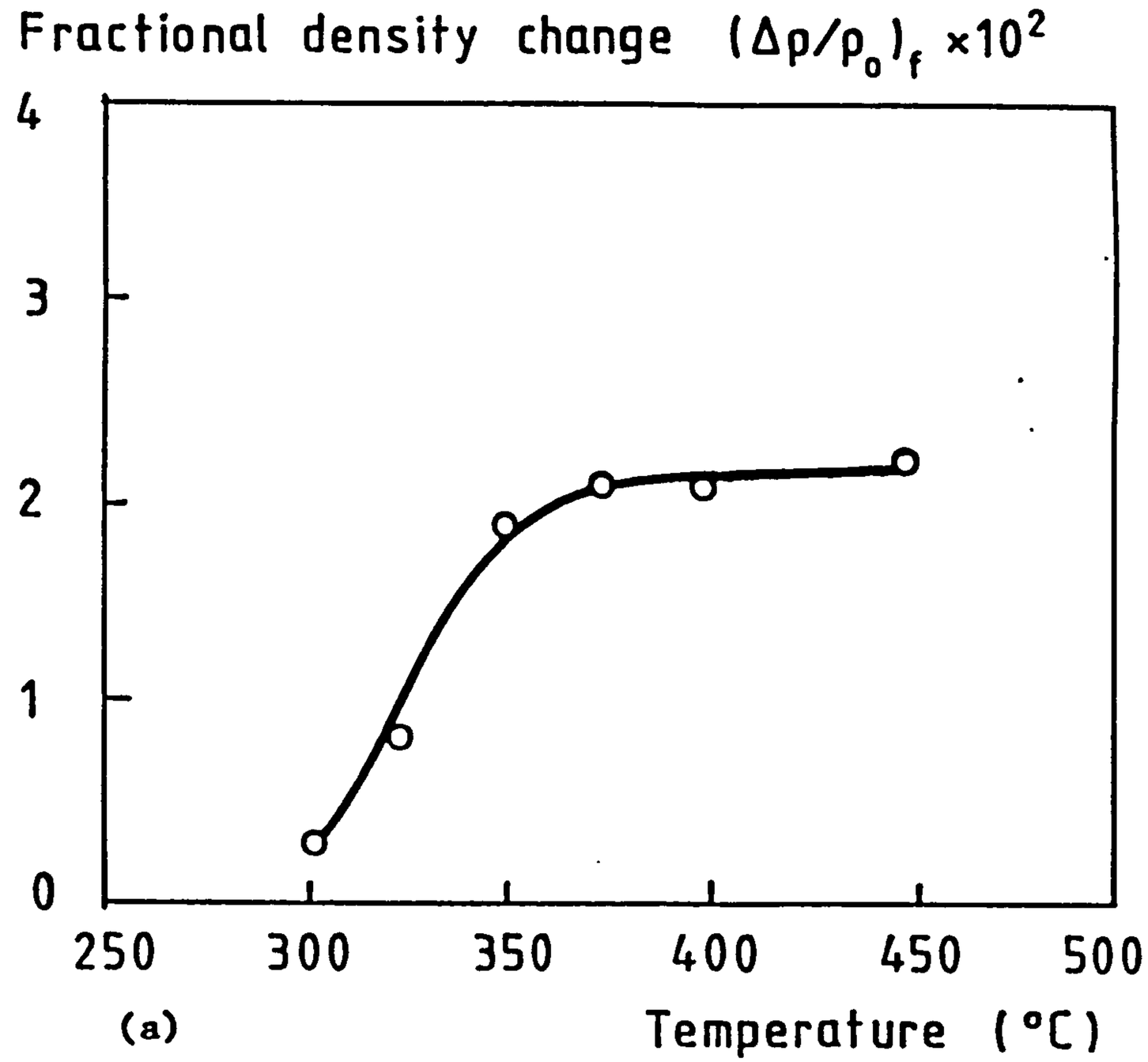

(a)

● Before HIP

○ After HIP

Region C

21 MPa

Figure 62 – The effect of temperature on cavitation in SPF Supral 150 using 21 MPa HIP pressure. (a) The fractional density change after HIP at various temperatures.

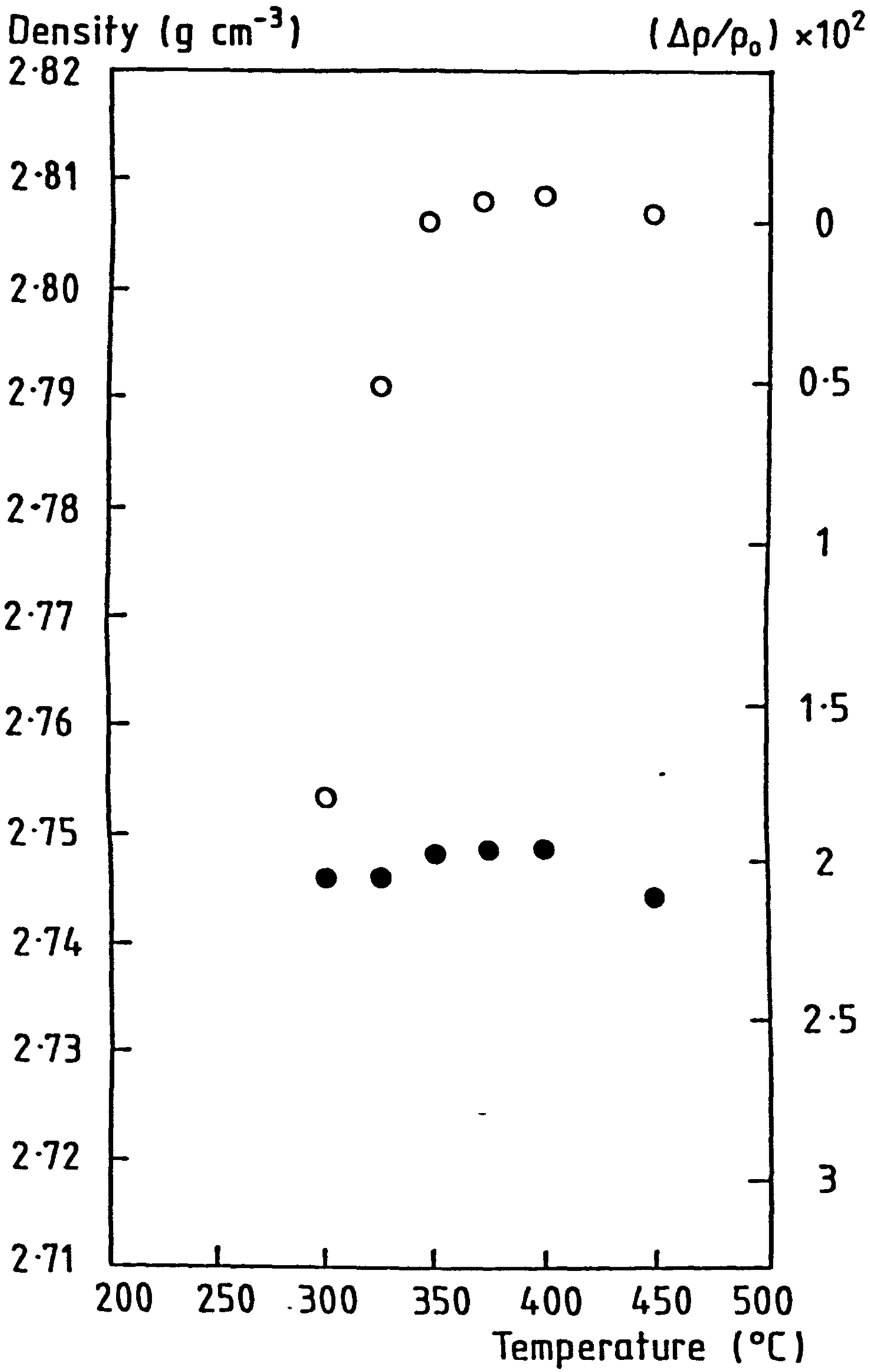

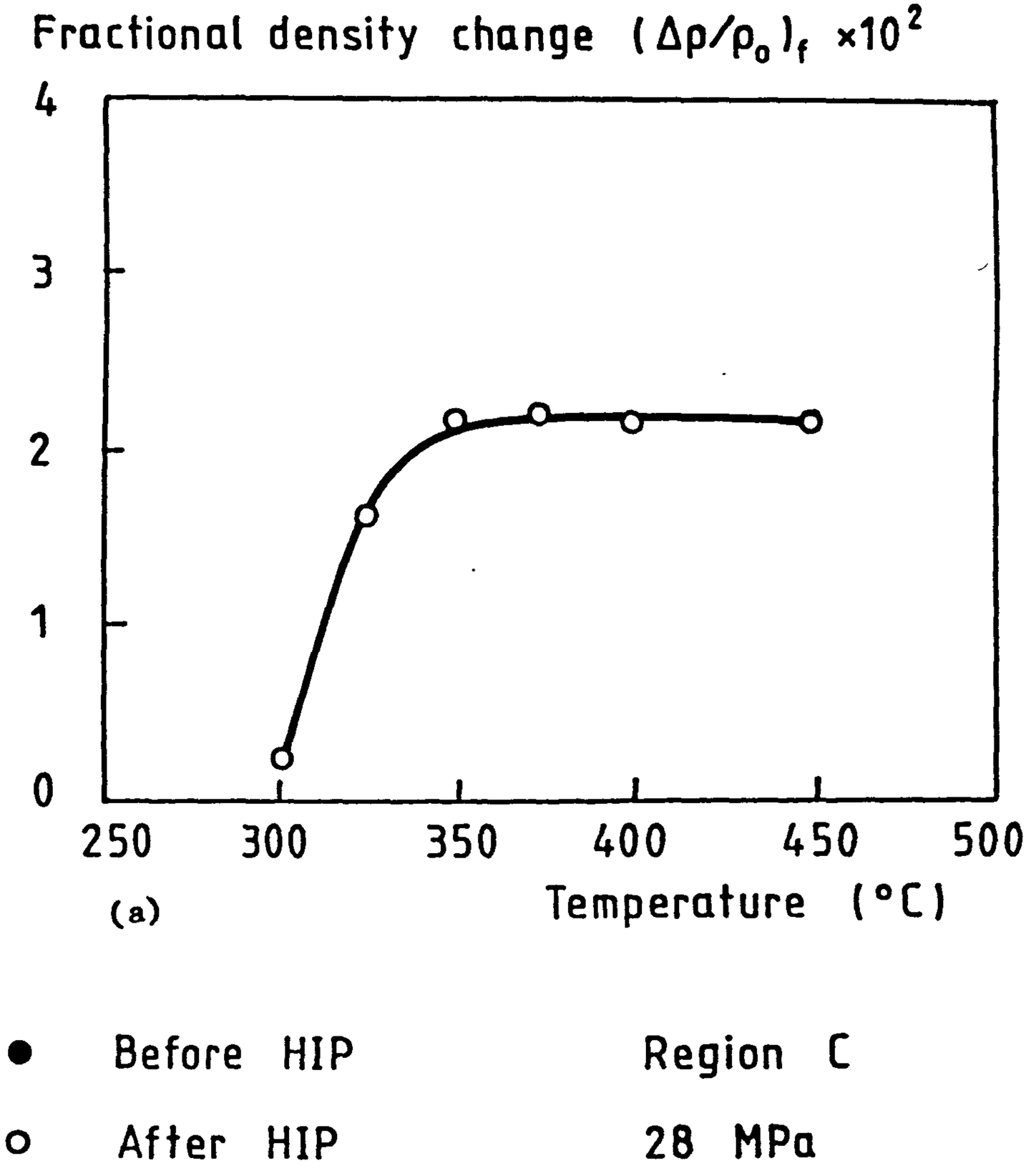

Figure 63 – The effect of temperature on cavitation in SPF Supral 150 using 28 MPa HIP pressure. (a) The fractional density change after HIP at various temperatures.

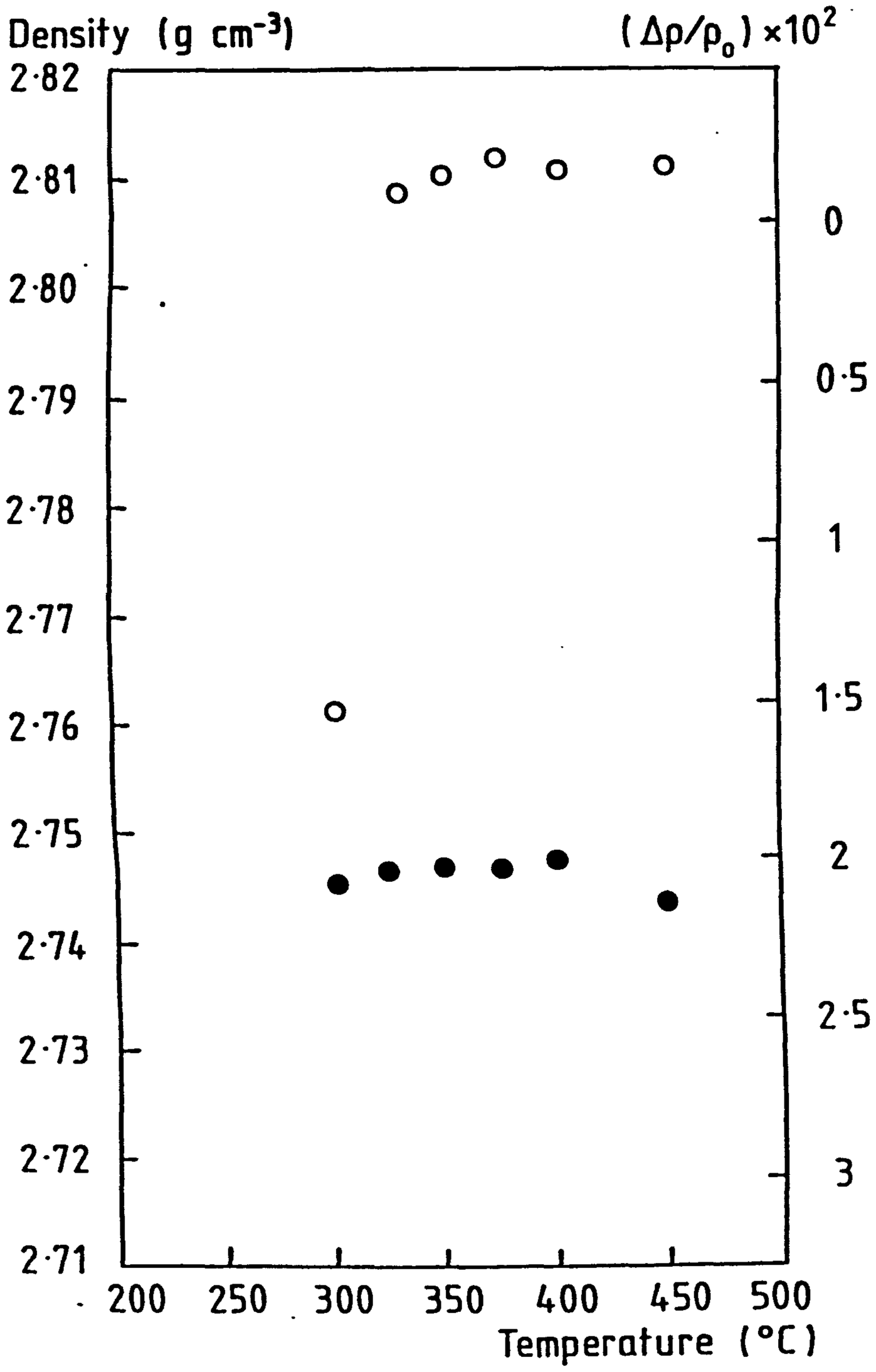

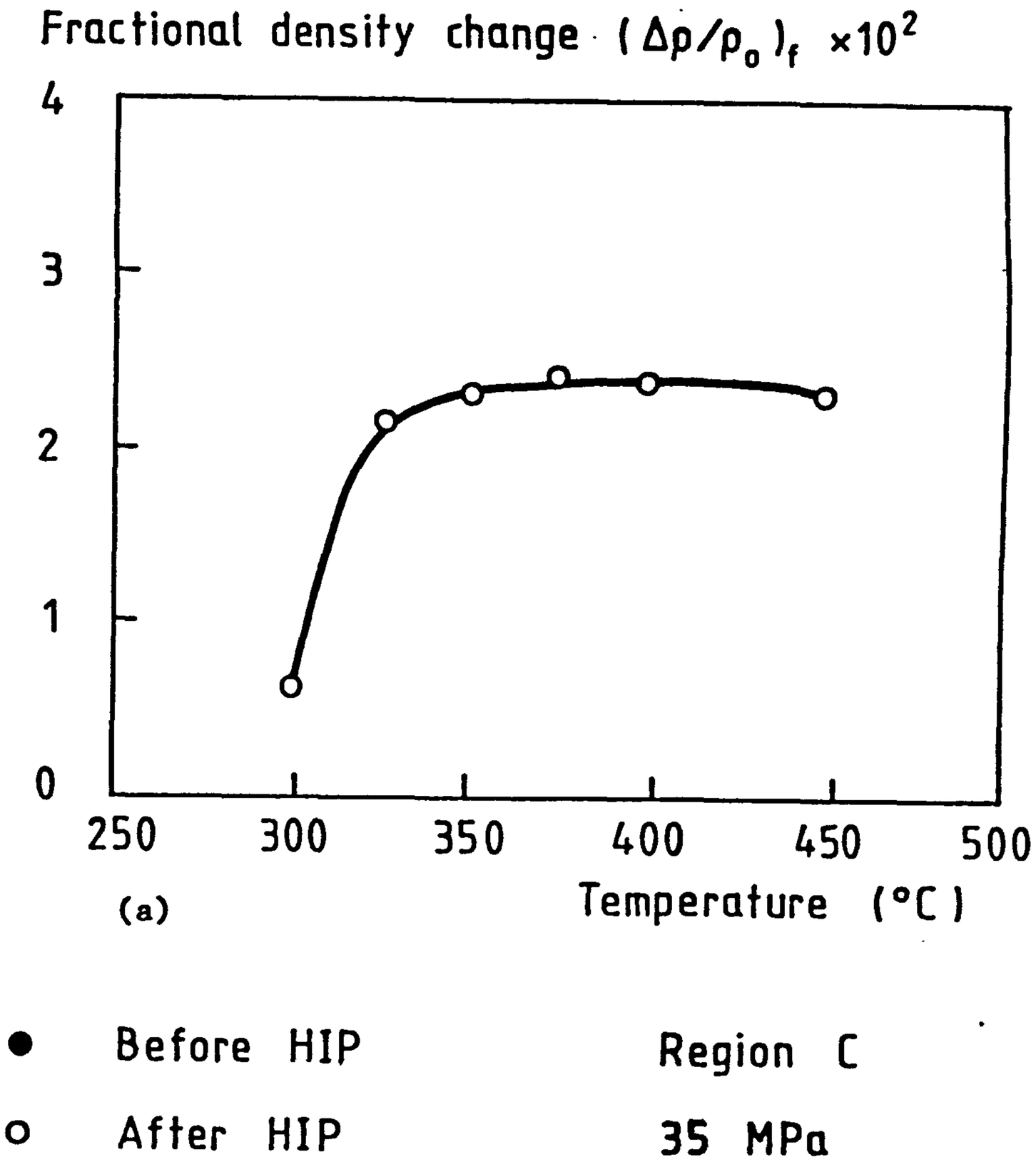

Figure 64 – The effect of temperature on cavitation in SPF Supral 150 using 35 MPa HIP pressure. (a) The fractional density change after HIP at various temperatures.

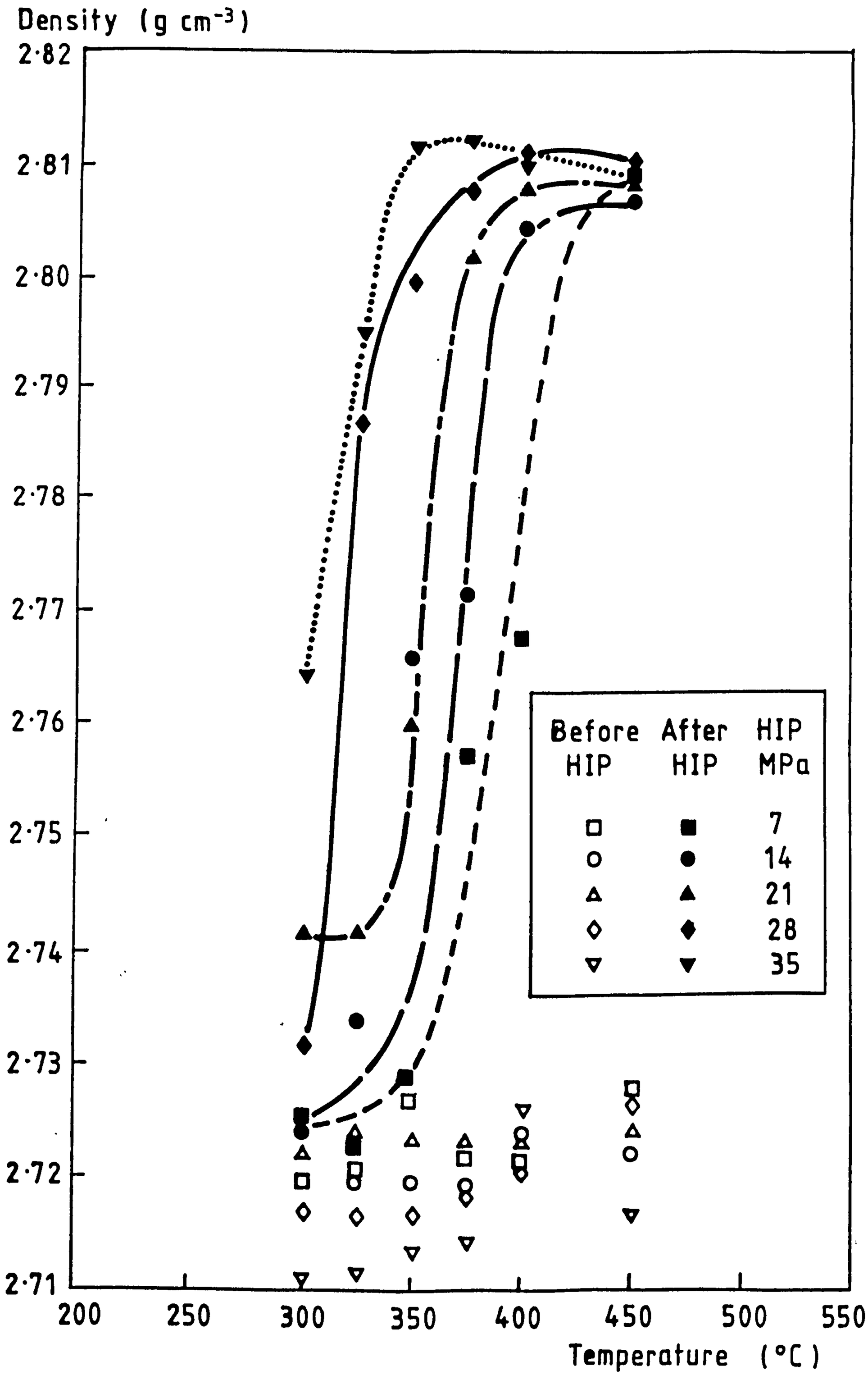

Figure 65 - Plot showing the effect of HIP temperature and pressure on cavitation in material taken from Region A (initial cavitation levels ~ 3%)

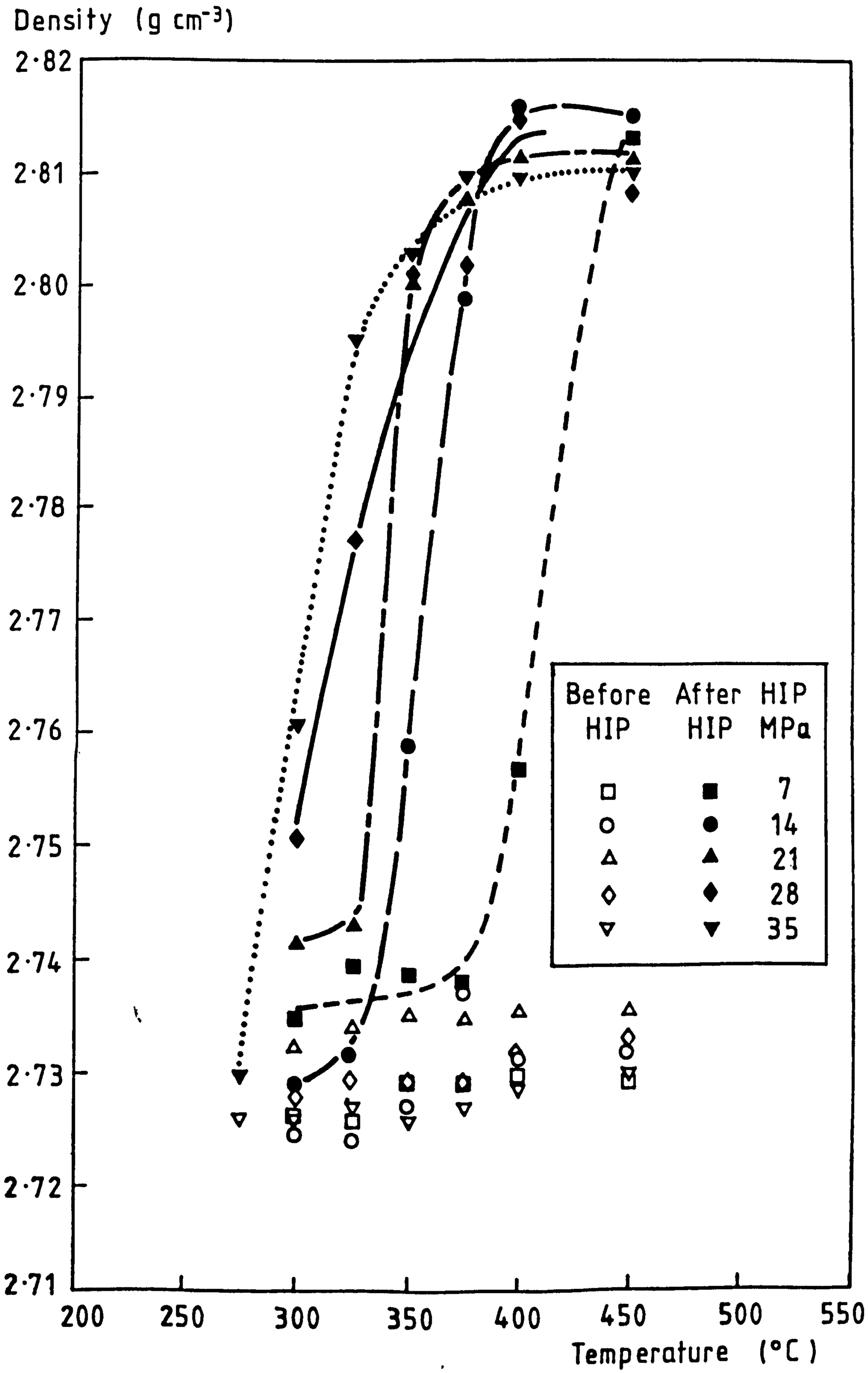

Figure 66 - The effect of HIP temperature and pressure on cavitation in SPF Supral 150 taken from Region B (initial cavity level ~ 2.5%).

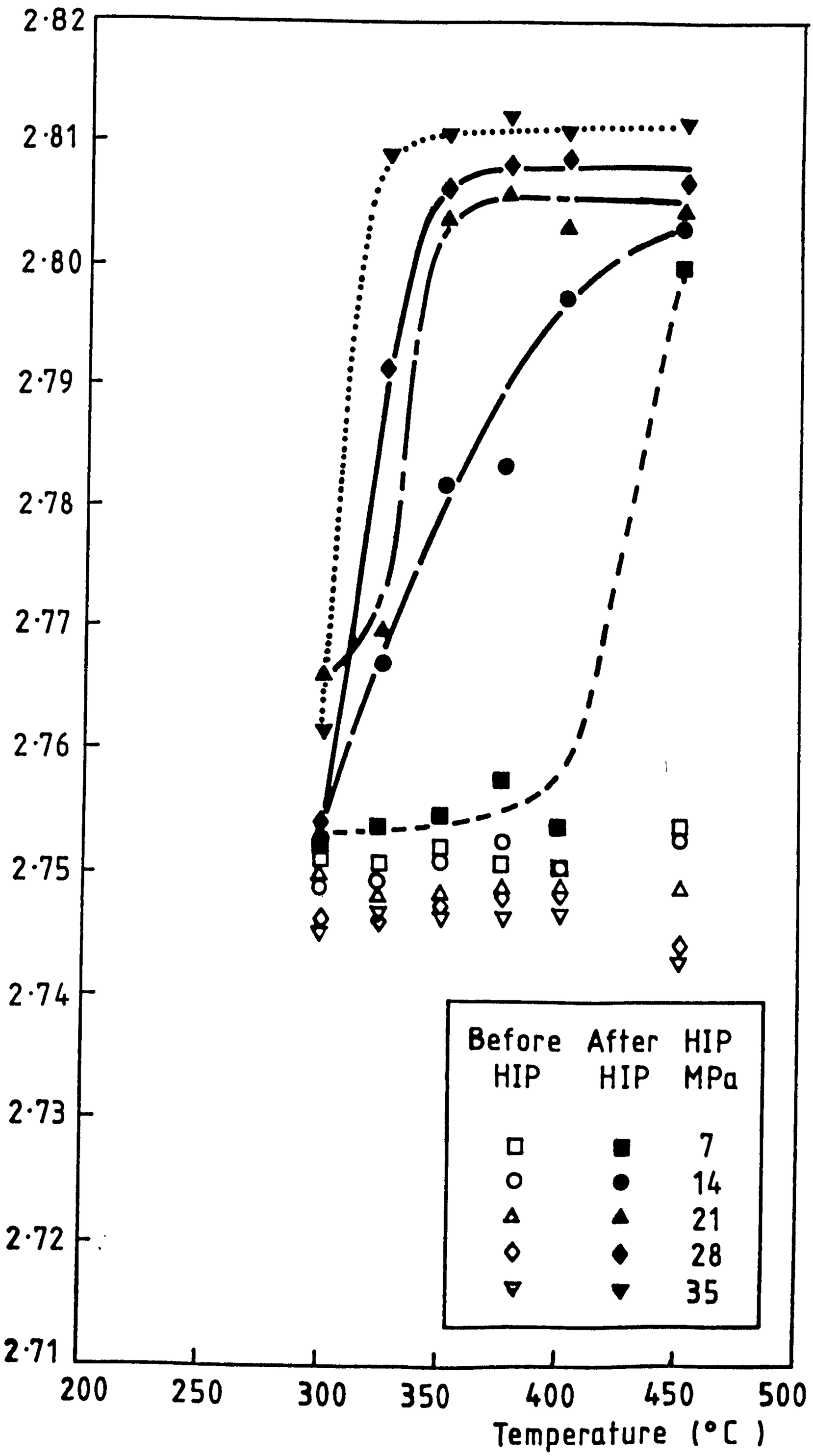

Figure 67 - The effects of HIP temperature and pressure on cavitation in SPF Supral 150 from Region C (initial cavity levels ~ 1.75%).

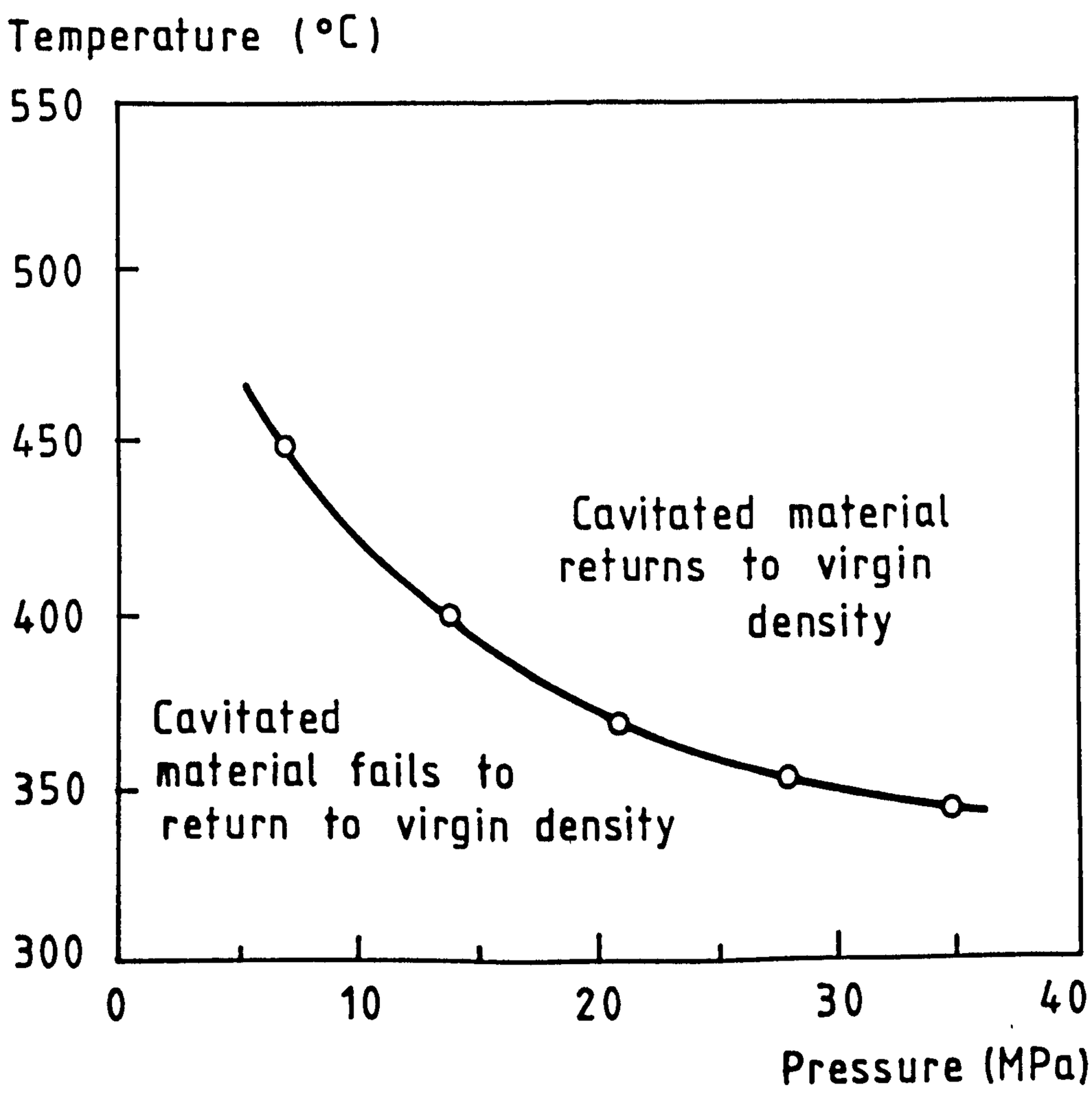

Figure 68 - Shows the conditions of temperature and pressure which return cavitated material to theoretical density.

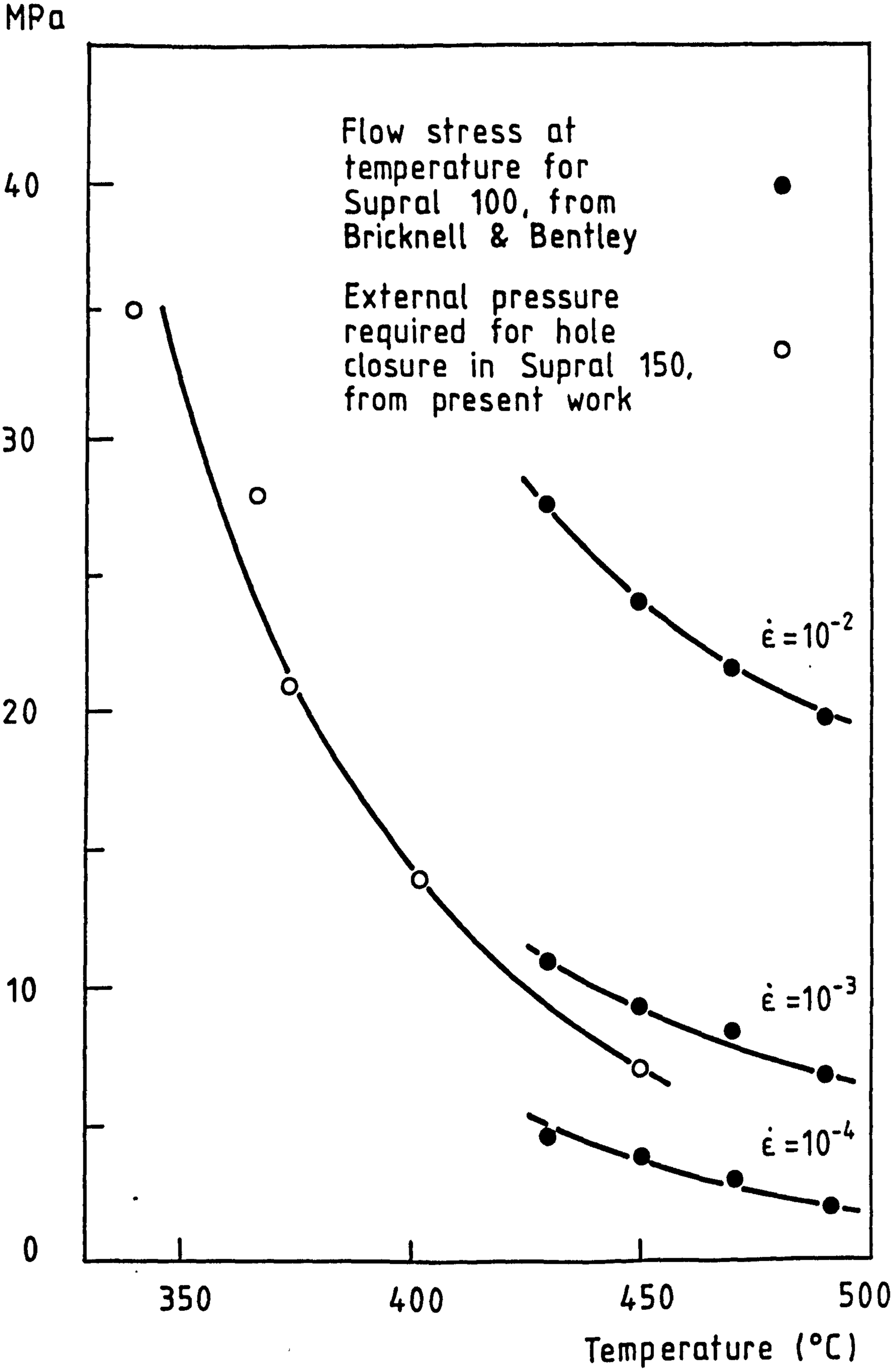

Figure 69 - Figure showing the variation of flow stress with temperature and strain-rate in Supral (from Bricknell and Bentley (158)) along with the values of external pressure and temperature required for complete cavity closure, from Figure 68.

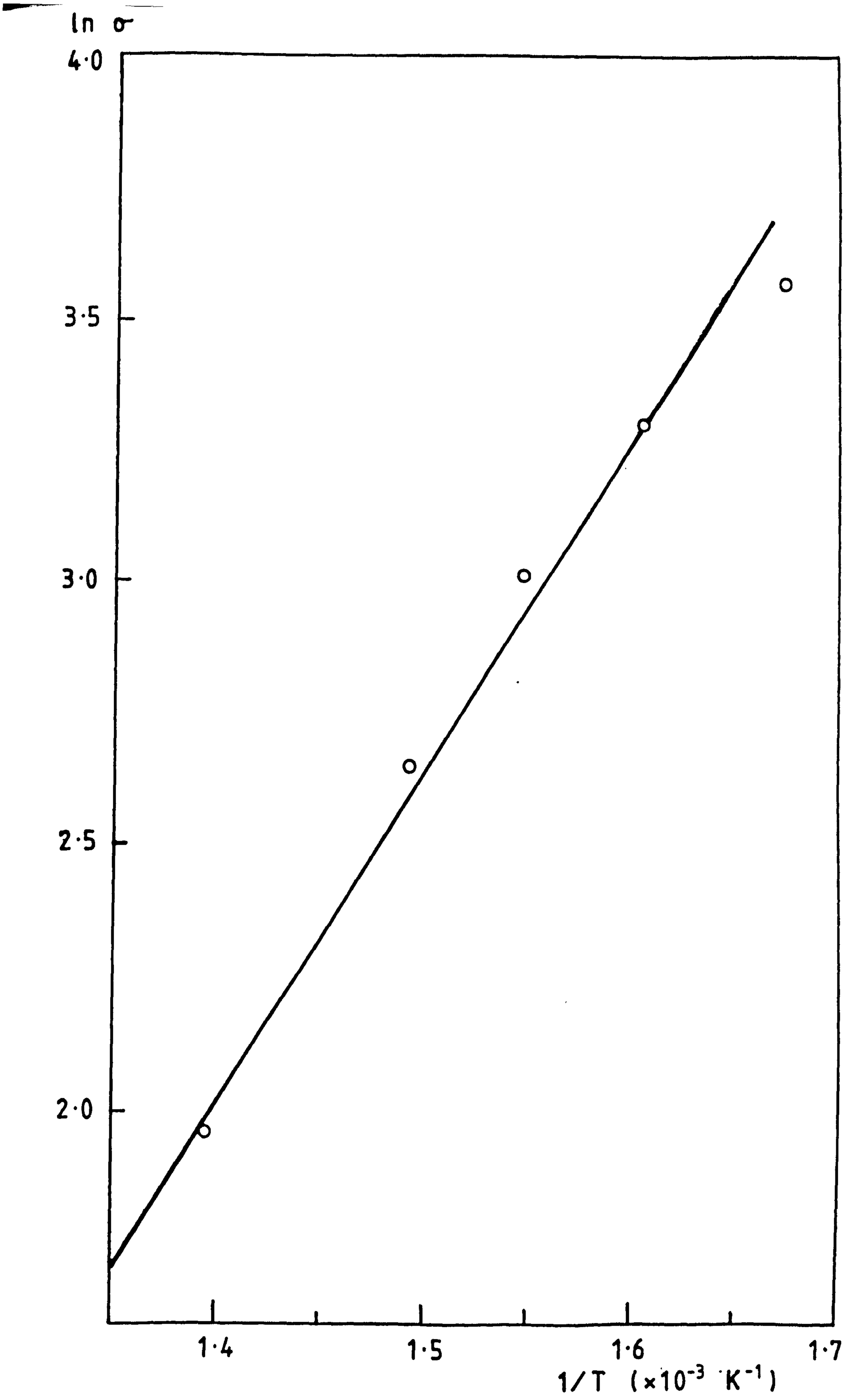

Figure 70 - The Arrhenius plot used to determine activation energies at constant strain-rate ($Q_{\dot{\varepsilon}}$) from the data in Figure 68, assuming the external pressure needed for hole closure equals the flow stress of the material at that temperature and strain-rate, giving a value of $Q_{\dot{\varepsilon}}$ of 53.54 KJ mol^{-1}.

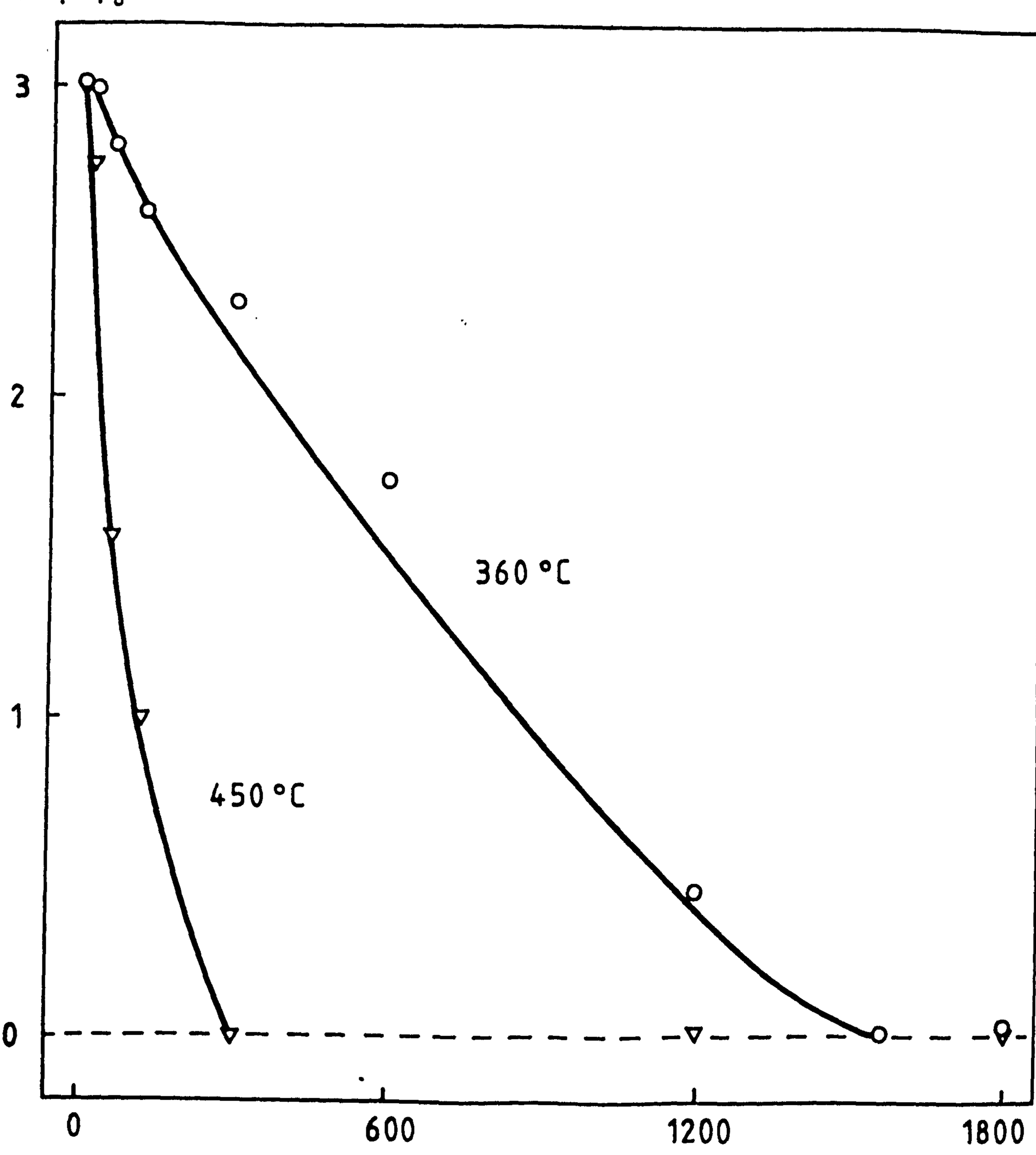

Figure 71 - The time needed for cavity closure under 28 MPa at 360°C and 450°C in Supral 150.

(x 40)

Figure 72 - Micrograph of SPF Supral 150 after HIP (450°C, 28 MPa, ½hr) showing no visible cavitation (x 40).

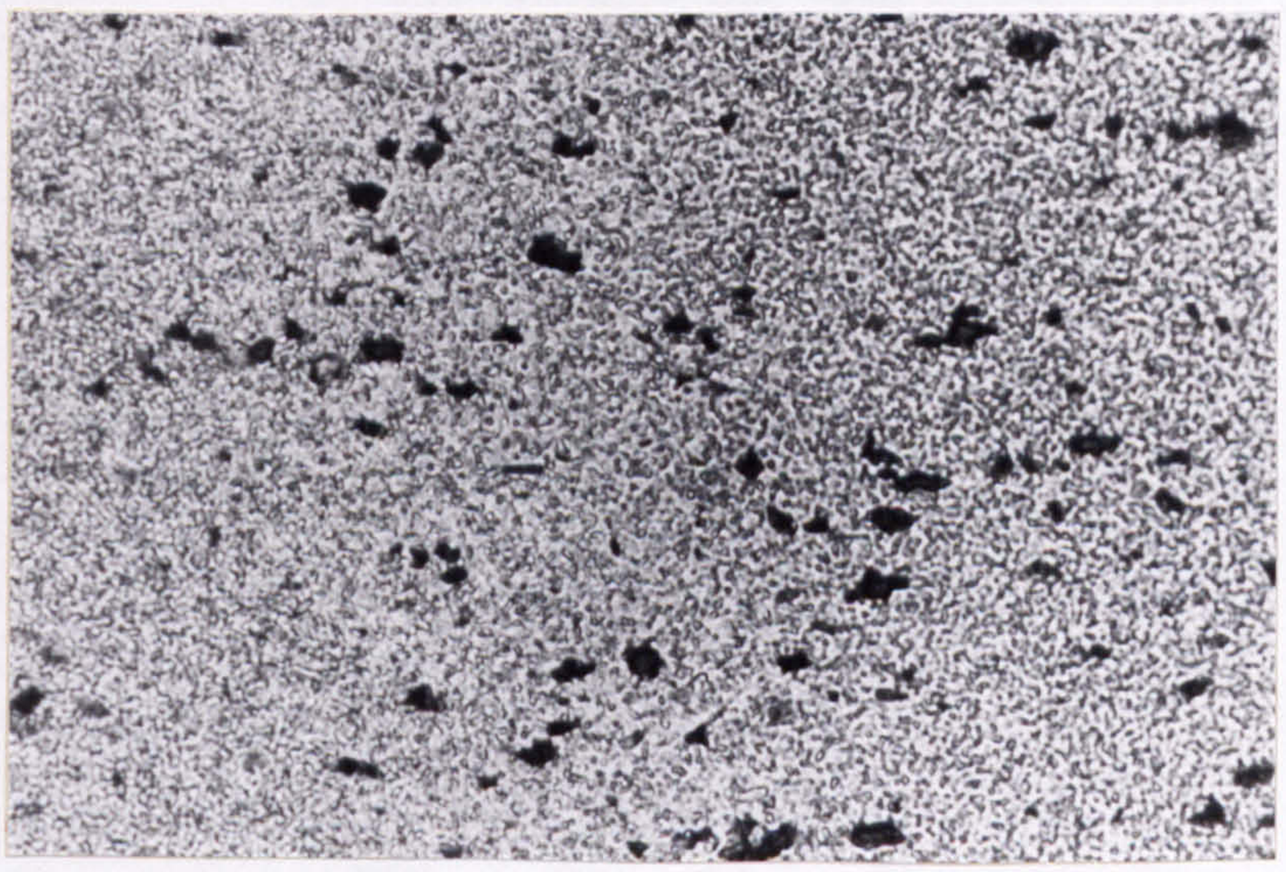

(x 300)

Figure 72(a)- As above, but etched to show structure (x 300).

(x 75)

Figure 72(b)- Optical micrograph of SPF Supral 150 after HIP (28 MPa, 450°C, ½hr) + T6 (x 75).

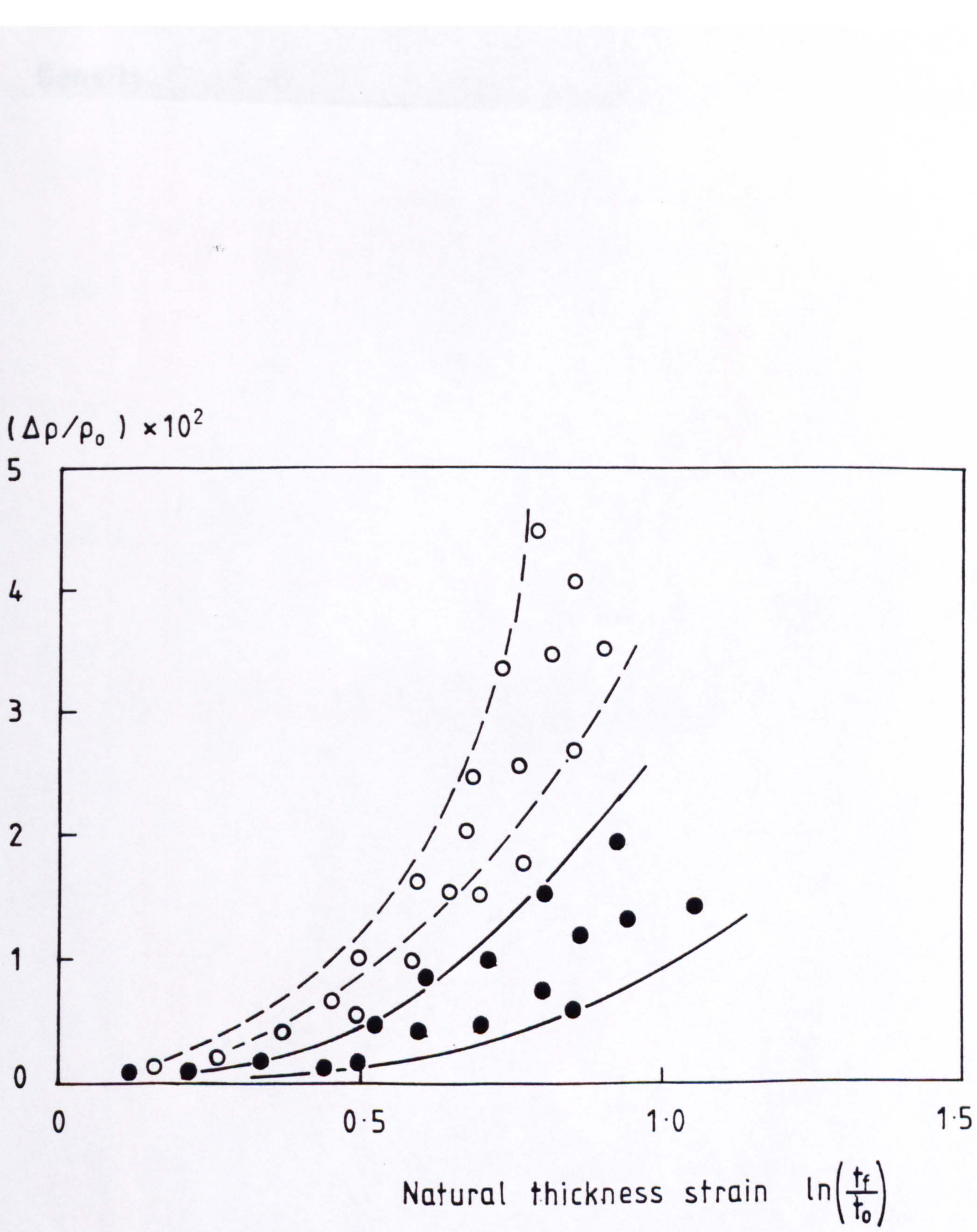

Figure 73 - Effect of solution-heat treatment on cavitation in SPF Supral 150.

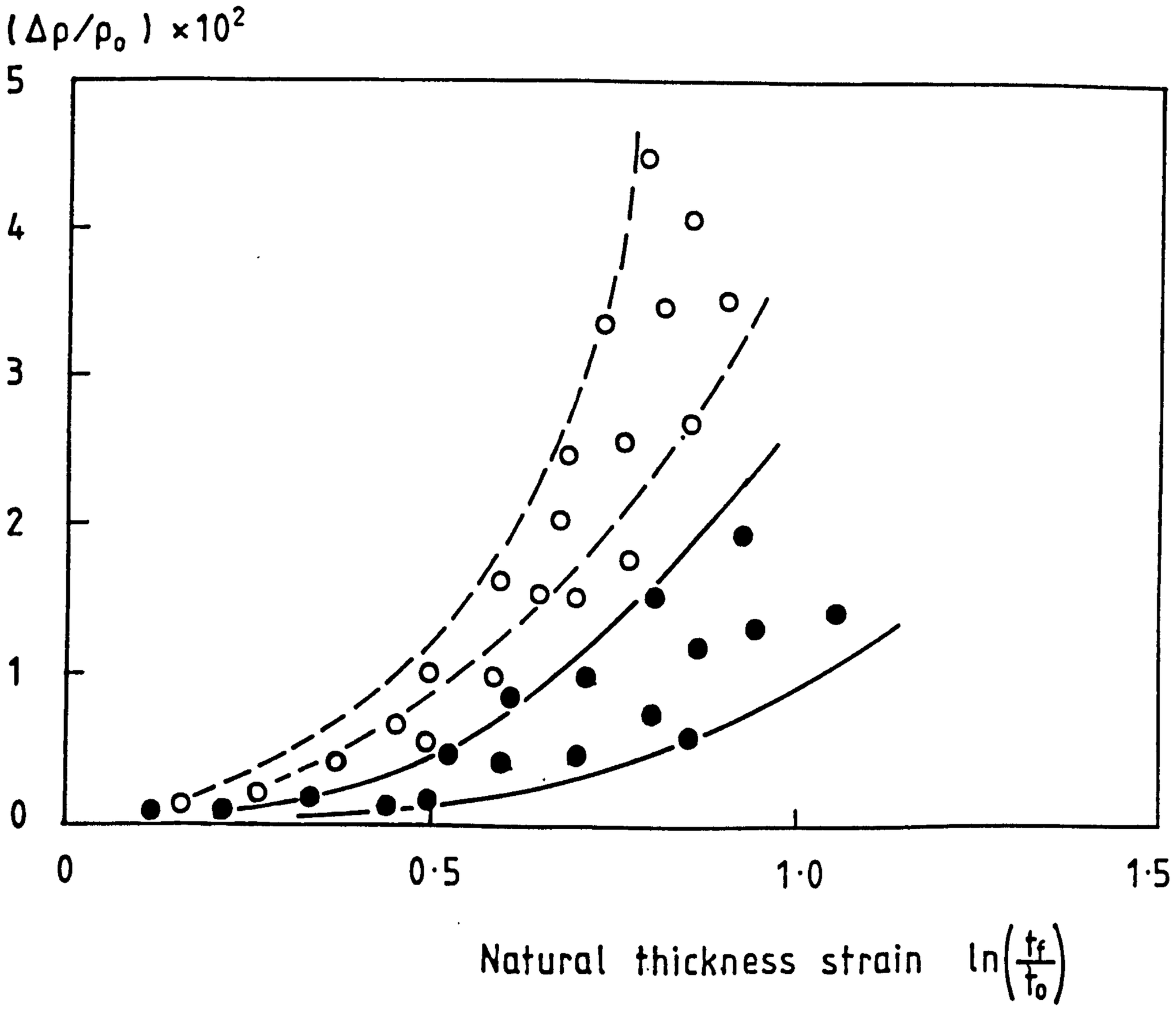

Figure 73 - Effect of solution-heat treatment on cavitation in SPF Supral 150.

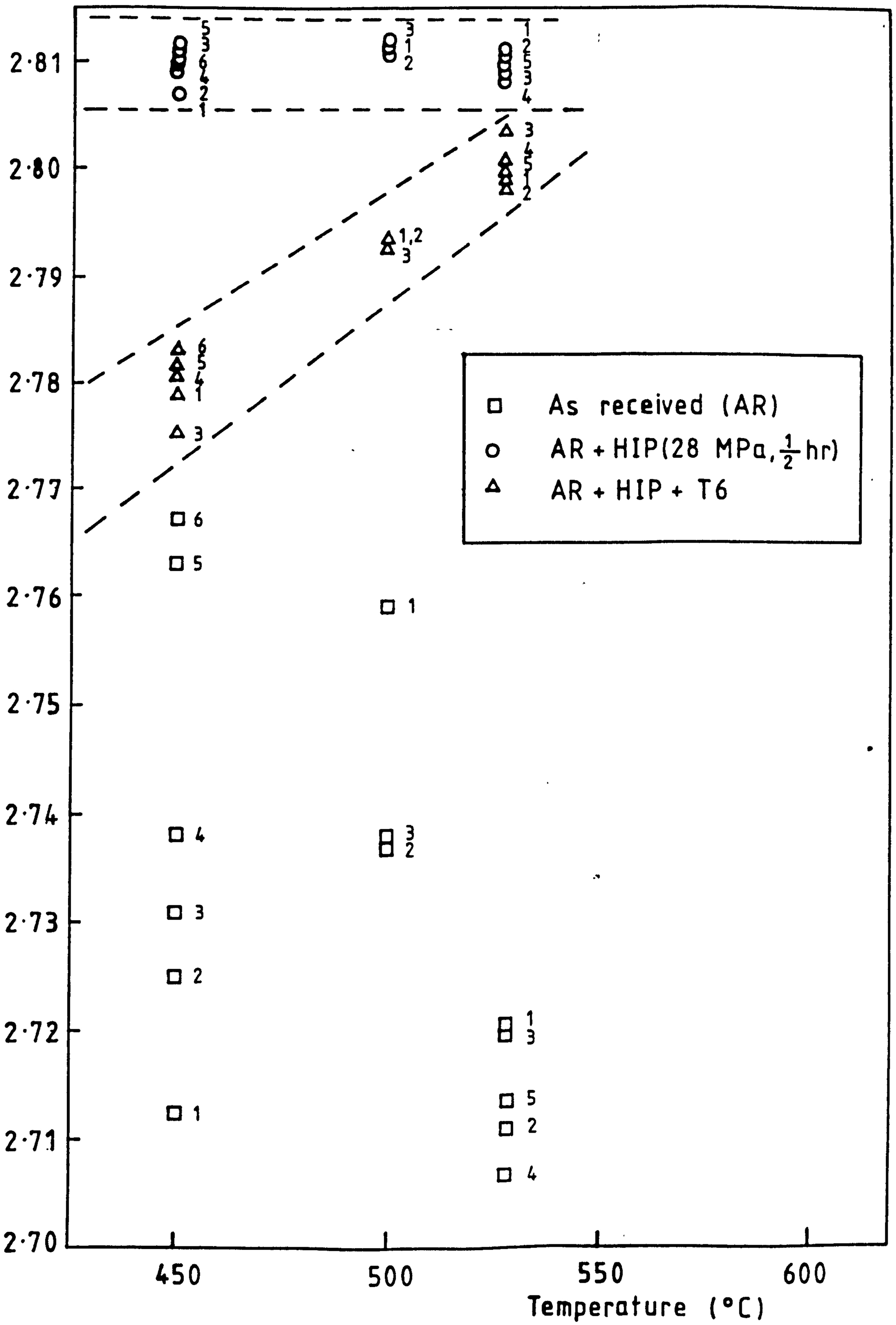

Figure 74 - The influence of HIP temperature (at 28 MPa, ½ hr) on the extent of porosity reappearance on heat-treatment in SPF material originally returned to theoretical density.

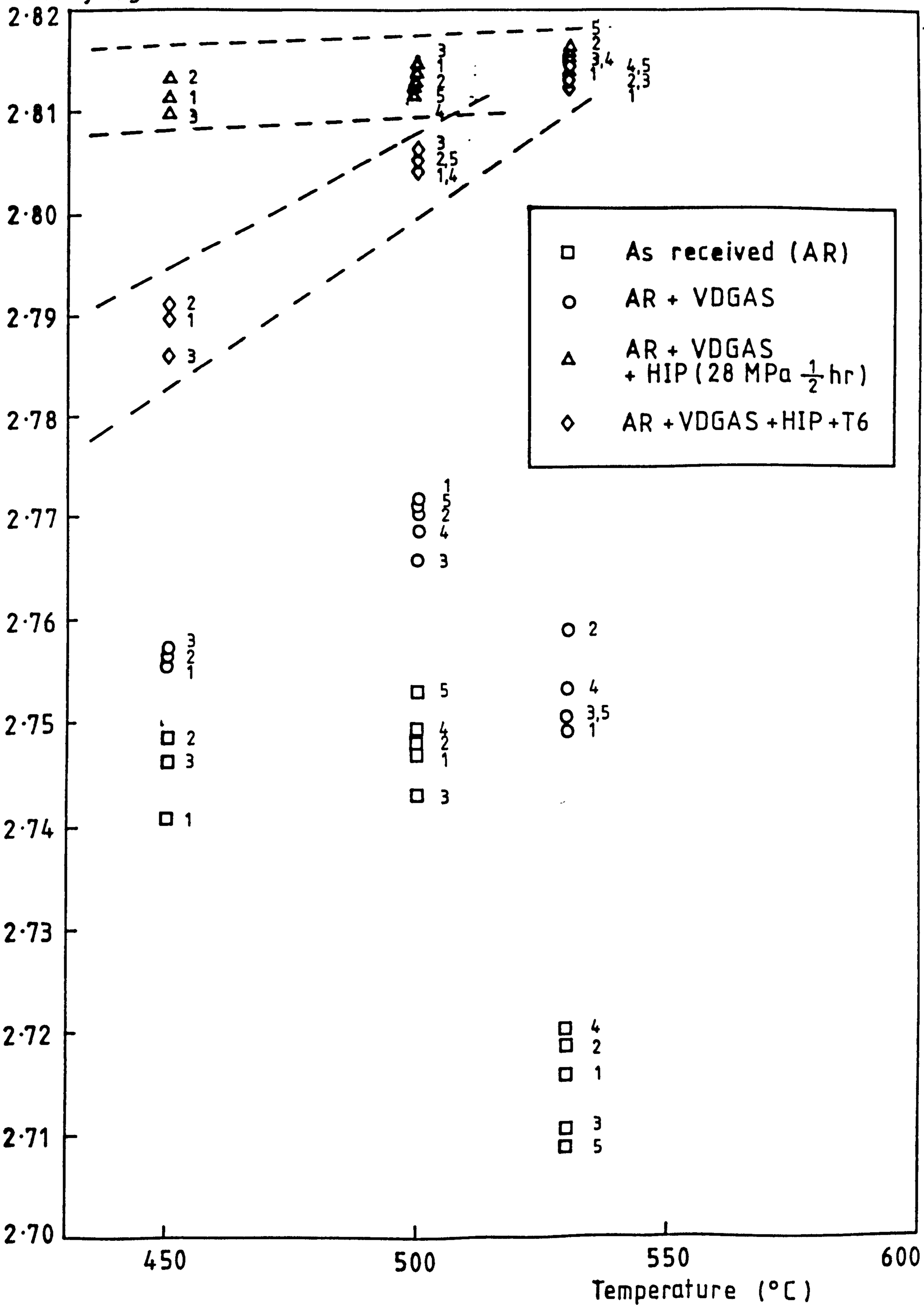

Figure 75 - The influence of vacuum degassing and HIP temperature (at 28 MPa, ½hr) on the extent of porosity reappearance in cavitated Supral (HIPped to theoretical density) after subsequent heat treatments.

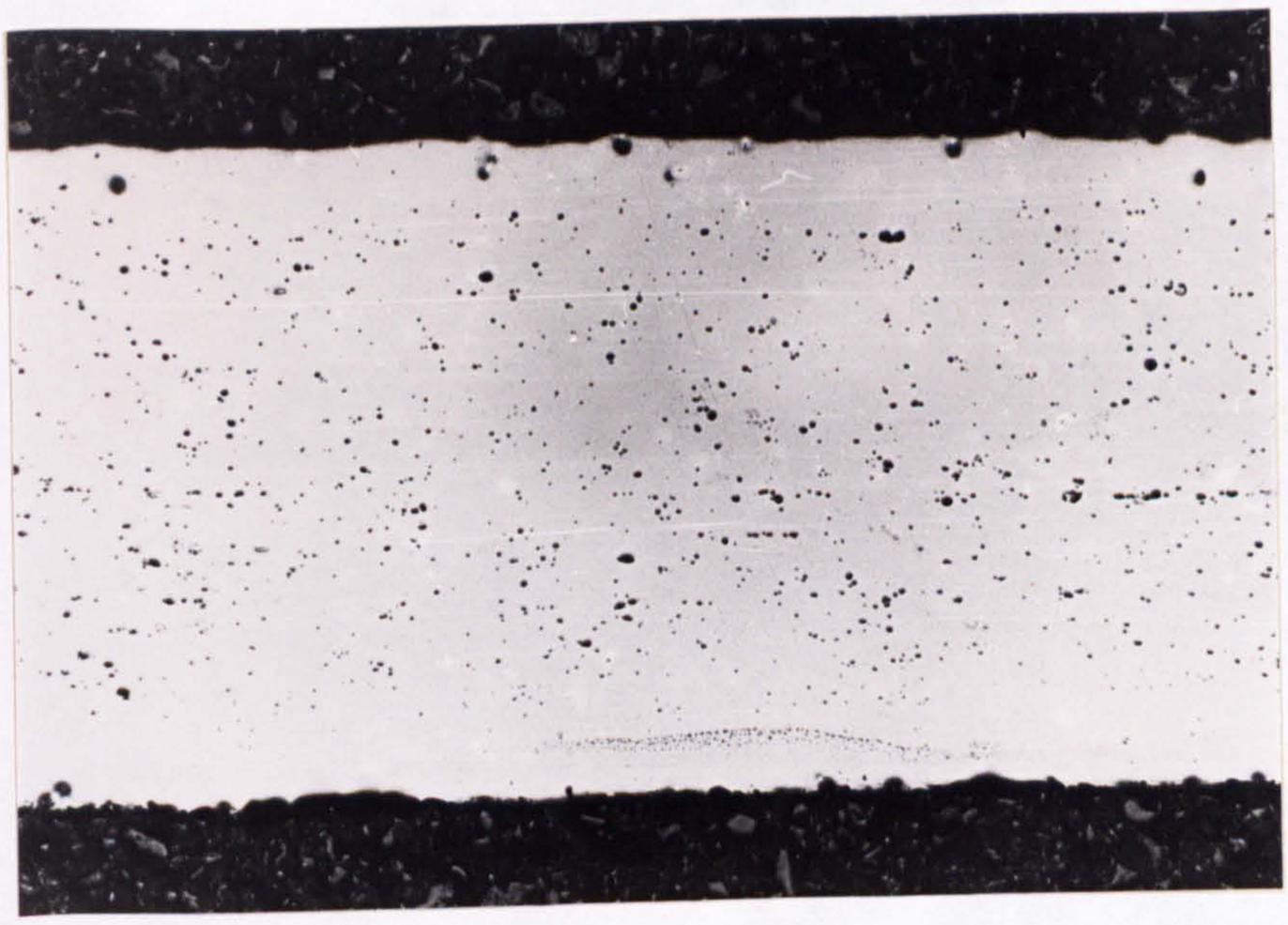

(x 40)

Figure 76 - The nature of porosity reappearance in SPF Supral 150, HIPped (450°C, 28 MPa, ½hr) to theoretical density and solution heat treated (T6) (x 40).

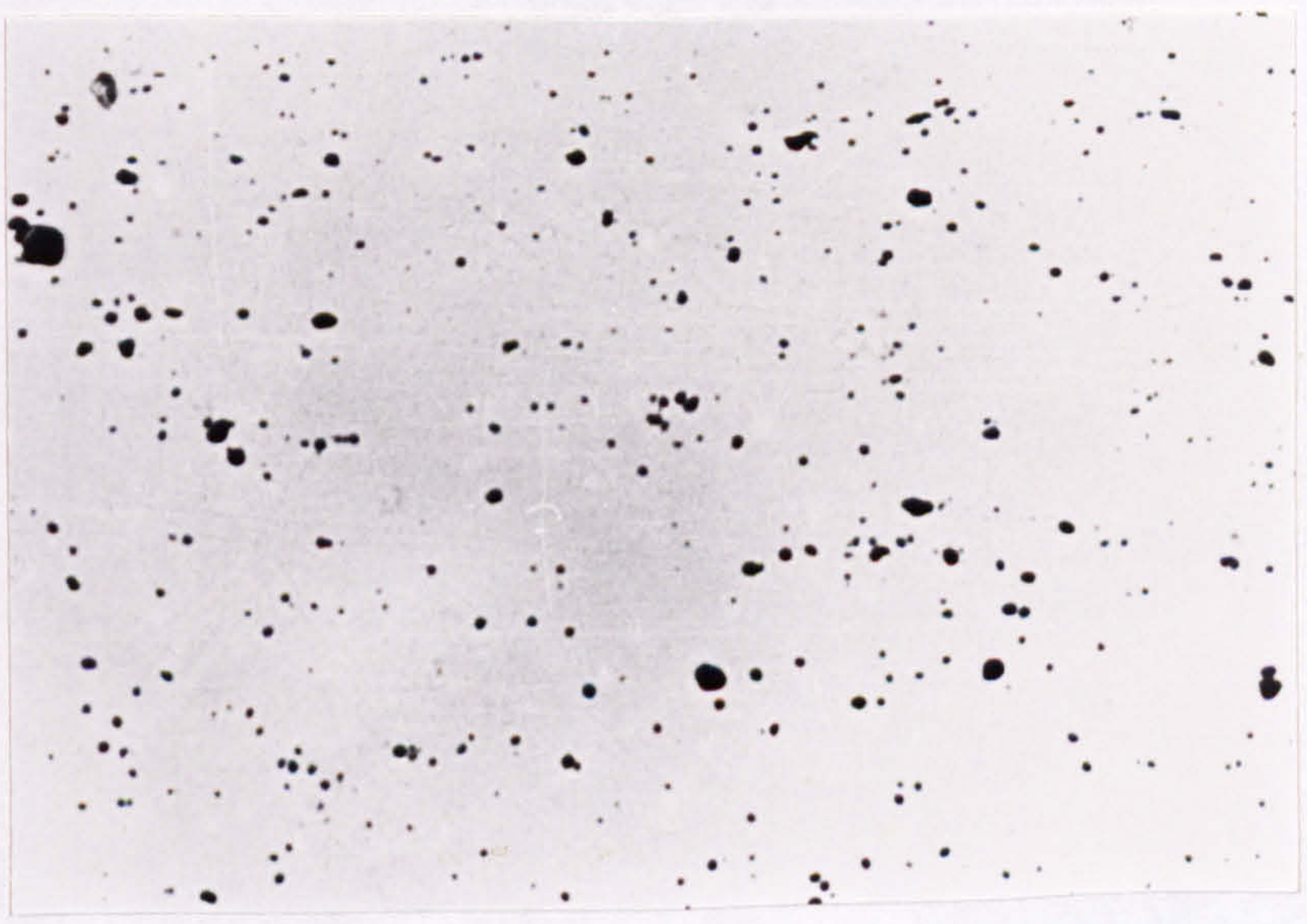

(x 75)

Figure 76(a)- The nature of porosity reappearance in SPF Supral 150, HIPped (450°C, 28 MPa, ½hr) to theoretical density and solution heat treated (T6) (x 75).

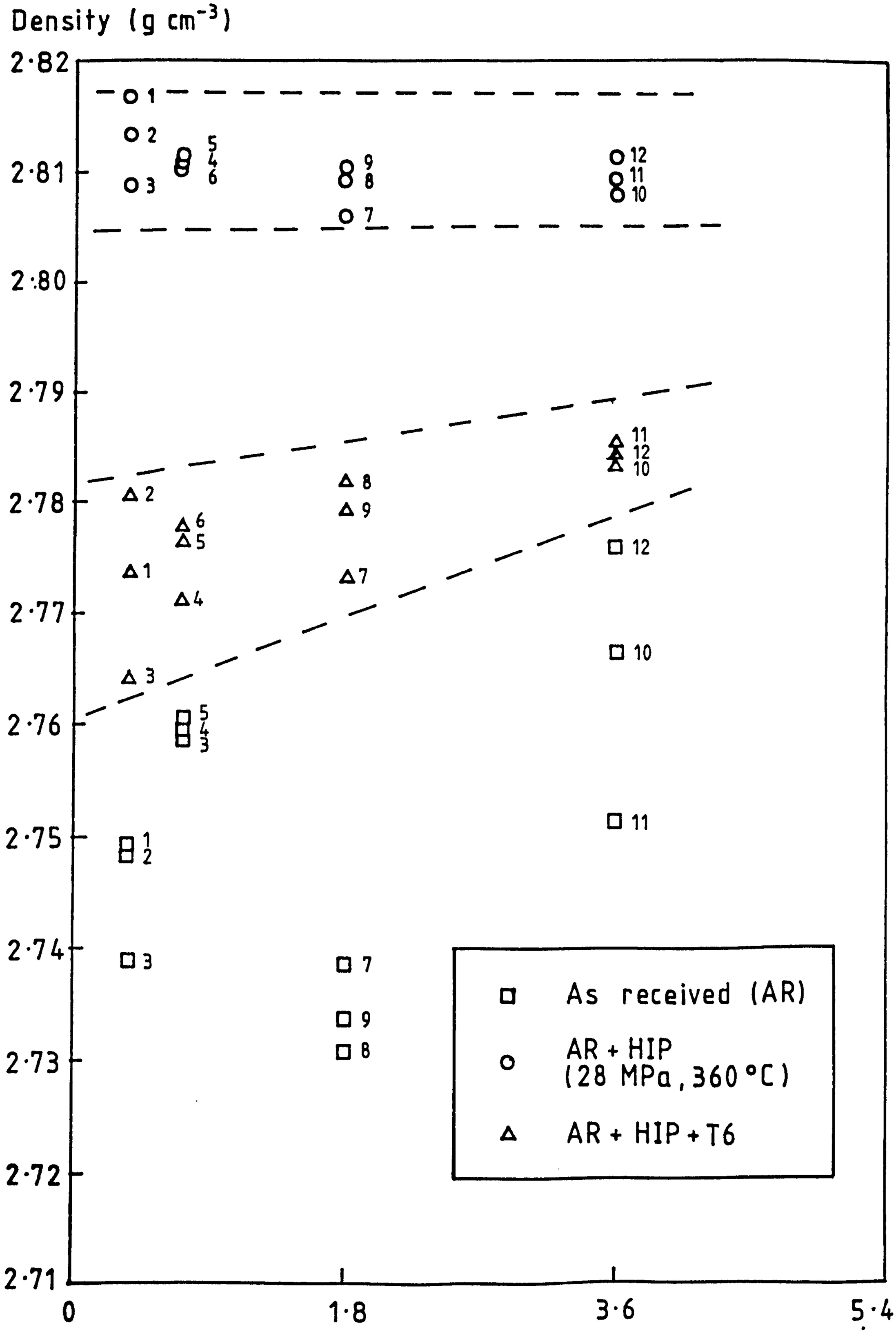

Figure 77 - The effect of increasing time of HIP (at 28 MPa, 360°C) on porosity reappearance during subsequent T6 treatment.

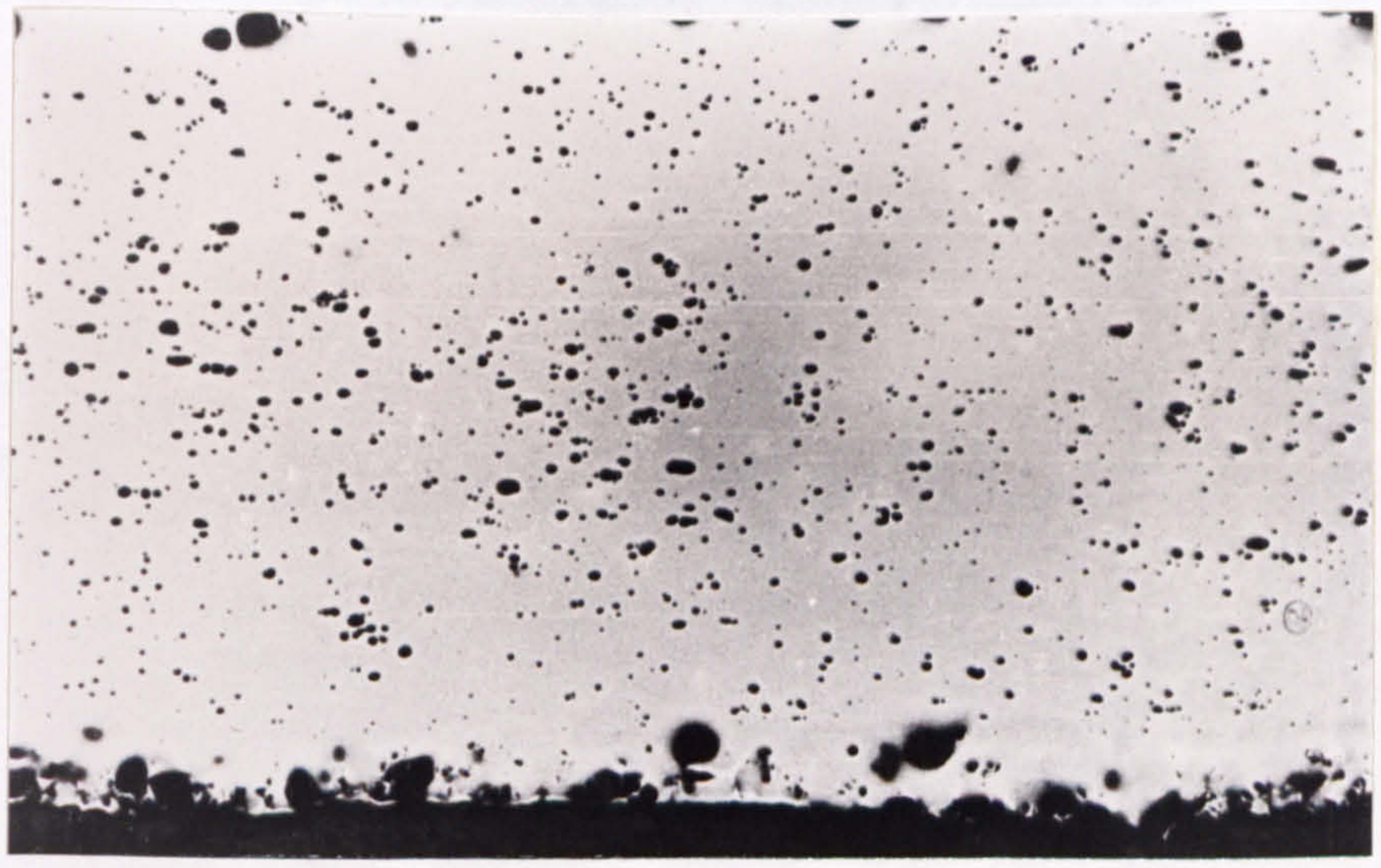

(x 40)

Figure 78 - The effect of heat treatment on SPF cavitation in Supral 150, cavities have become rounded (x 40).

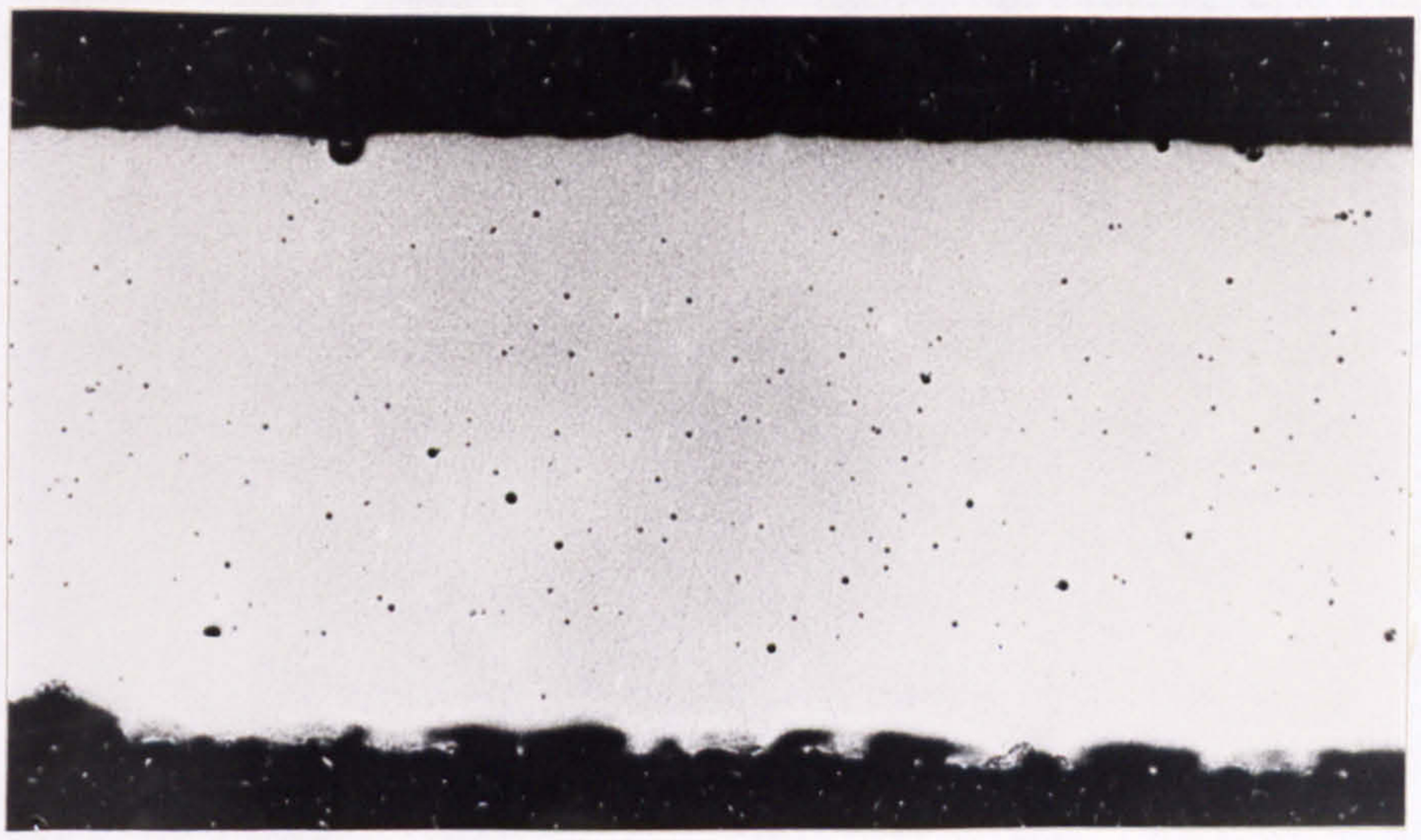

(x 40)

Figure 79 - The nature of the fine porosity reappearance in cavitated Supral 150 (returned to theoretical density [at 500°C, 28 MPa, ½hr]) on subsequent T6 heat treatment (x 40).

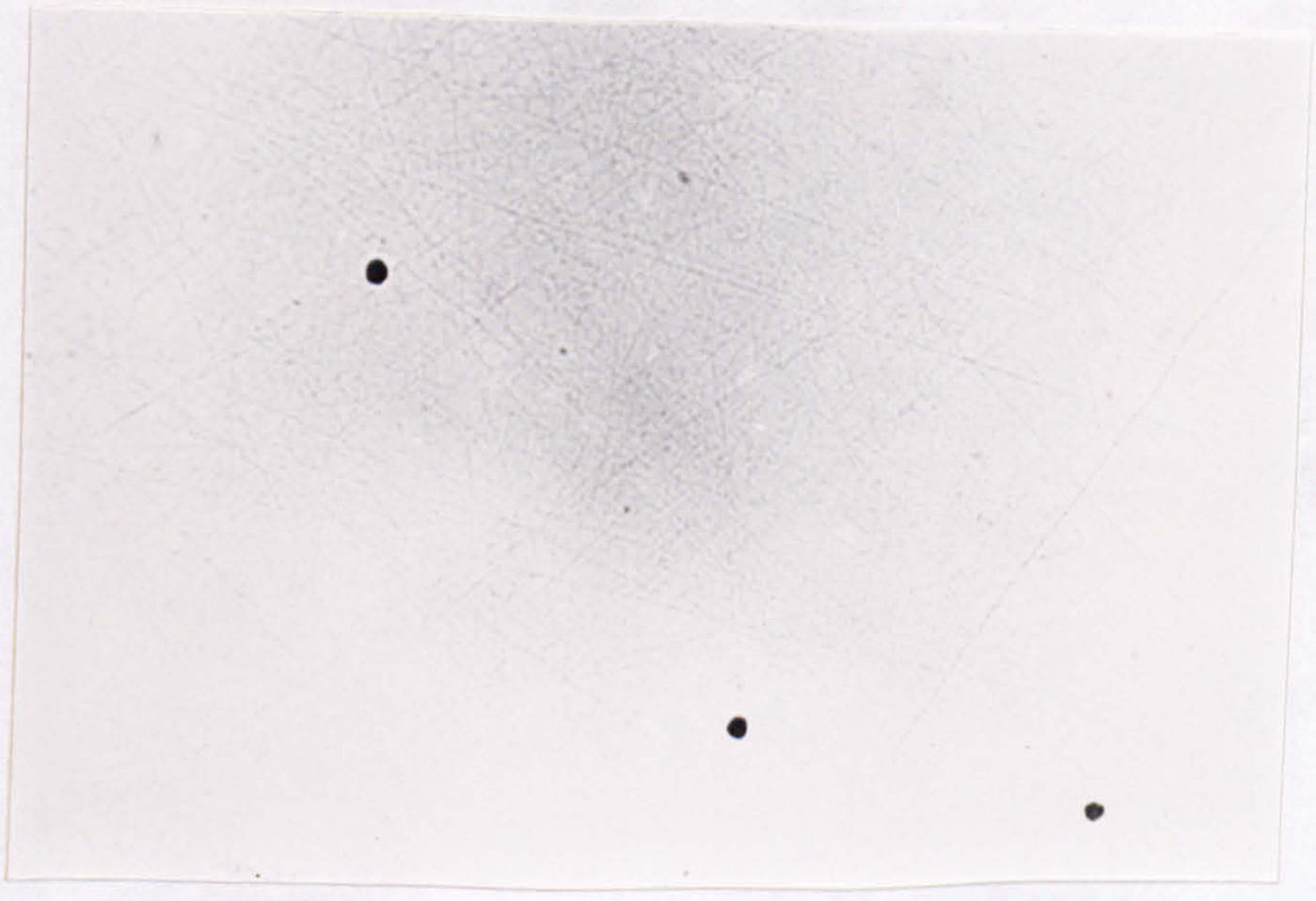

(x 300)

Figure 79(a)- The nature of the fine porosity reappearance in cavitated Supral 150 (returned to theoretical density [at 500°C, 28 MPa, ½hr]) on subsequent T6 heat treatment (x 300).

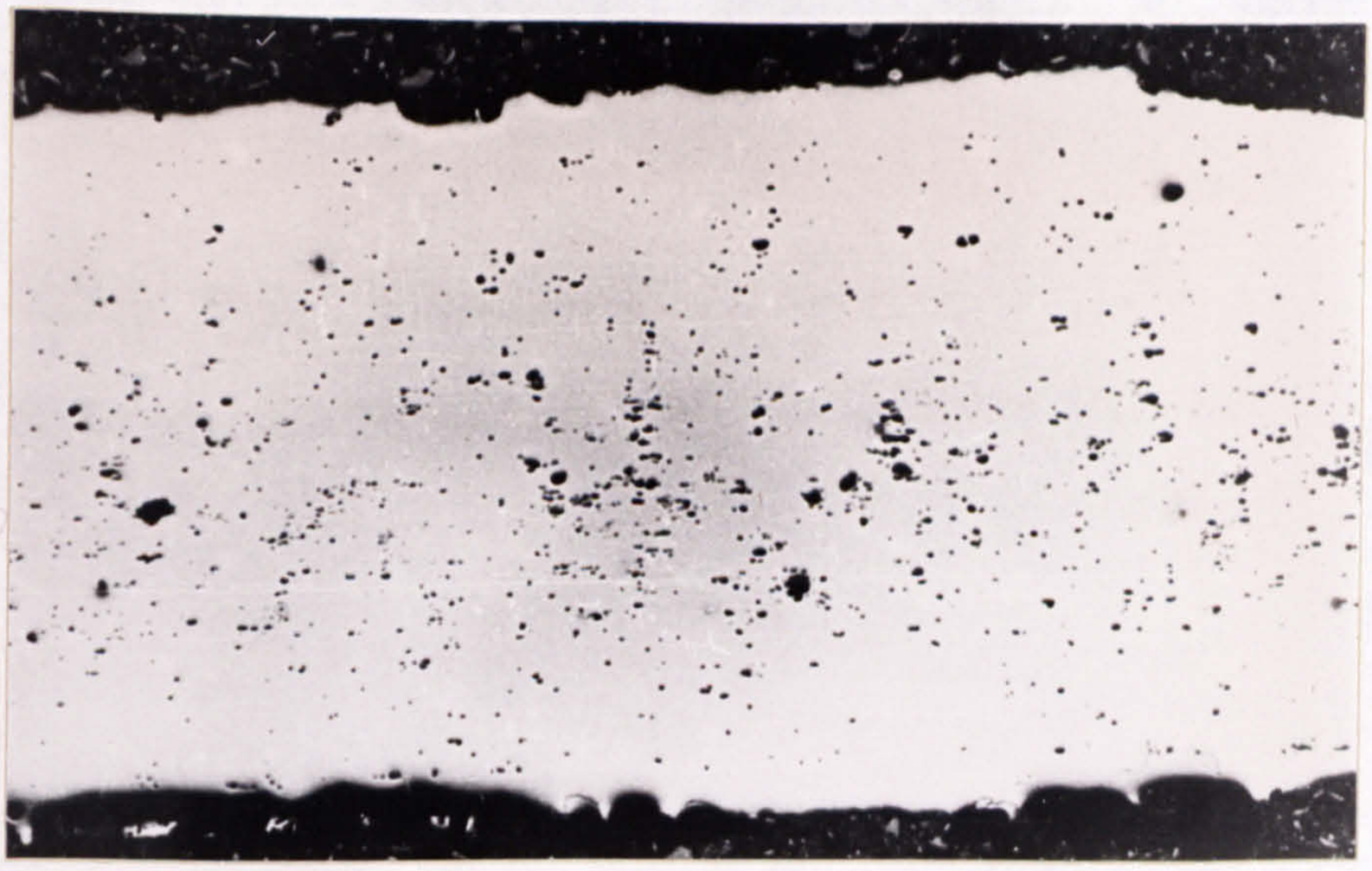

(x 40)

Figure 81 - The nature of cavitation in SPF Supral 150 which has been vacuum degassed (500°C, 10^{-6} torr, 1 hour) and subsequently T6 heat treated (x 40).

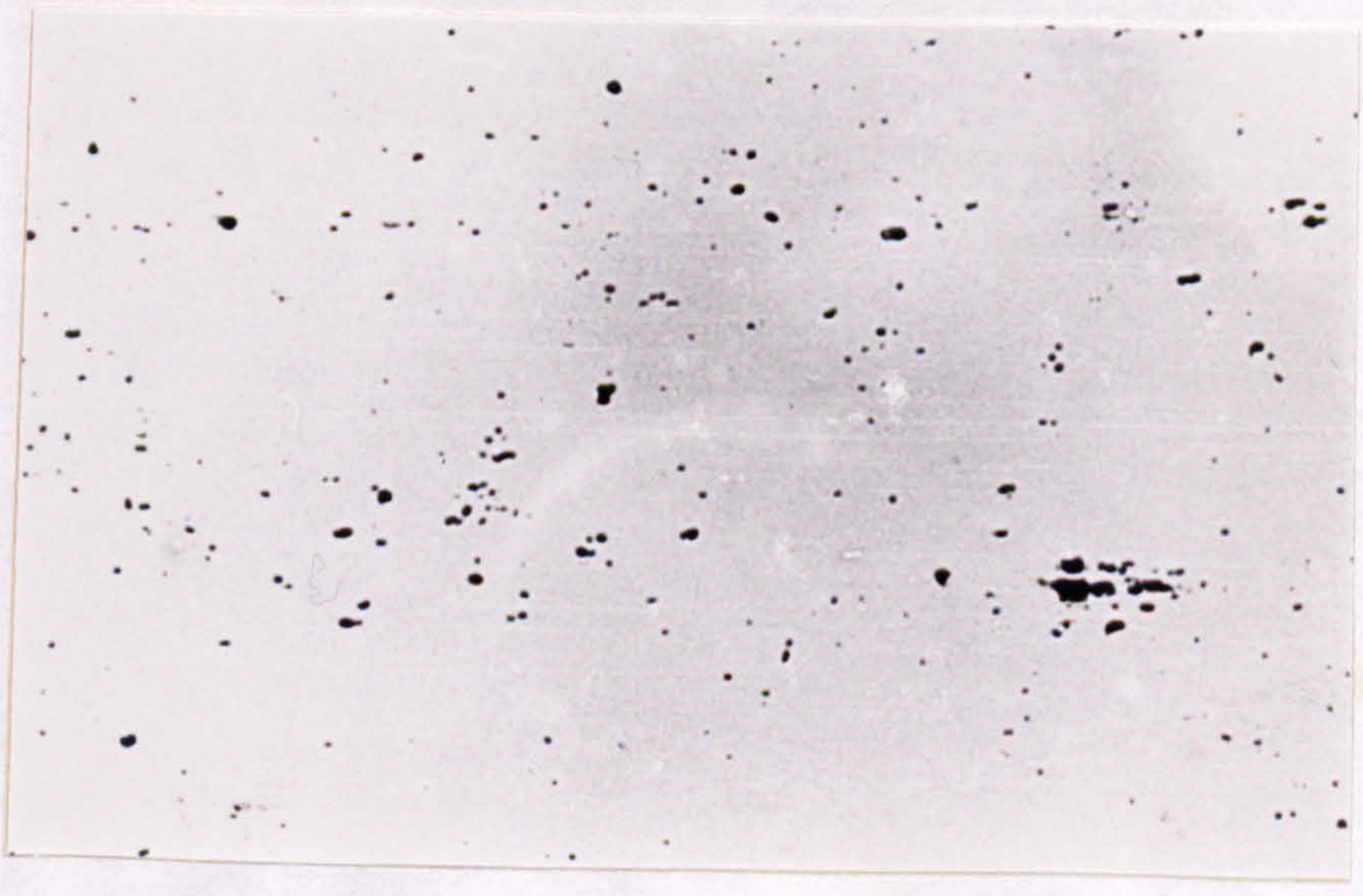

(x 75)

Figure 81(a)- The nature of cavitation in SPF Supral 150 which has been vacuum degassed (500°C, 10^{-6} torr, 1 hour) and subsequently T6 heat treated (x 75).

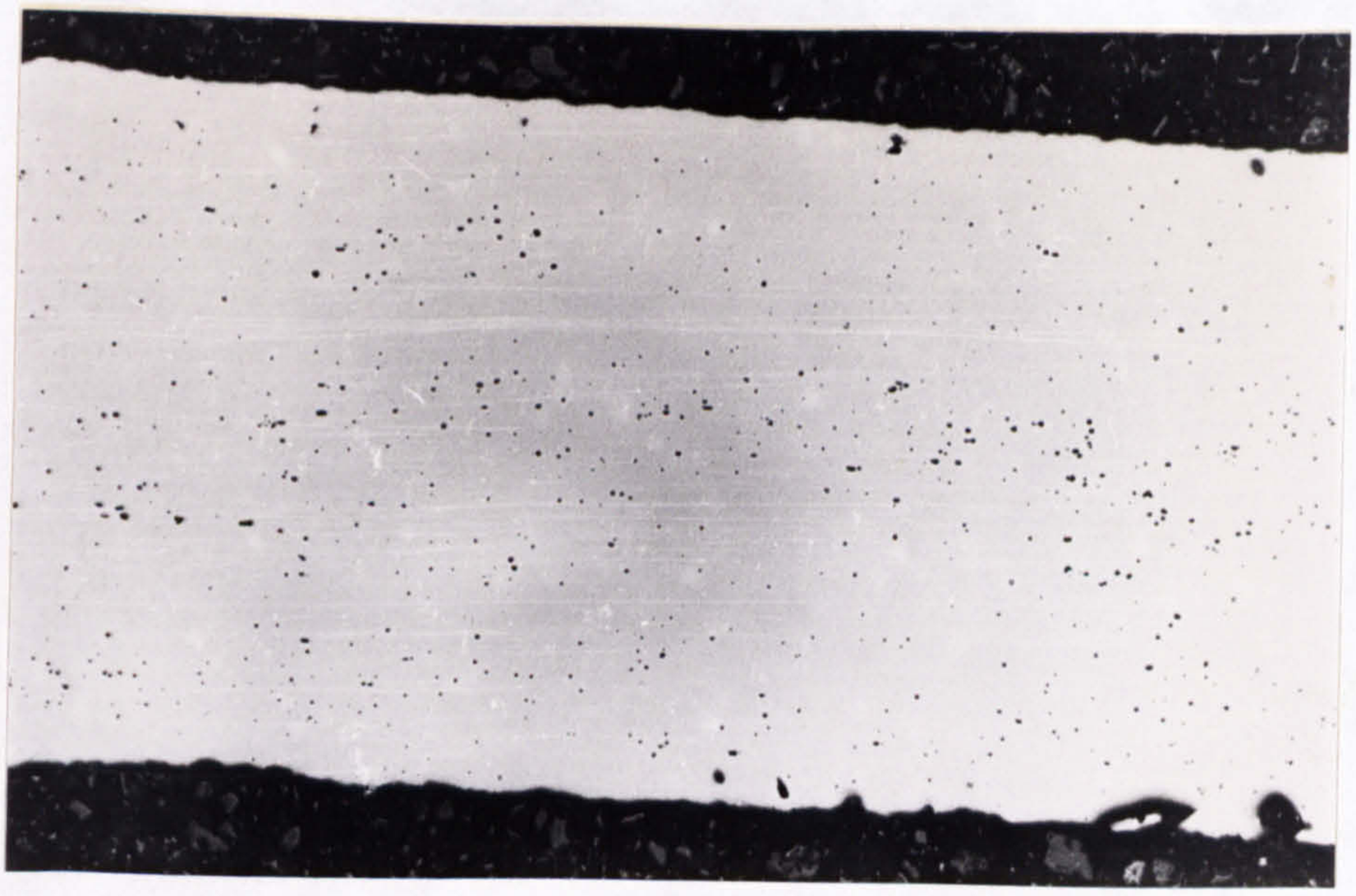

(x 40)

Figure 82 - Optical micrographs showing the porosity which reappears on T6 treating SPF Supral 150 which has been vacuum degassed and HIP (450°C, 28 MPa, ½hr) back to theoretical density (x 40).

(x 300)

Figure 82(a)- Optical micrographs showing the porosity which reappears on T6 treating SPF Supral 150 which has been vacuum degassed and HIP (450°C, 28 MPa, ½hr) back to theoretical density (x 300).

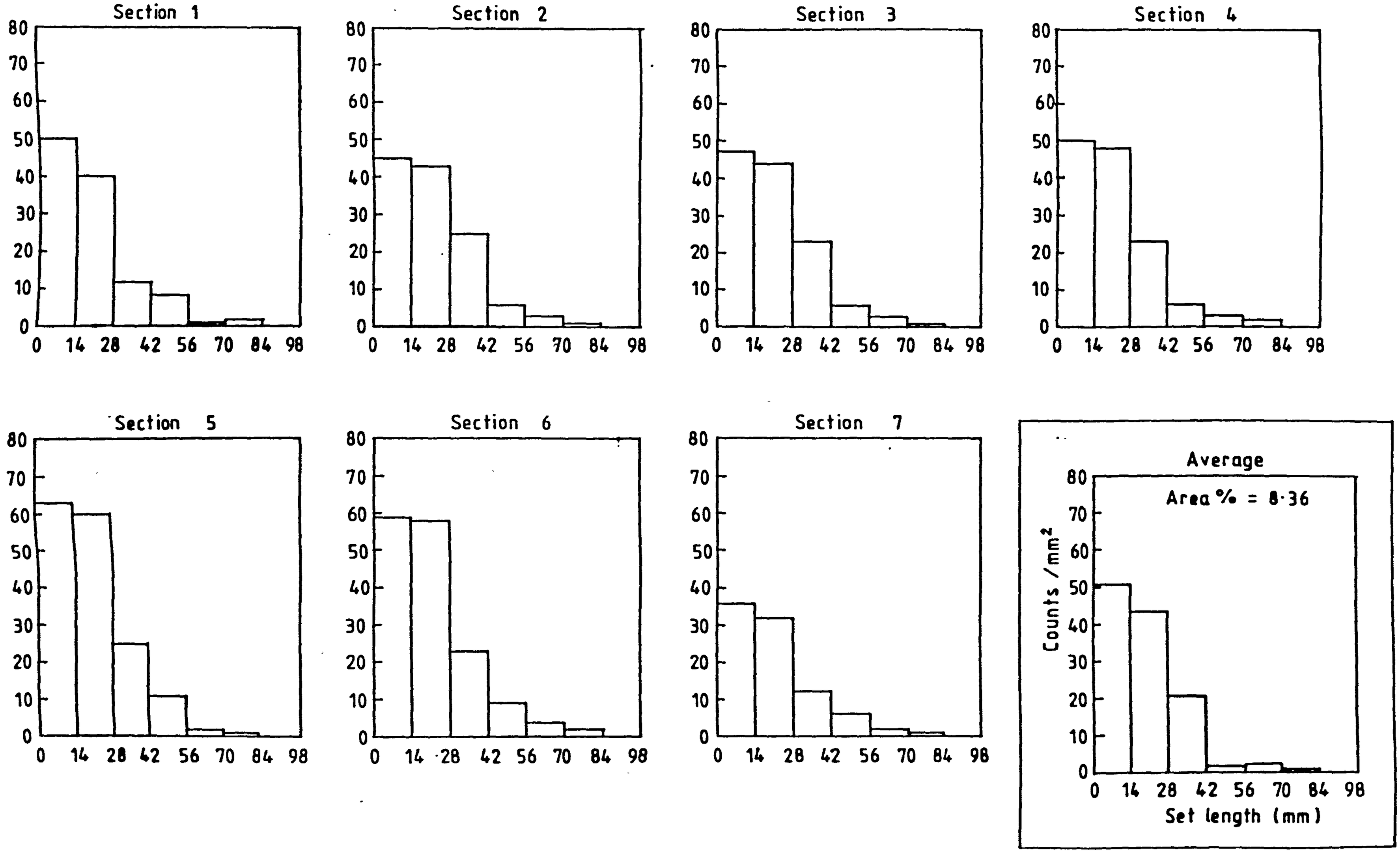

Figure 83 - Quantimet Image Analysis of the variation in the number and size of cavities along edge section of SPF Supral 150.

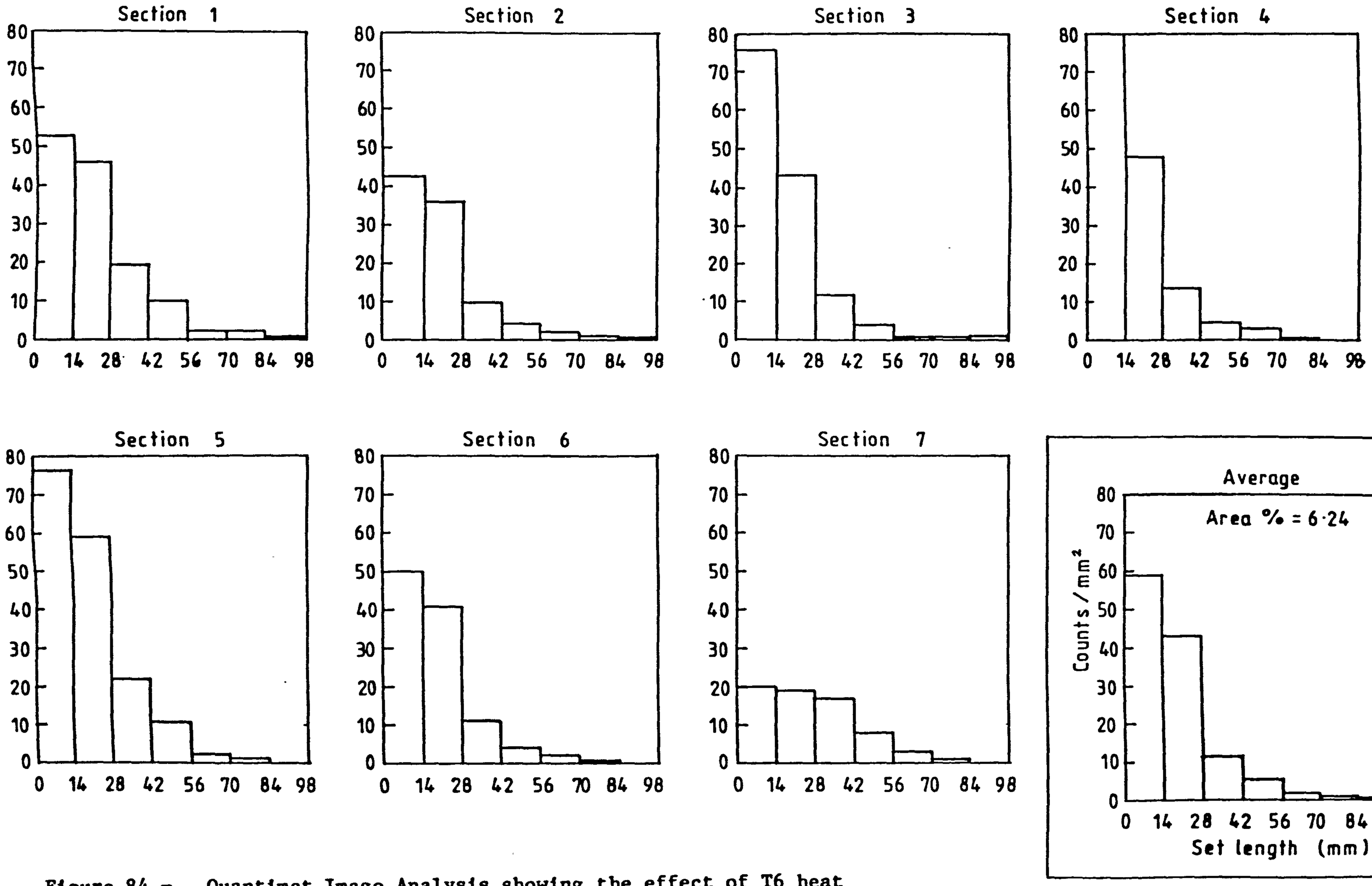

Figure 84 - Quantimet Image Analysis showing the effect of T6 heat treatment on the number and size of cavities along edge section in SPF Supral 150.

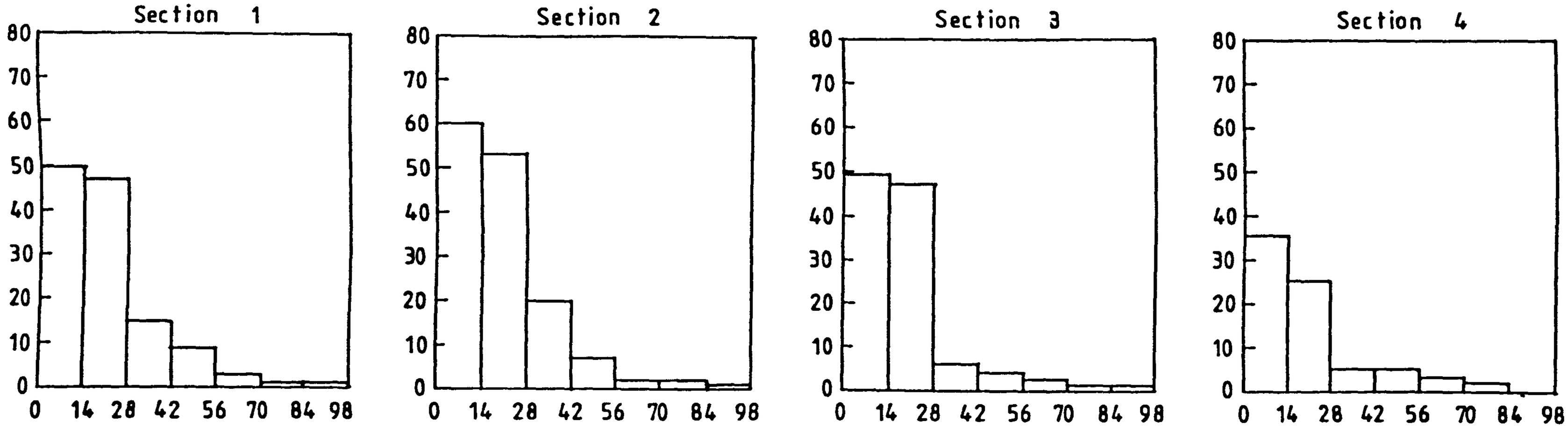

Figure 85 – Quantimet Image Analysis of the number and size of porosity reappearing in SPF material originally HIPped (450°C, 28 MPa, ½hr) to theoretical density and T6 heat treated.

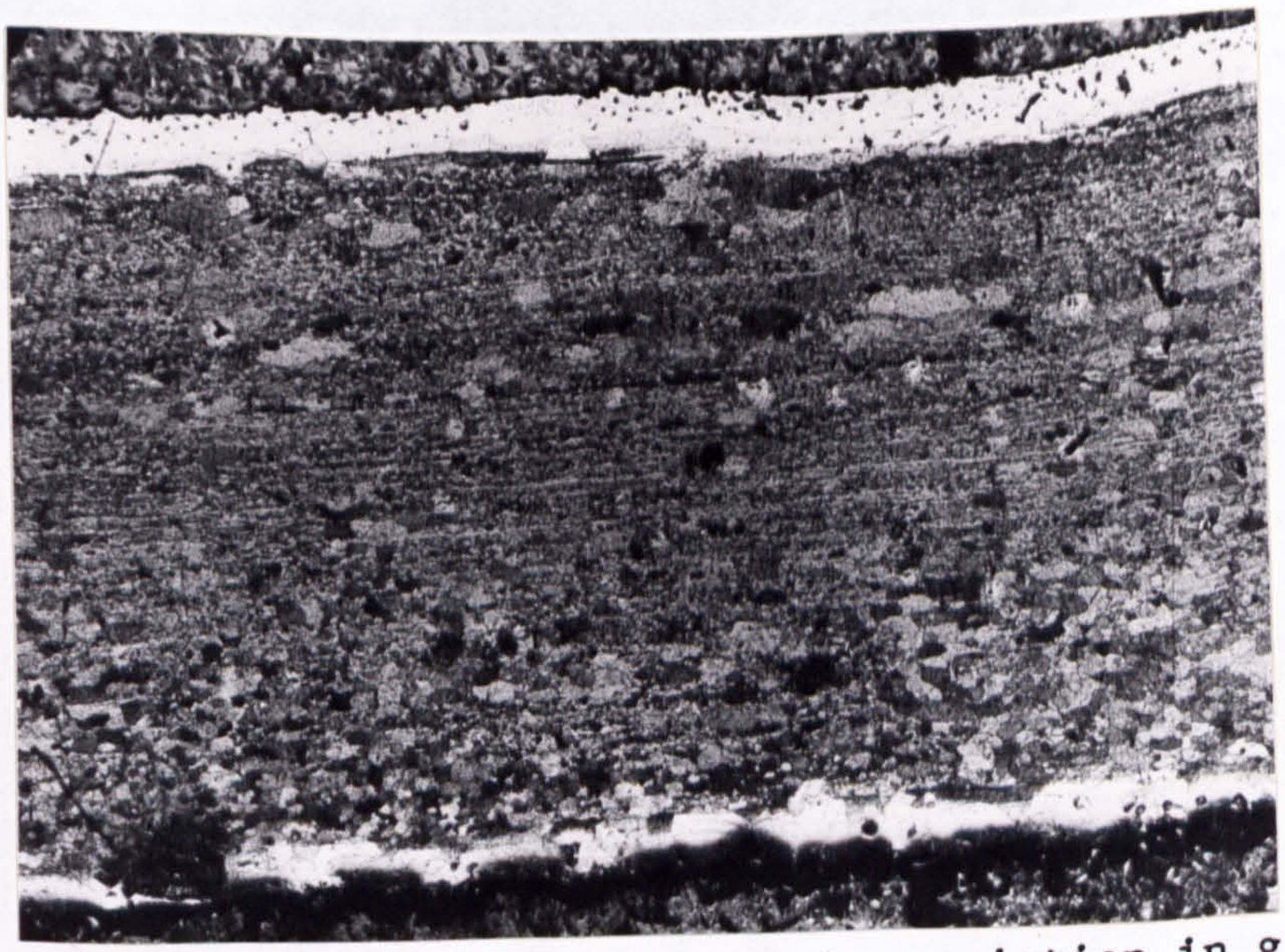

(x 40)

Figure 86 - Optical micrograph showing the variation in grain size encountered in SPF Supral 150 which has been vacuum degassed (500°C, 10^{-6} torr, 1 hour) and T6 heat treated (x 40).

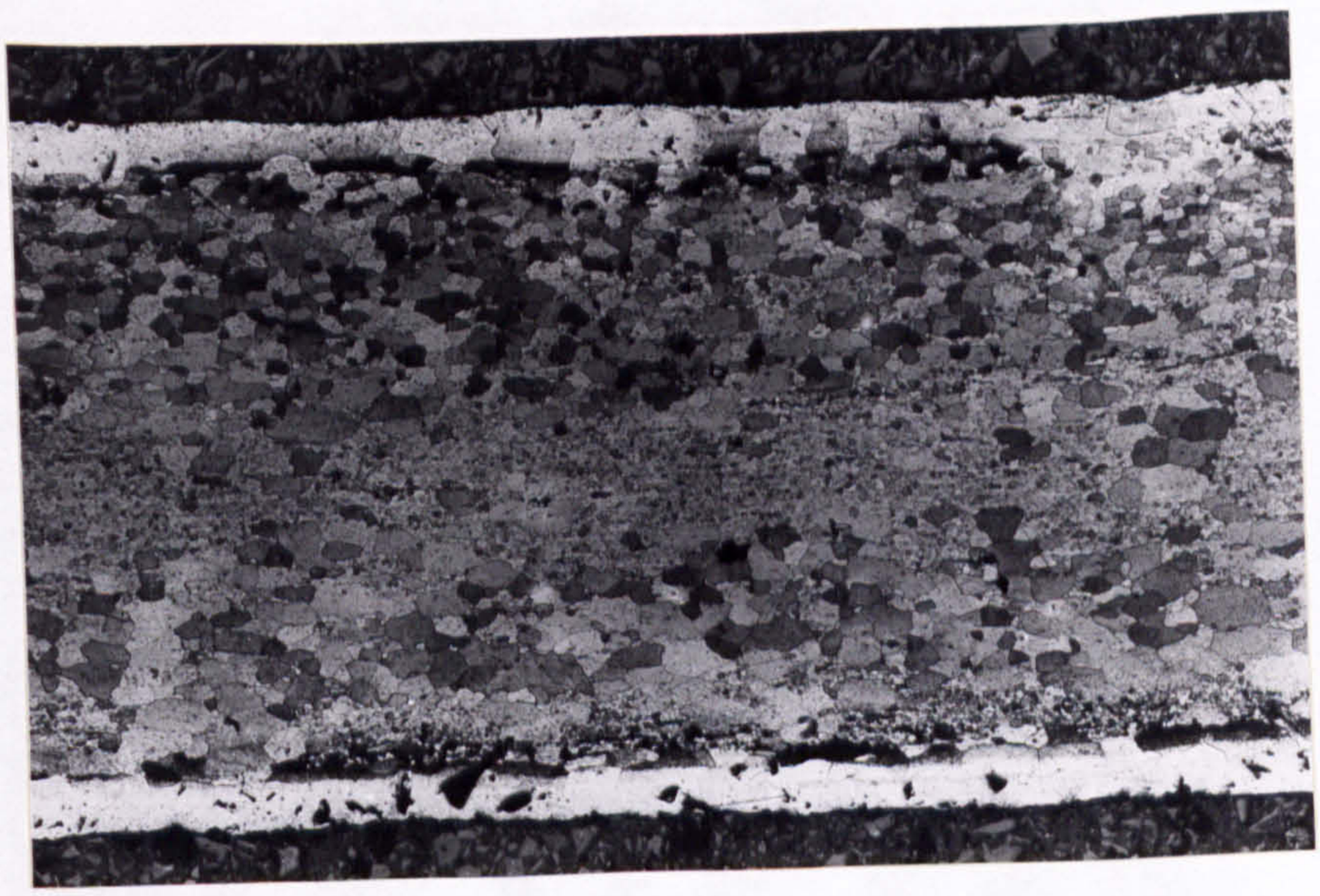

(x 40)

Figure 87 - Variation in grain size of SPF Supral 150 which has been vacuum degassed, HIPped (450°C, 28 MPa, ½hr) and T6 heat treated (x 40).

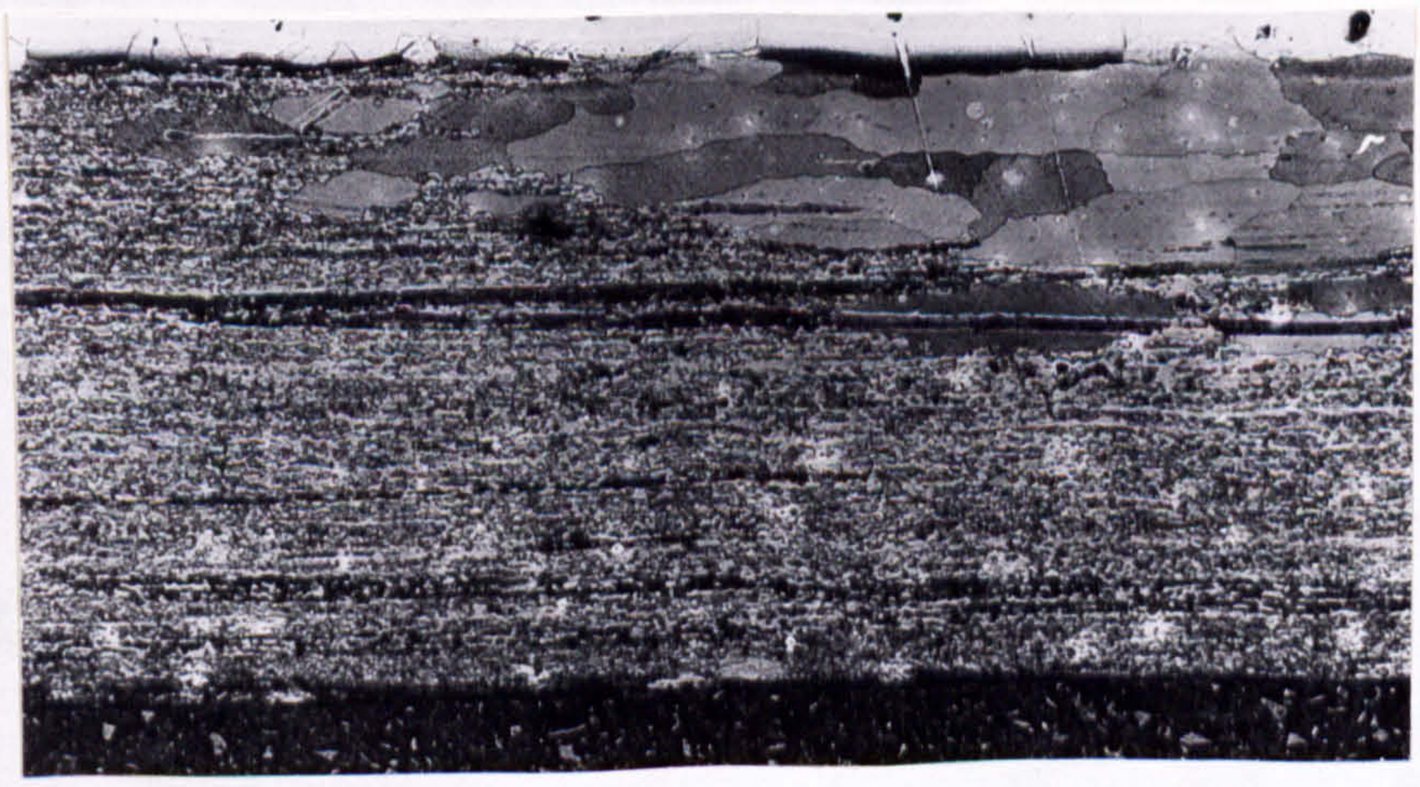

(x 40)

Figure 87(a)- As in Figure 87 but for different specimen (x 40).

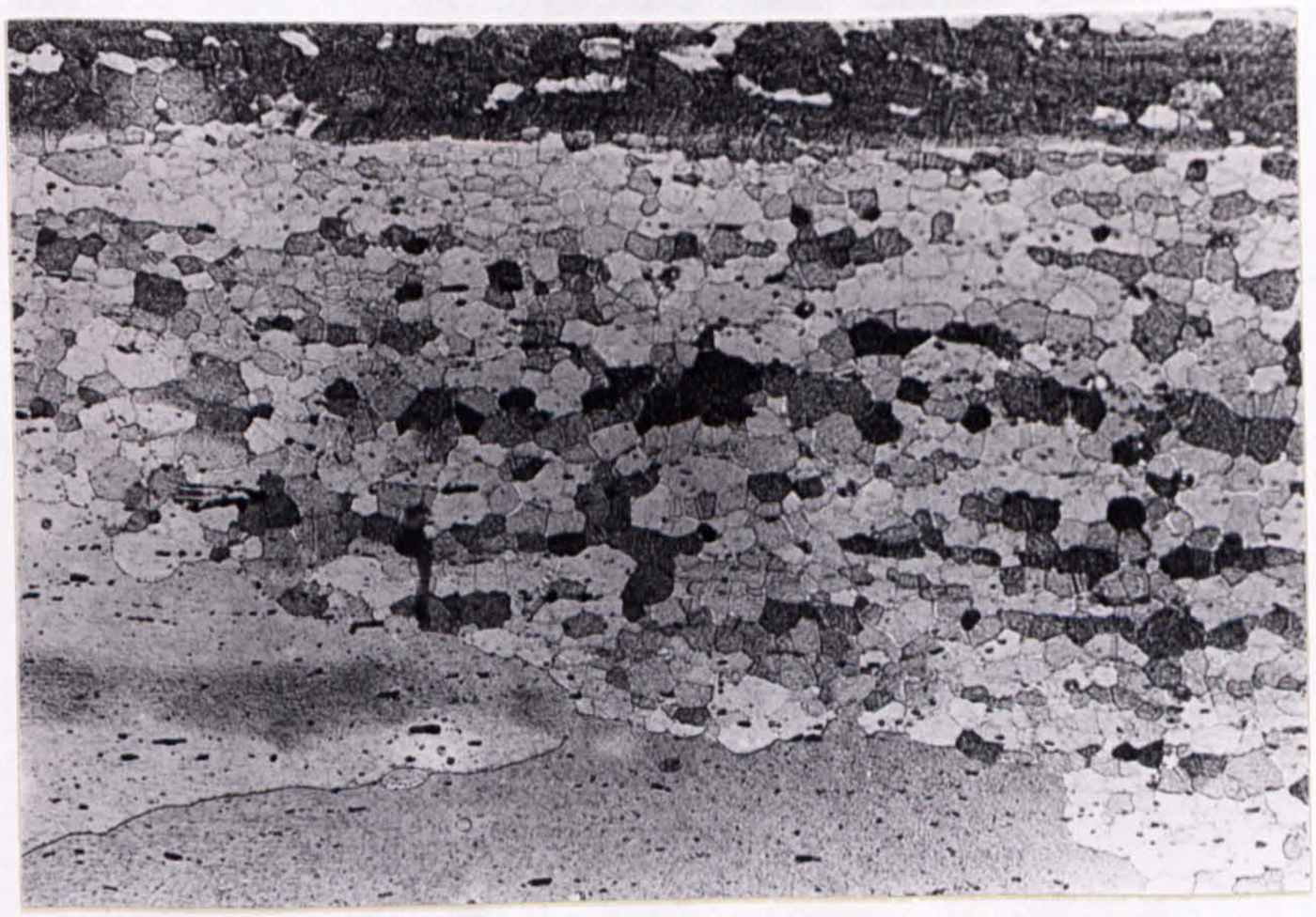

(x 300)

Figure 87(b)- As in Figure 87 but for different specimen (x 300).

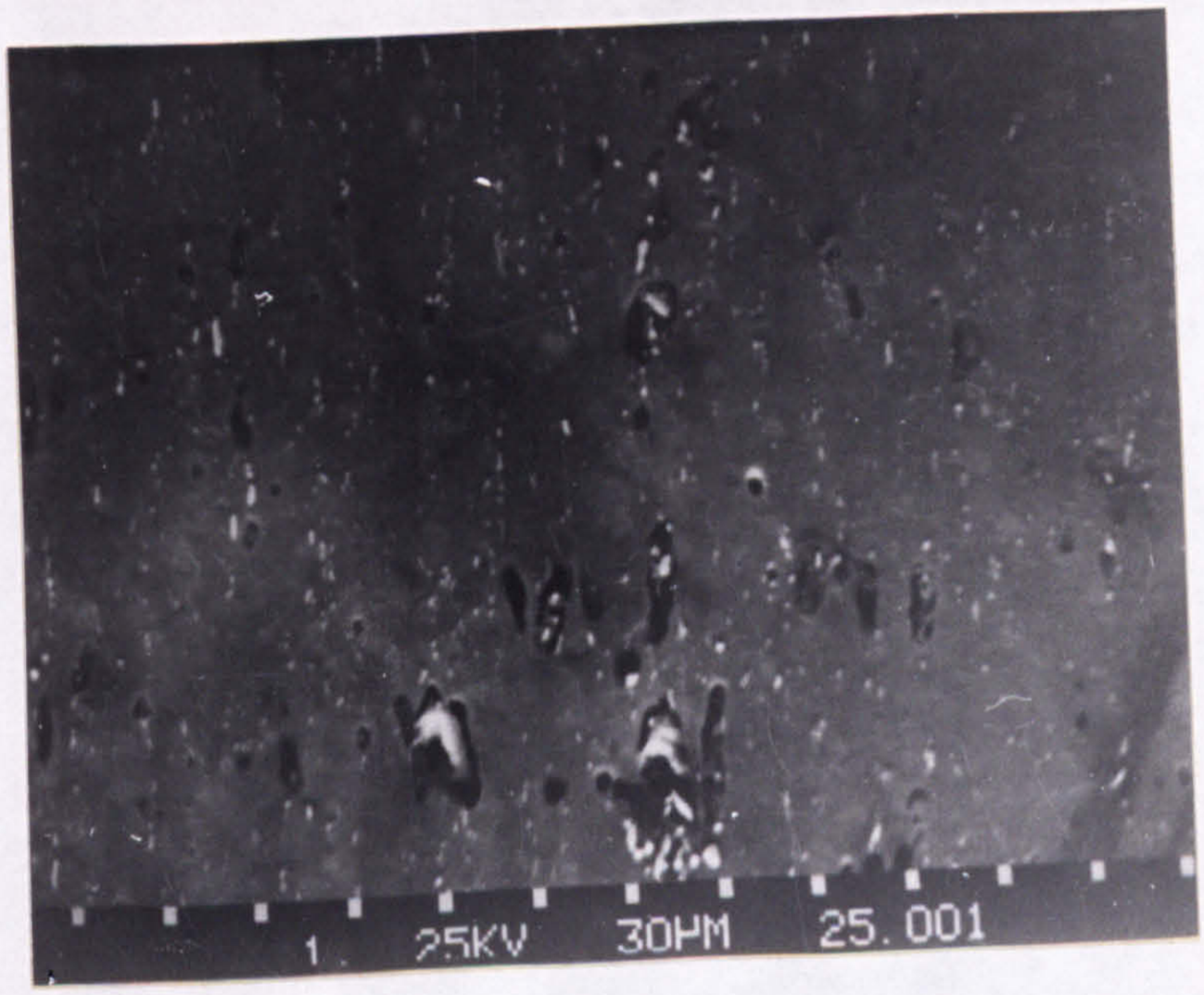

Figure 88(a)- SEM micrograph showing the nature of cavitation and distribution of precipitates in SPF and heat treated Supral 150.

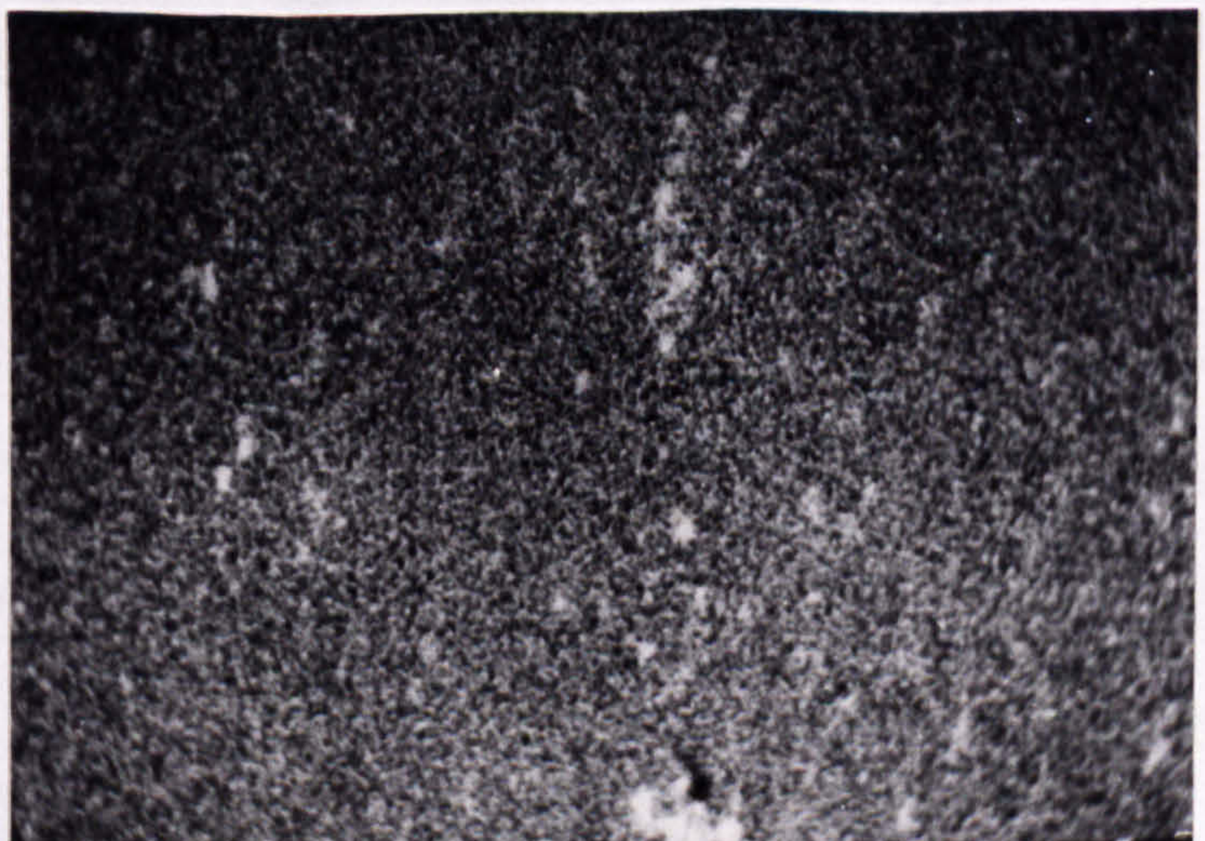

Figure 88(b)- Distribution map for copper of above using wavelength dispersive analysis facilities on SEM.

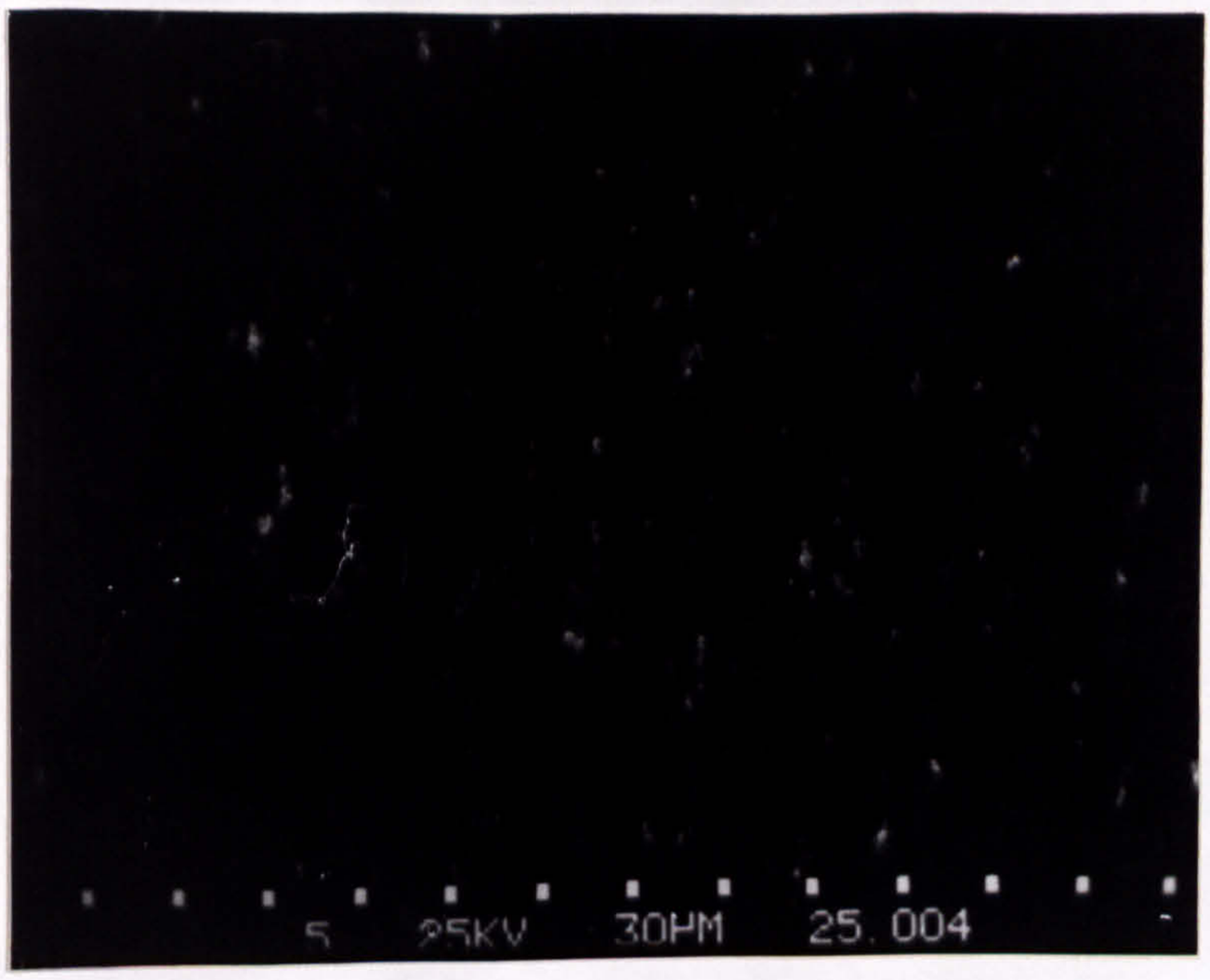

Figure 88(c)- Distribution map for area in Figure 88(a) of iron.

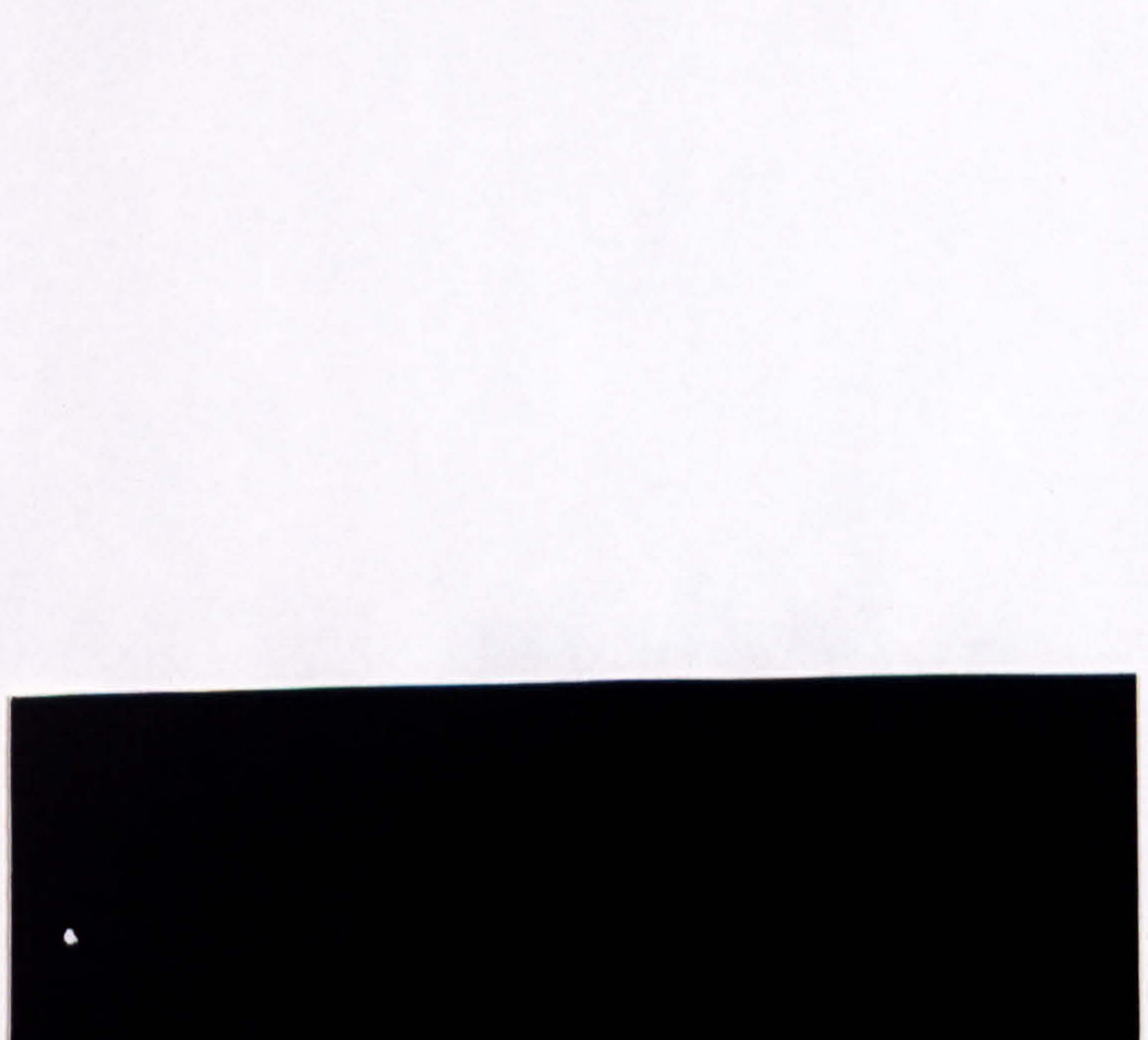

Figure 88(d)- Map for area in Figure 88(a) of silicon.

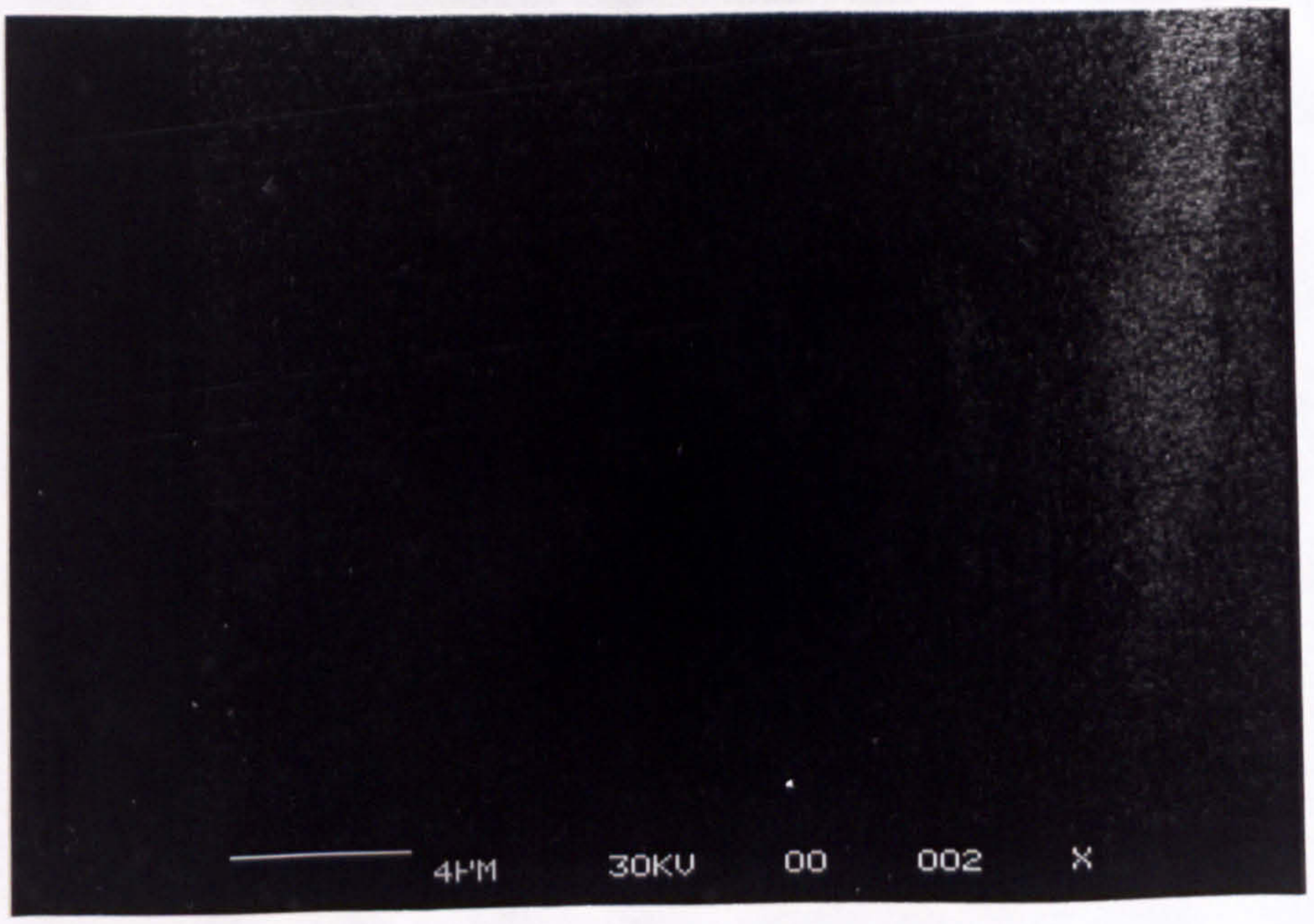

Figure 89 - Distribution map for zirconium using energy dispersive analysis on SEM which is able to detect large $ZrAl_3$ particle, shown in Figure 89(a).

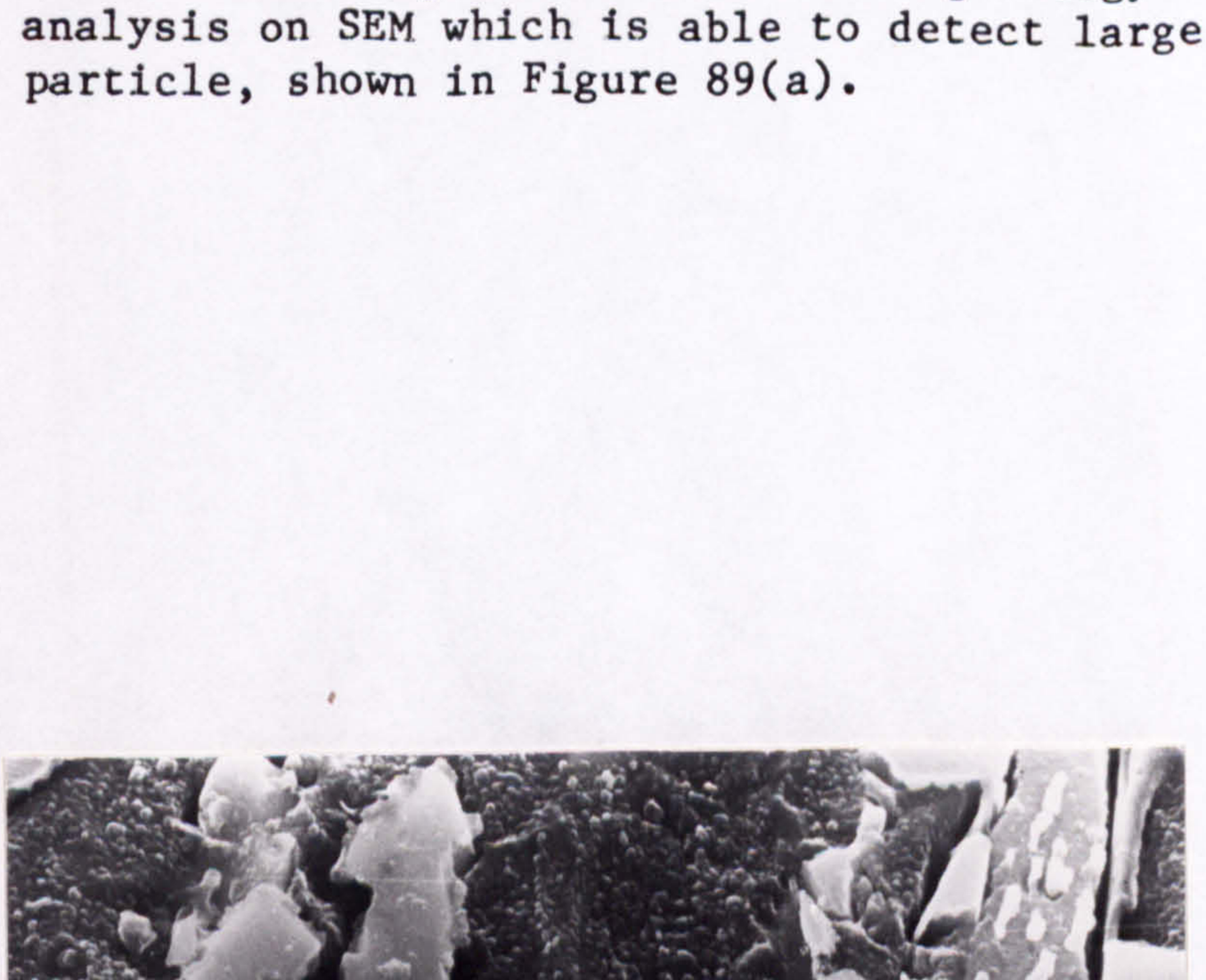

Figure 89(a)- Photograph of SPF Supral 150 containing $ZrAl_3$ particle.

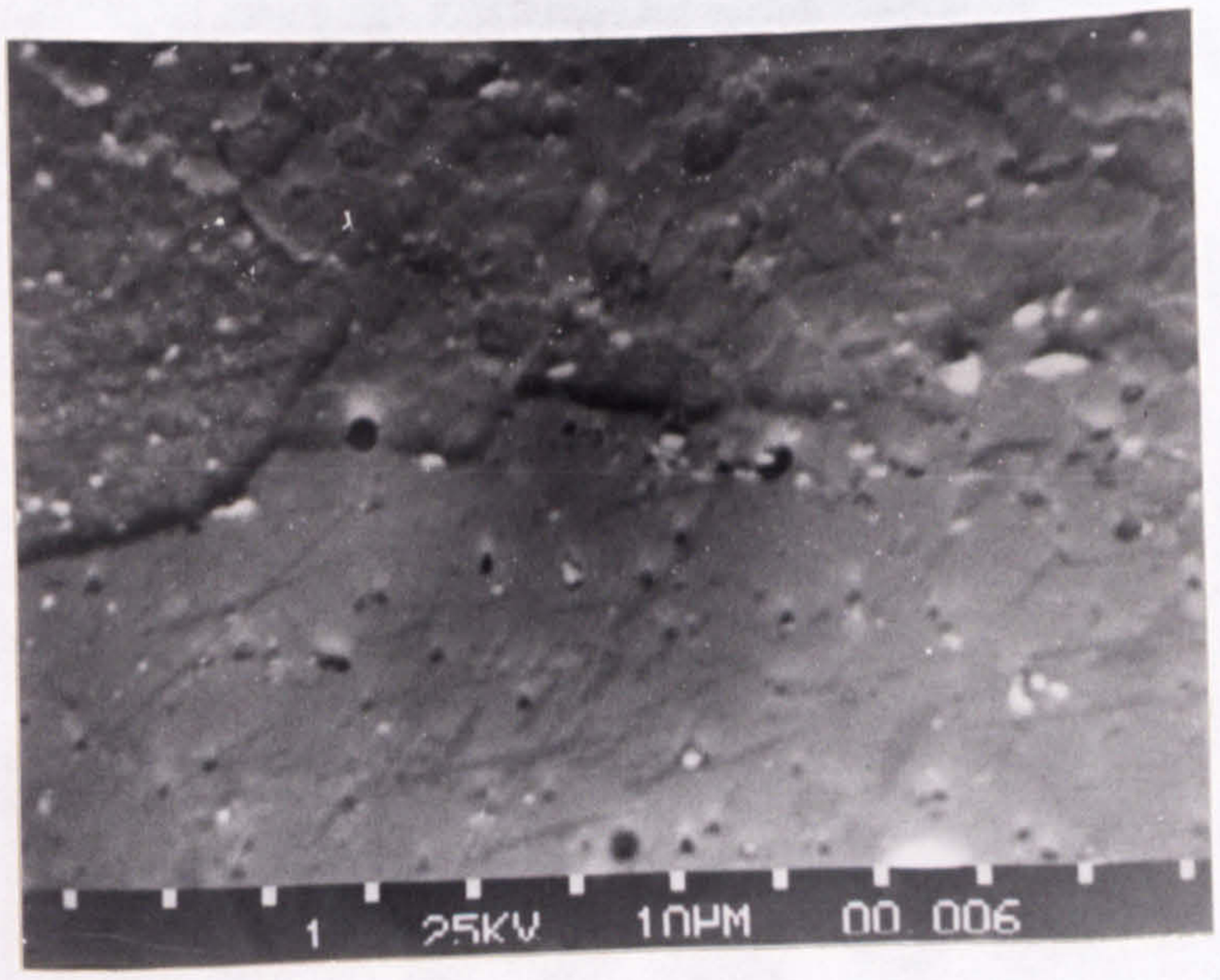

Figure 90(a)- SEM micrograph showing a variation in grain size of SPF Supral 150 which has been vacuum degassed, HIPped (500°C, 28 MPa, ½hr) + T6.

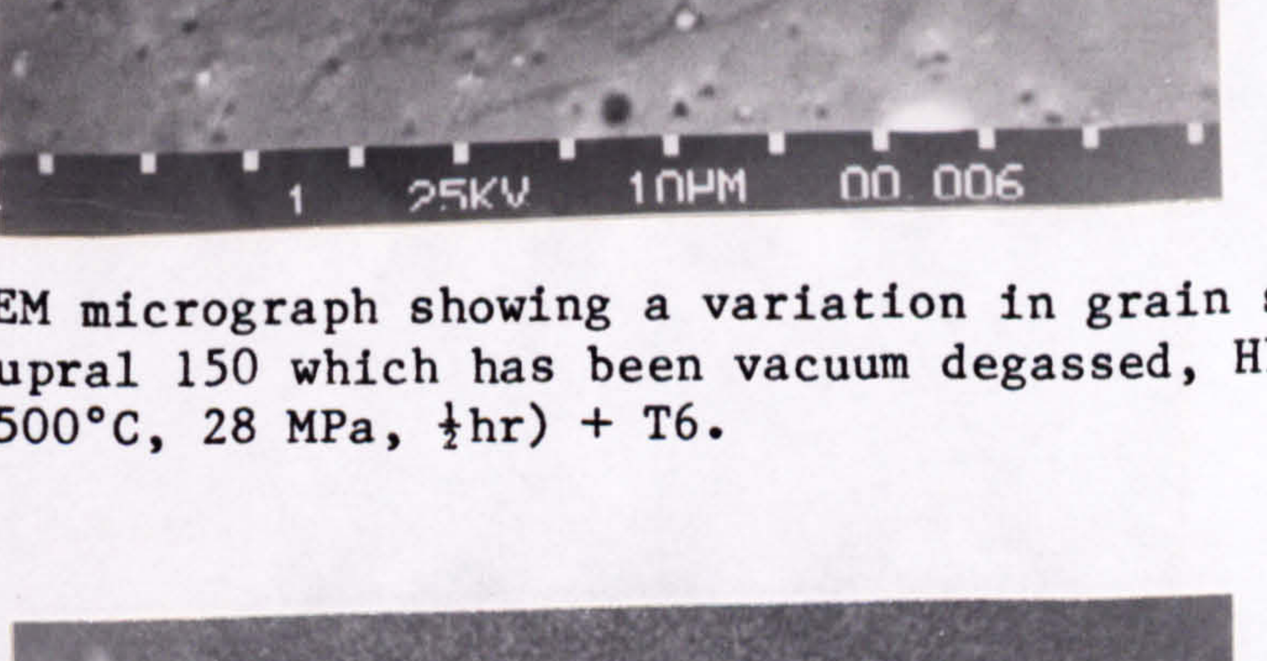

Figure 90(b)- Distribution map for zirconium in above area fails to detect any variation in zirconium distribution with grain size.

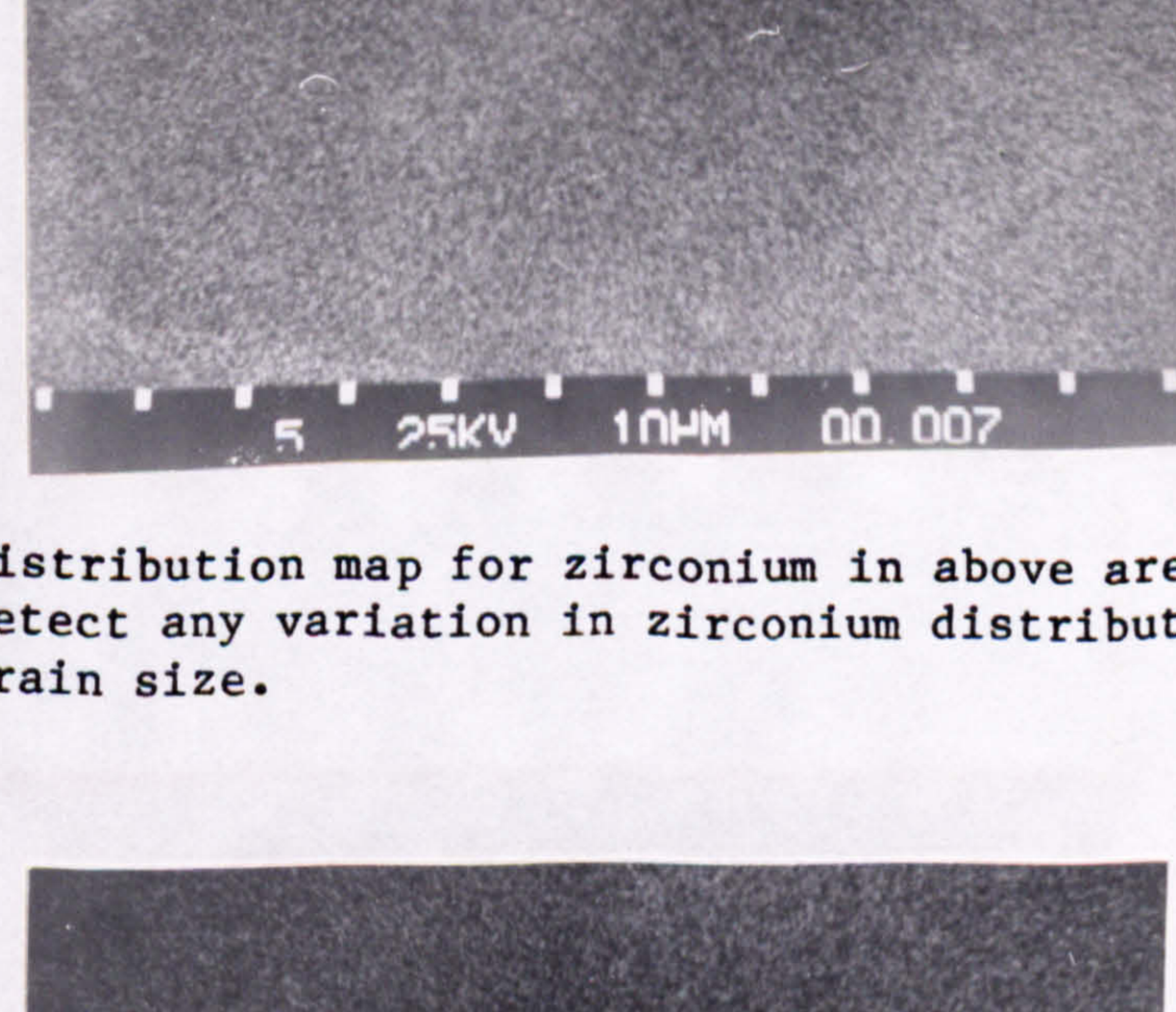

Figure 90(c)- As above but at higher magnification.

Figure 91 - SEM micrograph of SPF Supral 150 which has been vacuum degassed, HIPped (500°C, 28 MPa, ½hr) + T6, used for spot analysis across the edge section.

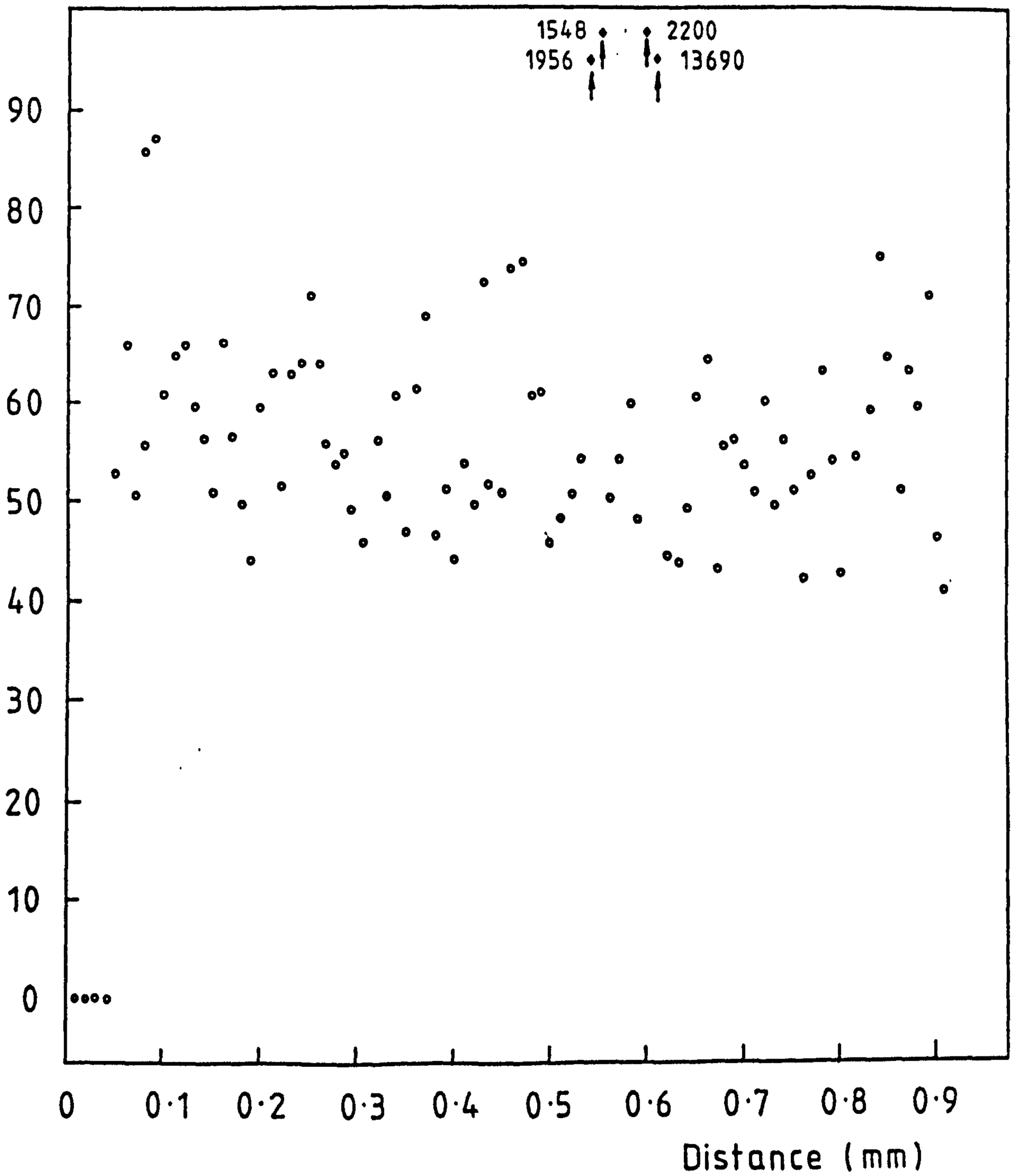

Figure 92 - Spot analysis results for zirconium across section in Figure 91, showing no zirconium in cladding, but fairly homogeneous distribution in matrix.

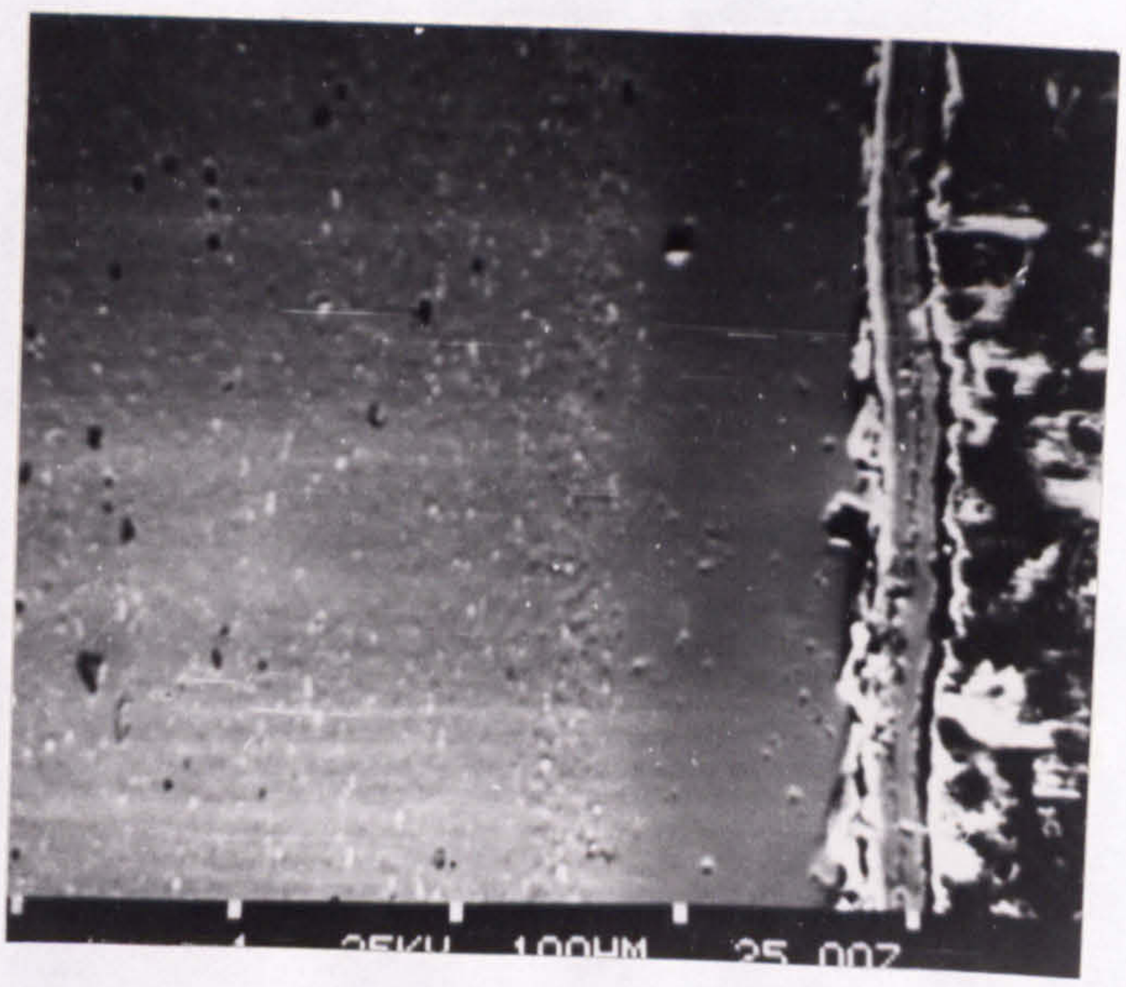

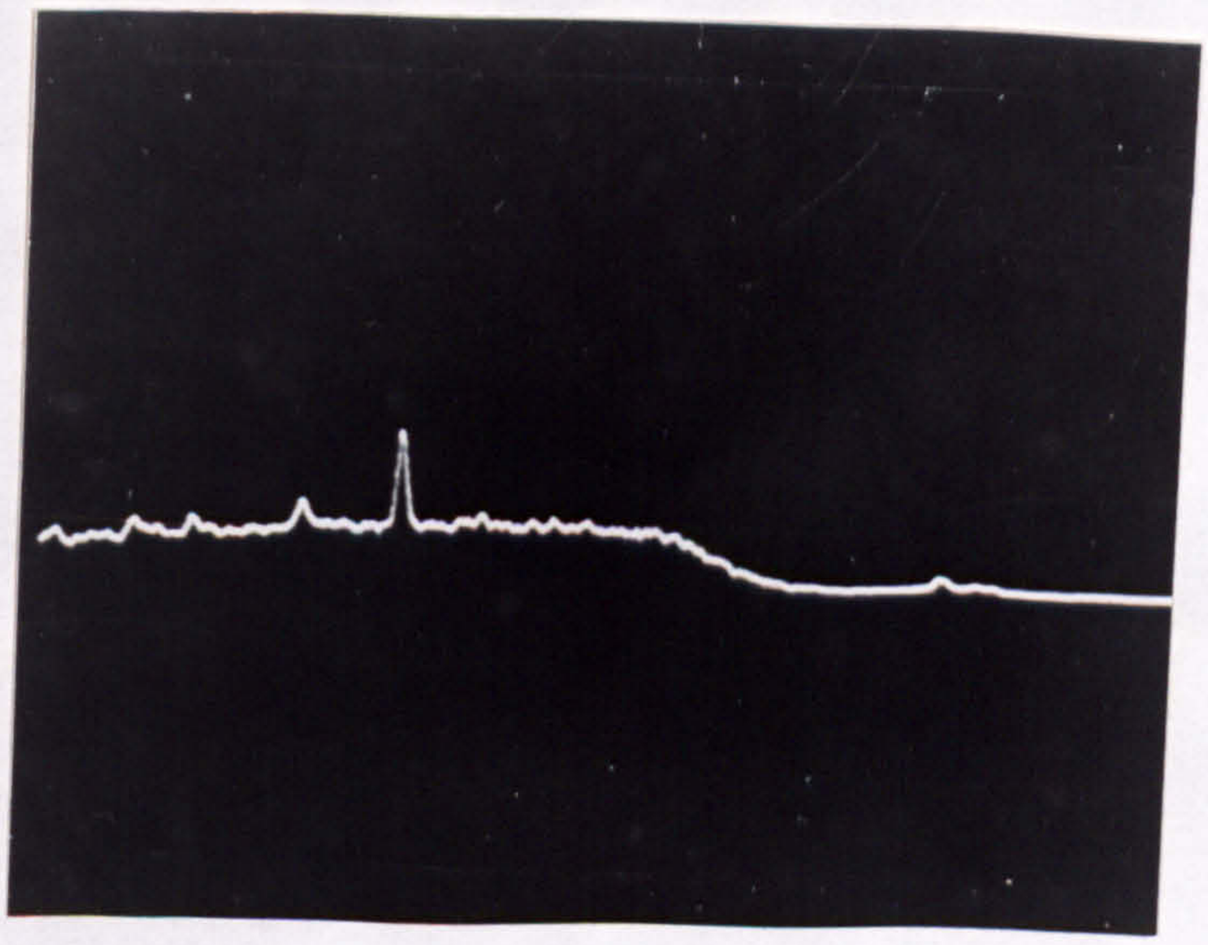

Figure 93 - Line scan for copper across matrix/cladding interface showing some copper in cladding in SPF Supral 150 after heat-treatment.

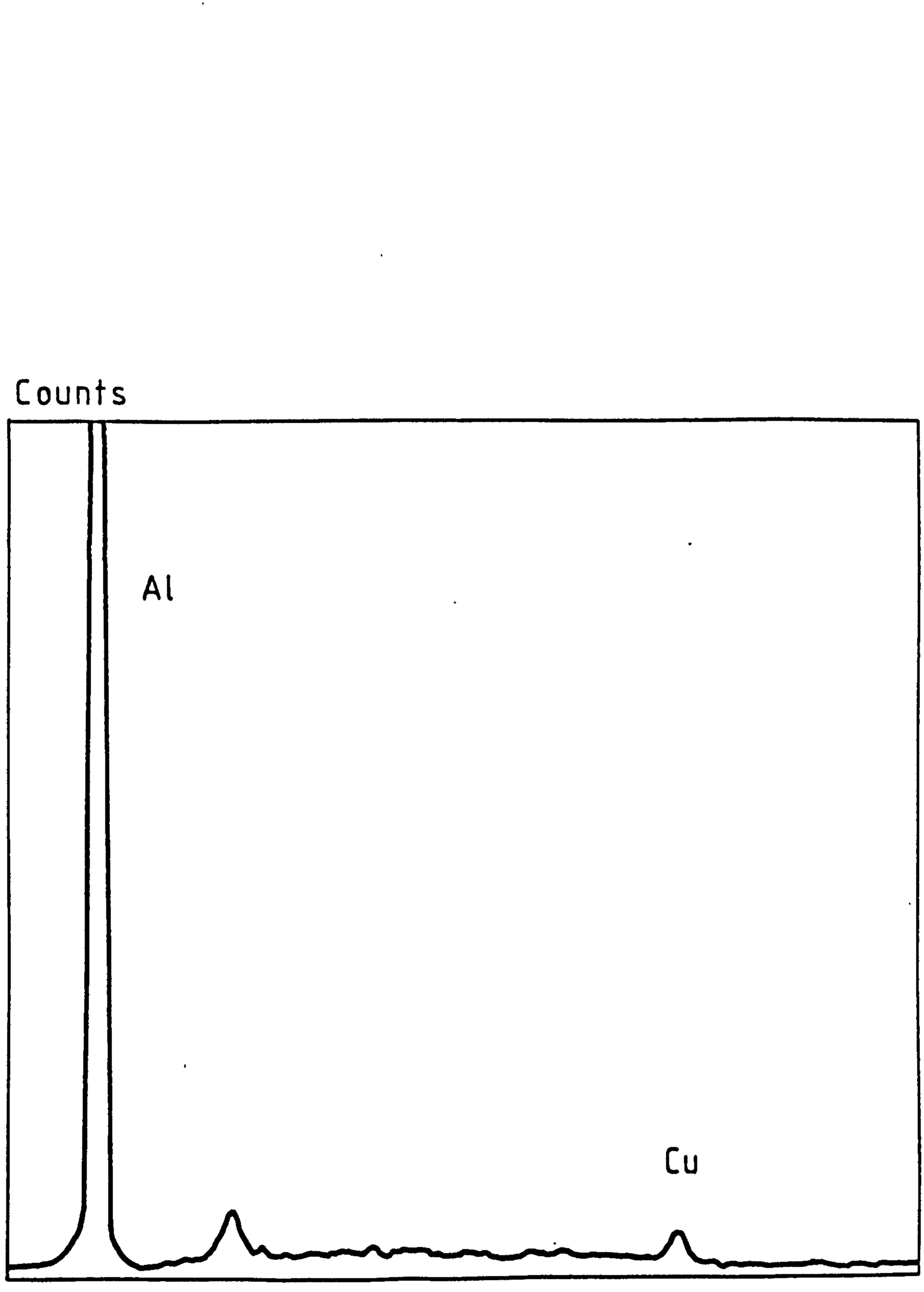

Figure 93(a)- Spot analysis for copper in clad layer showing a small concentration of copper.

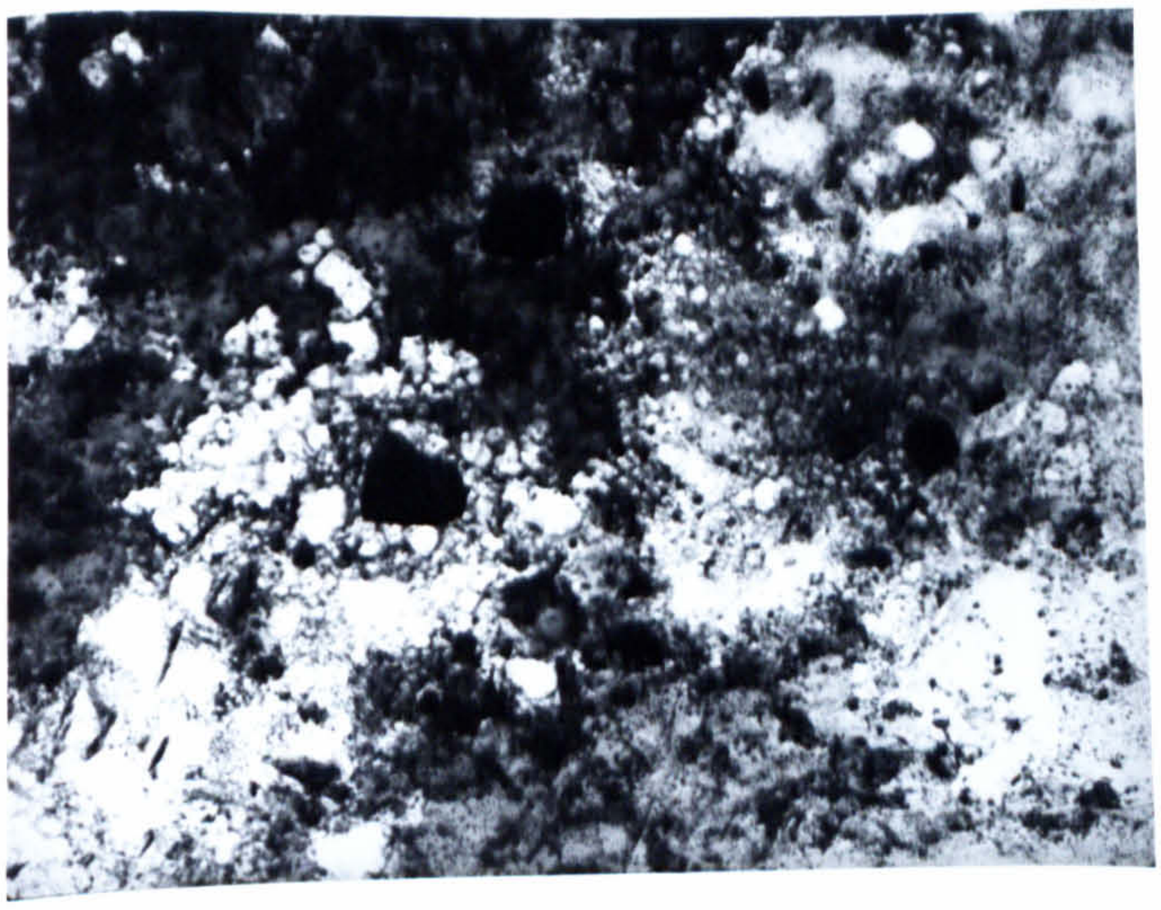

Figure 94(a)- TEM micrograph of as-received virgin Supral 150 showing heavily dislocated structure (x 5K)

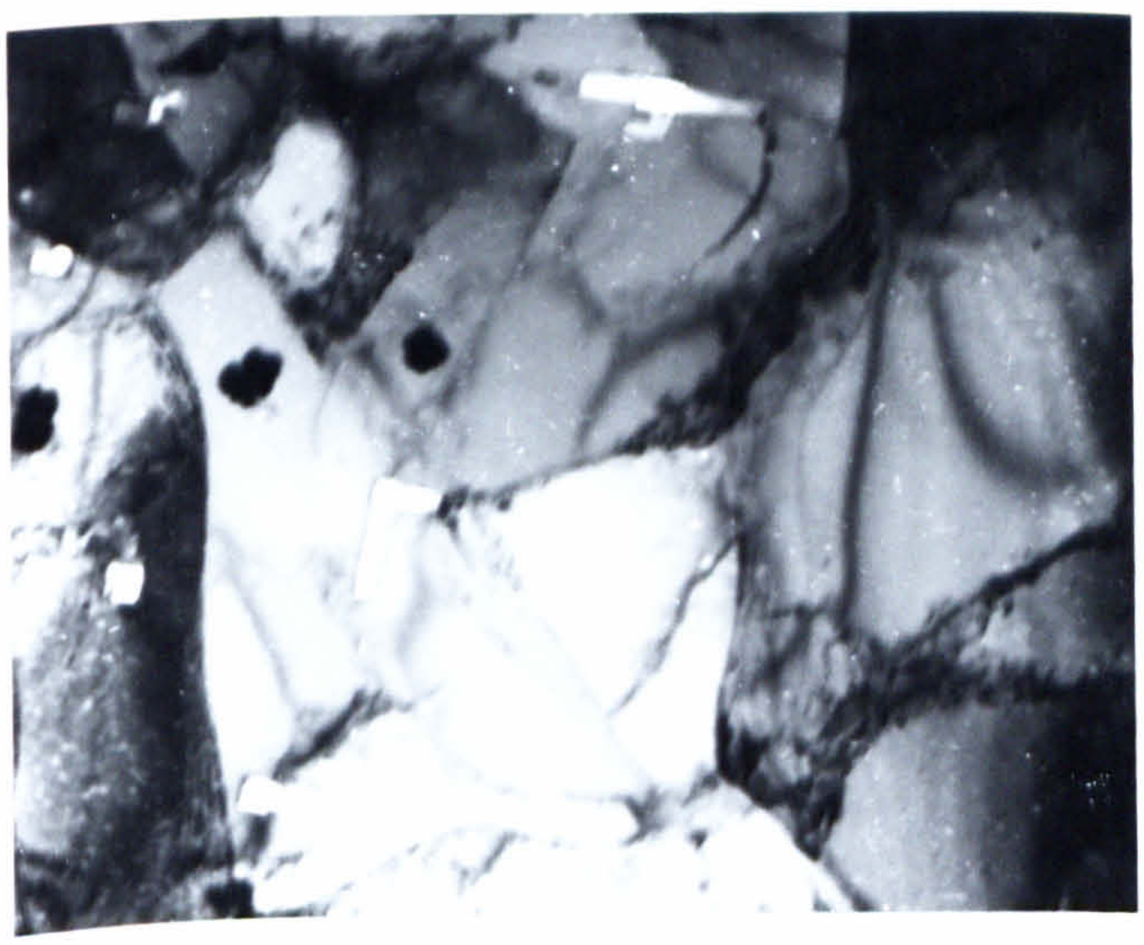

Figure 94(b)- TEM micrograph of as-received virgin Supral 150 showing heavily dislocated structure (x 17K)

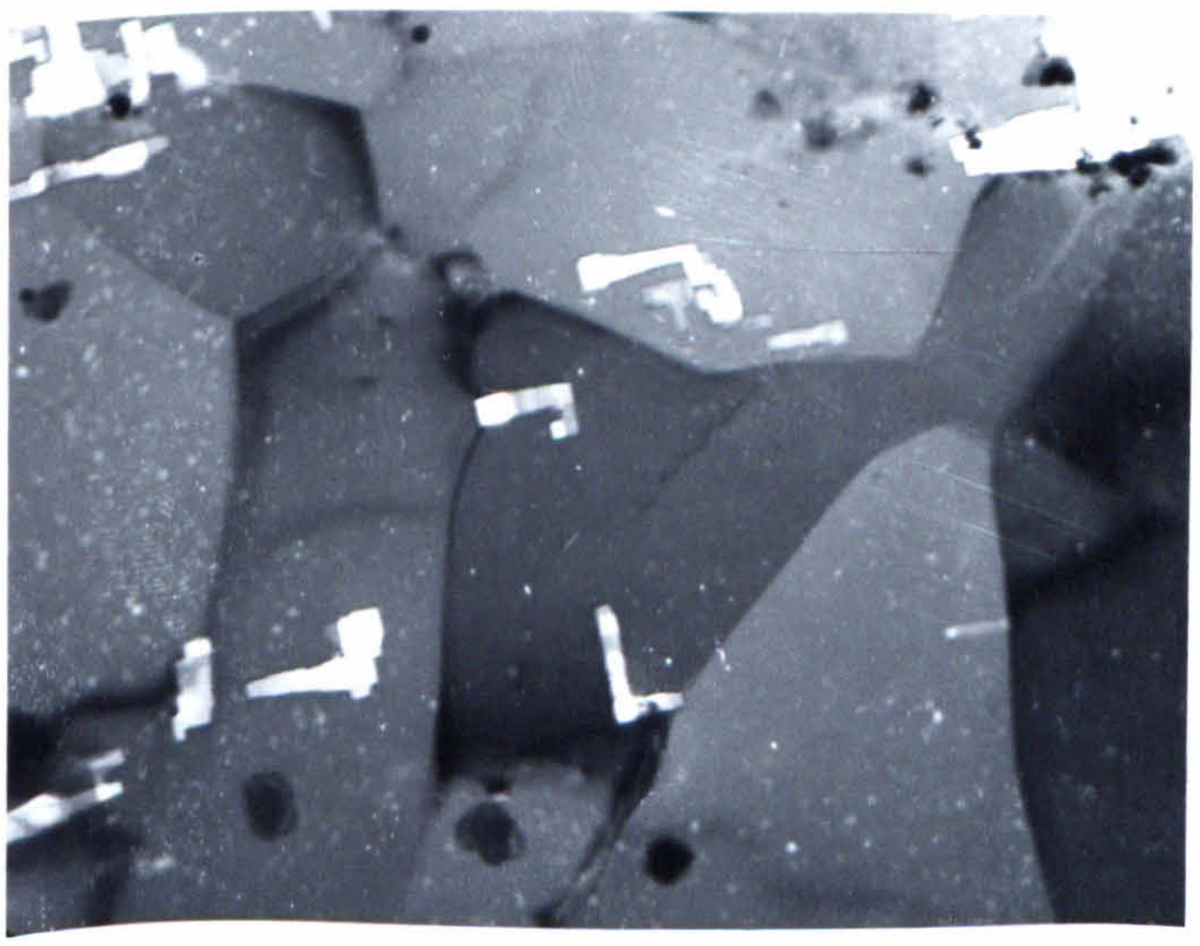

Figure 94(c)- Effect of increasing temperature (in TEM hot stage) to 450°C, producing dislocation free sub-grains (x 17K)

x 200

Figure 95 - Optical hot stage micrograph of SPF Supral 150 at 530°C under a vacuum at start (x 200).

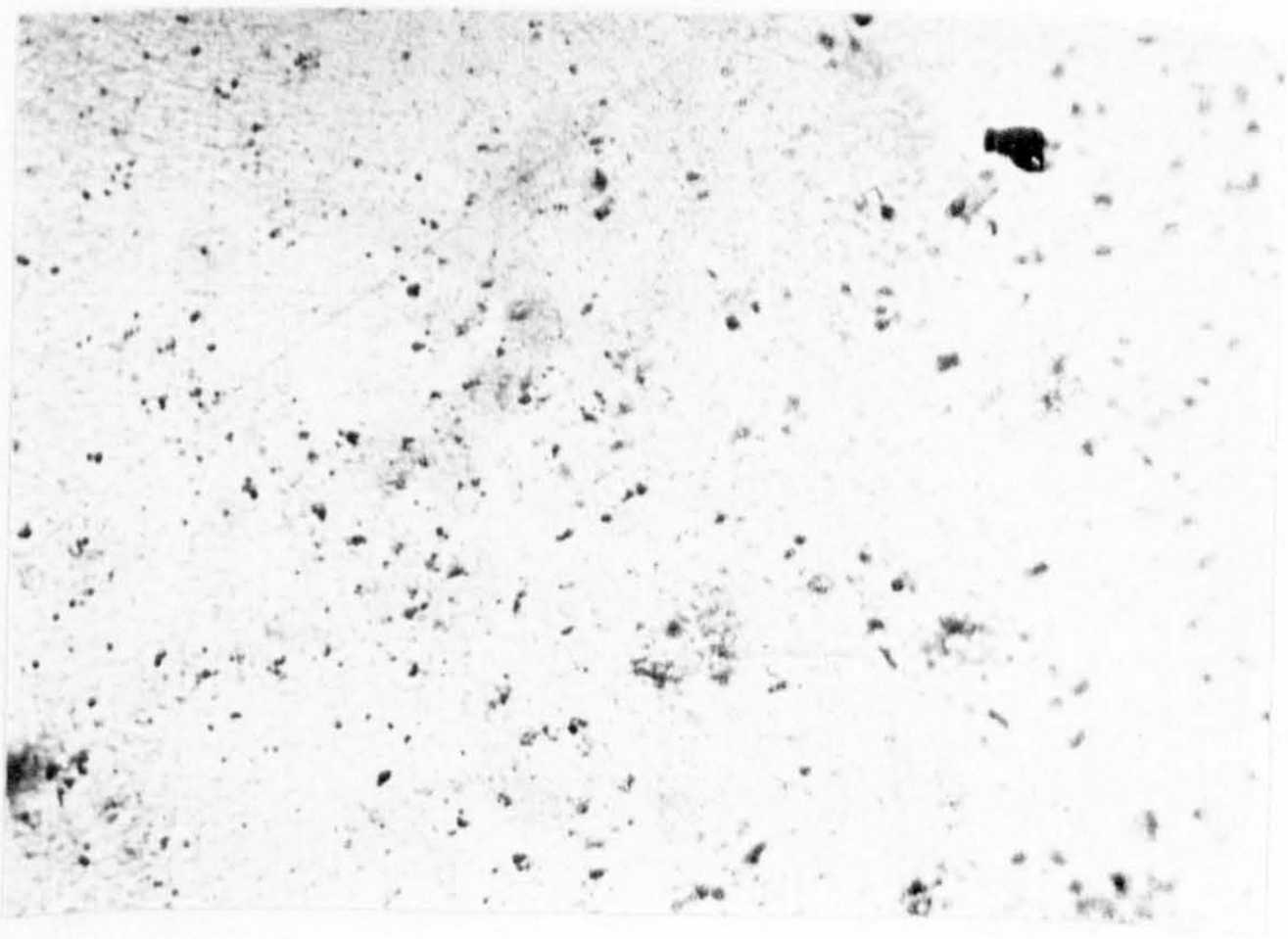

(x 200)

Figure 95a - Optical hot stage micrograph showing how there is little effect on the surface of SPF Supral 150 (which has been HIPped to theoretical density) when heated in a vacuum at 530°C for ½ hr (x 200).

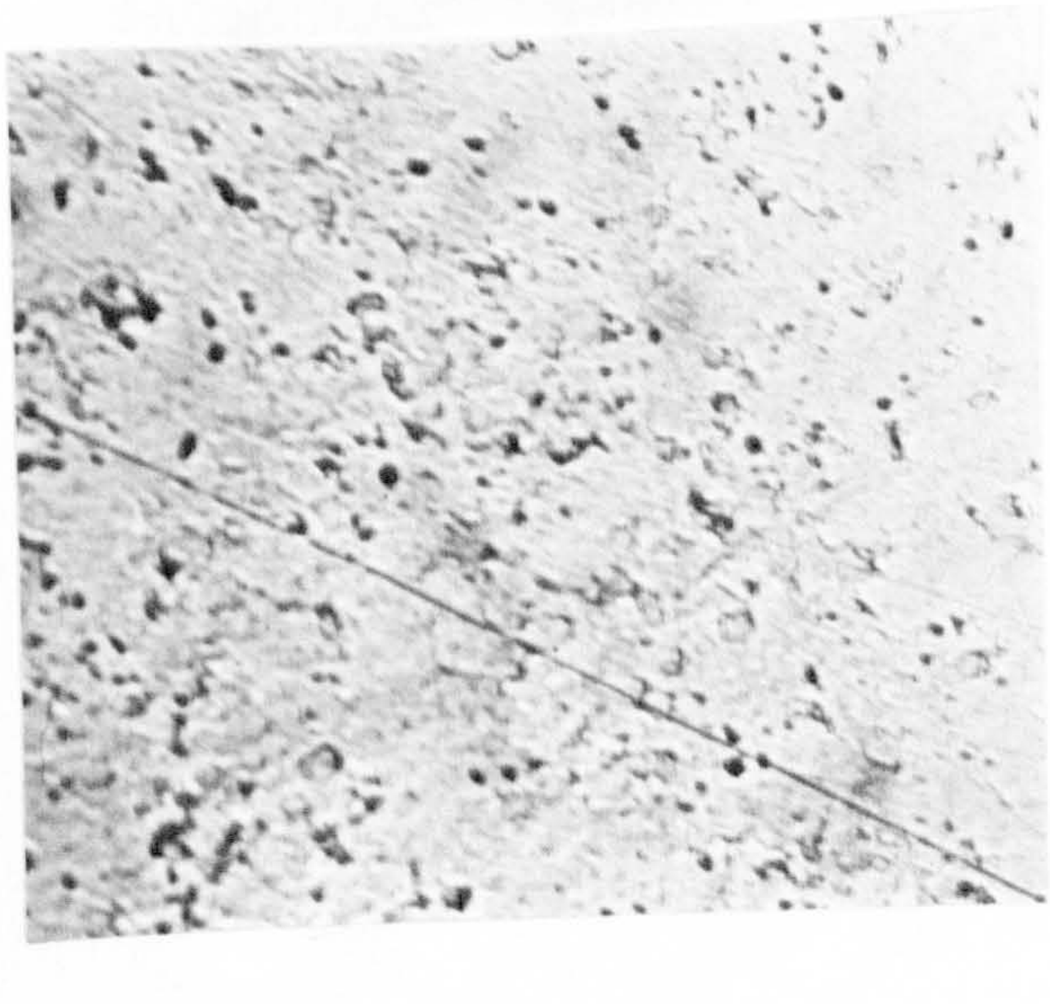

(a)

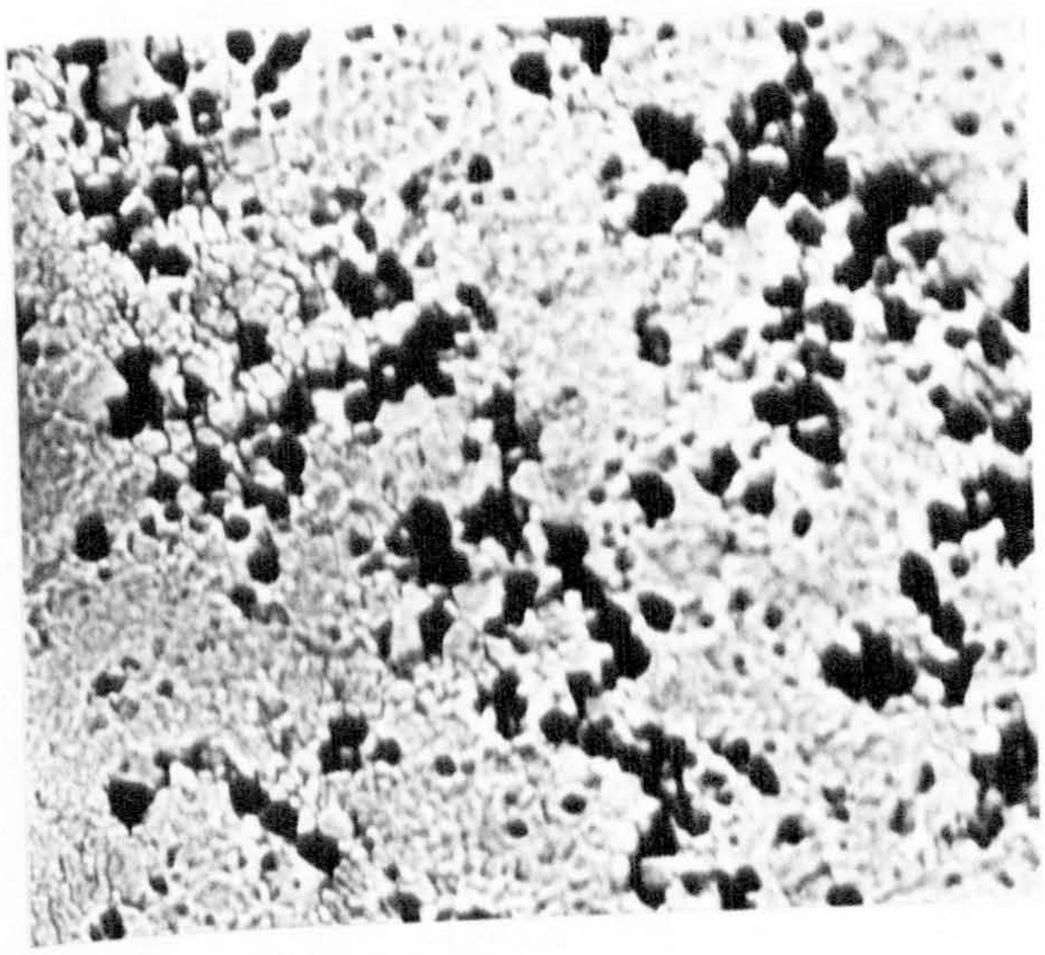

(b)

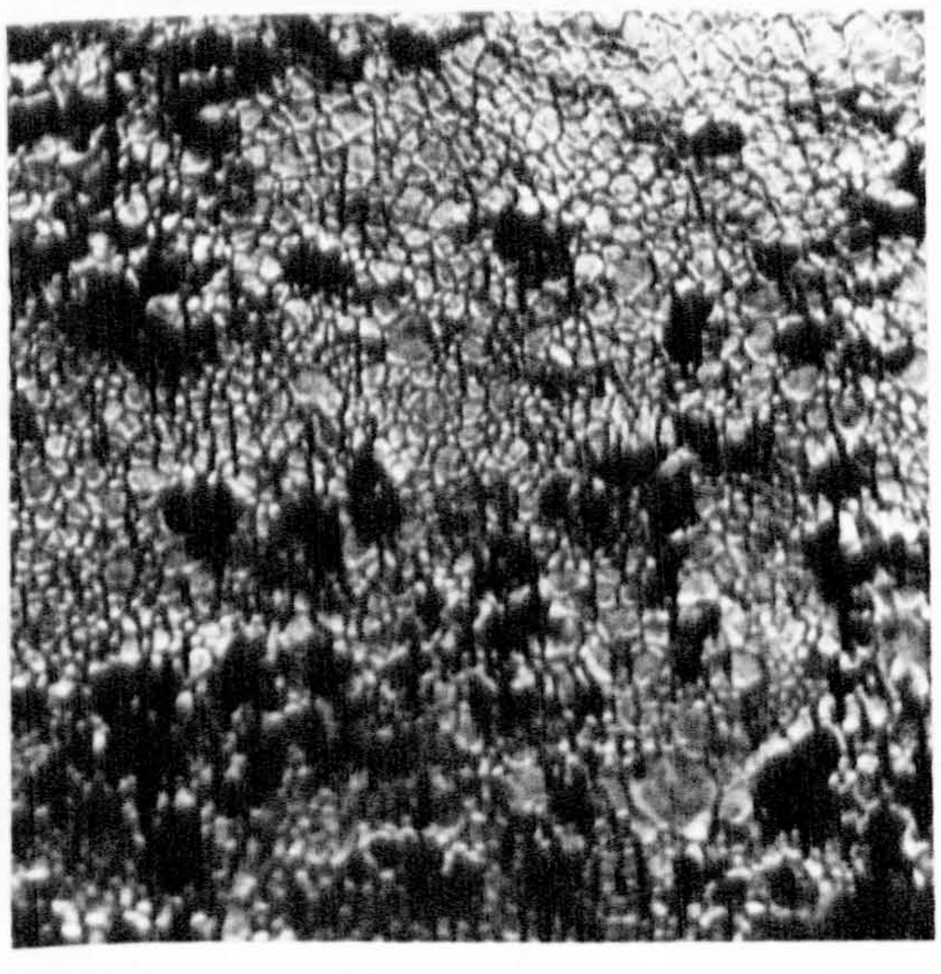

(c)

Figure 96 - Optical hot stage micrographs of SPF Supral 150, HIPped (450°C, 28 MPa, ½ hr) + T6 (a) shows surface when in vacuum at start, raised temperature to 530°C, no change. (b) Introduced Argon, in 15 minutes have oxide layer and porosity, as in (c) also. All x 200.

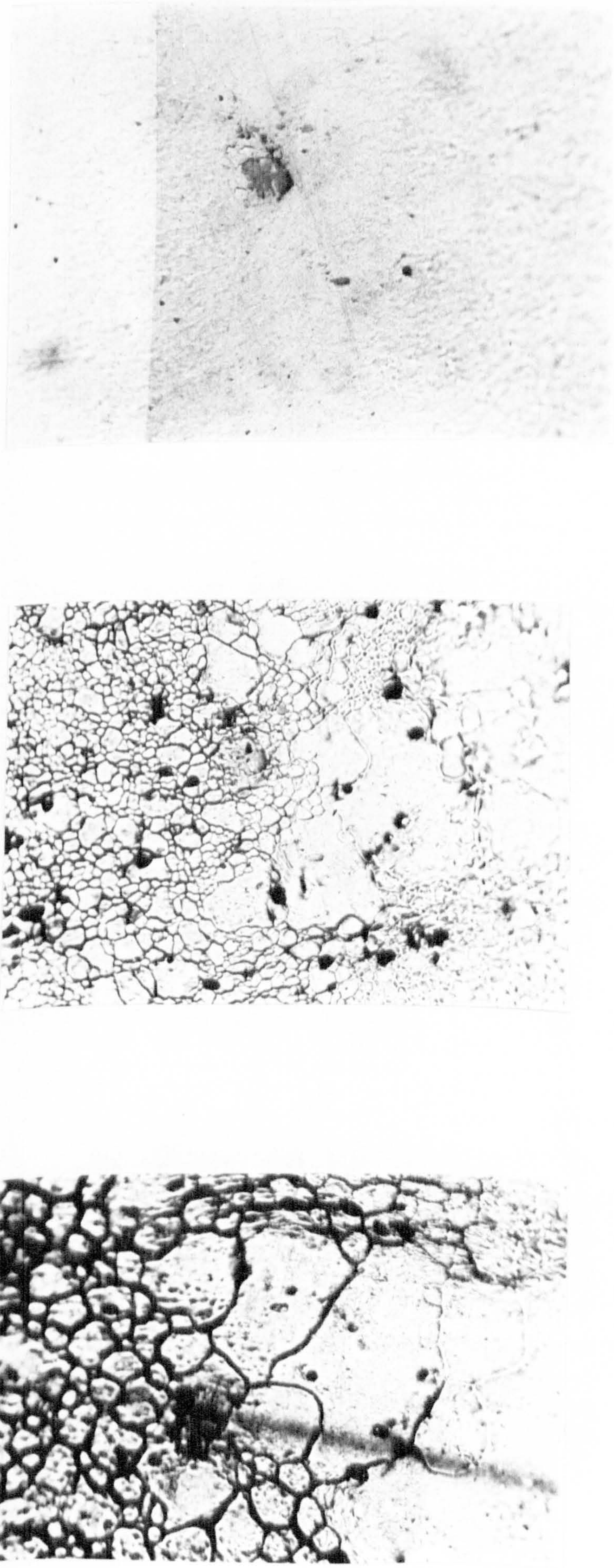

Figure 97 - Optical hot stage micrographs of the surface of SPF Supral 150 when heated in Argon at 530°C, shows the development of the oxide layer and porosity (x 200).

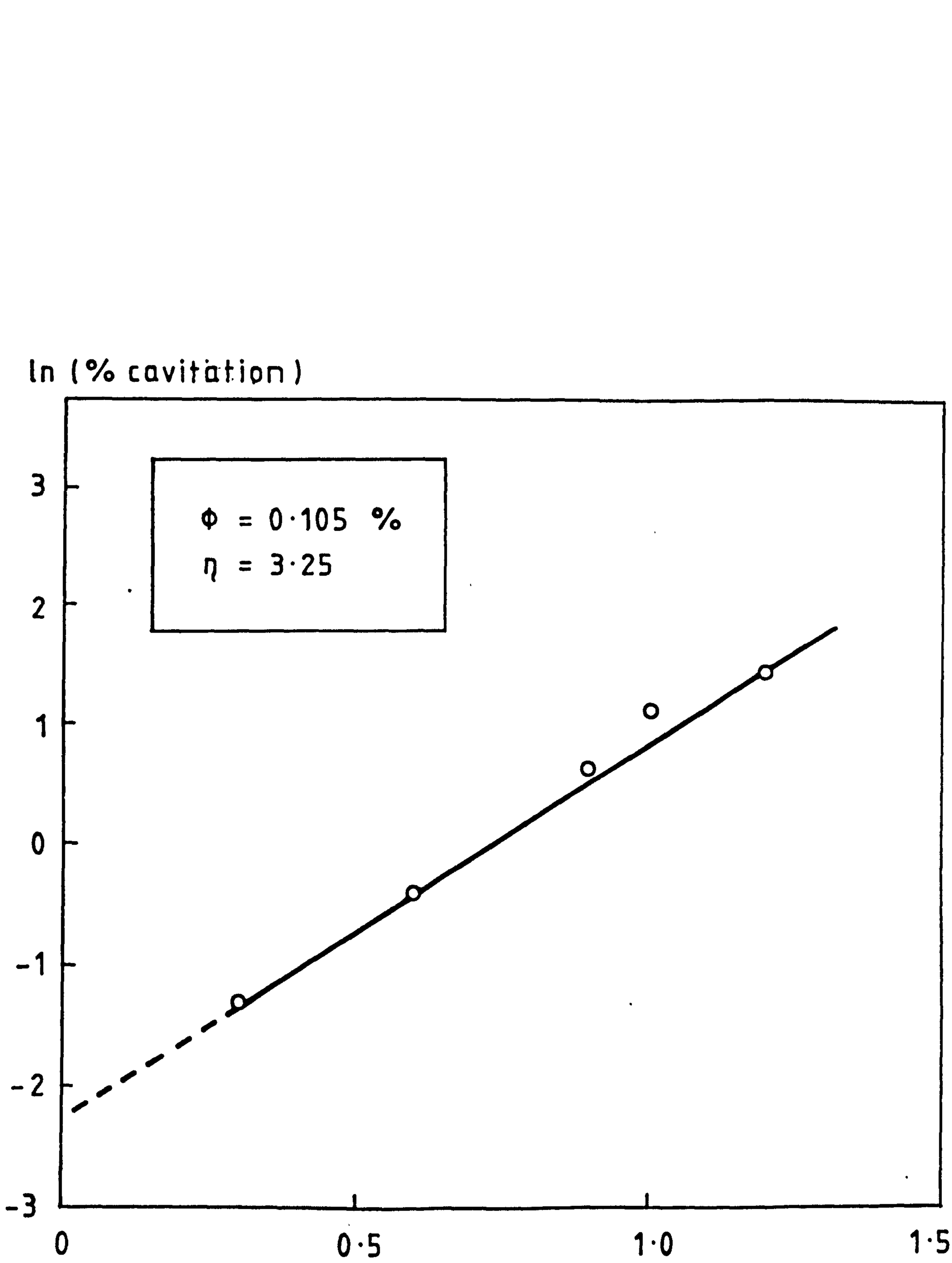

Figure 98 - Variation of cavitation with natural strain for SPF Supral 150 using the Stowell Analysis (69).

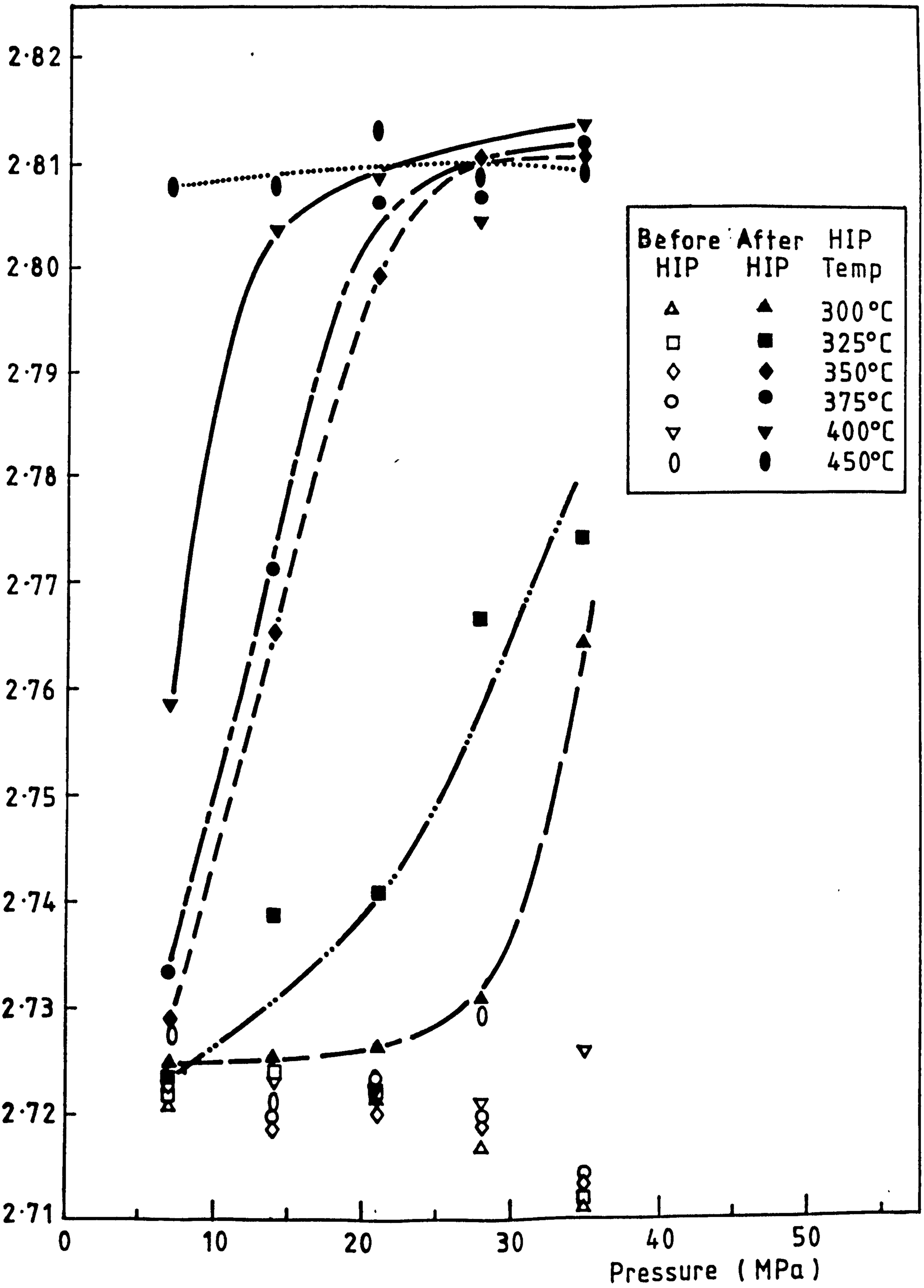

Figure 99 - Plot showing the variation of density in SPF Supral 150 with external pressure and temperature.

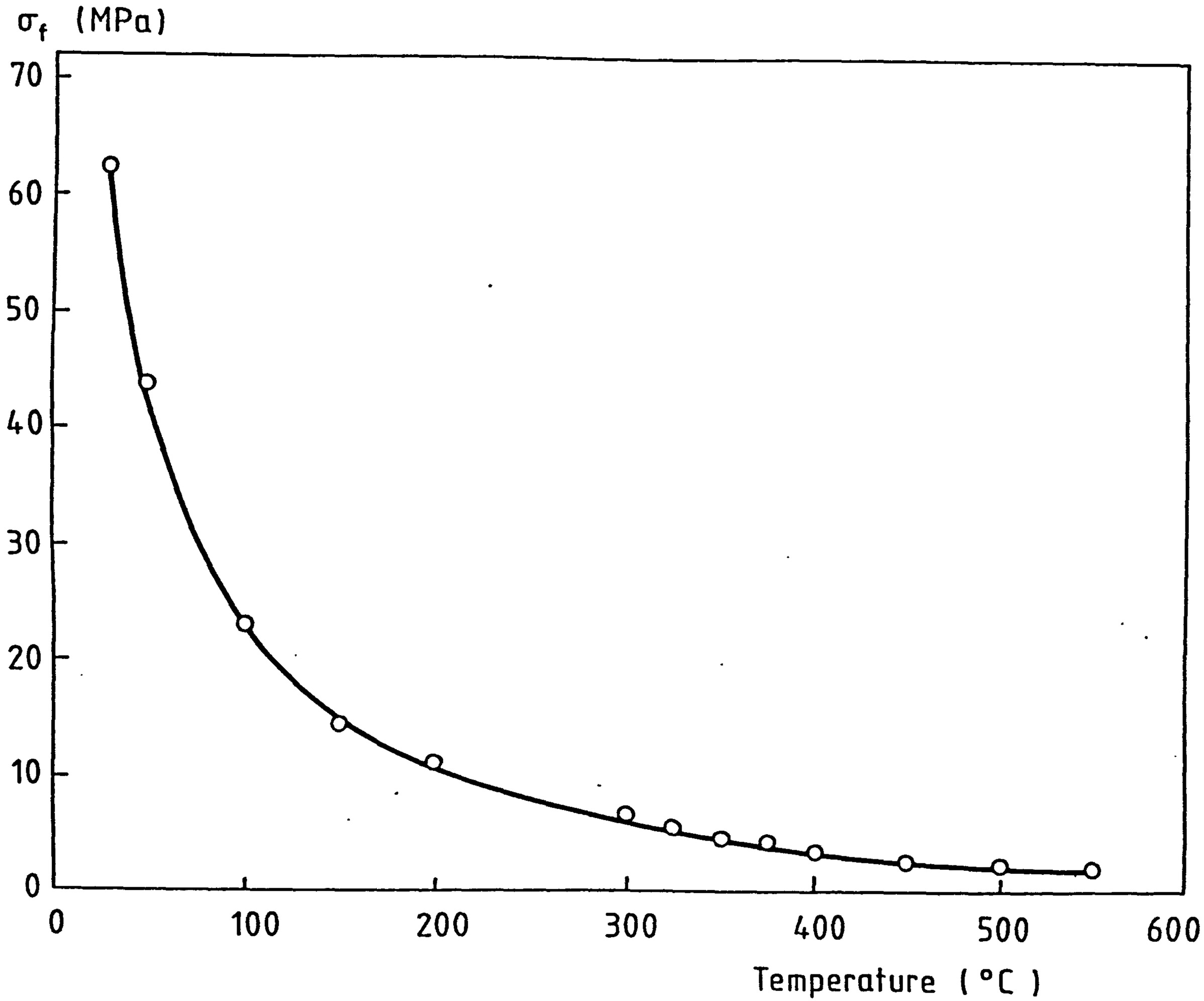

Figure 100 - The variation of flow stress (σ_f) with the temperature for a strain-rate of 1×10^{-4} sec^{-1} in Supral 100 from the results of Bricknell and Bentley (158).

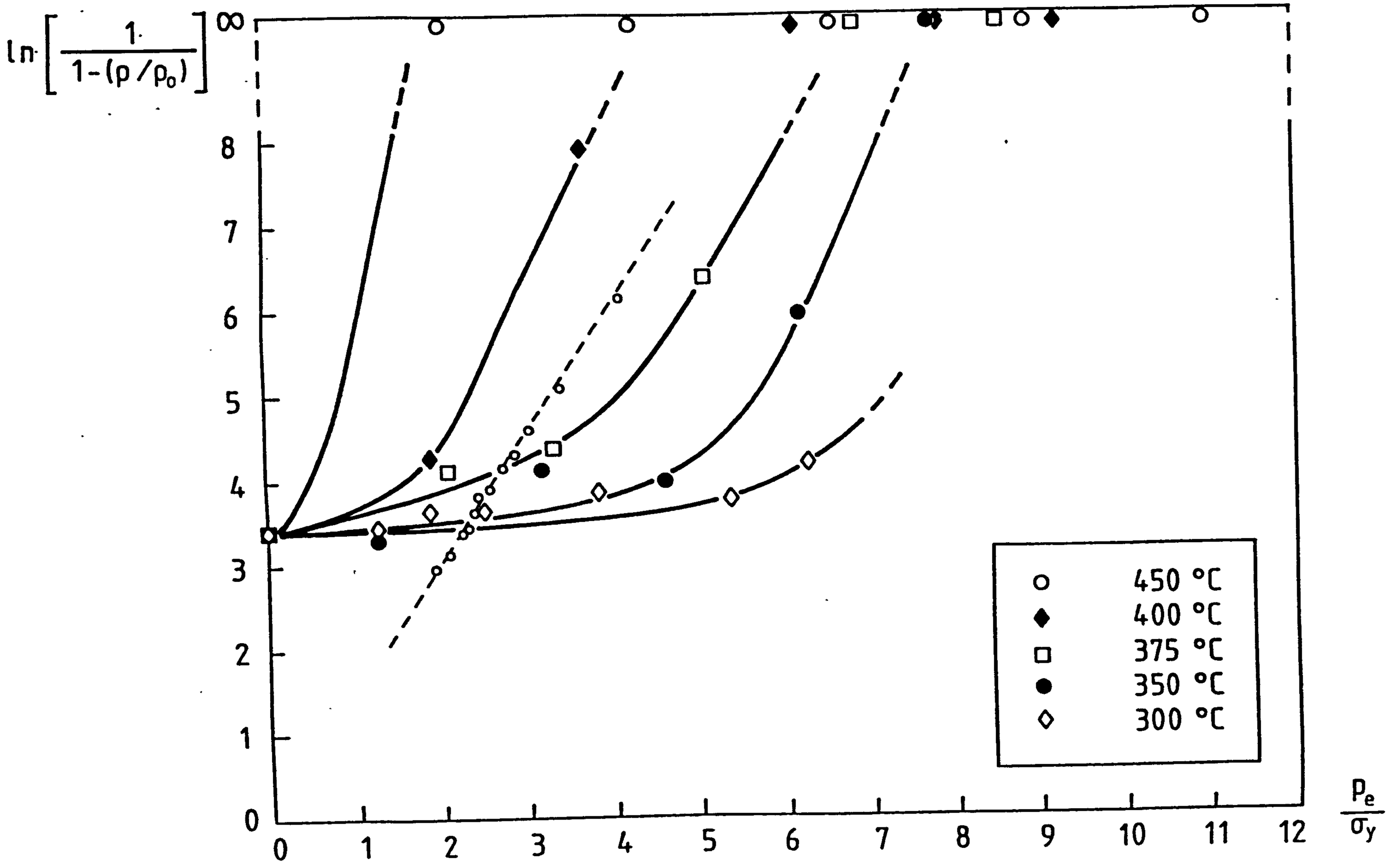

- Figure 101 - Densification data for Supral 150 by plastic yielding. Ashby (136) model plotted as broken line. Note, as $\rho \rightarrow \rho_o$ then complete densification; and vertical axis

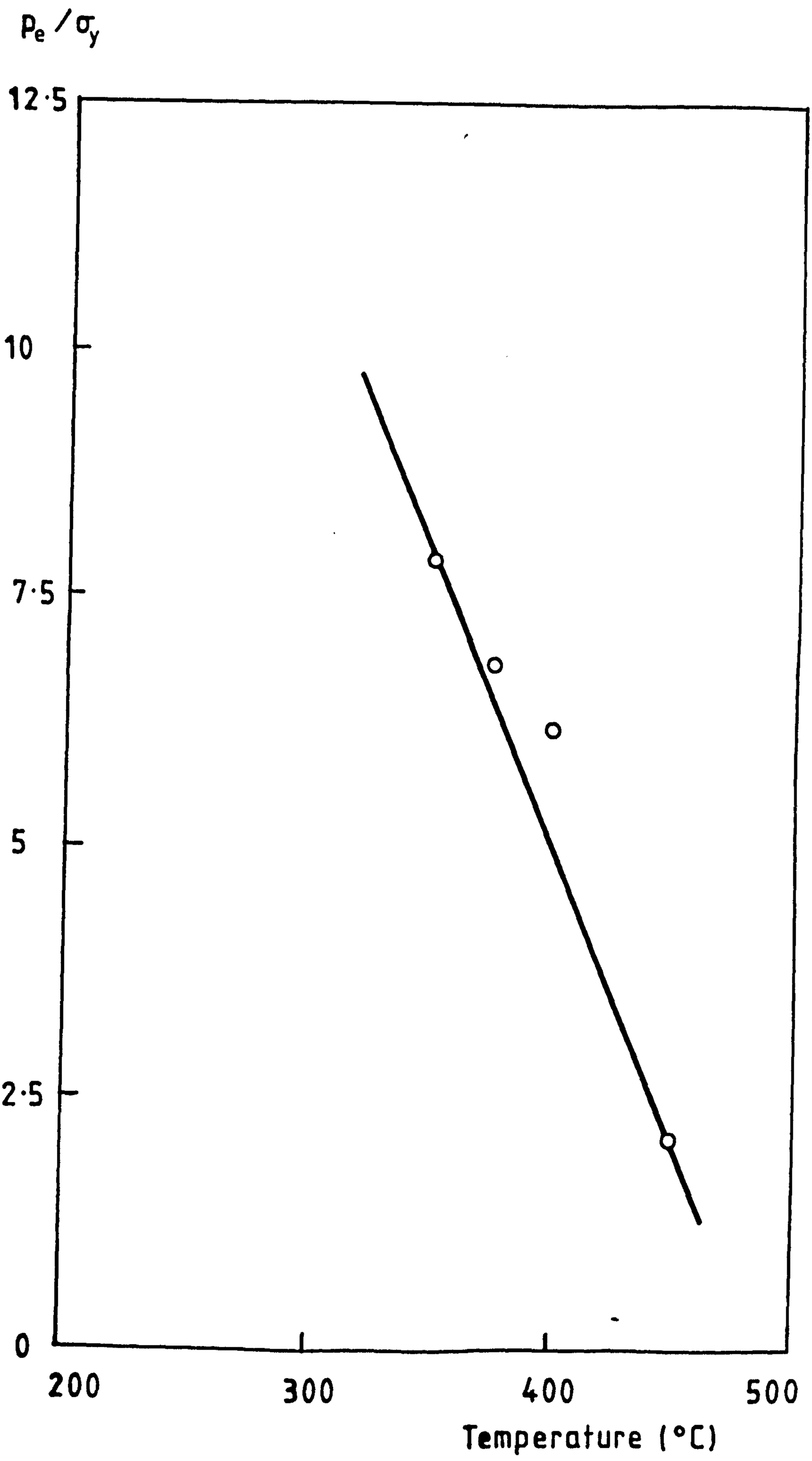

Figure 102 - Plot of the variation of the ratio of external pressure (P_e) to flow stress (σ_f) at a particular temperature and strain-rate, with temperature.

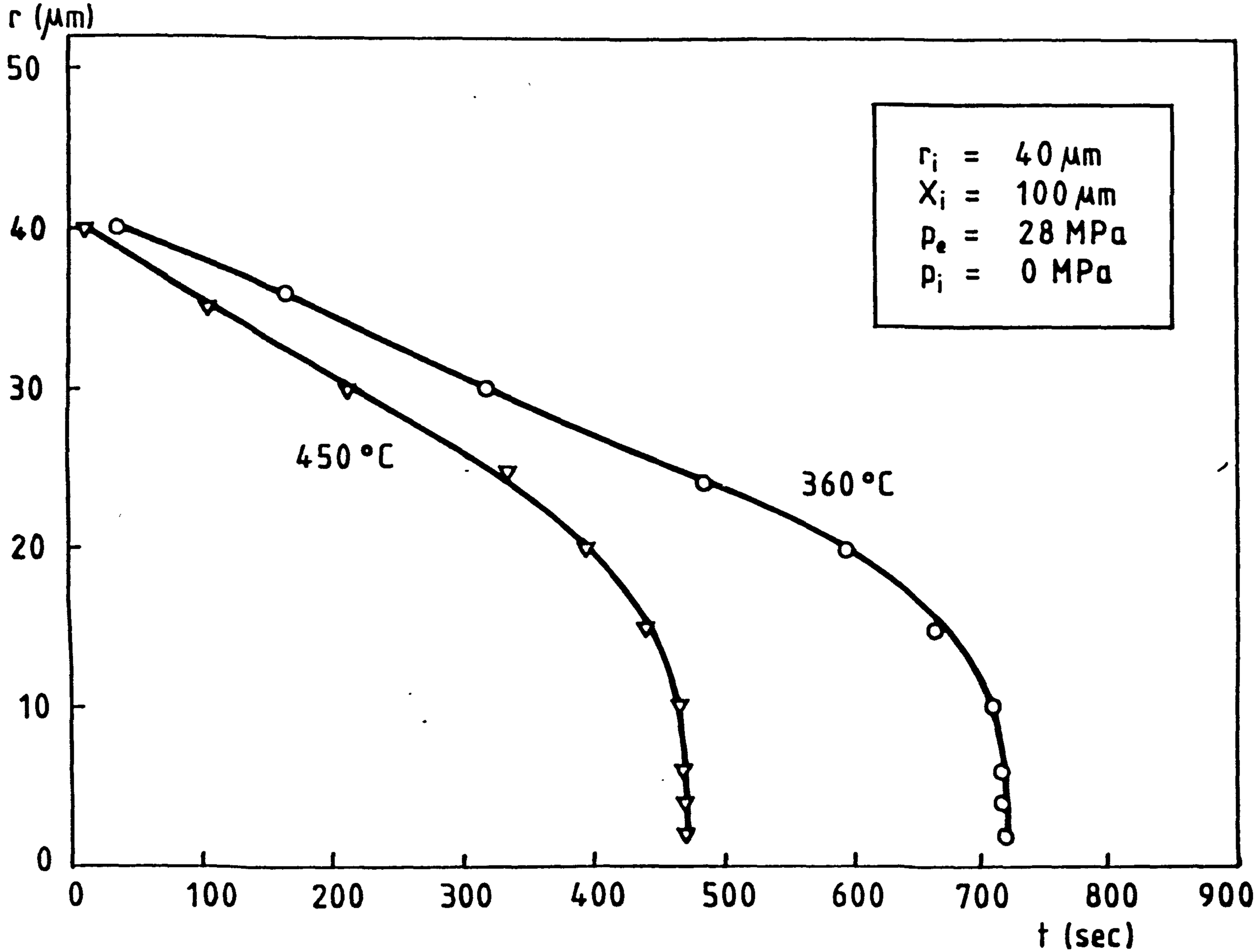

Figure 103 - Prediction of cavity closure sintering time using Ashby (135) theory for closure of grain boundary cavities by diffusion in Supral 150.

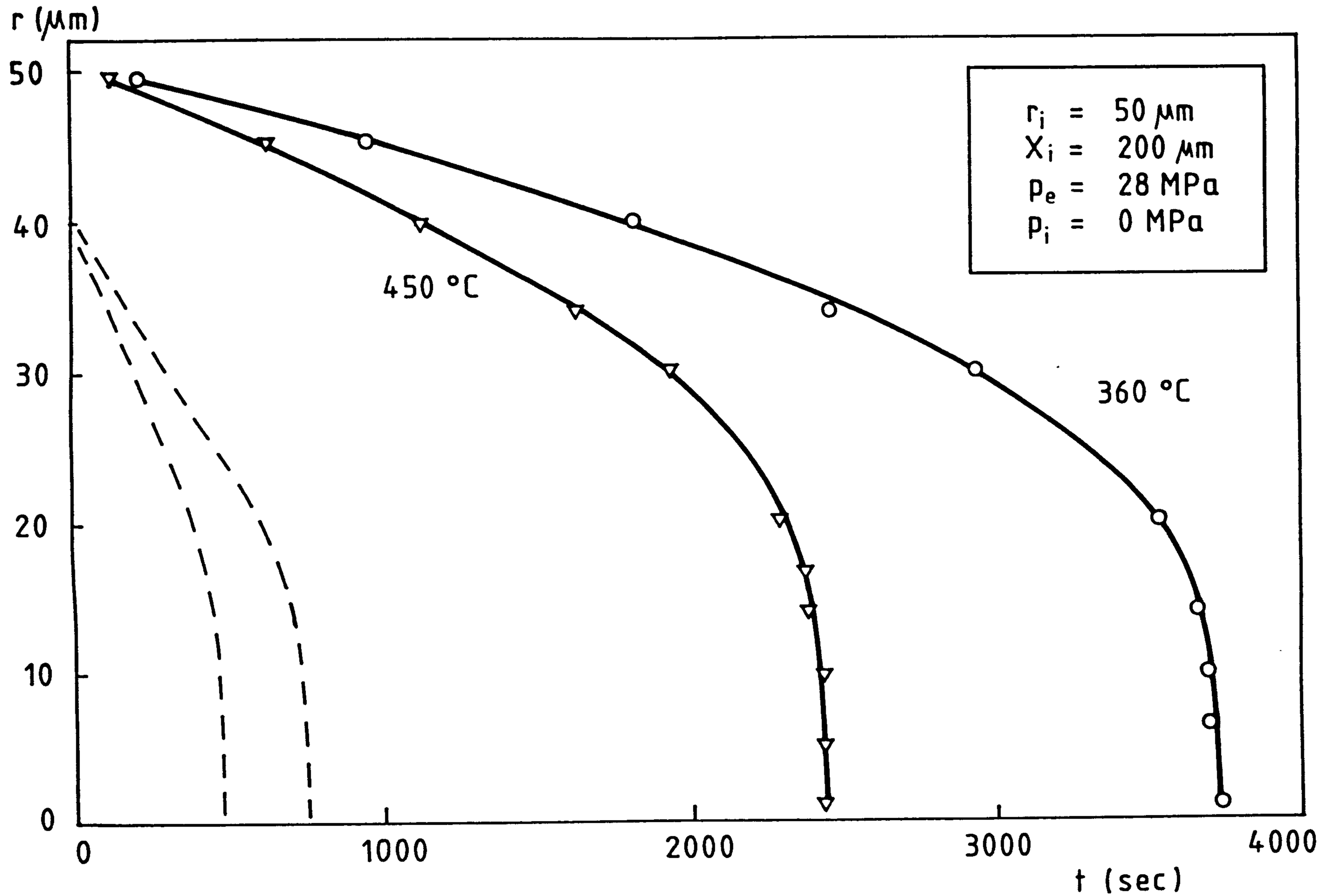

Figure 104 - Prediction of cavity closure sintering time using Ashby (135) theory for closure of grain boundary cavities by diffusion in Supral 150 for initial cavity radius (r_i) of 50 μm and cavity spacing of 200 μm. Dotted plot shows the result from Figure 103.

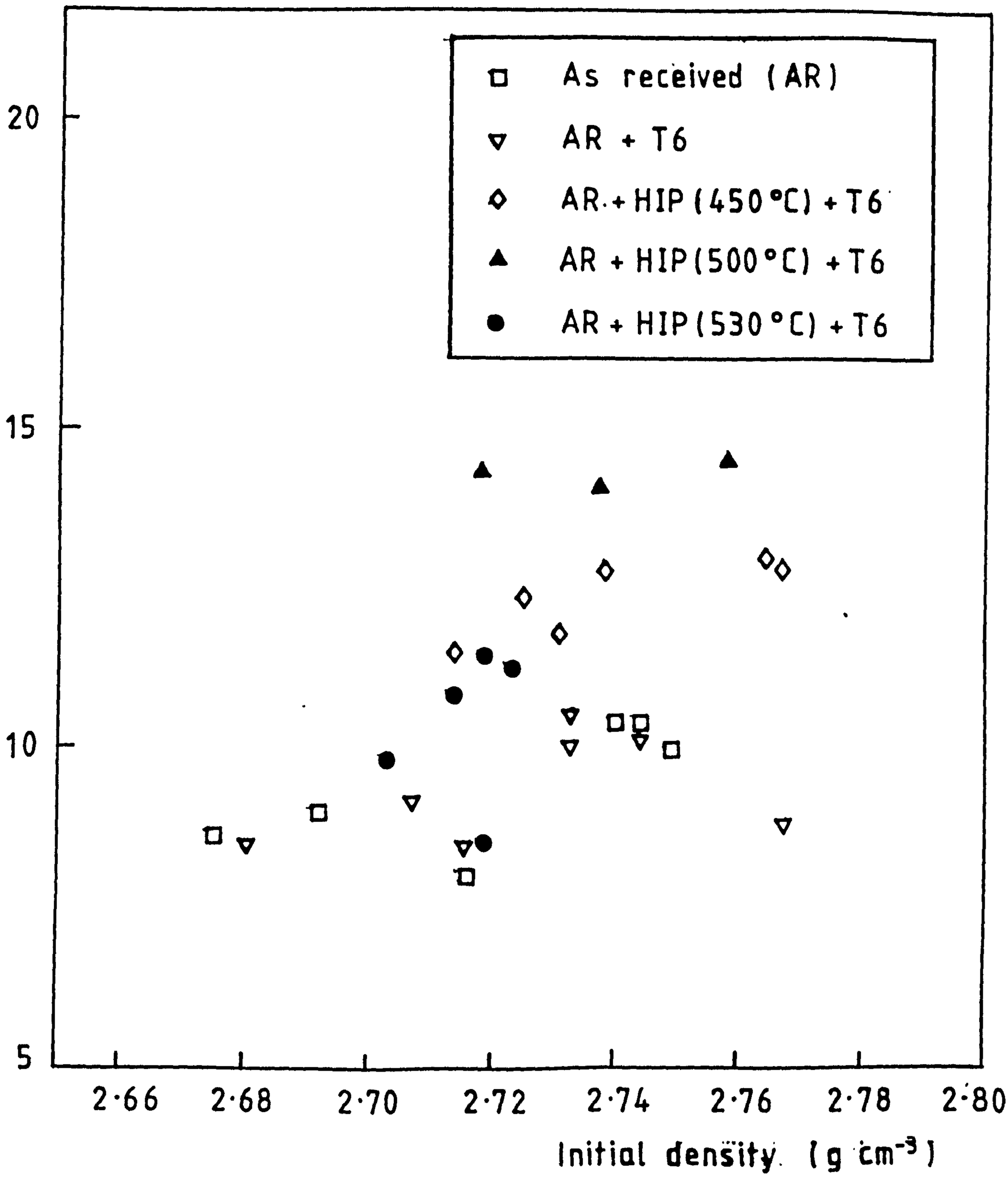

Figure 105 - Effect of initial cavity levels (measured by density) and subsequent treatments on final elongation in room temperature tensile tests on SPF Supral 150.

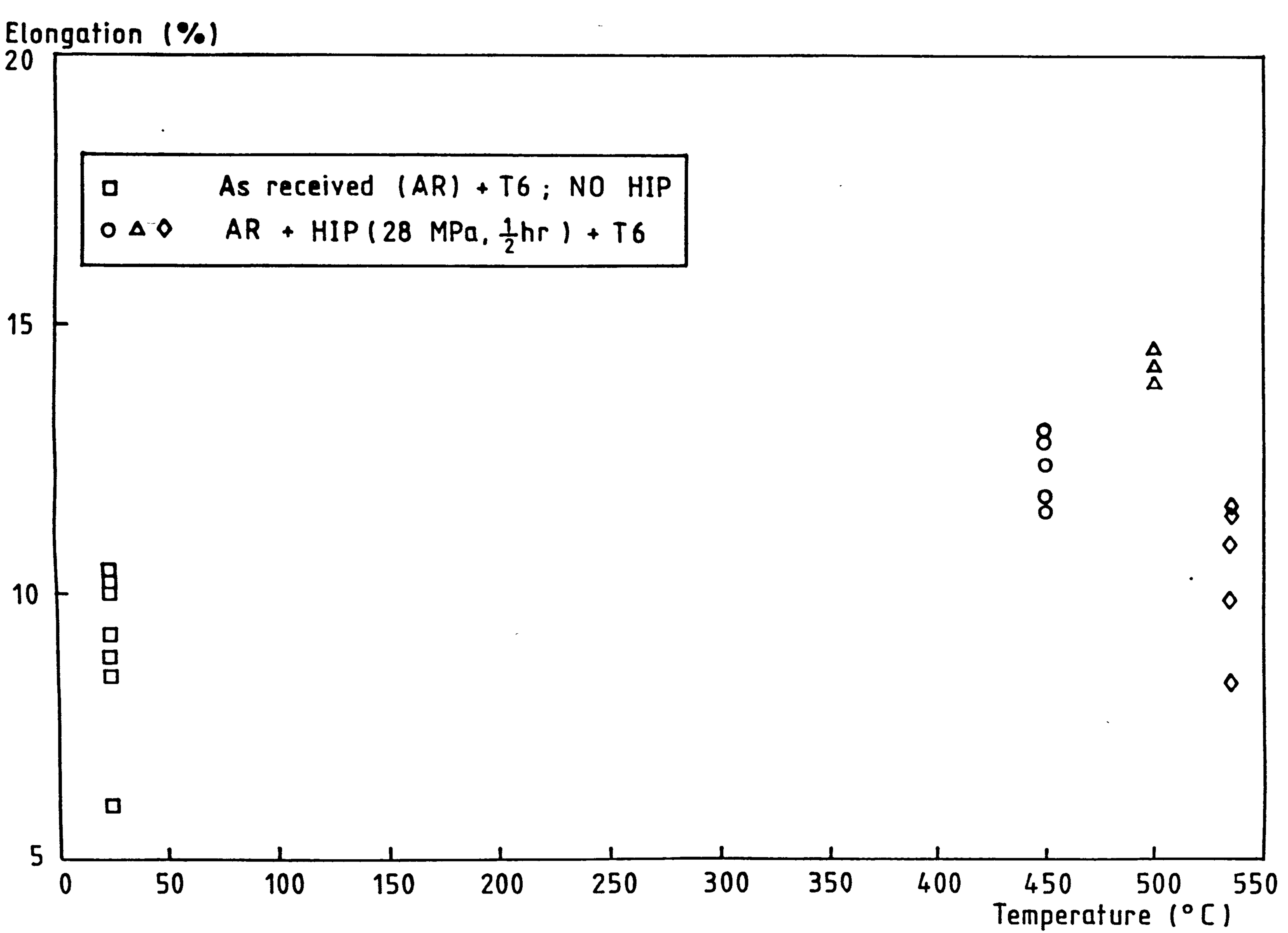

Figure 106 - The effect of HIP temperature on elongation in Supral 150 tensile tested at room temperature. The highest elongation is obtained after HIP at 500°C, (28 MPa, ½hr)

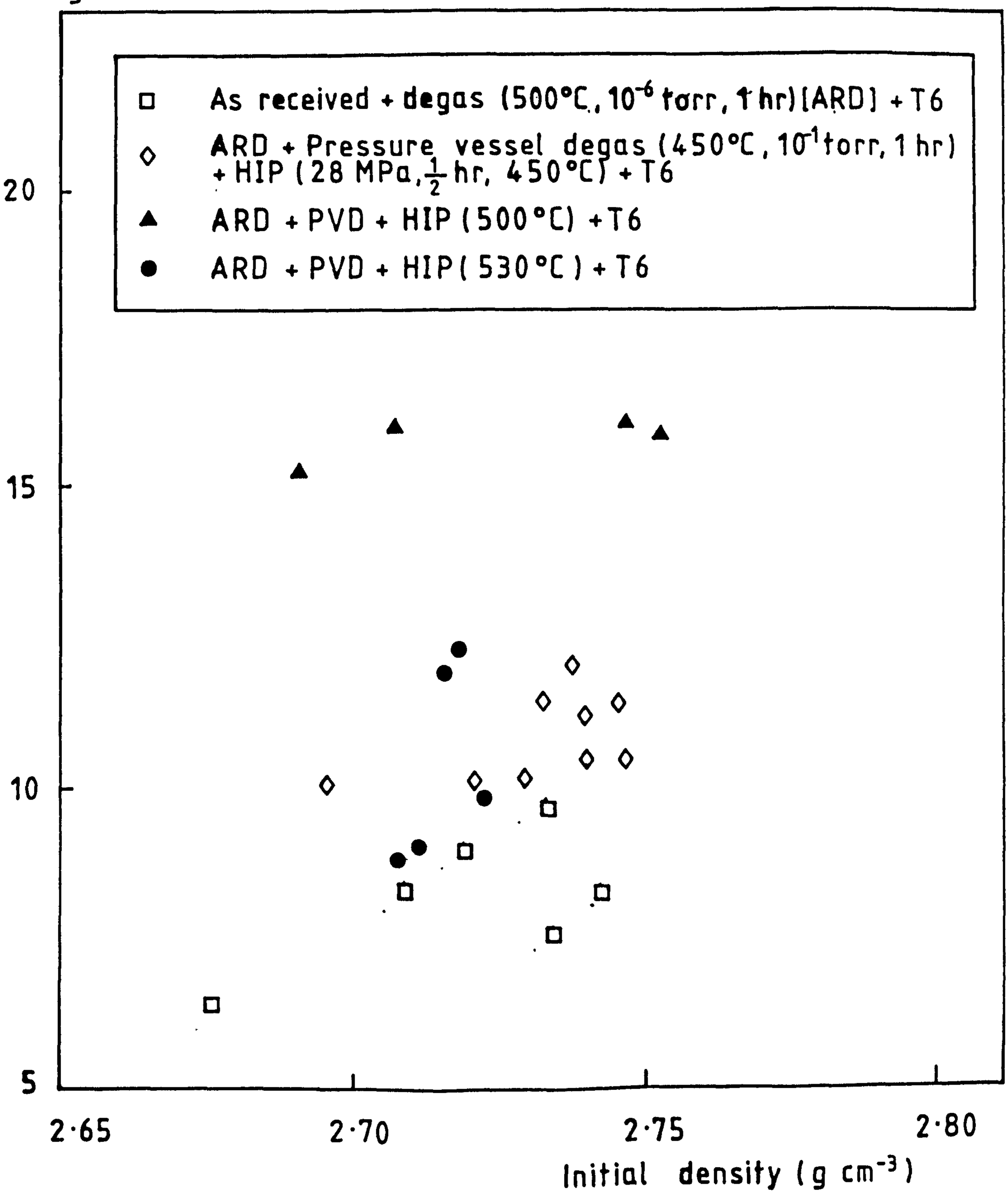

Figure 107. Effects of initial specimen density and subsequent treatments on room temperature ductility in vacuum degassed SPF Supral 150.

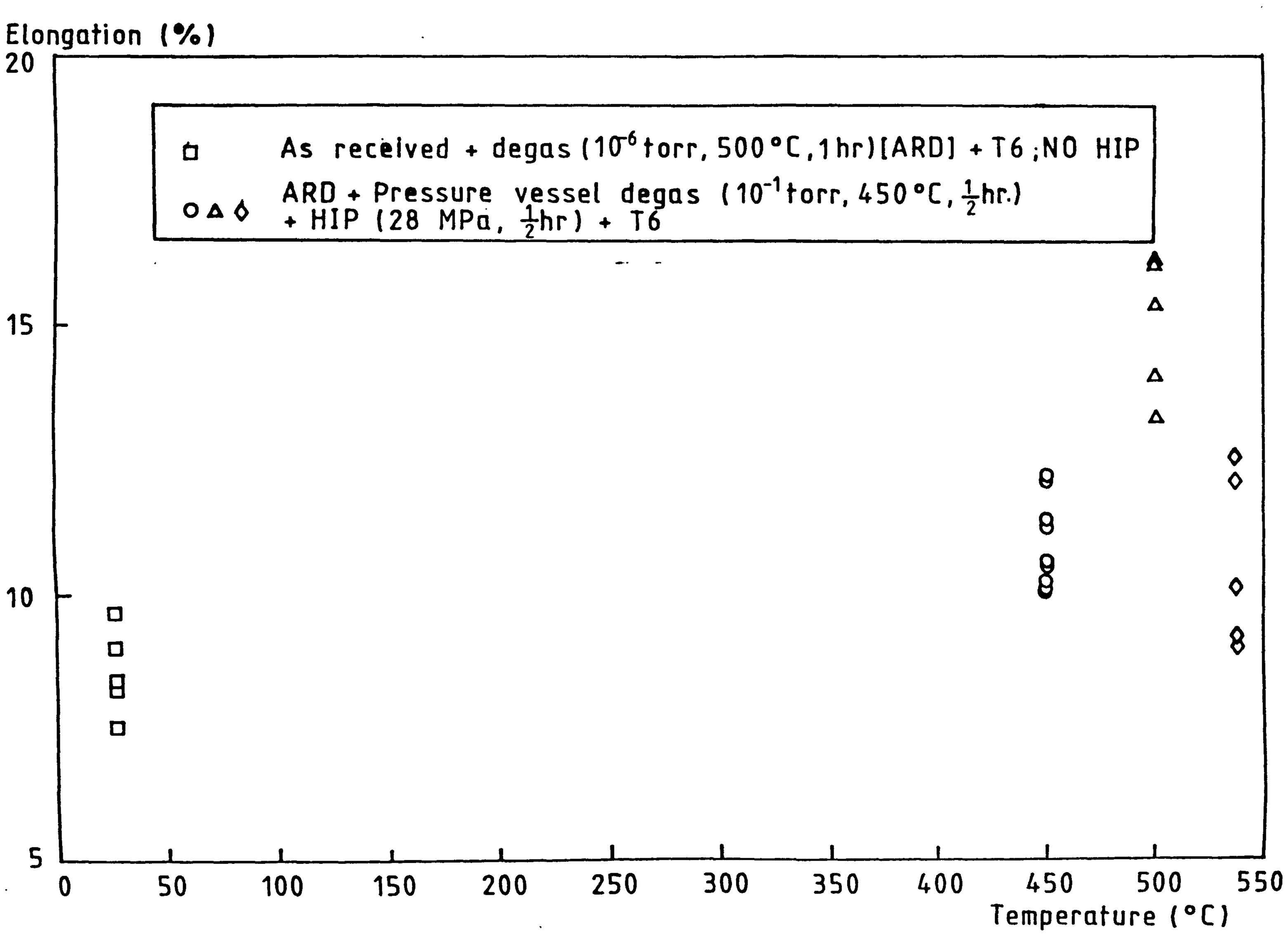

Figure 108 - The effect of HIP temperature on room temperature ductility of degassed SPF Supral 150.

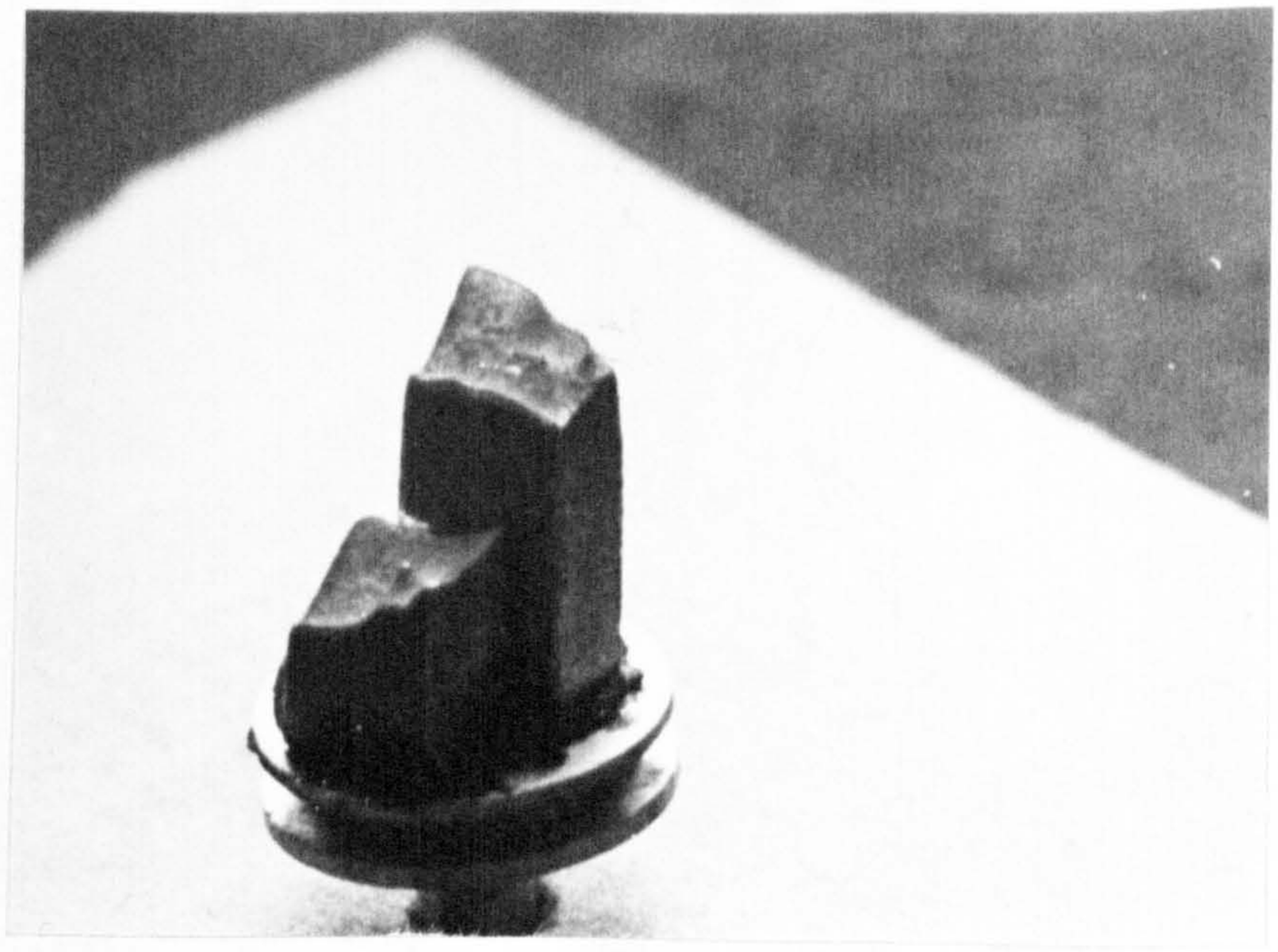

Figure 109(a) Photograph showing the fracture surface of virgin Supral 150 tensile test specimen. Note the 45° Shear fracture surface.

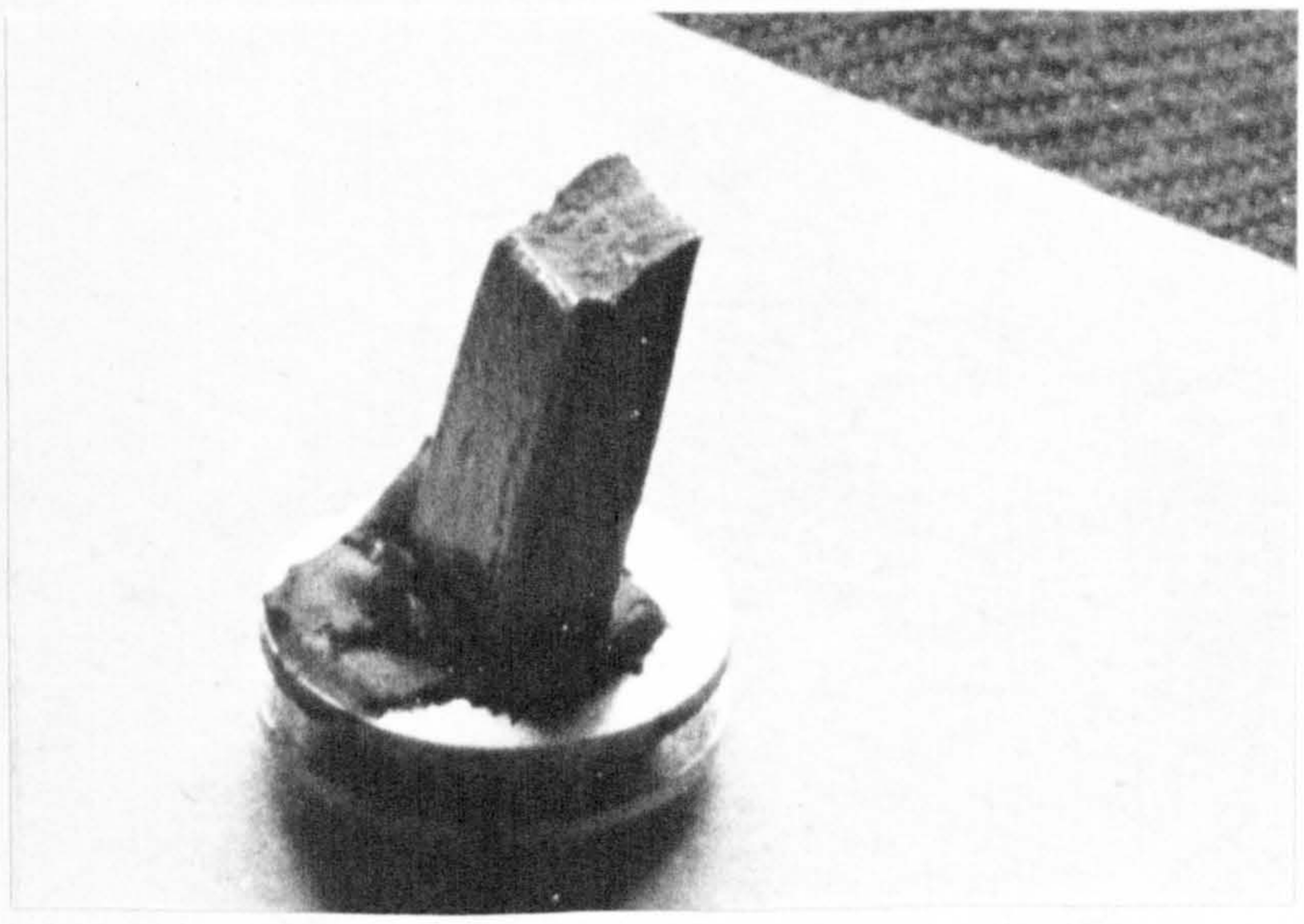

Figure 109(b) As above but HIPped (450°C, 28 MPa, ½hr) and T6 showing the ductile shear fracture.

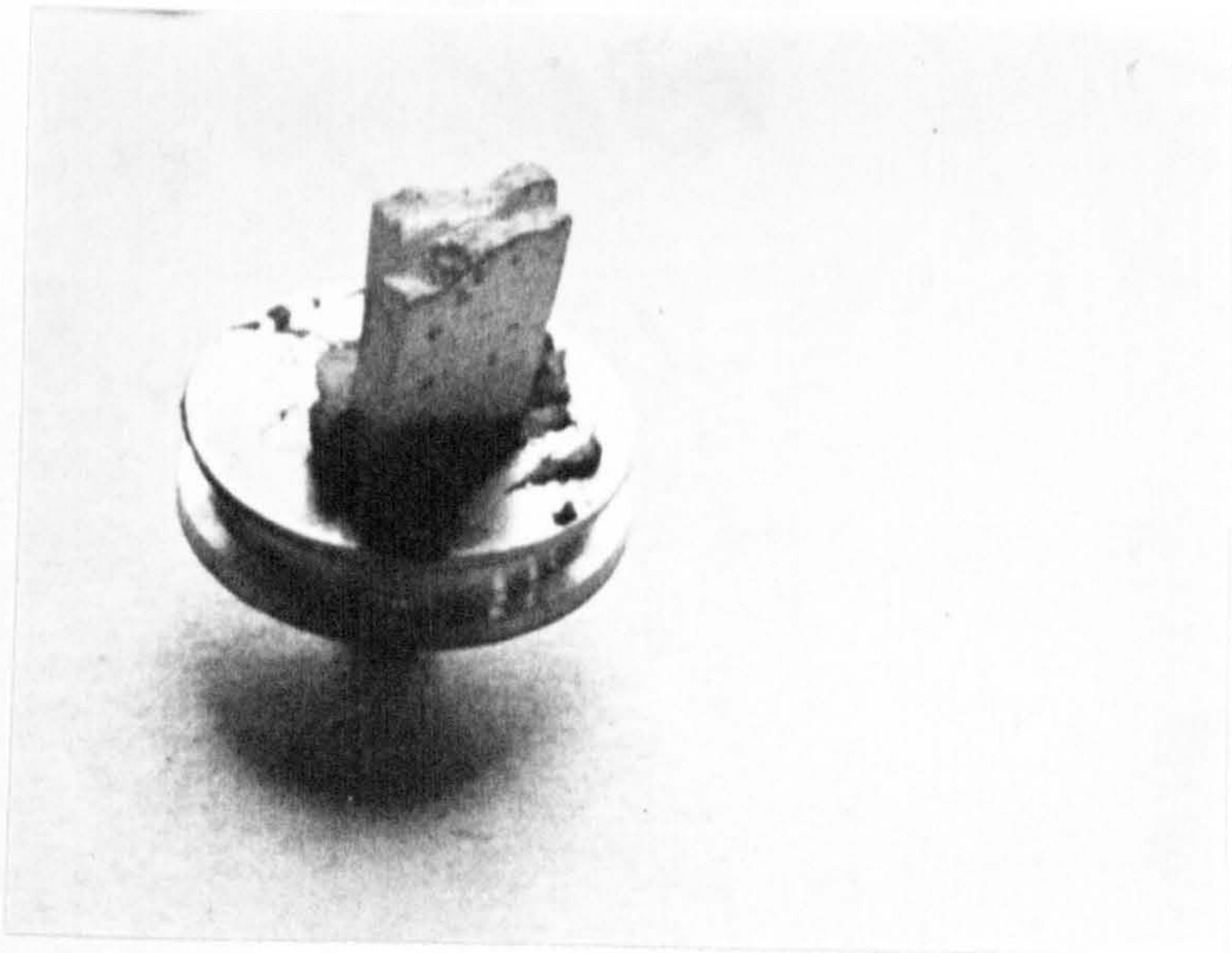

Figure 109(c) Fracture surface of SPF cavitated Supral 150; note jagged appearance where shear fracture direction is changed by cavitation.

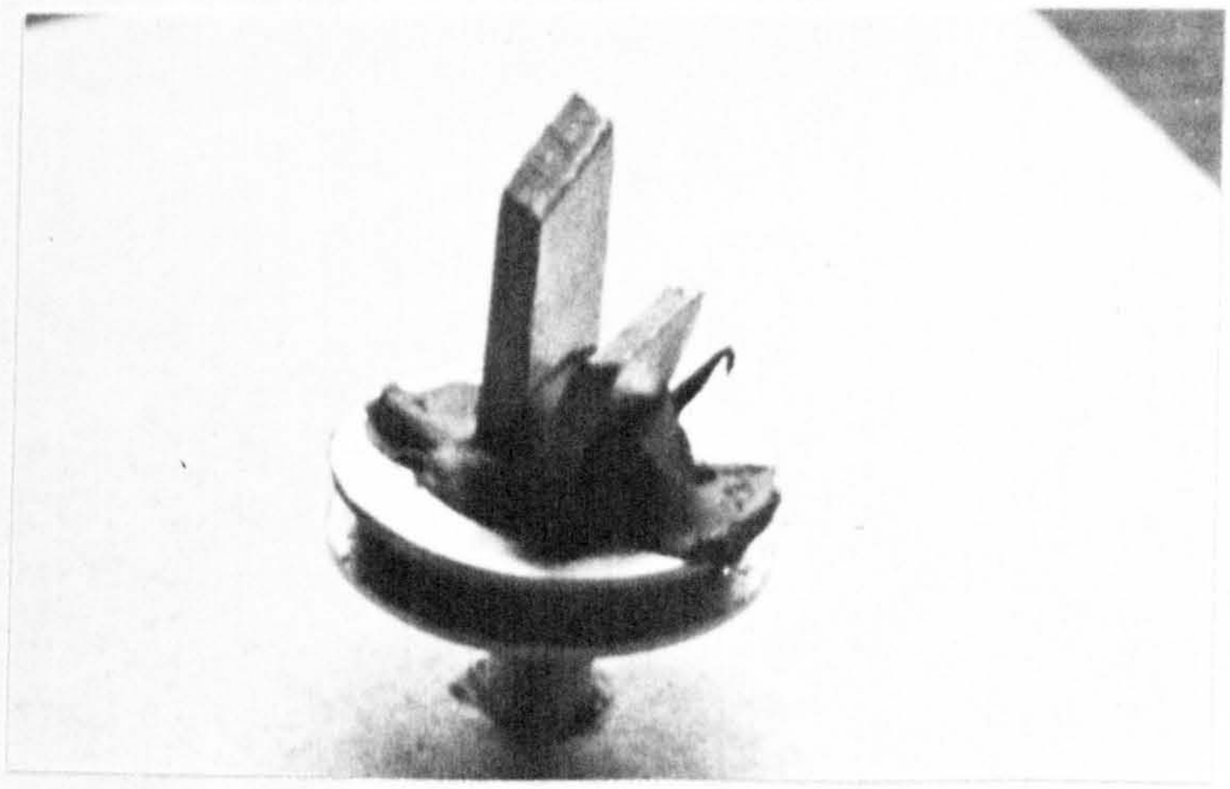

Figure 109(d) As above, but after HIP (450°C, 28 MPa, ½hr) and T6 showing the return to the 45° shear fracture seen in Figure 109(b).

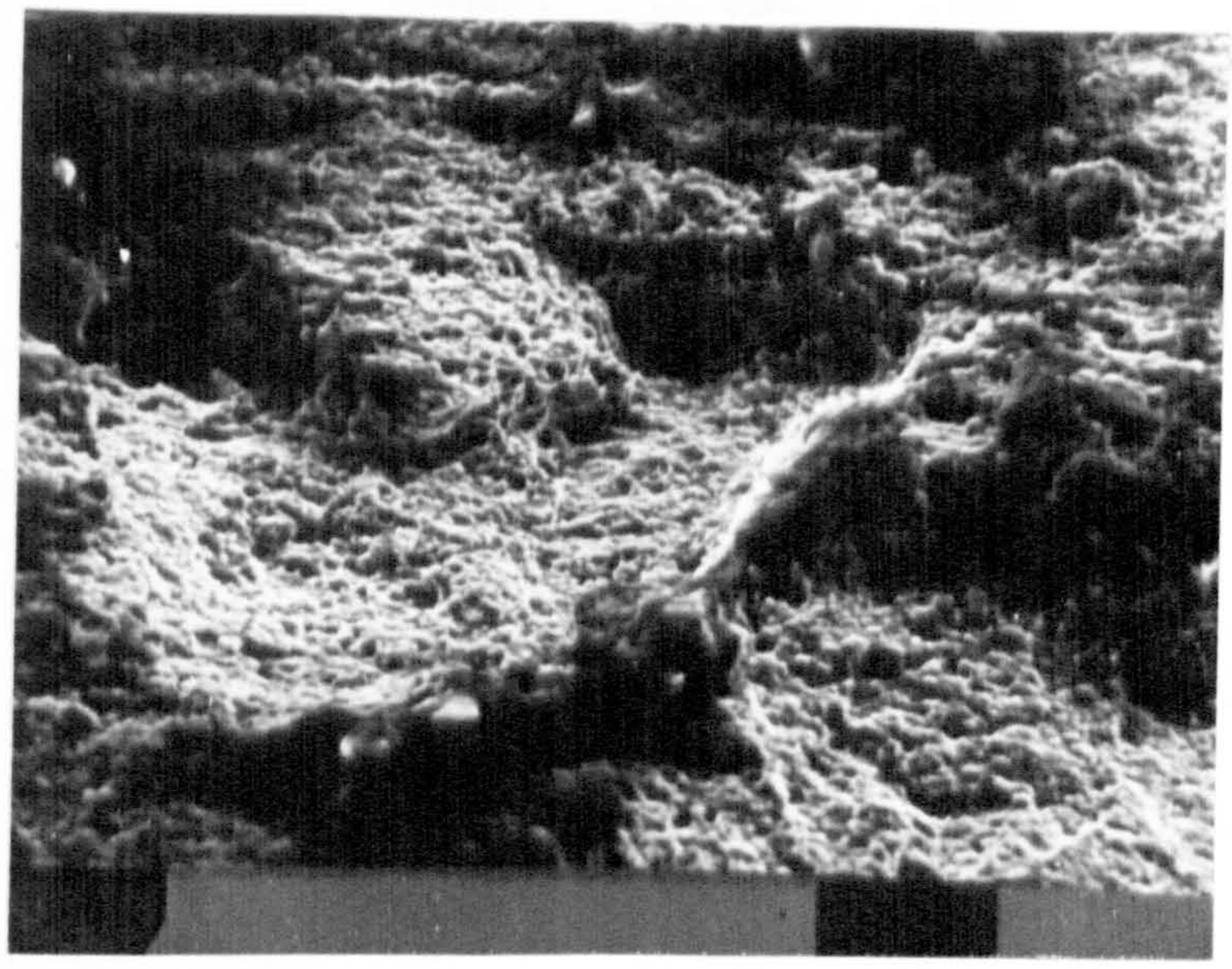

Figure 110 - SEM micrograph showing the cavitated nature of the fracture surface in Supral 150 tensile tested at room temperature.

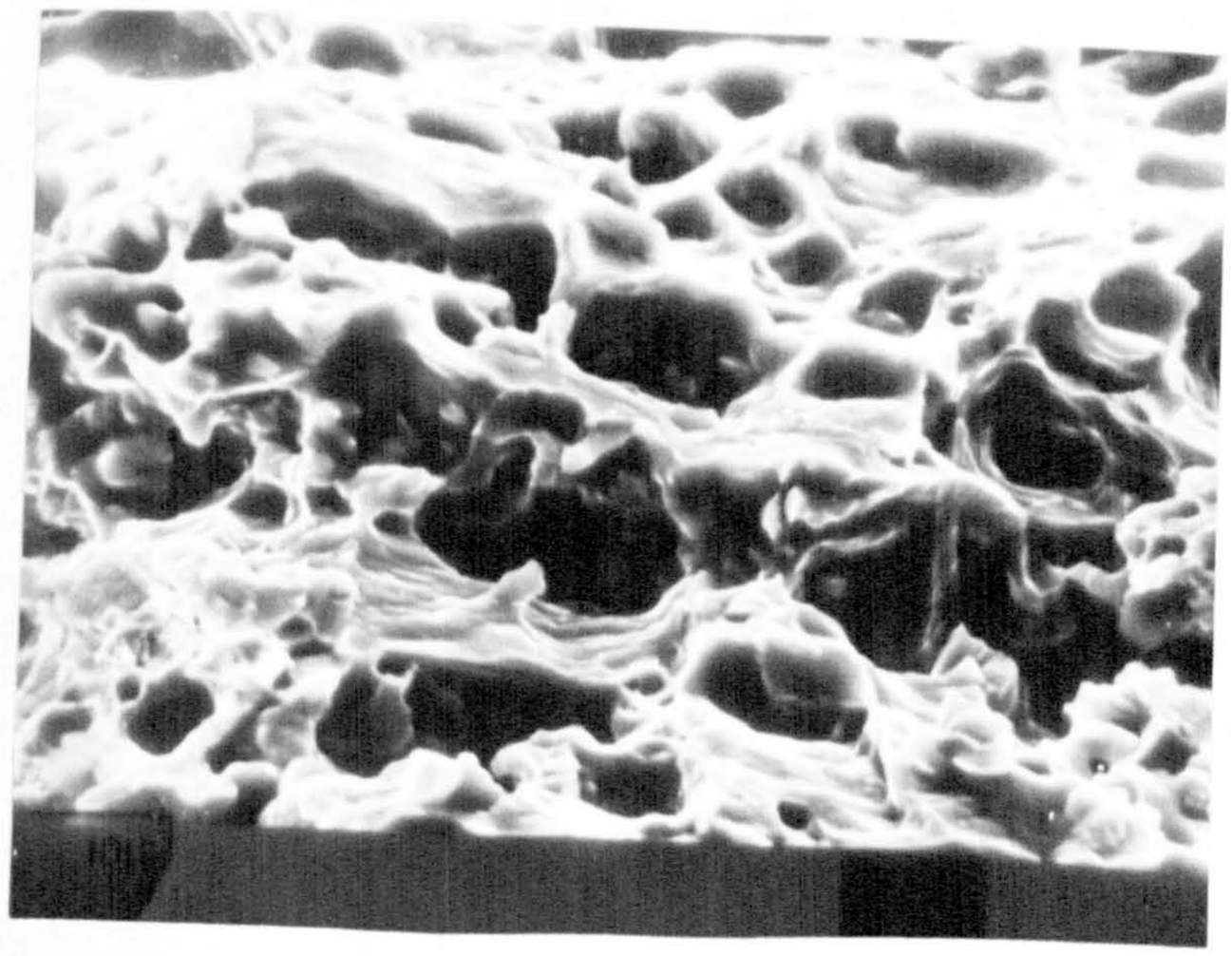

Figure 110(a) As above but showing failure by cavity interlinkage.